Optical Rephasing Techniques with Rare Earth Ion Dopants for Applications in Quantum Information Science

Patrick Matangaro Ledingham

A thesis submitted for the degree of
Doctor of Philosophy at the University of Otago,
Dunedin, New Zealand.

June 2011

Abstract

This thesis explores the use of cryogenic rare earth ion doped solids for applications in quantum information science. A theoretical analysis of optically rephased memory protocols, namely the two pulse photon echo, is developed. This analysis is a fully quantum mechanical analysis. The two pulse photon echo suffers from collective amplified spontaneous emission in the output mode due to gain along the direction of propagation. This noise can be 'rephased' with a π pulse, much like a two pulse photon echo, resulting in time separated nonclassical correlations. This thesis aims to characterize this noise and experimentally realize these nonclassical correlations.

A theoretical analysis is presented for a hybrid photon echo rephasing protocol. The protocol uses strong optical rephasing pulses as well as external electric fields to rephase coherence in a two level ensemble of atoms. The Stark effect is utilized to reduce the collective spontaneous emission caused by inversion. We find that the protocol is noise free and has a theoretical maximum efficiency of 54% in the forward direction and 100% in the backward direction.

The necessary task of laser frequency stabilization is presented in this thesis. The laser is locked using electronic and optical feedback, named the 'hybrid' lock. A theoretical analysis is presented as well as experimental results. The laser locking was sufficient for phase stable photon echo experiments to be conducted.

Three experiments are presented in this thesis. The first experiment involved the characterization of the detection mode and the two pulse photon echo. Benchmark values are given to the photon echo efficiency, echo lifetime and Rabi frequency.

The second experiment is the characterization of the amplified spontaneous emission from inverting a two level ensemble of cryogenic rare

earth ions doped in a solid. These experiments were conducted on different optical depths on the inhomogeneous line of Tm^{3+}:YAG. We find that indeed there is phase independent noise after the inversion with a bandwidth given by the Fourier width of the inverting pulse. It was seen that the noise measured increased exponentially with the optical depth, as expected from the theoretical analysis.

The third experiment was the measurement of rephased amplified spontaneous emission and the nonclassical time separated correlation between the noise and the rephased noise. As outlined by the theory, the amplified spontaneous emission can be rephased with a π pulse. This experiment is implemented on different optical depths on the inhomogeneously broadened line of Tm^{3+}:YAG. For optical depths of 0.25 and greater, it was seen that the correlations were classical. For an optical depth of 0.046, the correlation was seen to violate the inseparability criterion. This violation of the criterion means that the ASE and RASE fields can not be described as a separable state. This correlation measurement was made with a confidence interval of 95.15%.

For Mum and Dad.

Acknowledgements

I first have to thank Jevon Longdell, the primary supervisor of my Ph.D. research. Your talent and expertise with experiments, theory, computer programming and electronics is inspiring and I owe the skills I have now to you. I am grateful for your guidance, support and friendship over the course of my Ph.D research. LTJ!

I must also thank Matt Sellars, the secondary supervisor of my research. Thank you for your giving me the opportunity to work in your lab and for the support over the years.

Thank you to members of the Physics department for the awesome environment that you have provided over the many years I have been here. The Physics department was like a home away from home, thank you for the great conversations and friendships, fast internet and heated rooms.

I would like to thank the staff of the mechanical workshop, Peter Stroud and Richard Sparrow. It always felt that my items were top priority and I thank you for the speed at which items were made for our lab. Cheers boys.

I would also like to thank the staff of the electronic workshop; Peter McCabe, Myles Thayer, Dave Hardisty and Barbara Buchanan. The skills, expertise and advice regarding electronic design was priceless in the construction and running of my experiments.

Thank you to Brent Pooley for cutting the 0.5mm thin crystal which led to the nonclassical correlation measurement.

Thank you to The University of Otago for providing the scholarship that payed for the Ph.D. fees and living costs. Thank you also to the Physics department for funding the oversees conferences I attended.

To my family, I thank you for all the support you have given over the duration of my undergraduate and postgraduate studies.

To all my friends in Dunedin and those who stalk me on Facebook, thanks for the good times. No doubt there will be many more good times to come.

Finally, thank you Rosanna for being there.

Contents

Contents **vii**

List of Papers **x**

List of Conferences **xi**

1 Introduction **1**

1.1 Outline of this Thesis 2

2 Rare Earth Ion Doped Media and Optical Rephasing **5**

2.1 Rare Earth Ion Doped Media 5

2.2 Probing the Inhomogeneous Line 15

2.3 Coherent Interaction of Atoms and Light 17

2.4 Optical Rephasing Techniques 20

3 Quantum Memory for Light **27**

3.1 Quantum Optical Memory 27

3.2 Current Quantum Memory Technology using Rare Earths 30

3.3 The Quantum Repeater 39

4 Theory of Optically Rephased Memory Protocols **47**

4.1 Quantized Maxwell-Bloch Equations 48

4.2 The Two Pulse Photon Echo 49

4.3 Amplified Spontaneous Emission 53

4.4 Rephased Amplified Spontaneous Emission 55

4.5 Implementation of RASE 63

4.6 Application to the DLCZ Protocol 65

4.7 Hybrid Photon Echo Rephasing 67

5 Experimental Description **75**
5.1 Laser . . . 75
5.2 Locking . . . 77
5.3 Hybrid Laser Locking . . . 81
5.4 Detection of ASE and RASE . . . 88

6 Experimental Techniques **95**
6.1 Experimental Set-up . . . 96
6.2 The Local Oscillator Mode . . . 99
6.3 Two Pulse Photon Echoes . . . 102
6.4 Optical Nutation . . . 108

7 Amplified Spontaneous Emission: Experiment **111**
7.1 Experiment with 20mm Crystal . . . 111
7.2 Experiment with 4mm Crystal . . . 115
7.3 Discussion . . . 117

8 Rephased Amplified Spontaneous Emission: Experiment **123**
8.1 Pulse Sequence . . . 123
8.2 Experiment with 20mm Crystal . . . 124
8.3 Experiment with 4mm Crystal . . . 132
8.4 Experiment with 0.5mm Crystal . . . 137

9 Conclusion **143**

Appendix A General Purpose Detector **145**

Appendix B Hybrid Photon Echo Rephasing - Workings **149**
B.1 Region 1 - before Stark shift . . . 149
B.2 Boundary 1 - Region 1 and 2 . . . 150
B.3 Region 2 . . . 151
B.4 Boundary 2 - Region 2 and 3 . . . 152
B.5 Region 3 . . . 153

Appendix C Rephased Amplified Spontaneous Emission - Workings **157**
C.1 Cauchy-Schwarz Inequality . . . 158
C.2 ASE and RASE Variance . . . 160
C.3 Commutation Relations . . . 160

C.4 Cauchy-Schwarz Inequality and Variance - Final Form 164

Appendix D Average Photon Number per Mode **167**

Appendix E Inseparability Criterion with a Heterodyne Detector **169**

References **173**

List of Papers

The following papers were published:

(I) P. M. Ledingham, W. R. Naylor, J. J. Longdell, S. E. Beavan, M. J. Sellars,"*Nonclassical photon streams using rephased amplified spontaneous emission*", Phys. Rev. A **81**, 012301 (2010). [1]

(II) J. W. Tay, P. M. Ledingham and J. J. Longdell, "*Coherent optical ultrasound detection with rare-earth ion dopants*", Appl. Opt. **23**, 4331–4334 (2010). [2]

(III) S. Beavan, P. Ledingham, J. Longdell, and M. Sellars, "*Photon echo without a free induction decay in a double-*Λ *system*", Opt. Lett. **36**, 1272-1274 (2011). [3]

The following paper has been accepted for publication:

(IV) D. L. McAuslan, P. M. Ledingham, W. R. Naylor, S. E. Beaven, M. P. Hedges, M. J. Sellars and J. J. Longdell, "*Photon echo quantum memories in inhomogeneously broadened two level atoms*", arXiv: 1104.4134v1. [4]

The following papers are to be published:

(V) W. G. Farr, J. W. Tay, P. M. Ledingham, D. Korystov and J. J. Longdell, "*Hybrid optical and electronic laser locking using spectral hole burning*", arXiv:1008.0229v1. [5]

(VI) P. M. Ledingham and J. J. Longdell,"*Noise and Correlations using the Two Pulse Photon Echo in* Tm^{3+}*:YAG*".

This thesis discusses papers I, IV, V and VI. Parts of paper V are discussed in the thesis of Tay [6]. Parts of paper IV are discussed in the theses of McAuslan [7] and Beavan [8]. Papers II and III are discussed in the thesis of Tay [6] and Beavan [8], respectively.

List of Conferences

I presented work featured in this thesis at the following Australasian, Asia-Pacific and international conferences:

(1) Australasian Conference on Optics, Lasers and Spectroscopy, ACOLS. Adelaide, Australia. November 2009.

"*Non-Classically Correlated Photon Streams Using Rephased Amplified Spontaneous Emission*".

P. Ledingham, W. Naylor and J. Longdell

(2) 10th Quantum Communication, Measurement & Computing Conference, QCMC. Brisbane, Australia. July 2010.

"*Coherent Characterization of Amplified Spontaneous Emission*".

P. Ledingham, S. Beavan, J. Longdell and M. Sellars

(3) 3rd Annual HOPE Meeting. Tokyo, Japan. March 2012.

"*Quantum Correlations using Strong Optical Pulses in Rare Earth Ion Doped Crystals*".

P. Ledingham and J. Longdell

(4) Conference on Lasers and Electro-Optics, CLEO. Baltimore, Maryland, USA. May 2012.

"*Quantum Correlations using Strong Optical Pulses in Rare Earth Ion Doped Crystals*".

P. Ledingham and J. Longdell

Chapter 1

Introduction

Entanglement is a key resource in quantum information science. The motivation of the research in this thesis starts with the desire to create entanglement over large distances in order to extent the range of quantum networks [9]. The concept of entanglement came from Einstein's dissatisfaction of the Copenhagen interpretation of quantum mechanics. In the famous paper by EPR [10], a source produces a pair of particles, A and B, in a quantum state, and then the particles move apart. Strong correlations exist between the position and momentum of the separated particles such that a measurement of the position of particle A, allows the prediction of the position of particle B, with certainty due to the correlation they share regardless of spatial separation. This is the key feature of entanglement motivating much research toward exploiting entanglement to be utilized for communication.

To achieve entanglement over large distances the *quantum repeater* was proposed [11]. This proposal draws similarities with quantum teleportation [12, 13], a protocol that exploits entanglement allowing the teleportation of a photon with an unknown state from one location to a spatially different location. For a quantum repeater, two entangled pairs are probabilistically created, for example, particles 1 and 2 (3 and 4) are entangled. The particles are distributed spatially such that particles 1 and 4 are located at remote locations A and C separated a distance L, whereas particles 2 and 3 are located at location B, a distance L/2 from both A and C. A Bell measurement [12] on particles 2 and 3 projects particles 1 and 4 into an entangled state. This process is know as entanglement swapping. The quantum repeater requires a quantum memory for light, as entanglement creation is probabilistic. For example, the entanglement in particles 1 and 2 can be stored with quantum memories, while the creation of entanglement takes place for particles 3 and 4. This

fact further narrows the motivation: We need a quantum memory for light.

One form of optical data storage is the well known photon echo memory based on optically rephasing of atomic coherence [14, 15]. Such memories have the capability to store large amounts of information at high bandwidth for long storage times, properties which make the photon echo a good candidate for a quantum memory for light. The question that motivates the entirety of this research is: *Can an optically rephased photon echo based memory be a quantum memory for light?*

1.1 Outline of this Thesis

This thesis consists of two parts. The first part contains background information on fields relevant to the research presented in this thesis. The first part of Chapter 2 details the optical properties of rare earth ion doped inorganic crystals, while the second part considers the coherent interaction between light and the atomic system with emphasis on techniques for the optical rephasing of atomic coherence. Chapter 3 contains a review of the quantum memory for light, in particular the techniques of controlled reversible inhomogeneous broadening (CRIB) and atomic frequency comb (AFC) that have recently seen an increased implementation in rare earth ion doped systems.

The second part of this thesis contains the theoretical and experimental work conducted throughout the duration of this Ph.D. research. The first research goal was to develop an analytical description of the quantum two pulse photon echo (2PE) allowing an investigation of the suitability of the 2PE as a quantum memory for light. This is presented in Chapter 4 as well as the new theory of creating time separated entangled photons using these optical rephasing techniques, which has been published in Paper I. Also detailed in this chapter is the analytical description of the hybrid photon echo rephasing (HYPER) protocol for a quantum memory for light, which is to be published in Paper IV.

Chapter 5 contains the details of the novel hybrid electronic and optical laser locking system developed for the experiments in Chapters 6, 7 and 8, which is to be published in Paper V. Also in this chapter are the details of the noise detection system.

The second research goal was to characterize the quantum noise in the 2PE. Chapter 6 outlines the experimental techniques used for the quantum noise measurements. Experiments of this nature were carried out in cryogenically cooled Tm^{3+}:YAG, and are presented in Chapter 7. The third research goal was to exper-

imentally realize time separated entangled photon streams, a scheme theoretically proposed in Chapter 4. The experiments are carried out on the inhomogeneously broadened two level system of cryogenically cooled Tm^{3+}:YAG. The results are presented in Chapter 8 which are to be published in Paper VI.

Finally, the thesis finishes with a summary of the results achieved. The future of the RASE protocol is discussed.

Chapter 2

Rare Earth Ion Doped Media and Optical Rephasing

This chapter is in two parts. The first part describes the atomic system used to perform quantum information processing experiments, namely rare earth ion doped systems. As we will see, these systems offer properties desirable for classical and quantum information processing. The second part of this chapter describes techniques that probe this type of system. Such techniques include spectral hole burning and photon echo phenomena using optical rephasing.

2.1 Rare Earth Ion Doped Media

Rare earth ions doped into solid state hosts have been studied extensively and have many optical applications. These include phosphors for lighting, solid state lasers [16], optical amplification waveguides in glasses [17] and polymers [18] and relevant to this thesis, classical information processing [15]. In this section we discuss rare earth ion doped media in the context of quantum information storage.

Chemical Properties

The rare earth series of elements (Table 2.1), often referred to as the Lanthanide series, are characterized by partially filled $4f$ orbitals inside filled $5s$ and $5p$ orbitals. Due to the strong spin-orbit coupling of the $4f$ electrons, it is energetically favourable to defer the filling of the $4f$ orbital and fill the $6s, 5s$ and $5p$ orbitals first, as these electrons have lower spin orbit coupling energies. Figure 2.1 shows that the $4f$ orbitals are spatially located inside the $5s$ and $5p$ orbitals.

Z	57	58	59	60	61	62	63	64	65	66	67	68	69	70
Name	La	Ce	Pr	Nd	Pm	Sm	Eu	Gd	Tb	Dy	Ho	Er	Tm	Yb

Table 2.1: The Lanthanide series. The series are the elements including and between lanthanum ($Z = 57$) and ytterbium ($Z = 70$), although this is not necessarily the common point of view. It is noted that promethium (Pm) is artificially prepared. The rare earth of which experiments are conducted in this thesis is thulium (Tm).

An interesting chemical feature of rare earth ions is that the ionic radii decreases as the $4f$ orbital is filled. This effect, known as the lanthanide contraction, arises due to the poor screening by the $4f$ electrons of the positively charged nucleus.

As mentioned earlier, rare earths can be doped into different hosts for the implementation of different optical applications. Here we consider the case of trivalent rare earth ions doped in inorganic crystal hosts, for example yttrium due to its similar size. Typical doping levels are of the order of 0.1% resulting in a small perturbation of the host crystal lattice.

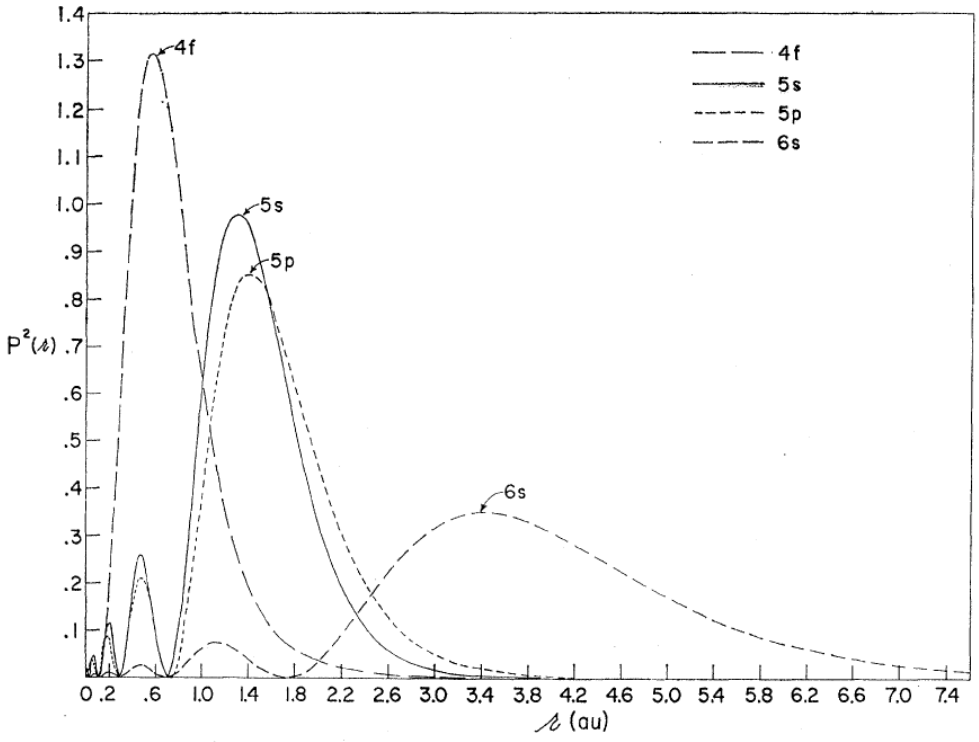

Figure 2.1: A theoretical prediction of the radial distribution functions of the orbitals of the rare earth ion Gd^+, illustrating that the $4f$ orbital lies spatially within the $5s$ and $5p$. Figure taken from [19].

Optical Properties

This section presents the interesting properties of the interaction of light with cryogenically cooled rare earth ion solids. This field of physics is well established with extensive investigations presented by A. A. Kaplyanskii and R. M. Macfarlane in [20] and G. Liu and Y. C. Sun in [16].

The optical properties of trivalent rare earth ions are primarily due to transitions between $4f^N$ states (see Chapter 1 of [16]). The level structure of rare earth ions doped in a solid host is similar to the free ion case. This is due to the fact that the transitions are shielded by filled outer orbitals, as explained in the previous section. When the host material is optically inactive, the system can be described as a frozen gas of ions, in the sense that it is like the free ion case with the exception that the ions have a fixed spatial position. One exception to this interpretation is the presence of *inhomogeneous broadening* [21] which is the broadening of the individual ions of *homogeneous* spectral width.

As there are many elements in the lanthanide series, different metals give rise to different transition wavelengths ranging from the visible to the infrared. In the context of quantum information processing, experiments focus on the use of europium (Eu), Praseodymium (Pr) , thulium (Tm), neodymium (Nd), and erbium (Er) as the dopants for often yttrium orthosilicate (YSiO), yttrium aluminium garnet (YAG) or lithium niobate (LiNbO). These metals have transition wavelengths of 580nm, 606nm, 793nm, 880nm and 1532nm respectively. The laser stabilization and RASE experiments in this thesis were conducted on thulium doped yttrium aluminium garnet (Tm^{3+}:YAG) at 0.1% doping. Results presented on the HYPER protocol were conducted in praseodymium doped yttrium orthosilicate (Pr^{3+}:Y_2SiO_5).

Energy Levels

As mentioned earlier, the optical transitions are shielded by full outer shells giving rise to 'free ion' type spectroscopy. For a free ion in a coulombic potential the states are degenerate. These degenerate states are split due to the strong spin-orbit interaction, giving rise to J-manifolds of states. This splitting gives rise to the optical transitions. It is noted that the effect of the host on these transitions is small and is generally treated as a perturbation. The energy levels for trivalent rare earth ions embedded in lanthanum trichloride are shown in Figure 2.2. The energy levels are similar for other hosts, since they are mostly determined by the strong spin-orbit interaction, rather than the crystal field interaction.

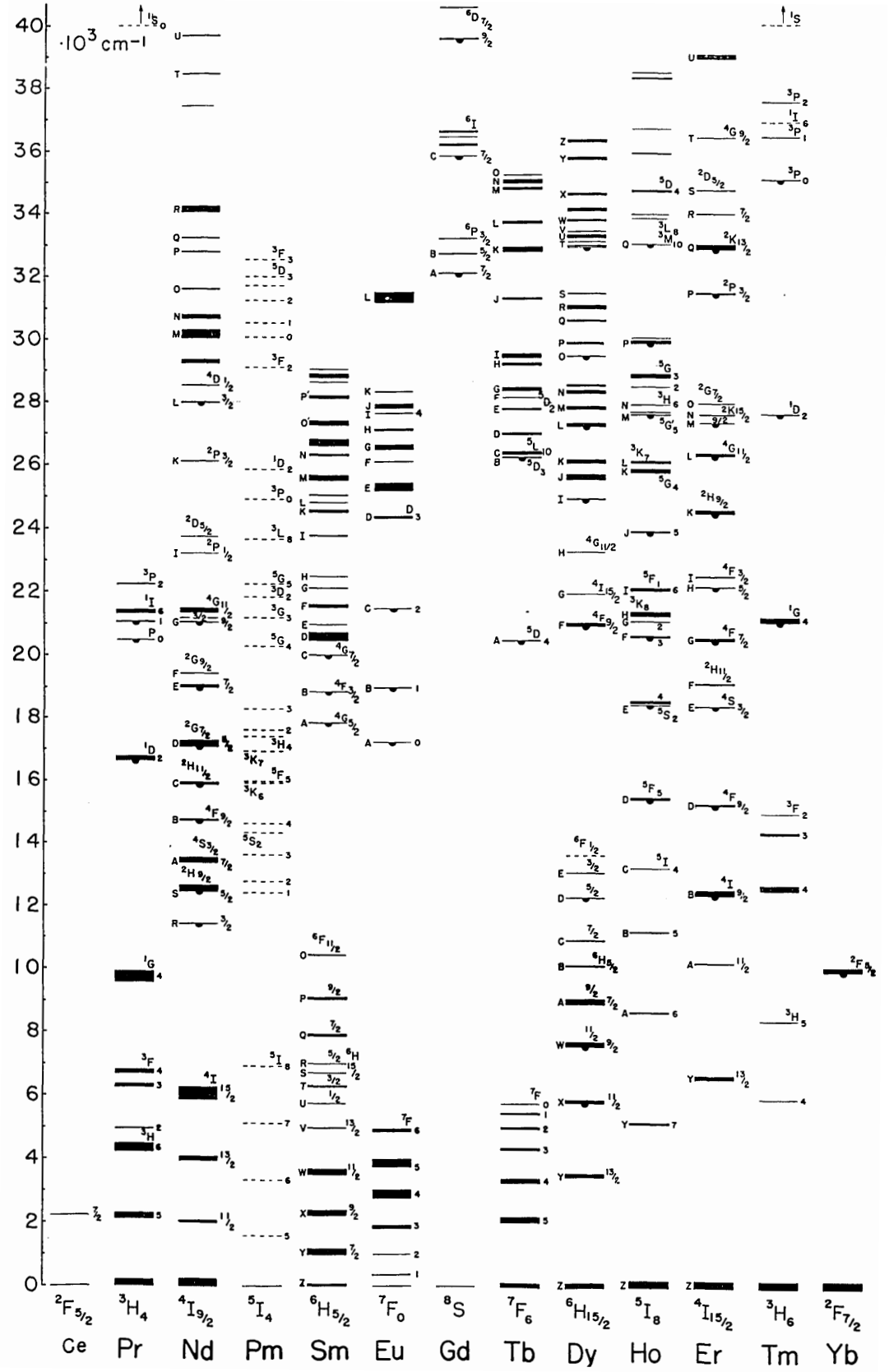

Figure 2.2: The Dieke diagram as seen in [22], showing the energy levels of trivalent rare earths.

The crystal field interaction splits the J-manifolds into at most $2J + 1$ levels with separation ranging from 10 - 100cm^{-1}. It is noted that J are approximately good quantum numbers and the labeling of states is that of the free ion states (e.g. ^{3}H$_4$, ^{3}H$_6$). The higher energy '$2J + 1$' levels of the manifold usually relax rapidly thorough phonon emission thus we restrict ourselves to transitions of the lowest level of the ground state to the lowest level of an optically excited state. These 'lowest to lowest' transitions are referred to as zero-phonon lines as absorption and emission of phonons are not involved in these type of transitions. The transition we use in the RASE experiments described in this thesis is the ^{3}H$_6 \leftrightarrow ^3$ H$_4$ in Tm with wavelength 793nm.

Depending on the number of $4f$ electrons, even or odd, the rare earth ions form what are referred to as the non-Kramers or Kramers ions, respectively [23]. For Kramers ions, due to the unpaired electron, the state levels form a Kramers doublet with a magnetic moment of the order of the Bohr magneton. For non-Kramers ions, with even numbers of electrons, the levels are electronic singlets and the angular momentum is said to be 'quenched' by the crystal field, having zero angular momentum. An important exception to this is if the ions are located at sites with axial or higher symmetry, in which case non-Kramers doublets can occur, due to the non-zero angular momentum around the symmetry axis. These types of ions experience large first order Zeeman and hyperfine interactions with short dephasing times. For thulium, the number of electrons are even and the electronic levels are singlets thus no first-order interactions.

For rare earths with a nuclear spin of greater than $\frac{1}{2}$, the levels are split into hyperfine levels by second-order hyperfine and quadrupole interactions. For the case of Pr which has a nuclear spin of $\frac{5}{2}$, the hyperfine splittings are on the order of 10MHz for the ground state and 5MHz for the excited state in zero field [16]. For thulium, there is no zero field hyperfine structure due to the nuclear spin being $\frac{1}{2}$.

Homogeneous Broadening

The homogeneous linewidth Γ_h is the spectral linewidth of which an individual ion will absorb or emit light. The effect of shielding the $4f$ electrons minimizes the effect of broadening by phonons, resulting in very narrow 'lowest to lowest' widths. The broadening of an ion's resonance is due to dynamic processes and relaxation, and is the same for all ions. The linewidth is related to the coherence time as $\Gamma_h = 1/(\pi T_2)$, where T_2 is the coherence time. This width is temperature depen-

dent as thermal broadening (coupling to phonons) dominates at high temperatures. For liquid helium temperatures, i.e. $\sim$ 3K, contributions from phonon absorption and emission are negligible. For crystalline hosts, this results in linewidths on the order of a few kHz. When the dephasing processes have been minimized, linewidths approaching 122Hz have been reported for Eu^{3+}:Y_2SiO_5 [24] and 50Hz reported with Er^{3+}:Y_2SiO_5 [25].

In addition to phonon coupling, there are other mechanisms that can increase the homogeneous linewidth. One such process arises from fluctuating fields due to spin flips in neighbouring atoms. With this in mind, one wants to thus embed the rare earth ion in a host with low nuclear magnetic moments to minimize this effect. Silicates are an example of a host with low nuclear magnetic moment. Also, these fluctuations can be prevented with the application of an external magnetic field [26, 27]. This is an effective method, in particular, for ions with an odd number of $4f$ electrons [28] as the Kramers ions have short dephasing times due to magnetic interactions, as mentioned earlier. Non-Kramers ions in lower than axial symmetry sites have non-magnetic electronic levels giving rise to the long optical coherence times. Kramers ions can have long optical coherence times if large external magnetic fields are applied (e.g. 580 μs in [29])

Another contribution to homogeneous line broadening is instantaneous spectral diffusion [30–32]. This arises from ion-ion interactions, an effect that is actually desirable for quantum computing applications. The easiest way to minimize this effect is to decrease the doping level in the host hence increasing the distance between neighbouring ions. This effect is noticeable for ions undergoing optical excitation or a decay process as the interaction with neighbouring ions changes resulting in instantaneous frequency shifts of the neighbouring ion.

With such narrow homogeneous linewidths, optical coherence times approaching ms timescales are achievable, which is an exciting prospect in the context of quantum information storage.

Inhomogeneous Broadening

Rare earth ions are embedded in a crystalline host of finite size. Hence, the ions at different locations in the lattice experience slightly different crystal strain effects [21, 33, 34]. This results in the transition frequency of ions to differ from other ions, causing inhomogeneous broadening of the absorption line. The absorption profile of an ensemble is the sum of the homogeneously broadened lines of the individual ions

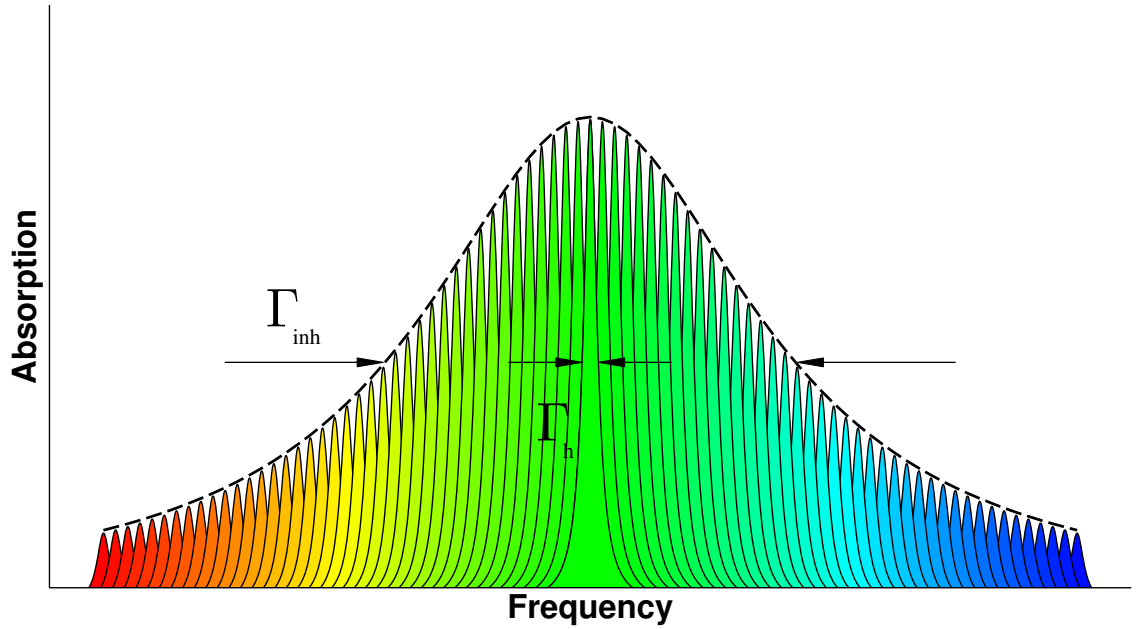

Figure 2.3: Inhomogeneous broadening. Variations in the crystal strain causes the resonant frequency of ions to shift relative to others dependent on the location of the ion in the crystal. The inhomogeneous broadening is illustrated by the broad dashed line with the FWHM labelled Γ_{inh}. The homogeneous line is labelled Γ_h and it is seen that the inhomogeneous line is greater than that of an individual ion's linewidth. The height of an individual line is indicative of the atomic density such that a high peak means lots of absorbers and a low peak means few absorbers. The figure is not to scale, the ratio between the lines can be 10^8 [25, 37].

(see Figure 2.3). The effect is similar to the effect seen in gases, where the resonance is Doppler shifted dependent on the atoms relative motion to the light source.

Typical inhomogeneous linewidths, Γ_{inh} are on the order of 1 up to 100's of GHz. The linewidth is increased as the doping concentration is increased since more impurities leads to more interactions and crystal strain [35]. Hence, narrow inhomogeneous widths are achieved with low concentration doping. Using low strain, isotopically pure crystal hosts, inhomogeneous widths as narrow as 40MHz have been reported [36].

At cryogenic temperatures, the inhomogeneous broadening is orders of magnitude greater than the homogenous broadening. Hence, an individual ion only interacts with light of particular frequency, meaning that different groups of ions can be addressed by tuning the frequency of the source, the size of the group determined by the linewidth of the source. The capacity for information processing is determined by the number of frequency classes available. The minimum frequency width of a class of ions is the homogenous width Γ_h. The capacity is then the ratio of inhomogeneous

to homogeneous broadening Γ_{inh}/Γ_h. For rare earth ion doped media, this ratio is on the order of 10^8 [25, 37], making the system ideal for information processing and storage.

Hyperfine Levels

We now discuss hyperfine level theory. Many quantum memory applications require the presence of hyperfine levels for the long lived spin coherence time and for the use of population management (see Chapter 3).

For non-Kramers ions in sites with lower than axial symmetry, there is no first order hyperfine interaction ($I \cdot J = 0$). In this case, the Hamiltonian that describes the hyperfine structure is given by [16]

$$H_{\text{hfs}} = P\left[I_z^2 - \frac{1}{3}I(I+1) + \frac{\eta}{3}(I_x^2 - I_y^2)\right] \tag{2.1}$$

where P and η describe the nuclear electric quadrupole interaction, and I is the nuclear spin quantum number. In the zero magnetic field regime, for ions with nuclear spin greater than 1/2 these levels are doubly degenerate. In zero field, it is clear that there is no hyperfine structure for the case of ions with nuclear spin equal to 1/2, a case applicable to thulium. The levels are labelled with the quantum number I, for example for Pr with $I = 5/2$, $|\pm 1/2\rangle, |\pm 3/2\rangle, |\pm 5/2\rangle$. Hyperfine level separations differ for different isotopes and for different crystal hosts.

The hyperfine levels can have long storage times (e.g. [38]). Coherence can be transferred from an optical transition to a hyperfine level by optical pumping or by using radio frequency fields resonant with the hyperfine transition. At cryogenic temperatures where the phonon interactions are low, the ion population relaxes due to spin-spin interactions with the host nuclei. As mentioned earlier, the effect of fluctuating magnetic fields of the host can be inhibited by the use of an external static magnetic field. In fact, significant improvements to coherence times can be achieved with the correct external magnetic field size and orientation, Zeeman shifting the levels so that the levels become insensitive to magnetic field fluctuations. Using this technique, coherence times of 82ms were achieved for Pr^{3+}:Y_2SiO_5 [39]. This value was further improved by using dynamic coherence control [40], yielding a coherence time of 30s.

The hyperfine transitions are inhomogeneously broadened for identical reasons to the optical transition. Typical inhomogeneous widths are on the order of a few

tens of kHz [34, 41, 42].

Stark Shifts

The energy levels of the ion can be manipulated using what is known as the Stark effect [43]. Of particular interest, in the context of CRIB (Chapter 3) and HYPER (Chapter 4), is the linear Stark effect, observable in rare earth ions in low symmetry sites. An applied electric field $\mathbf{E}_s$ shifts the energy levels of both the ground and excited states due to the interaction of the field with the permanent electric dipole moment of these states. A shift of the resonant frequency of the ions is given by

$$\Omega = -\left[\frac{\boldsymbol{\mu}_e - \boldsymbol{\mu}_g}{\hbar}\right] \cdot \mathbf{E_S}, \tag{2.2}$$

where $\boldsymbol{\mu}$ is the permanent dipole moment with the subscript indicative of ground (g) or excited (e) state. For low symmetry sites where the permanent dipole moment exists, and provided there is a difference in dipole moment between the ground and excited states, the Stark shifting effect is present. This is the case for $Pr^{3+}:Y_2SiO_5$, in which the CRIB protocol takes advantage of this to implement a quantum memory. For Tm^{3+}:YAG, there is no Stark effect as the permanent dipole moment of ions doped in YAG is small or almost vanishing, due to the high symmetry of the ion sites, as stated in [44].

Properties of Tm^{3+}:YAG

We now describe the properties of thulium doped into a YAG host, as this is the sample in which experimental work has been conducted in this thesis. This sample was chosen for its poor holeburning properties as to avoid random FIDs occurring after excitation. As mentioned earlier, the transition of interest is the 'lowest to lowest' transition $^3H_6 \leftrightarrow {}^3H_4$ which when doped into YAG has a transmission wavelength of 793.156nm in air (see Figure 2.4). There is also a metastable $^3F_4$ level in which population in the excited state can relax to via the short lived $^3H_5$ level [45].

For 0.1% doping, the excited state lifetime is $800\mu s$ [16]. The lifetime in the metastable $^3F_4$ state is on the order of 10ms, which allows for spectral holes to last for this timescale, relevant for locking a laser to a hole (Chapter 5). The literature value of the inhomogeneous linewidth on the 793nm transition is 20GHz [16]. The samples we used had an inhomogeneous width comparable to this.

When doping Tm into YAG, the Tm^{3+} ions substitute for the Y^{3+} ions which

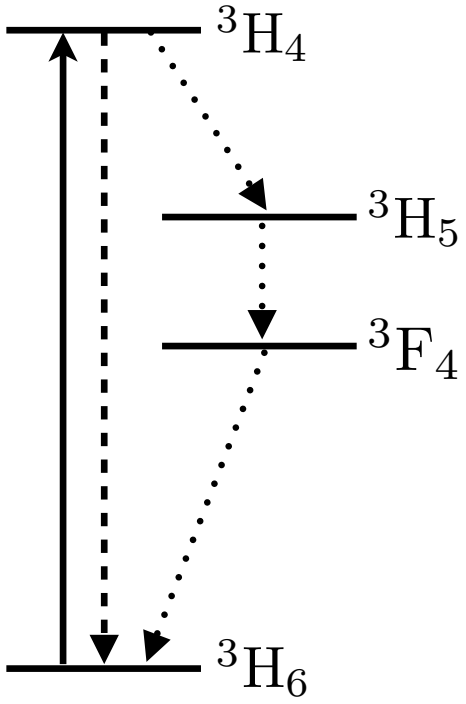

Figure 2.4: The energy levels of Tm^{3+} [16]. The 'lowest to lowest' transition of 793nm is indicated by the solid arrowed line. The excited state lifetime is 800 μs and population decays to the ground state via the same transition (dashed arrowed line). The population can also relax to the metastable $^3F_4$ state (lifetime $\sim$ 10ms) via the short lived $^3H_5$ state (dotted arrowed line).

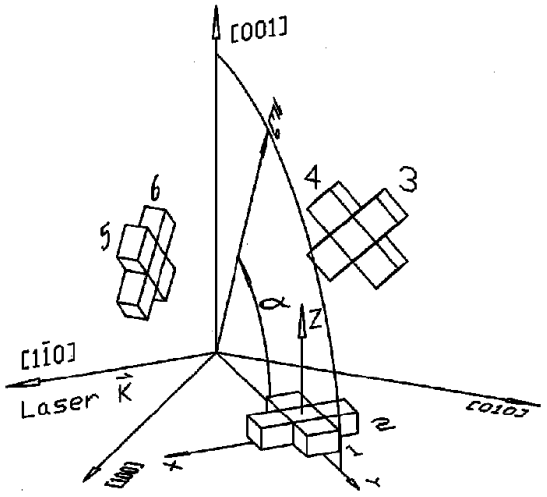

Figure 2.5: Orientations of the 6 sites of the Y^{3+} ion in YAG. The laser propagation is in the $[1\bar{1}0]$ direction with the polarization E_0 at an angle α with respect to the [110] axis. When $\alpha = 90$, i.e the polarization is along the [001] axis the dipoles at sites 3, 4, 5 and 6 are addressed. For $\alpha = 35.3$, i.e. polarization along the [111] axis, sites 1, 3 and 5 are equally addressed. Figure is referenced from [46].

are located in sites of D_2 point symmetry [46]. Figure 2.5 shows the site symmetry, where x, y and z are the local orthogonal C_2 axes for D_2 symmetry of site 1. The transition dipole moments lie along these axes. When light with electric field vector E_0 makes unequal angles with all 6 dipoles, unequal Rabi frequencies will result for different sites. Thus it is favourable to align the electric field vector either in the [001], or [111] axis to ensure a unique Rabi frequency. The [001] orientation gives equal angles with sites 3, 4, 5, and 6 and is perpendicular to sites 1 and 2. The [111] orientation gives equal angles with sites 1, 3 and 5 and is perpendicular to sites 2, 4 and 6. Addressing dipoles at equal angles results in one Rabi frequency given by $\Omega = -\vec{p} \cdot \vec{E_0}/\hbar$, where $\vec{p}$ is the transition dipole moment. For the experiments in this thesis, the laser propagates in the $[1\bar{1}0]$ direction and the polarization is adjusted to [001] giving one Rabi frequency visible in the optical nutation signal [46].

2.2 Probing the Inhomogeneous Line

We now detail techniques used to probe the inhomogeneous line of rare earth ion doped media. Provided one has access to a laser whose linewidth is as narrow or narrower than the homogeneous linewidth of the ion, one can access all the frequency registers in the inhomogeneous line. With the invention of tunable narrow line laser sources, such techniques became possible. Many of these techniques are detailed in [20]. Here we discuss the important techniques (in the context of this thesis) of spectral hole burning and optically rephased echos, namely the two pulse photon echo.

Spectral Hole Burning

As mentioned previously, the homogeneous line of rare earth ions can be 10^8 times smaller than that of the inhomogeneous line. A narrowband light source makes it possible to selectively excite ions at a particular frequency. After the ions are promoted to the excited state, a decrease in the absorption profile of the inhomogeneous line is formed, referred to as a *spectral hole*. In a two level system, the lifetime of the hole is exactly the excited state lifetime. For a system where there exists different states into which an excited ion can relax, population can be transferred to this state and the hole lifetime is increased, for example, in Tm^{3+}:YAG [16]. For materials which have hyperfine structure on the ground state (such as Pr^{3+}:Y_2SiO_5), population can be transferred to another ground state that is not resonant with the laser.

Since these ground states are long lived, *permanent spectral holes* are formed at the laser frequency. The hole burning spectrum is not as simple as a 'dip' where the laser burnt a hole. Consider the case of several ground and excited state hyperfine levels. Since the inhomogeneous broadening is so large compared to the hyperfine splitting, any narrowband laser resonant on the line necessarily is resonant with all possible transitions, but for different frequency subsets of ions. There will be *side-holes* at frequencies corresponding to the transitions from the ground state to each excited state level. There will be *anti-holes*, i.e. regions of increased absorption, in the hyperfine states to where the ions have been pumped. Thus, the effect of burning a hole at a single frequency actually gives rise to a complex pattern of side-holes and anti-holes, which gives you information of the hyperfine splittings.

Hole burning is a required feature for quantum memory protocols such as CRIB and AFC (see Chapter 3). The former requires a spectrally narrow feature to be prepared within a 'trench' burnt in the inhomogeneous line. For optimum operation the trench should have a low absorbing background. Spectral hole burning is important for the creation of the trench, redistributing the population to other hyperfine ground states. Optical pumping can be used to place ions back into the centre of the trench, and thus a narrow feature is formed. For the AFC protocol, again fine tailoring of the inhomogeneous line has to be done, in this case a series of absorbing peaks. Like CRIB, AFC requires a low absorbing background. Efficient optical pumping and spectral hole burning is vital for both these protocols.

In the context of this thesis, spectral hole burning is important for the stabilization of the diode laser used for these experiments. A spectral hole is burnt into cryogenically cooled Tm^{3+}:YAG and is used as the frequency reference for the locking. The hole lifetime in Tm^{3+} is $\sim$ 10ms [16], so a continuous wave beam is used to continually burn the hole, the intensity of the beam is low so as to avoid power broadening of the hole.

Although a spectral hole is required for locking the laser frequency, spectral holes are not desirable for the ASE and RASE experiments (Chapters 7 and 8). Hole-burnt features can lead to FID phenomena (see Section 2.4) resulting in unwanted coherent emission flooding the temporal mode of interest. This motivates the choice of Tm^{3+}:YAG as the sample, as this sample has a lower oscillator strength (compared to Pr^{3+}:Y_2SiO_5 for example) and hence it is inherently a poorer hole burning material. This fact aids in suppressing the unwanted FID phenomena mentioned earlier.

2.3 Coherent Interaction of Atoms and Light

Before describing the optical rephasing techniques that can be used to probe the inhomogeneous line of rare earth ions, we first establish the well-known theory of coherent interaction between atoms and light. The previous sections described the transfer of population between states using a light field of a specific energy. The requirement is that the energy of the light matches the energy difference between the states. Experiments conducted in this thesis involve the use of a *coherent* light source, i.e. a source of well defined phase. Theory of the coherent interaction between light and an ensemble of absorbers is well known [47, 48]. Essential to the understanding of the dynamics are the *Maxwell-Bloch equations* and the *Bloch sphere* representation. In this section the Maxwell-Bloch equations are presented with the application of the two pulse photon echo.

Maxwell-Bloch Equations

Two Level Atoms

It is assumed that the atomic system of interest is a two-level system. As outlined in the previous section, the energy levels of rare earth ions are vast in number, but the physics described by a two-level system is a sufficient description in many cases.

The state of a two-level atom is given by

$$|\psi(t)\rangle = c_g(t)|g\rangle + c_e(t)\mathrm{e}^{-i\omega_0 t}|e\rangle \tag{2.3}$$

where $\omega_0 = (E_g - E_e)/\hbar$ is the resonant frequency of the the atom, and the coefficients $c_g(t)$ and $c_e(t)$ are the probability amplitudes of states $|g\rangle$ and $|e\rangle$ respectively.

The interaction of an atom with a time varying electric field $\mathbf{E}(t)$ can be described by the perturbation $-\mathbf{d}\cdot\mathbf{E}(t)$ where $\mathbf{d}$ is the transition dipole moment. The Hamiltonian that describes the system is given by

$$H = H_0 - \mathbf{d}\cdot\mathbf{E}(t) \tag{2.4}$$

where H_0 is the unperturbed Hamiltonian for a free atom. The time evolution of the atom coupled to an electric field can be obtained from this Hamiltonian and the Schrödinger equation. This model only considers the interactions between the atom and the field with no consideration for relaxation processes. These will be considered later.

A monochromatic electric field with frequency ω can simply be described as $\mathcal{E}(t)\cos(\omega t)$. We define the generalized Rabi frequency as

$$\Omega_G = \sqrt{\Omega^2 + \Delta^2} \tag{2.5}$$

where $\Omega = \mathbf{d}.\mathbf{E}/\hbar$ and Δ is the detuning $\omega_0 - \omega$. Solving the Schrödinger equation in the rotating wave approximation gives the following solutions [49]

$$\begin{aligned} c_g(t) &= \left\{ c_g(0) \left[\cos\left(\frac{\Omega_G t}{2}\right) - i\frac{\Delta}{\Omega_G}\sin\left(\frac{\Omega_G t}{2}\right)\right] + i\ c_e(0)\left[\frac{\Omega}{\Omega_G}\sin\left(\frac{\Omega_G t}{2}\right)\right]\right\} \mathrm{e}^{i\Delta t/2} \\ c_e(t) &= \left\{ c_e(0) \left[\cos\left(\frac{\Omega_G t}{2}\right) + i\frac{\Delta}{\Omega_G}\sin\left(\frac{\Omega_G t}{2}\right)\right] + i\ c_g(0)\left[\frac{\Omega}{\Omega_G}\sin\left(\frac{\Omega_G t}{2}\right)\right]\right\} \mathrm{e}^{-i\Delta t/2}. \end{aligned} \tag{2.6}$$

In the rotating wave approximation, the counter-rotating terms proportional to exp[$\pm i(\omega_0 + \omega)t$] are neglected. These terms vary rapidly and average out to zero for timescales exceeding $1/\omega$.

A simple case to consider is when the initial conditions are such that the population is entirely in the ground state i.e. $c_g(0) = 1, c_e(0) = 0$, and the field is resonant with the transition i.e. $\Delta = 0$. The solutions then reduce to

$$c_g(t) = \cos\left(\frac{\Omega t}{2}\right), \quad c_e(t) = i\sin\left(\frac{\Omega t}{2}\right). \tag{2.7}$$

Physically, this means that a resonant field driving a two level atomic ensemble will cause the population to oscillate between the ground and excited states. These oscillations are known as *Rabi oscillations*, and the Rabi frequency describes the rate at which population transfer takes place. The product of the Rabi frequency and the interaction time (Ωt) determines the state in which the atoms are left in. This product is referred to as the *pulse area*. A pulse area of $\pi/2$ transfers the atoms into an equal amplitude superposition of the ground and excited states. A pulse area of π promotes the population entirely into the excited state i.e. inverting the medium.

Bloch Sphere Representation

A convenient way to visualize and understand the time evolution of a two level system subject to driving fields is the *Bloch sphere representation*. Here, different variables are used X, Y, Z which can be expressed in terms of the probability

amplitudes $c_g(t)$ and $c_e(t)$,

$$\begin{aligned} X(t) - iY(t) &= 2c_g(t)c_e^*(t) \\ Z(t) &= |c_e(t)|^2 - |c_g(t)|^2. \end{aligned} \tag{2.8}$$

Here, Z describes the probability of finding atoms in the excited state compared to being found in the ground state, referred to as the *inversion*. X describes the part of the atomic state that is oscillating in-phase with the driving electromagnetic field and Y describes the part of the atomic state that is oscillating out of phase with the driving electromagnetic field.

The atomic state can now be represented as a *Bloch vector* on the Bloch sphere, pointing from the origin to (X, Y, Z). For an atom in a pure state, the vector is normalized such that $X^2 + Y^2 + Z^2 = 1$. If the vector is used to represent an ensemble average, and dephasing and relaxation processes are included, the vector can point anywhere in the Bloch sphere. For the case where the ensemble is in the ground state, $Z = -1$ and $X = Y = 0$ since there is no coherence between ground and excited states. A vector of $(1, 0, 0)$ corresponds to a superposition state oscillating in-phase with the driving field. For a completely mixed state, the vector is $(0, 0, 0)$, meaning it is equally as likely to find the atom in any state.

The dynamics of the Bloch vector in the rotating reference frame are described by the optical Bloch equations [48],

$$\dot{X} = -\Delta Y - \frac{X}{T_\mathrm{d}} \tag{2.9a}$$

$$\dot{Y} = \Delta X - \frac{Y}{T_\mathrm{d}} + \Omega Z \tag{2.9b}$$

$$\dot{Z} = -\frac{Z - Z_{eq}}{T_\mathrm{inv}} - \Omega Y \tag{2.9c}$$

where the phenomenological decay constants T_d and T_inv have been included. The former is simply taking into account dephasing mechanisms, while the latter describes the relaxing of the atoms toward some equilibrium Z_{eq} in the absence of a coherent driving field.

In order to complete the description of the interaction between two-level atoms and a light field, a description of the action that the atoms have on the field needs to be considered. An ensemble of atoms can give rise to a macroscopic polarization which will affect the field given by Maxwell's wave equation. For an inhomogeneously

broadened medium , the polarization induced by the applied electric field is

$$P(z,t) = N|\mathbf{d}|\mathrm{Re}\left[\int_{-\infty}^{\infty}(X(z,t,\Delta) - iY(z,t,\Delta))\mathrm{e}^{-i(\omega t - kz)}g(\Delta)d\Delta\right], \tag{2.10}$$

where N is the number of atoms per unit volume and $g(\Delta)$ is the inhomogeneous line shape. As stated previously, the electric field is of the form $E = \mathcal{E}(t)\cos(\omega t)$ and $\mathcal{E}$ varies slowly allowing the use of the reduced wave equation

$$\left(\frac{\partial}{\partial z} - \frac{n}{c}\frac{\partial}{\partial t}\right)\mathcal{E} = i\frac{N|\mathbf{d}|\hbar\omega}{2n\epsilon_0 c}\int_{-\infty}^{\infty}\left[X(z,t,\Delta) - iY(z,t,\Delta)\right]g(\Delta)d\Delta \tag{2.11}$$

where n is the refractive index of the material. This equation (Equation 2.11) together with the optical Bloch equations (Equations 2.9) provide a complete description of the interaction between an ensemble of atoms and a coherent electric field.

Finally, a more compact form of both Maxwell and Bloch equations can be formed. Although not offering any additional physics, the compact form is useful for analytical investigation. The Maxwell-Bloch equations are

$$\frac{\partial}{\partial t}D = i\Delta D - i\Omega Z - \frac{D}{T_\mathrm{d}} \tag{2.12a}$$

$$\frac{\partial}{\partial t}Z = -\mathrm{Re}\left[\Omega^* iD\right] - \frac{Z - Z_{eq}}{T_\mathrm{inv}} \tag{2.12b}$$

$$\frac{\partial}{\partial z}\Omega = \frac{i\alpha}{2\pi}\int_{\infty}^{\infty} Dg(\Delta)d\Delta \tag{2.12c}$$

where the following definitions have been made: $D \equiv X + iY$ is the atomic dipole moment and $\alpha = (N\pi|\mathbf{d}|\hbar\omega)/(n\epsilon_0 c)$ is the optical depth parameter. These equations form the basis for the analytical theory presented in Chapter 4.

2.4 Optical Rephasing Techniques

We now describe some optical rephasing techniques used to probe the inhomogeneous line. The theory that describes these coherent transient phenomenon is outlined in the previous section. First, the two pulse photon echo is described. This particular technique is the centre point of this research. We also briefly describe the three pulse photon echo.

The Two Pulse Photon Echo

The two pulse photon echo using optical transitions in solid state systems was first realized by Kurnit, Abella, and Hartmann in 1964 [50]. Here, Q-switching lasers where used on ruby. In 1966 the article entitled 'Photon Echoes' was published by I. D. Abella, N. A. Kurnit, and S. R. Hartmann [51] where similar methods were used. Spin echo phenomena pre-date these experiments. In 1950, Hahn published the appropriately titled Physical Review article 'Spin Echoes' [14], the first realization of echo phenomena. Here, strong RF pulses were used on spin ensembles in liquids, making use of nuclear magnetic resonance. Indeed spin echos provided inspiration and motivation for similar experiments using electric dipoles and optical frequencies.

We first introduce the phenomenon known as *free induction decay*. If a strong, brief pulse of light (t_p) is incident on an inhomogeneously broadened ensemble of atoms in the ground state, excitation of a particular bandwidth of ions occurs. The bandwidth is given by the inverse of the pulse duration ($\nu = 1/t_p$) provided t_p is shorter than the coherence time T_2. In the Bloch sphere picture, if the pulse has an area θ, the state of the atoms will have a component in the $X - Y$ plane, resulting in an oscillating dipole moment and the atoms will radiate. The maximum dipole radiation occurs for a pulse of area $\pi/2$, where the state of the atoms is *in* the $X - Y$ plane. It is noted, for a perfect area π pulse, there is no component in the $X - Y$ plane. Immediately after the pulse of duration t_p, the atoms are oscillating in phase and strong coherent emission in the direction of the applied pulse will be the case. However, since each ion oscillates at a different resonant frequency due to the inhomogeneous broadening, the ions will quickly dephase, causing the coherent emission to decay. This is known as free induction decay or *FID*. For a large spread of frequencies, the FID will decay quickly, whereas the FID can be long lasting for a narrow band of excitation. The duration of the FID is approximately that of the exciting pulse. For the case of weak excitation there are no FID phenomena.

An FID can result from atomic shot noise on the absorption line. The absorption line inherently has 'structure' due to atoms being discrete. This structure occurs with a frequency interval given by the homogeneous linewidth of the atoms. A pulse of light incident on this structure can cause coherent ringing giving an FID with a timescale given by the coherence time.

We now describe the *Two Pulse Photon Echo* or *2PE* using the Bloch sphere picture. The pulse sequence is seen in Figure 2.6 and the corresponding Bloch dynamics are illustrated in Figure 2.7. First, a pulse ideally with an area of $\pi/2$

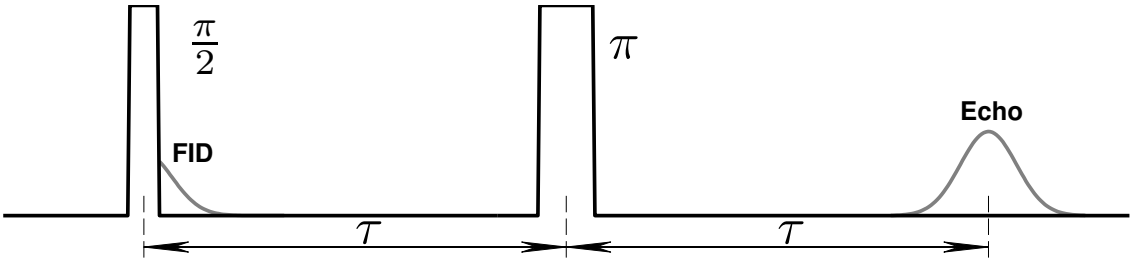

Figure 2.6: The two pulse photon echo sequence. The $\pi/2$ pulse causes coherent emission in the form of an FID. After a delay of time τ a π pulse is applied resulting in the coherent emission on a photon echo at a time 2τ with respect to the initial pulse.

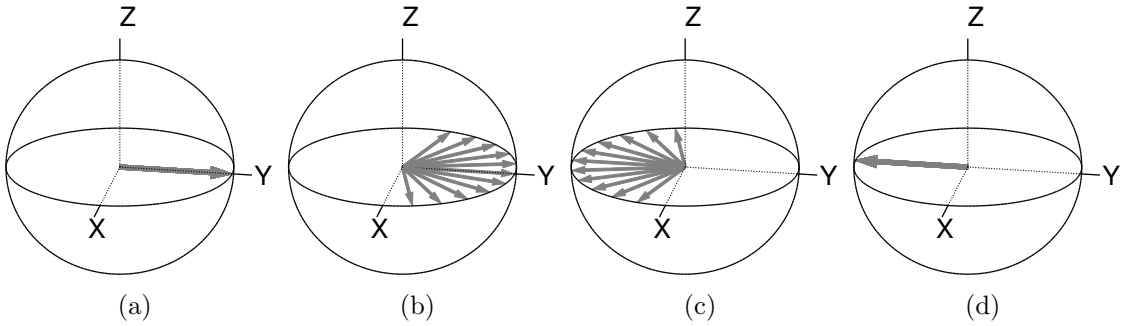

Figure 2.7: Bloch sphere representation of the two pulse photon echo. (a) shows the atomic state just after absorption of the $\pi/2$. At a time τ the ions have dephased as shown in (b). Directly after (b) a π pulse is applied rotating the vector about the X axis by 180° as shown in (c). After an additional time of τ the ions rephase and coherent emission results - the photon echo (d).

is incident on the ensemble, which causes a rotation of the atomic state up to the $X-Y$ plane. The axis of rotation is determined by the phase of the excitation field, in this simplified case about the X axis. The ions initially oscillate in-phase, but due to inhomogeneous broadening this coherence dephases and an FID results. Each ion acquires a phase difference relative to the laser at a rate determined by its detuning. After a time τ a pulse of area π is applied, rotating each Bloch vector through an angle of 180°, about the same axis as before. Atoms that acquired a negative phase difference start to acquire phase positively and vice versa. After a time of τ after the π pulse, the atomic state has rephased such that the ions once again oscillate in phase and strong coherent emission results. This coherent emission is referred to as the echo. It is noted that the first pulse need not be a $\pi/2$ and that a pulse that creates any population difference can be rephased.

The Fourier width of the π pulse determines the bandwidth of excitation. It

is important to note that the Fourier width of the π pulse is not optimal for all frequencies, since the probability of inverting an atom varies depending on the detuning that atom has from the driving field (see Equations 2.6). Furthermore, atoms driven off-resonantly will be rotated about an axis that has some angle with the X axis and is proportional to the atoms detuning. Ideally, the bandwidth of excitation wants to be narrow compared to the Rabi frequency. Thus, the 2PE benefits with large Rabi frequencies compared to the homogeneous line of the atoms.

The two pulse photon echo is a useful tool to measure the coherence time. As the delay between the $\pi/2$ and π pulse is increased, the atomic state relaxes to the ground state and therefore the amount of ions that get rephased by the π pulse decreases resulting in the decreased intensity of the echo. Hence, for delay times much larger than the relaxation time, no echo phenomena is seen.

Properties

The 2PE can be used to store spatial and temporal information of a laser pulse [15]. Further to this, the bandwidth of the 2PE can be broad. The bandwidth of operation of the 2PE is dependent on the Fourier width of the pulse, and the frequency distribution of the storage medium. For rare earth ion doped medium, the inhomogeneous broadening is on the order of 10's of GHz, so the bandwidth of the 2PE is limited mainly by the intensity of the laser and the ability to implement fast pulses. Recall from Section 2.3 that the pulse area is given by the Rabi frequency multiplied by the interaction time and that the Rabi frequency depends on the laser intensity. If one has access to large enough laser power, then the temporal width of the π pulse can be arbitrarily small and hence the bandwidth width can be arbitrarily large. Laser sources are readily available with powers on the order of 100mW easily achievable. Using acousto-optic modulators with appropriate RF fields can achieve pulse durations of 100's of nanoseconds, allowing for MHz bandwidths for the 2PE.

A method for broadband operation that does not suffer from power limitations is the optical rephasing using chirped pulses [52, 53]. Here, the bandwidth is determined by the frequency range of the chirp. The power needed in the chirped pulse is such that $\Omega^2 >> r$, where Ω is the Rabi frequency and r is the chirp rate (Hz s^{-1}).

The temporal multimode capacity of the 2PE is dependent on the bandwidth of the memory but also on the density of absorbers. The higher the density of absorbers, the more temporal modes that can be absorbed and rephased.It is noted

that this type of memory is a 'first in last out' (FILO) memory. High optical densities are easily achievable with rare earth ion doped media, by increasing the dopant level or by increasing the interaction length.

Using the Maxwell-Bloch equations it can be shown that the efficiency of the echo is $4\sinh^2(\frac{\alpha z}{2})$ where αz is the optical depth of the sample. A derivation of this is presented in Chapter 4, also see [54]. The efficiency of this protocol can be very high by choosing a highly dense ensemble of absorbers [55].

These properties make the 2PE implemented in rare earth doped media an excellent candidate for optical data storage, and in the context of this thesis, an excellent candidate for a quantum memory for light. The motivation for the research in this thesis is the suitability of the 2PE as a quantum memory for light. Chapters 4 and 6 show the analytical and experimental analysis of the 2PE as a quantum memory for light.

The Three Pulse Photon Echo

We now discuss the three pulse photon echo. The pulse sequence is shown in Figure 2.8. In this case, a $\pi/2$ pulse is used to create coherence in the $X-Y$ plane. Without loss of generality, we assume the phase of the laser is such that the atomic state is along the Y axis of the Bloch sphere. As always, the coherence will dephase due to the ions detuning. After some time τ_1 a second $\pi/2$ pulse is applied. Ions whose Bloch vector is in the positive-Y half of the $X-Y$ plane, will be rotated toward the excited state, whereas those with a negative-Y component will be rotated toward the ground state. Hence a periodic modulation of the population in the ground and excited states is created, referred to as a *population grating*. The application of a third $\pi/2$ pulse at a time τ_2 transfers the ions in the ground state to the positive-Y half of the $X-Y$ plane, and the excited atoms to the negative half. At a time of τ_1 after the third pulse, the ions have rephased and an echo forms.

Here the echo intensity depends on the excited state lifetime. If the excited state population is transferred to some metastable state, then the population grating in the ground state will remain and an echo will still form. An alternate method of creating the grating is to use many pulses separated by τ_1 allowing the build up of the population grating. The quantum memory technique known as the atomic frequency comb (AFC) uses exactly this technique [56].

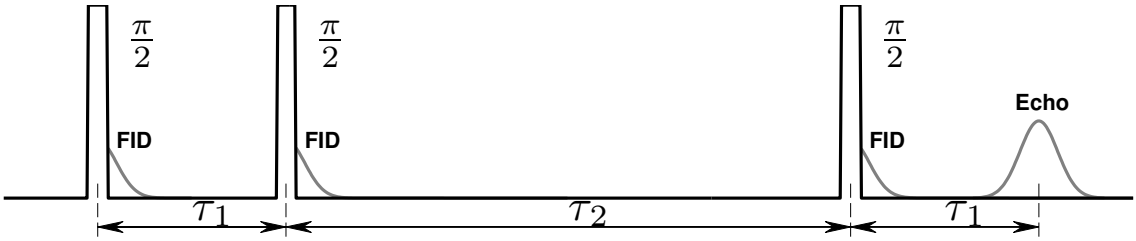

Figure 2.8: The three pulse photon echo sequence. A pair of $\pi/2$ pulses separated by τ_1 are applied creating a population grating. A third pulse is applied after a long delay at τ_2, and an echo is formed at a time τ_1 after the third pulse.

Chapter 3

Quantum Memory for Light

In the previous chapter the two pulse photon echo was reviewed. Being a rephasing technique, high bandwidths of memory can be achieved by having temporally short π pulses. The previous chapter also outlined rare earth ion doped media, an excellent system to implement rephasing memory protocols with due to the long lived coherence lifetimes, large inhomogeneous optical lines with narrow homogeneous linewidth atoms and the ability to easily have large optical depths.

In this chapter we review the quantum memory for light. Many review articles are available on the subject of the quantum optical memory [57–61]. Here, the technology is first introduced and we outline how it should perform and mention the potential applications this technology has. Then, the current technology is reviewed, with emphasis on the controlled reversible inhomogeneous broadening (CRIB) [62–70] and atomic frequency comb (AFC) [56, 71–74] techniques. Both techniques have been implemented thoroughly in rare earth ion doped media. We review the application of a quantum repeater using photon pair sources and a quantum memory for light.

3.1 Quantum Optical Memory

The research topic of quantum optical memories was inspired by the work done using a classical optical memory [15]. The development of quantum information and quantum communication theories [75] has also fueled interest in optical storage. These theories boast unprecedented computational capacity using a quantum computer (for certain problems) [75–80] and unconditional maximal communication security using quantum cryptography [81, 82]. Just like classical information pro-

cessing, quantum information processing (QIP) requires the capability to temporally store data. QIP requires a quantum memory for light.

A classical memory works by measuring the state to be stored and recording what it is in order to be reproduced at a later time. This type of memory does not work for the storage of quantum data. It is clear that the measurement process irreversibly collapses the quantum state to some eigenstate of the observable, hence changing the quantum information [83]. A quantum state can only be measured with a certain precision, as stated by the uncertainty principle [84] making the 'measure and prepare' quantum memory with high fidelity operation impossible. Also, the no-cloning theorem [85, 86] states that an arbitrary quantum state can not be cloned, meaning 'backing up' the data is not possible.

A quantum optical memory stores the quantum state of light without measuring it. The challenge is to reversibly map quantum information between photons and atoms. Photons are the ideal quantum information carrier where information can be encoded into the polarization of single photons or time-bin qubits can be used. Atoms are the ideal stationary carrier for the storage of quantum information.

Applications

The development of quantum optical memory technology would allow the implementation of a number of other technologies. One such technology is the implementation of a deterministic single photon source. Non-deterministic sources of entangled photon pairs can be achieved by using parametric down conversion and are a well developed technology [87–89]. One could realize a deterministic photon source by detecting one of the photons and storing the other photon in a quantum memory. Detecting one photon heralds the fact that the quantum memory has a photon stored in it and can be used as a single photon source. To implement the 'perfect' single photon source, the detection of the heralding photon needs to be near 100% and the quantum memory needs to be near 100% efficient. Deterministic single photon sources are important for the implementation of quantum computing and for some quantum repeater technology [90].

Another technology that the development of a quantum optical memory is vital for is the quantum repeater [11]. The quantum repeater enables the long distance communication of quantum states, essential for the development of a quantum network [9]. Distributing quantum states of light directly by using optical fibers suffers in that the communication channel is lossy at large (>100km) distances. The

quantum repeater overcomes this by distributing entangled states with the help of quantum memories. The protocol involves dividing the long communication channel into many elementary links, creating and storing entanglement on each link and then by using entanglement swapping extending the entanglement to the entire distance. A more detailed review of the quantum repeater will follow the review of quantum memories. The quantum repeater is only possible using quantum memories as entanglement generation is probabilistic, a quantum memory would allow the storage of entanglement on one elementary link, while other links are being prepared. With this in mind, the quantum memory needs to have high efficiency and long storage times.

Criteria and Requirements

It is useful to have figures of merit when assessing the performance of a quantum memory. In this section we discuss the criteria of a quantum memory for light.

The *fidelity* of a quantum memory is given by the overlap between the quantum state that is written to the memory and the state that is read out of the memory. For memories that store and re-emit single photons, the fidelity is given by the overlap of the single photon wave packet that was the input to the memory and the one that is the output of the memory. In this case it is referred to as the *conditional* fidelity, as the fidelity is conditional on the re-emmision of the photon. For memories that are designed to store general states of light for example coherent states, squeezed states, and cat states one considers the *unconditional* fidelity. A quantum memory with high fidelity is the experimental goal.

Another criteria to mention is the *efficiency* of the quantum memory. For memories that store and emit a single photon, it is simply the probability of emitting the stored photon. In atomic ensembles, collective interference effects can lead to efficiencies nearing unity. For single atom systems, the efficiency is often small but can be increased by the use of optical cavities. For memories that store general states of light, the efficiency is not always the best measure and the fidelity is more appropriate here. Even though the desirable efficiency is clearly 100%, it is not always necessary to have high efficiency for the memory to be useful.

Storage time is another very important criteria for a quantum memory for light. Again, it depends on the application which is being implemented. Long storage times are especially required for long distance communication protocols where the storage time needs to be at least longer than the time it takes to communicate to

distant nodes. For the quantum repeater, communicating a distance of L can only be achieved if quantum memories with storage times on the order of L/c or longer, where c is the speed of light in the channel [59].

Another measure of a quantum memory's practicality is the *bandwidth*. The bandwidth determines the repetition rate and the multiplexing capacity. Of course, the desired bandwidth is as large as possible. For example, when implementing a non-deterministic photon pair source, the photons are broadband. Hence one would require a broadband quantum memory to implement the deterministic single photon source outlined earlier. *Multimode capacity* is another feature a quantum memory should have. A large multimode capacity results in the ability to store several modes.

Finally, we mention the operational *wavelength* of the quantum memory. For long distance applications, it is beneficial to operate at a wavelength that is in the region of low absorption in optical fibers. For the quantum repeater that uses photon pair sources and quantum memories, one can down convert a photon to obtain a photon pair in which one of the pair is matched in wavelength to the quantum memory and the other of the pair is matched to telecommunication optical fibers. Alternate options do exist in the form of free space coupling and wavelength conversion techniques [91–93].

3.2 Current Quantum Memory Technology using Rare Earths

We now look at technology developed using rare earth ion doped media (see Chapter 2), namely the controlled reversible inhomogeneous broadening technique (CRIB) and the atomic frequency comb technique (AFC).

Controlled Reversible Inhomogeneous Broadening

This memory scheme involves rephasing coherence that was absorbed by an ensemble, much like the two pulse photon echo. The problem with optical rephasing techniques is that additional noise is added with the use of the strong optical fields used to trigger the rephasing mechanism, a phenomenon of which the major results of this thesis is based on. CRIB is a protocol that rephases with out adding noise.

The scheme was initially proposed in a gas and the rephasing of coherence is due to the fact that frequency shifts due to the Doppler effect are opposite for counter-propagating fields [62]. Here, we describe the scheme in a solid state rare

earth system [63, 64]. Figure 3.1 illustrates the protocol. This protocol starts with a narrow optically thick absorption line by selective optical pumping [94]. Then, using the linear Stark shift [43], a controlled inhomogeneous broadening of this absorption line is implemented by the application of an electric field gradient that shifts the resonant frequencies of ions at different positions by different amounts. When the line is broadened, an input state whose bandwidth matches the spectral width of the broadened line is absorbed by the line and the coherence naturally dephases. To recall the absorbed light, the sign of the electric field is changed and hence inverts the line about the central frequency. The coherence rephases and the light is re-emitted.

To understand the rephasing process, we see that atoms with a detuning Δ from the carrier accumulate a phase shift of $\mathrm{e}^{-i\Delta\tau}$ between absorption at $t = 0$ and electric field polarity switching at $t = \tau$. Switching the polarity of the external field triggers the inverting of the atoms detunings i.e $\Delta \rightarrow -\Delta$. Hence at a time $t = 2\tau$ the atoms accumulate an additional phase of $\mathrm{e}^{i\Delta(2\tau-\tau)}$ such that the sum of this accumulated phase and the previous one is zero. Hence the coherence rephases and light is re-emitted. It is noted that this protocol is similar to the two pulse photon echo in that the coherence is rephased in a similar way.

There is freedom to choose the orientation of the external field, either causing frequency shifting in the transverse or longitudinal direction with respect to the input pulse direction. In the simplest case, the re-emitted light propagates in the forward direction. To implement recalling in other directions, the coherence can be transferred to and from some auxiliary state using π pulses and the wave-vectors of the pulses used to do this determines the recall direction. For example, for counter-propagating π pulses, the input and output are counter-propagating. The efficiency has been calculated by others for different propagation and broadening cases [66, 95]. For transverse broadening and recalling in the backward direction the recall efficiency is

$$\eta_b^t = (1 - \mathrm{e}^{-\alpha l})^2, \tag{3.1}$$

where αl is the optical depth of the narrow feature after broadening, subscript b indicates backward propagation and superscript t indicates transverse broadening. This efficiency has been calculated assuming that the spectral width of the input pulse is small compared to the broadened absorbing feature. The efficiency can be seen as the probability of absorbing light squared. This is the case since the probability of re-emitting is identical to absorbing in the backward propagating case. It can be seen that in the limit of large optical depth, this efficiency can

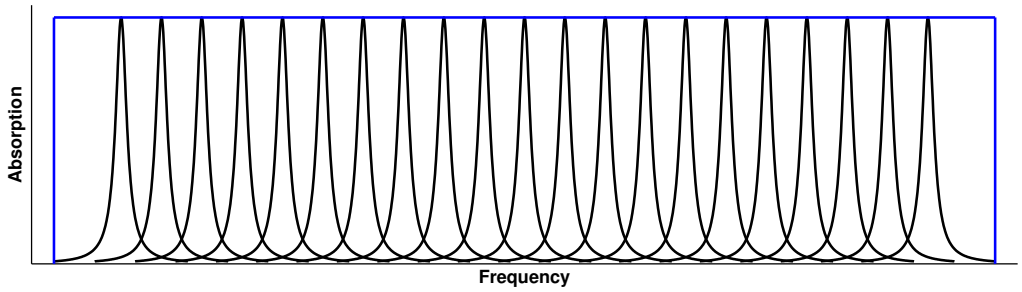

(a) Inhomogeneous Broadening

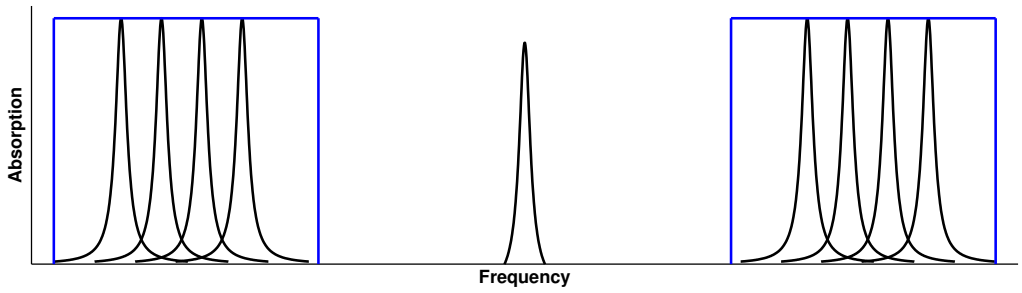

(b) Narrow Feature by Optical Pumping

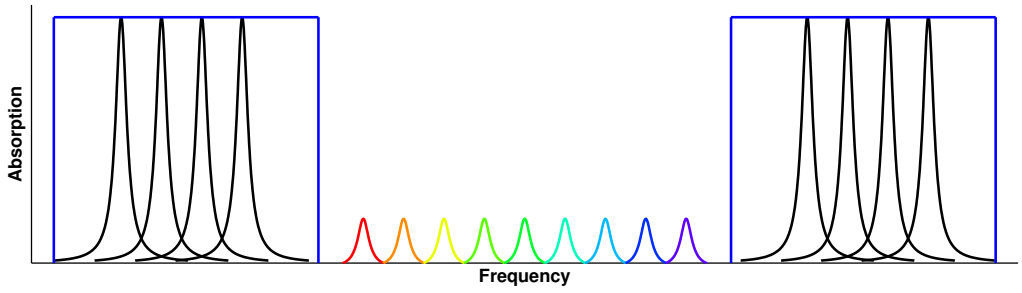

(c) Broaden Feature with External Field and Linear Stark Shifts

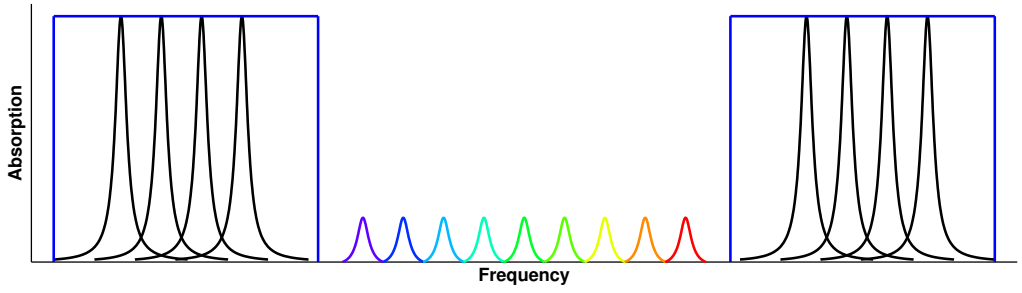

(d) Trigger Re-emission by Switching External Field Polarity

Figure 3.1: Controlled reversible inhomogeneous broadening. (a) shows the natural inhomogeneous broadening of a rare earth doped solid. The narrow feature seen in (b) is prepared by frequency selective optical pumping. An external field then broadens this feature seen in (c) in which a photon is absorbed. To trigger the re-emission (d) the electric field polarity is switched thus inverting the atoms detunings.

become unity.

For the case of recalling in the forward direction with transverse broadening, the efficiency is [66]

$$\eta_f^t = (\alpha l)^2 \mathrm{e}^{-\alpha l}. \tag{3.2}$$

In this case, the protocol suffers from reabsorption of the echo for large optical depths which results in a clear maximum efficiency of 54% for an optical depth of $\alpha l = 2$.

For the case of longitudinal broadening, that is, broadening such that the detunings of the atoms vary monotonically along the direction of propagation, the efficiency for both the forward and backward propagating cases is of the same form as Equation 3.1 [69, 96].

Experimental Realization

The first experimental realization of CRIB was realized by Alexander et al. in cryogenically cooled europium doped yttrium orthosilicate (Eu^{3+}:Y_2SiO_5) [64], where the transition of interest is near 580nm and the ground and excited states have three hyperfine states. A narrow feature of 25kHz and 40% absorption was prepared by first creating a 3MHz transparent window in the line by sweeping the laser, then pumping back an anti-hole at the centre of the window using RF and optical fields. This peak was then broadened using an electric field gradient applied with four electrodes in a quadrupole arrangement around the sample. The sample had an expected Stark shift of 35kHz Vcm^{-1} and the applied electric field was $\pm$25V giving around 2MHz of broadening. Input pulses of 1μs duration were absorbed into the sample and the electric field gradient was switched at a time $t = \tau$ to give an echo at $t = 2\tau$. The echo intensity decayed with a time constant near 20 μs. For this experiment the echo efficiency was limited by the low optical depth used. The narrow 40% absorbing peak after being broadened is reduced to 1% absorption.

More recently, a CRIB experiment was conducted that gave high efficiency storage [94]. In this seminal work the problem of preparing a highly absorbing feature with sharp frequency rolloff and low background absorption was overcome. The sample used here was cryogenically cooled praseodymium doped yttrium orthosilicate (Pr^{3+}:Y_2SiO_5) with an optical transition near 606nm and with three hyperfine states in the ground and excited state. The sample was long in the direction of pulse propagation and thin in the transverse directions. The feature was prepared by probing the sample with a focused beam from the front and a large unfocused

beam from the side. A broad spectral trench over the full length of the crystal was burnt into the absorption line by sweeping both beams ±7MHz. Then a narrow 140kHz feature was burnt back into the central 14mm of the crystal using a beam from the side (see the supplementary information of [94]). The feature had an absorption of 140 dB. This feature is longitudinally broadened to 1.6MHz with a monotonic electric field provided by a quadrupole electrode arrangement. The storage efficiency was 69% for a temporally Gaussian input of 0.6 μs and a delay of 1.3 μs. To date this is the most efficient demonstration of the CRIB technique. The technique also showed levels of noise added by the memory that were lower than the classical and no-cloning limits.

A demonstration of multimode capacity has been shown using Eu^{3+}:Y_2SiO_5 in which a train of four distinct pulses were stored and recalled [67]. The authors also demonstrated that phase information was preserved in the memory. The experimental parameters were identical to the case of the first proof of principle experiment mentioned earlier.

There has also been an implementation of CRIB at telecommunication wavelengths [70]. Here, the sample used was cryogenically cooled erbium doped yttrium orthosilicate which has a transition at 1536nm. The pulses stored were of duration 200ns and at the single photon level. The storage lifetime was 370ns. The efficiency was of the order of 0.2%, the limiting factor was a large absorbing background due to imperfect optical pumping when preparing the feature. Nevertheless, the authors demonstrated a proof of principle quantum memory at telecommunication wavelengths and at the single photon level.

Another implementation of the CRIB protocol has been realized in a Raman feature in a warm gas of rubidium, often referred to as the gradient echo memory (GEM). A three level lambda system is addressed with a detuned coupling beam on one leg of the lambda, allowing the ground states to form a two level system. The linear Zeeman effect is utilized and monotonic external magnetic fields are applied to this two level system. Like the CRIB protocol, the rephasing is triggered by switching the polarity of the applied external magnetic field. The first realization of this technique in warm rubidium was presented by [97]. The most recent realization of this technique was shown in [98]. Here, the efficiency of the protocol was 42% for a temporally Gaussian shaped pulse of duration 10 μs and with a storage time of 10 μs. Again, the limiting factor was the low optical depth achieved in the vapor. Multimode capacity was shown by the storing and recalling of four temporal pulses. The fact that one has the freedom to switch polarity of the fields and turn the

coupling beam on and off allowed the ability of recalling the stored pulses in any order, as well as temporal modification of the stored pulse width, albeit with reduced efficiency ($\sim 5\%$).

Atomic Frequency Comb

Realizations of the CRIB protocol showed high efficiency, low noise, quantum memories albeit with limited multimode capacity. It has been shown [99] that multimode capacity of EIT and Raman protocols scales as $\sqrt{\alpha l}$ and the capacity of CRIB protocols scales as αl for a given memory efficiency. Hence, obtaining large multimode capacity with high efficiency relies on seemingly unrealistically large optical depths. The atomic frequency comb protocol [56, 71] is a protocol in which the multimode capacity is independent of optical depth.

A description of the AFC protocol follows. The scheme requires the fine spectral tailoring of an inhomogeneous absorption line into a series of narrow absorbing peaks, often referred to as the teeth of the comb (see Figure 3.2). The peaks have a spectral width of γ, height αl and are separated by a spectral distance Δ. The width of the comb and hence bandwidth of the memory is thus proportional to the number of comb teeth N_p. After this comb has been prepared, an input pulse of spectral width greater than the tooth separation but less than the comb bandwidth is collectively absorbed by the teeth of the comb. It can be show that for the absorption process the comb is indistinguishable from a smoothly varying distribution with an effective optical depth $\tilde{\alpha} l$ [71]. After absorption, dephasing of the atomic coherence occurs due to atoms acquiring a phase of $\mathrm{e}^{i\delta_j t}$ where δ_j is the detuning of atom j. For a comb, the detunings are approximately a discrete set, i.e. $\delta_j = m_j \Delta$ where m_j are integers. It can be seen that for a time $t = \frac{2\pi}{\Delta}$ rephasing will occur and coherent echo like emission is the result.

The storage time of this protocol is dependent on the tooth separation Δ, so the on-demand nature that is seen in other memories is not a feature here. In order to implement on-demand retrieval of light and also to increase the storage time, the excitation can be transferred to a long lived ground state by using coupling fields during the storage process. The transfer 'freezes' the evolution of the atomic dipoles and the state is now stored as a spin excitation. Then, transferring back the spin state to the excited state triggers the dipoles to evolve to the rephased state. One can choose the direction of the retrieved light by choosing the propagation direction of the coupling beams that enable the transfer. If the coupling fields are counter-

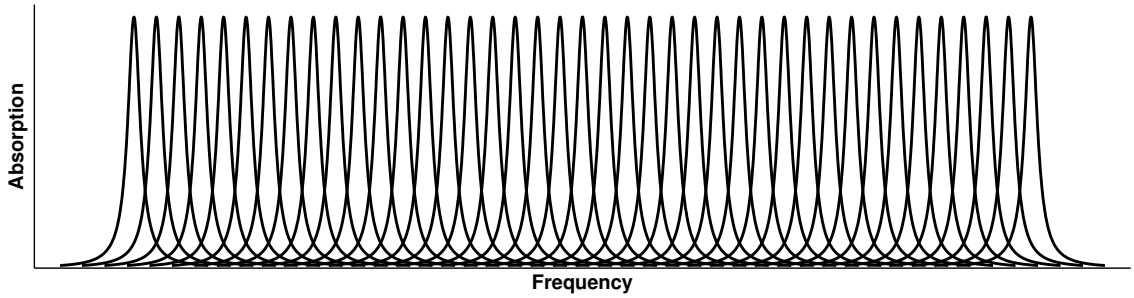

(a) Inhomogeneous Broadening

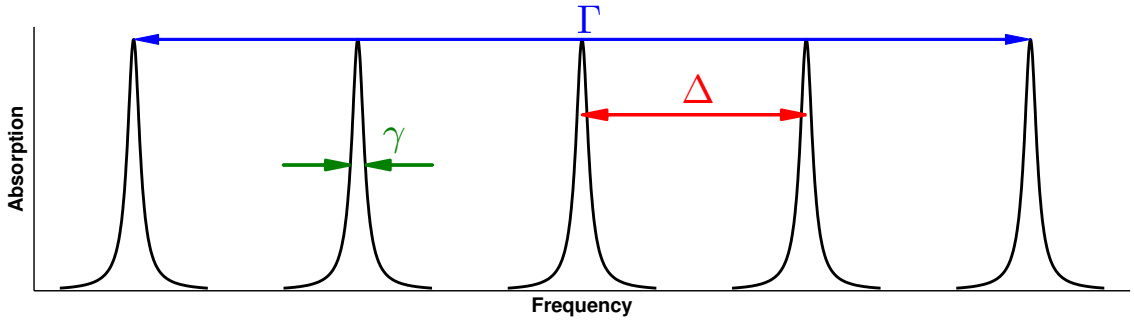

(b) Atomic Frequency Comb by Optical Pumping

Figure 3.2: Atomic Frequency Comb. (a) shows the natural inhomogeneous broadening of a rare earth ion doped solid in which an atomic frequency comb is tailored. Using frequency selective optical pumping, the AFC is formed, shown in (b). This schematic shows $N = 5$ teeth of width γ and separation Δ. The bandwidth is $\Gamma = N\Delta$.

propagating then the echo necessarily counter-propagates with respect to the input pulse. To achieve forward propagating, the coupling beams will be co-propagating.

The efficiency of this protocol has been calculated by others [71]. For forward propagation, the efficiency is identical in form to the forward propagation in transverse CRIB (Equation 3.2). There, the optical depth is for the broadened feature. Here the optical depth is the effective optical depth of the comb $\tilde{\alpha}l$, given approximately by $\frac{\alpha}{F}$, where F is the finesse of the comb $\left(\frac{\Delta}{\gamma}\right)$. As before, the maximum efficiency is 54% for $\tilde{\alpha}l = 2$.

For backward propagation, the efficiency is of similar form to Equation 3.1, given by

$$\eta_b \approx (1 - \mathrm{e}^{-(\alpha l/F)})^2 \mathrm{e}^{-\left(7/F^2\right)}. \tag{3.3}$$

We see that the absorption term is there and that an additional term is present that takes into account the finite width of the absorbing peaks. Note that for the CRIB protocol this term (of differing functional form) was omitted due to assumptions of the input pulse bandwidth. We see that there is a tradeoff in the choice of finesse. For good absorption one wants a low finesse, but for low dephasing effects, one wants a large finesse. The efficiency can be made close to 100% for large enough comb tooth optical depth and optimized finesse.

The multimode capacity of this protocol is as follows. One can have an input of duration T where there are N temporally distinguishable modes. The input duration can be close to the storage time, i.e. $T = \frac{2\pi}{\Delta}$. The shortest duration τ is limited only by the bandwidth of the comb $\sim 1/(N_p\Delta)$ meaning the number of modes stored $N = T/\tau \sim N_p$. We see that the multimode capacity is proportional to the number of teeth in the comb and independent of the optical depth. For solid state rare earth ion doped media which have large inhomogeneous broadening, large bandwidth combs can be produced with many teeth.

Experimental Realization

The first experimental realization of an AFC memory was implemented with cryogenically cooled neodymium doped yttrium orthovanadate (Nd:YVO_4) [56] which has a transition at 880nm with a lambda system arrangement of states, i.e. two ground states and an excited state. The comb is prepared by using frequency selective optical pumping from one ground state to the other ground state via the excited state. This is implemented by using a train of coherent pairs of pulses. In this sense, it is similar to the 3 pulse photon echo, mentioned in the previous chapter. Collec-

tive mapping of light at the single photon level to the comb was demonstrated. The sample was prepared with a grating spacing of 4MHz, resulting in a storage time of 250ns. The efficiency was rather low, measured to be 0.5%, mainly due to the poor optical pumping when preparing the comb. Multimode capacity was shown by storing four temporally distinct modes with a storage time of 500ns resulting in about 0.1% efficiency. The protocol was seen to also preserve phase information. Two gratings were superimposed in the line and two weak pulses are sent into the memory, which results in two echos at one storage time and two echos at a different storage time. If the time difference between the two inputs is the same as the time difference between the two gratings, then the result is three echos, in which the central echo can be enhanced or suppressed depending on the relative phase between the two inputs. A visibility nearing 95% was observed.

Since the first proof of principle experiment, many experiments have followed reporting better efficiency. At the single photon level, the efficiency saw an increase to 9% in thulium doped yttrium aluminum garnet (Tm^{3+}:YAG) [72] and a further increase to 17% by tailoring square shaped teeth as opposed to Lorentzian shaped teeth [100]. The efficiency received a further increase to 25% using praseodymium doped yttrium orthosilicate [101] and having narrower comb teeth and higher optical depth. Obtaining higher efficiencies requires finer spectral tailoring of the absorbing line, higher optical depths and the ability to optically pump efficiently reducing the absorbing background.

The multimode capacity has seen an increase from 4 temporal modes to 64, demonstrated in [102] with cryogenically cooled neodymium doped yttrium orthosilicate (Nd :Y_2SiO_5). There, the total input time was 1.28 μs with a 20ns mode separation and 5ns mode duration. The storage time was 1.32 μs and the efficiency was 1.4%. A more recent experiment realized storage of 1060 modes in Tm^{3+}:YAG [103]. The storage time was 1.6 μs with an efficiency of around 1%.

The AFC scheme has also been performed at telecommunication wavelengths [70]. The authors report an AFC efficiency of 0.7% for a delay of 360ns at the single photon level using cryogenically cooled erbium doped yttrium orthosilicate (Er:Y_2SiO_5) with a optical transition at 1536nm. The authors also presented a combined CRIB-AFC storage scheme. Here, a comb is prepared such that an echo is emitted at one storage time (τ) and a second echo is emitted at twice the storage time (2τ). Then, electric fields are applied to suppress the first echo using the Stark effect which also suppresses the second echo. If the electric field polarity is switched at τ, then the second echo is recovered at 2τ. This is an example of an on-demand

version of the AFC at telecommunication wavelengths.

An example of on-demand read-out using the AFC scheme is reported in [74]. Cryogenically cooled praseodymium yttrium orthosilicate ($Pr:Y_2SiO_5$) with optical transition 606nm was used. A comb is prepared on the ground state $\pm 1/2$ to excited state $\pm 3/2$ transition with a storage time of 4 μs and an efficiency of 5%. Control fields are applied to transfer the coherence to the long lived ground state hyperfine level $\pm 3/2$. With this arrangement, echo phenomena was seen for delays of up to 20 μs. Of course, the efficiency suffered due to spin dephasing in the hyperfine level, resulting in efficiencies nearing 0.5% for shorter delay times. Multimode capacity was demonstrated with the storage of 2 temporal input modes.

More recently, AFC technology has been used to store one photon of an entangled pair of photons whilst still preserving the nonclassical nature of the entangled pair [104]. Here, an entangled photon pair was created by down converting a green 532nm photon to an 883nm photon and a telecommunication 1388nm photon. The near infrared photon was stored in an AFC carved into a neodymium doped yttrium orthosilicate absorption line, while the telecommunication photon was sent into a fiber 50m long. The cross correlation between the retrieved AFC photons and the telecommunication photons stay well above the classical upper limit for storage times nearing 200ns.

3.3 The Quantum Repeater

This technology was first suggested in [11] and many modified versions followed it [90, 105–112]. Essentially, the repeater is technology that will allow for distribution of quantum states over long distances. Quantum states of light are typically at the single photon level, meaning using an optical fiber as a communication channel for quantum states is ineffective. This is largely due to the fact that optical fibers have loss. Even though telecommunication optical fibers have very low losses of around 0.2 dB/km, at distances around hundreds of kilometers the loss becomes significant. For example, for a 1 Hz quantum source the rate of transmission at 1000km would be 10^{-20}Hz, corresponding to 1 photon every 3×10^{12} years. Even if the repetition rate of the source is increased to a perhaps ambitious 1GHz, the transmission rate would be 1 photon every 3000 years.

In the classical regime, the problem of loss is solved by using amplification stages or repeaters over the channel. Such a solution is ineffective in the quantum regime, as the no-cloning theorem states that noiseless amplification of a set of nonorthogonal

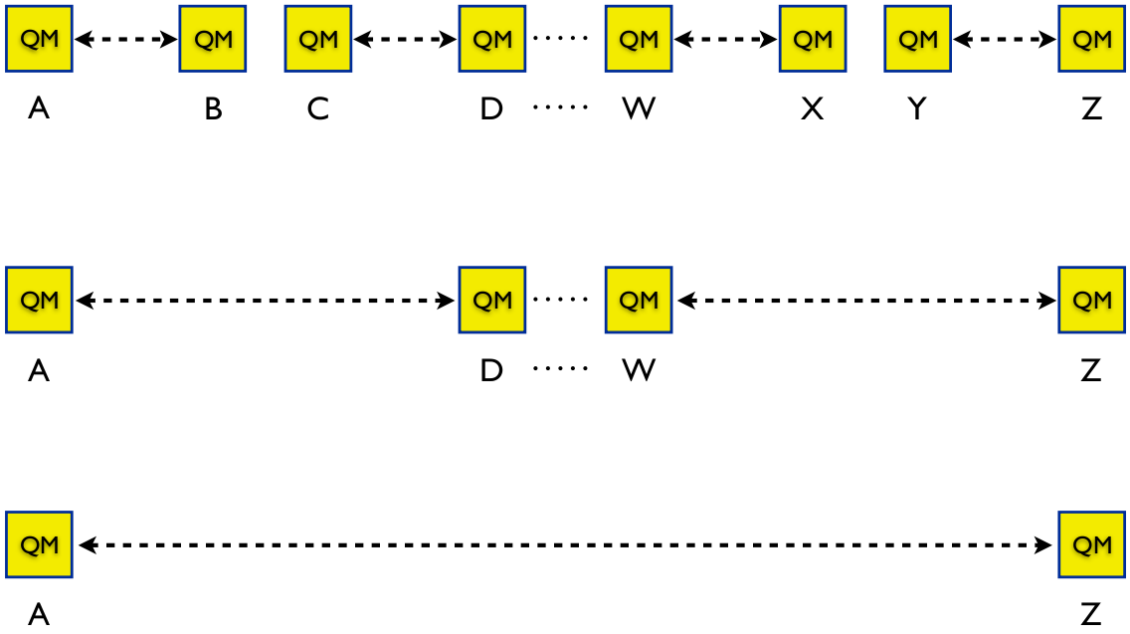

Figure 3.3: The quantum repeater approach to entangling locations A and Z. The top row shows 4 elementary links in which entanglement is created between quantum memories (QM) at locations A and B, C and D, ... , W and X, and Y and Z. The middle row shows the first entanglement swapping operation on B and C, ... , and X and Y. The result is entanglement between locations A and D, ... , and W and Z. The bottom row shows the final entanglement operation resulting in entanglement between locations A and Z. The yellow squares represent quantum memories and the dashed arrows between locations represents entanglement between those locations.

states is impossible [85]. The quantum repeater [11] is the proposed solution to the problem of loss.

The quantum repeater is based on entanglement generation and entanglement swapping [113]. Figure 3.3 shows the idea of the quantum repeater. The idea is that entanglement can be produced between two atomic systems separated a distance L by swapping entanglement between two entangled pairs each covering only a distance $L/2$. Each entangled pair can be created by another two entangled pair each covering a distance $L/4$ and so on. By dividing the distance L into $N = 2^n$ elementary links each covering a distance L_0, entanglement can be created over the distance L with n levels of entanglement swapping.

This quantum repeater protocol relies heavily of the creation of an entangled pair of atoms to form an elementary link. One way to create a link would be to create the entanglement between two systems locally and then send one of the systems to a distant location using a photon. This method would of course suffer from loss depending on how long the link needs to be. For a link of 100km the

transmission through optical fiber is about 1%. Another problem is knowledge of the entanglement without measuring the photon as this would destroy the entanglement. A better method of creating the link is as follows. The link is made of, for example, one atom at A and one at B separated by a distance L_0. Entanglement can be created by detecting a single photon that could have been emitted from either atom as long as the measurement can not determine which atom the photon came from. This method benefits in the fact that entanglement is heralded by the detection of a photon. If one detects zero or 2 photons, one then repeats the process.

Another essential ingredient for the repeater is the aforementioned quantum memory. A quantum memory allows for a created elementary link to be stored while the neighbouring link is being prepared, such that entanglement swapping between the links can then be performed. This higher level entanglement then needs to be stored while the neighboring higher level entanglement is being prepared and so forth. Without quantum memory technology, the entanglement generation and swapping would have to be successful on all links simultaneously, a highly improbable case.

Essential to the repeater is the entanglement swapping between elementary links. This involves a local joint measurement between two quantum memories projecting the two links into an entangled state.

Duan-Lukin-Cirac-Zoller Protocol

A proposal for realizing the quantum repeater is the Duan-Lukin-Cirac-Zoller (DLCZ) protocol [105]. The protocol involves the use of linear optics, atomic ensembles and single photon counting to realize the entanglement generation and swapping operations. The earlier description of the repeater suggested an elementary link is created by entangling single atoms, but in practice coupling light to a single atom is difficult. The protocol takes advantage of the strong coupling between single photons and an ensemble.

The DLCZ uses a level diagram shown in Figure 3.4. The three level system has two ground states $|g\rangle$ and $|s\rangle$ and an excited state $|e\rangle$. It is assumed that all N_A atoms are initially in the ground state $|g\rangle$. A write pulse is applied off-resonantly to the $|g\rangle \rightarrow |e\rangle$ transition resulting in the spontaneous emission of a Raman photon, often referred to as the Stokes photon. Detection of this photon without knowledge of which atom it came from creates an atomic state that is a superposition of all possible terms of $N_A - 1$ atoms in the $|g\rangle$ ground state and one atom in the $|s\rangle$

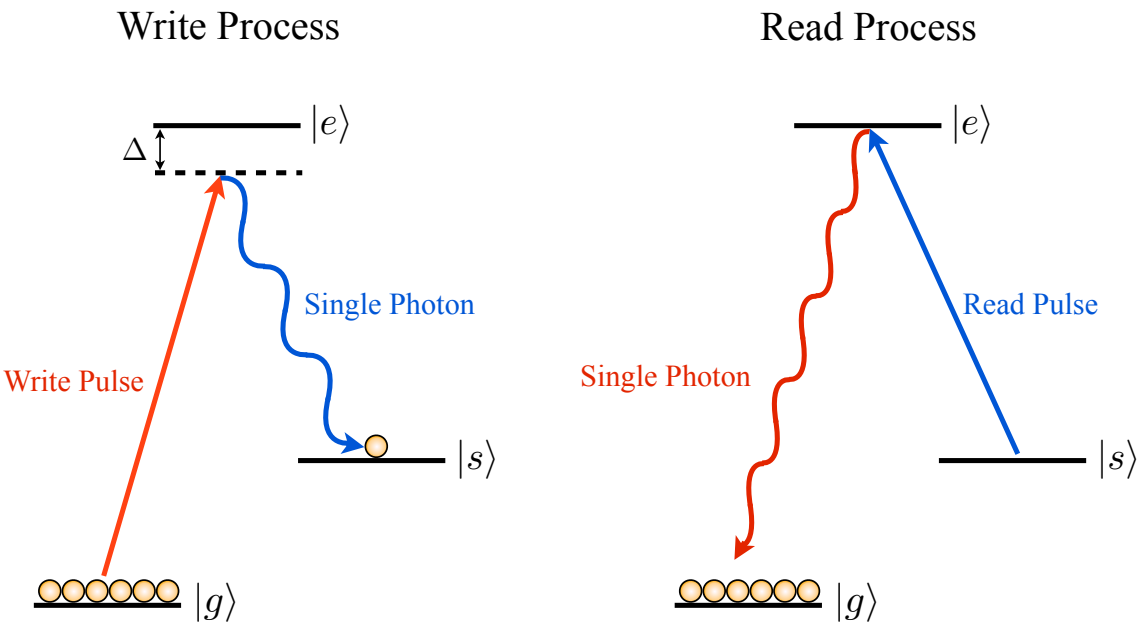

Figure 3.4: Level Scheme for the DLCZ protocol. For the write process, all atoms start in the ground state $|g\rangle$. A laser pulse then pumps the transition $|g\rangle \rightarrow |e\rangle$ off resonantly with a small probability of emitting a single photon on the $|e\rangle \rightarrow |s\rangle$ transition. An atom is left in the ground state $|s\rangle$. For the read process, a laser drives the $|s\rangle \rightarrow |e\rangle$ transition resulting in a single photon emitted in a well defined direction from the $|g\rangle \rightarrow |e\rangle$ transition.

ground state. The collective excitation is given by

$$\frac{1}{\sqrt{N_A}} \sum_{j=1}^{N_A} \mathrm{e}^{(\mathbf{k}_w - \mathbf{k}_s)\mathbf{x}_j} |g\rangle_1 |g\rangle_2 \cdots |s\rangle_j \cdots |g\rangle_{N_A-1} |g\rangle_{N_A}, \tag{3.4}$$

where $\mathbf{k}$ is the wave vector, the subscript w corresponds to the write laser, s denotes the Stokes photon, and $\mathbf{x}_j$ corresponds to the position of the jth atom.

Reading out this collective excitation is achieved by driving the $|s\rangle \rightarrow |e\rangle$ transition with a read pulse, leading to a similar state as before with $N_A - 1$ atoms in the $|g\rangle$ ground state and one atom in the $|e\rangle$ excited state and with wave vector $\mathbf{k}_r$. This state can then collectively decay to the ground state emitting a photon (referred to as the anti-Stokes photon with wave vector $\mathbf{k}_{AS}$) on the $|e\rangle \rightarrow |g\rangle$ transition. The phase matching condition which allows for all terms to constructively interfere is $\mathbf{k}_w - \mathbf{k}_S = \mathbf{k}_r - \mathbf{k}_{AS}$. For atomic ensembles with large N_A, this direction dominates over other directions allowing for highly efficient collection of the anti-Stokes photon.

Entanglement Creation

We now describe the method in which entanglement generation is achieved. We start with having an atomic ensemble at locations A and B as in Figure 3.5. The two ensembles are simultaneously driven such that a single Stokes photon is emitted corresponding to the state [105]

$$\left(1+\sqrt{\frac{p}{2}}(S_a^\dagger a^\dagger e^{i\phi_a}+S_b^\dagger b^\dagger e^{i\phi_b})+O(p)\right)|0\rangle. \tag{3.5}$$

Here, $a(b)$ denotes the Stokes photon, $S_a(S_b)$ denotes the atomic excitation corresponding to the atomic ensemble A(B), $\phi_a(\phi_b)$ is the phase of the driving field at location A(B) and $|0\rangle$ is the vacuum state for all photonic and atomic modes. The probability of emitting a single photon is p and is small such that higher order events that occur with lower probability ($O(p)$) can be neglected.

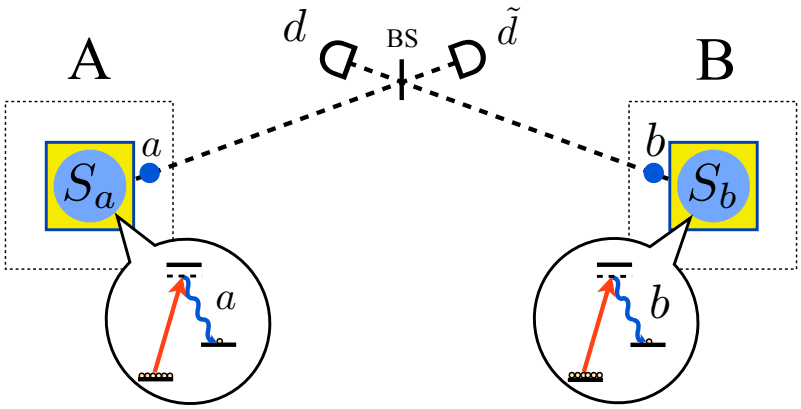

Figure 3.5: Entanglement creation between two ensembles A and B separated by a distance L_0. The light blue circle in yellow squares represent a DLCZ-type ensemble that emits single Stokes photons (dark blue circle) after driving fields are applied. The photons are sent down optical fibers (dashed lines) and are combined on a beamsplitter (BS), then detected. The detection of a single photon in either mode d or $\tilde{d}$ heralds the storage of a single excitation in one of the ensembles.

The stokes photons are then coupled to optical fibers and combined on a beamsplitter at some central station between A and B. The modes at the beam splitter are $d=\frac{1}{\sqrt{2}}(ae^{-i\xi_a}+be^{-i\xi_b})$ and $\tilde{d}=\frac{1}{\sqrt{2}}(ae^{-i\xi_a}-be^{-i\xi_b})$. The detection of a single photon in $d(\tilde{d})$ and no photon in $\tilde{d}(d)$ projects the state of the atomic ensembles into an entangled state given by

$$|\psi_{ab}\rangle^{\pm}=\frac{1}{\sqrt{2}}\left(|1_a\rangle|0_b\rangle\pm|0_a\rangle|1_b\rangle e^{i\theta_{ab}}\right), \tag{3.6}$$

where $|0_{a(b)}\rangle$corresponds to an empty $|s\rangle$ state of ensemble A(B), $|1_{a(b)}\rangle$ corresponds to the storage of a single atomic excitation and $\theta_{ab} = \phi_b - \phi_a + \xi_b - \xi_a$. Thus, the detection of a photon at either d or $\tilde{d}$ heralds the creation of entanglement. The probability of successful entanglement creation is given by $P = p\eta_d\eta_t$, where η_d is the detection efficiency, and η_t is the transmission efficiency of the optical fiber. Upon successful entanglement, an elementary link is created.

Entanglement Swapping

We now describe the process of entanglement swapping between elementary links leading to a higher level of entangled ensembles. Consider two links given by A-B and C-D seen in Figure 3.6. The system as a whole is described by $|\psi_{ab}\rangle \otimes |\psi_{cd}\rangle$. As described before, light resonant on $|s\rangle \rightarrow |e\rangle$ efficiently converts the atomic excitation $S_b(S_c)$ into anti-Stokes photons $b'(c')$. These modes are then combined on a beam splitter and the detection of a single photon on either detector ($\frac{1}{\sqrt{2}}(b' \pm c')$) projects the ensembles at locations A and D into

$$|\psi_{ad}\rangle^{\pm} = \frac{1}{\sqrt{2}}\left(S_a^{\dagger} \pm S_d^{\dagger} e^{i(\theta_{ab}+\theta_{cd})}\right)|0\rangle. \tag{3.7}$$

Hence, the detection of a single photon at either detector successfully entangles two elementary links, creating a higher level of entanglement. It is then easy to see that the higher levels of entanglement can be created by further entanglement swapping and thus establishing entanglement between more distant locations.

DLCZ using Photon Pair sources and Quantum Memories

We now briefly describe how the DLCZ protocol can be realized using photon pair sources and quantum memories. The motivation for this lies in the fact that to establish entanglement between two distant locations, a photon needs to travel 10's of kilometers hence its wavelength should match the telecommunication wavelength. This puts a limit on the operational wavelength of the DLCZ protocol, requiring a memory at telecommunication wavelengths. As was seen in the first half of the chapter, quantum memories at telecommunication wavelengths were of low efficiency.

A more sensible approach is proposed by [90]. Here, a photon pair source and quantum memories are used to form the DLCZ protocol (see Figure 3.7). Entanglement creation between two remote locations A and B requires a photon pair source and a quantum memory at each location. The sources are activated simultaneously

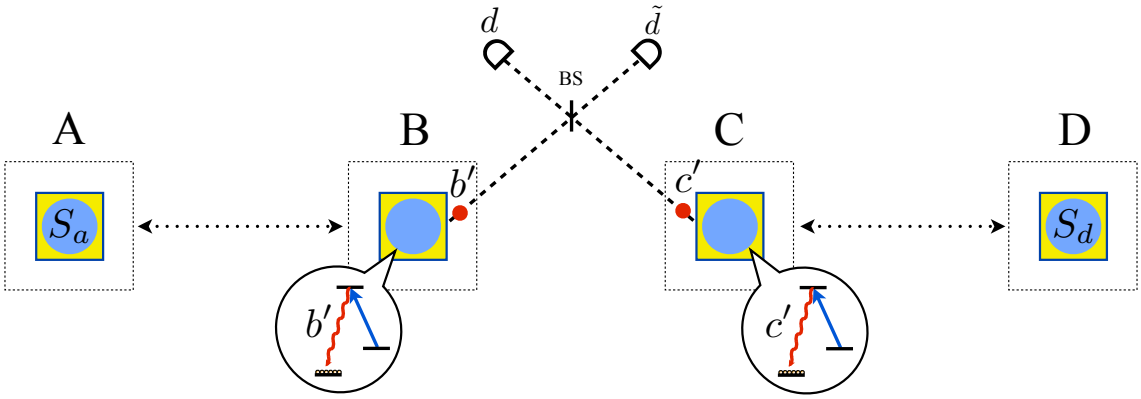

Figure 3.6: Entanglement swapping. The ensembles A and B, C and D, are entangled initially (dotted arrow). The atomic state of ensembles B and C are read out into anti-Stokes photons on the $|g\rangle \rightarrow |e\rangle$ transition using resonant light on the $|s\rangle \rightarrow |e\rangle$ transition. Photonic modes b' and c' (red circles) are steered onto optical fibers (dashed line) and the modes are combined on a beamsplitter (BS). The detection of a single anti-Stokes photon projects the remote ensembles at A and D into an entangled state.

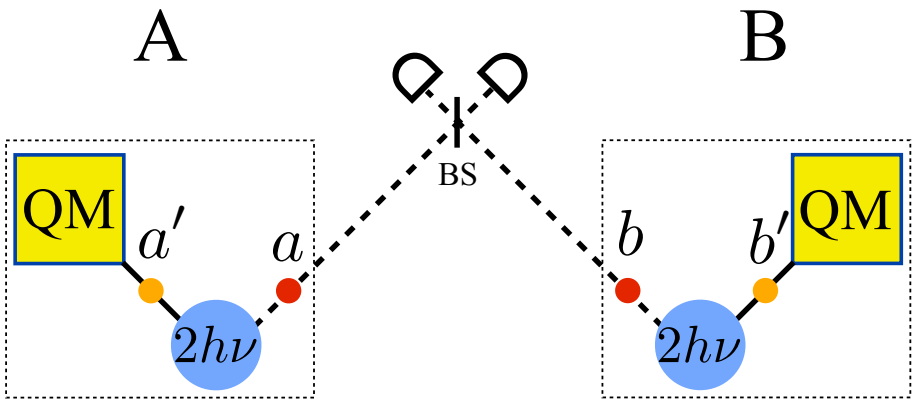

Figure 3.7: DLCZ protocol entanglement creation using photon pair sources and quantum memories. The blue circle represents a photon pair source ($2h\nu$) and the yellow square represents the quantum memory (QM). The source emits photons in modes a and a' for location A and b and b' for location B. The primed modes (orange circles) are stored locally in quantum memories and the unprimed modes (red circles) are sent along optical fibers (dashed line). These modes are then combined on a beamsplitter with the detection of a single photon heralding the creation of entanglement between locations A and B.

such that each of them has a probability of $\frac{p}{2}$ to emit a pair corresponding to the state

$$\left(1 + \sqrt{\frac{p}{2}}(a^\dagger a'^\dagger + b^\dagger b'^\dagger) + O(p)\right)|0\rangle. \tag{3.8}$$

The modes a and a' (b and b') correspond to two different directions at location

A (B). Higher order events are described by $O(p)$. We note that this equation is identical in form to Equation 3.5 with the phases set to zero. Modes a' and b' are sent to local memories while modes a and b are sent to a central station and combined on a beamsplitter. The detection of a single photon on either detector projects the atomic excitations stored in the quantum memories into an entangled state given by Equation 3.6. For this scheme, the modes a and b want photons at telecommunication wavelengths, but there is no constraint on the wavelength of modes a' and b'. Hence, this is a wavelength flexible DLCZ proposal. As was seen earlier, quantum memories in rare earth ion doped media have the greatest efficiency [94] and are multimode [102, 103], making them an ideal candidate for this implementation. Photon pair sources can be implemented using parametric down conversion in nonlinear optical crystals [87–89].

An issue with parametric down conversion is the photons produced are broadband compared to the memory bandwidth. In order to match the bandwidths, filtering using etalons of the a' and b' photons is implemented [104, 114]. An etalon would also need to be used on the a and b photons to avoid detecting photons outside the bandwidth of interest. An alternative to using parametric down conversion is proposed in this thesis (Chapter 4, [1]).

Chapter 4

Theory of Optically Rephased Memory Protocols

In Chapter 2 the optical properties of rare earth ion doped systems were presented as having coherence times on the order of ms on the optical transitions and even longer coherence times on the order of 30s using the hyperfine levels (see Section 2.1). Also in that chapter, the coherent process known as the two pulse photon echo was introduced. This type of optical memory can be implemented on the inhomogeneous line of a rare earth ion system and can operate at high bandwidth ($\sim$ MHz), high efficiency ($\sim$ 200%) and at high temporal mode capacity (see Section 2.4). These reasons make the two pulse photon echo an ideal candidate for a quantum memory for light. Chapter 3 reviewed the quantum memory for light. The CRIB and AFC protocols in rare earth ion systems boasted the greatest efficiency ($\sim$ 70% for CRIB [94]) and high multimode capacity (64 modes for AFC [102]), albeit requiring fine tailoring of the inhomogeneous line. An application of the quantum memory is the quantum repeater (see Section 3.3), a device that enables entanglement distribution over large distances. An ideal quantum repeater will have a quantum memory for light that is highly efficient, highly multimode and has a long storage time.

In order to investigate the suitability of this protocol as a quantum memory for light, a fully quantum mechanical analytical treatment of the two pulse photon echo is required, which is presented in this chapter. A clue as to how suitable this protocol is as a quantum memory for light is seen in the efficiency of the protocol. Efficiencies exceeding 100% are possible for small input pulses as the rephasing π pulse inverts the two level system into the excited state, allowing the echo to form in an amplifying medium. As will be seen, the output of the quantum two pulse photon

echo is additional noise due to collective amplified spontaneous emission caused by the gain in the system [115].

Further to this amplified spontaneous emission (ASE), this chapter proposes the new concept of rephased amplified spontaneous emission (RASE) [1]. With the application of another rephasing π pulse, the atomic coherence created by the ASE can be rephased. The result is that the time separated ASE and RASE fields share nonclassical correlations. This chapter details the analytics for this scenario and discusses the application to quantum repeater technology.

Finally, the chapter presents the hybrid photon echo rephasing (HYPER) protocol [4, 54], a quantum memory scheme based on optical rephasing and Stark shifting on the inhomogeneous line. The scheme is motivated by the fact that CRIB and AFC require fine spectral tailoring on the inhomogeneous line, whereas this scheme does not. The scheme allows the collective interaction between the excited state atoms and light to be 'switched off'. The chapter presents the analytical theory and an experimental realization.

4.1 Quantized Maxwell-Bloch Equations

The Maxwell-Bloch equations describe the two pulse photon echo and are presented in Chapter 2 in a classical form. Logically, to investigate the quantum two pulse photon echo it is necessary to formulate the *quantized Maxwell-Bloch equations*. Such equations can be derived by first dividing the atomic ensemble into thin slices and modelling each slice as an optically thin collection of atoms inside a Fabry-Perot resonator with the use of input-output theory [116, 117]. Then, the limit of the reflectivity of the mirrors is taken to zero and the following equations result:

$$\frac{\partial}{\partial t}\hat{\sigma}_-(z,\Delta,t) = i\Delta\,\hat{\sigma}_-(z,\Delta,t) - i\,\hat{a}(z,t)\,\hat{\sigma}_z(z,\Delta,t) \tag{4.1}$$

$$\frac{\partial}{\partial t}\hat{\sigma}_z(z,\Delta,t) = i\hat{a}(z,t)\,\hat{\sigma}_-(z,\Delta,t) - i\,\hat{a}^\dagger(z,t)\,\hat{\sigma}_+(z,\Delta,t) \tag{4.2}$$

$$\frac{\partial}{\partial z}\hat{a}(z,t) = \frac{i\alpha}{2\pi}\int_{-\infty}^{\infty}\hat{\sigma}_-(z,\Delta,t)\,d\Delta, \tag{4.3}$$

where $\hat{\sigma}_{+,-,z}$ represent the quantum atomic spin operators, $\hat{a}(z,t)$ is the quantum optical input field operator to the left hand side of the cavity, $\hat{a}(z+dz,t)$ is the output field at the right hand side of the cavity. α is the optical depth parameter with units m^{-1}, which depends on the coupling between the atoms and the field and

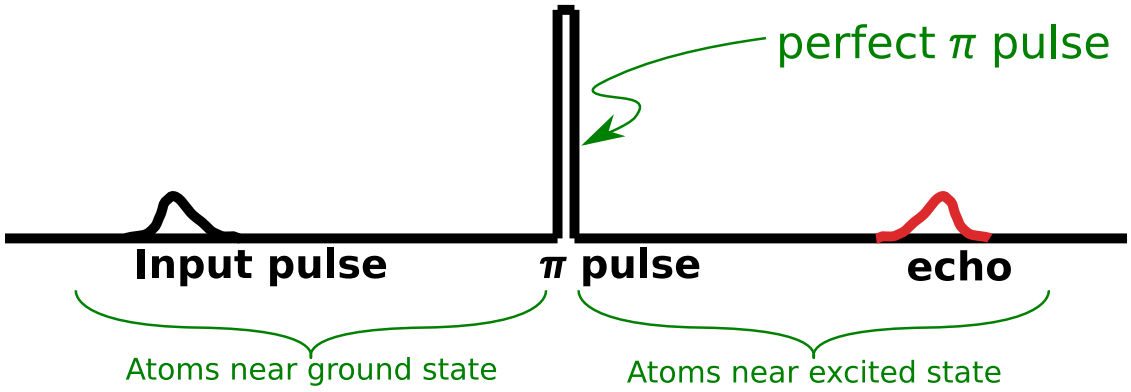

Figure 4.1: A two pulse photon echo sequence showing the approximations made in the treatment, a weak first pulse is applied to the system and is recalled using and ideal π pulse.

on the atom density, Δ is the detuning from some chosen resonant frequency and z is the distance along the propagation direction. Equations 4.1–4.3 are the quantized Maxwell-Bloch equations. It is noted that these equations are 1-D, and spontaneous emission into modes other than the 1-D input and output modes is neglected.

The operators have the following commutation relations:

$$[\hat{a}(z,t), \hat{a}^\dagger(z,t')] = \delta(t-t') \tag{4.4}$$

$$[\hat{\sigma}_i(z,\Delta,t), \hat{\sigma}_j(z',\Delta',t)] = \frac{\epsilon_{ijk}}{\alpha}\,\hat{\sigma}_k(z,\Delta,t)\,\delta(z-z')\,\delta(\Delta-\Delta'). \tag{4.5}$$

As can be seen from Equation 4.3, we take the density of atoms as a function of frequency to be a constant i.e. $g(\Delta) = 1$. Such an assumption is justified in the fact that for rare earth ion doped media, the inhomogeneous broadening on the optical transition can be 7 orders of magnitude larger than the homogeneous broadening of individual ion linewidths. For experiments where only a small band of frequencies (compared to the GHz wide inhomogeneous broadening) are addressed and for experiments with no spectrally tailored features, a constant density of atoms is a sufficient approximation.

4.2 The Two Pulse Photon Echo

The first application of these quantum Maxwell-Bloch equations will be in analysing a memory for light based on a two pulse photon echo. First, the problem is split into two regions as seen in Figure 4.2. Region 1 is the time region before the application of the π pulse, whereas region 2 is after the π pulse. The problem is made easier

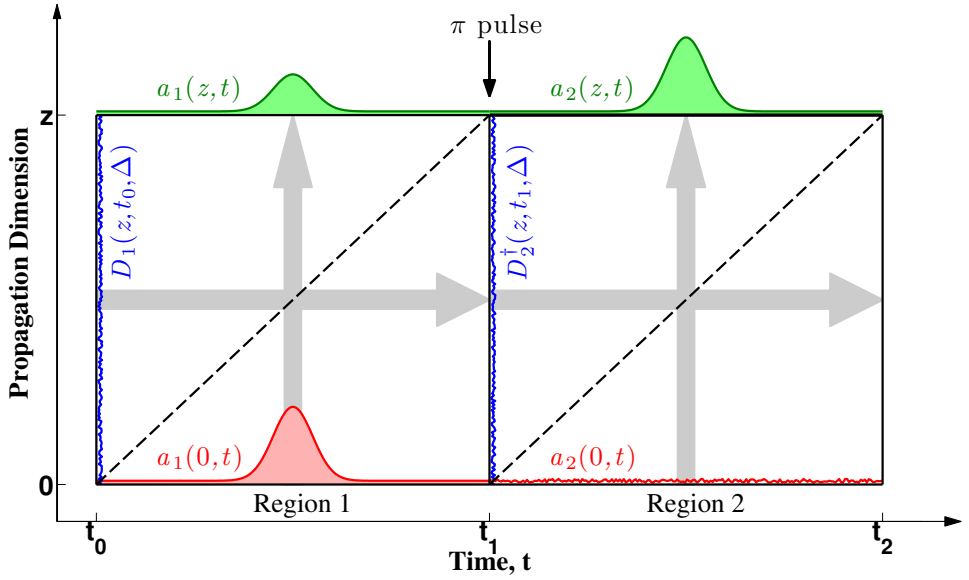

Figure 4.2: Time regions of integration for the two pulse photon echo. Region 1 is from time t_0 to t_1, region 2 is from time t_1 to t_2. For simplicity in the analytics, t_0 is set to zero. The π pulse is applied instantaneously at $t = t_1$. Red curves indicate the input optical fields at the front of the sample ($z = 0$) and green curves indicate optical output fields at the back end of the sample. The blue curves indicate the atomic boundary conditions.

by assuming that the input pulse in region is of weak intensity. In the Bloch sphere picture, when the input pulse is absorbed, the result is a small rotation of the Bloch vectors leaving a majority of the atomic state in the ground state ($\sigma_z \approx -1$). Hence, the atomic lowering operator σ_- can be approximated as a harmonic oscillator field D_1 (see Figure 4.1). Under this assumption, the non-linear Maxwell-Bloch equations reduce to the following linear equations

$$\frac{\partial}{\partial t}\hat{D}_1(z,\Delta,t) = i\Delta\,\hat{D}_1(z,\Delta,t) + i\,\hat{a}_1(z,t) \tag{4.6}$$

$$\frac{\partial}{\partial z}\hat{a}_1(z,t) = \frac{i\alpha}{2\pi}\int_{-\infty}^{\infty}\hat{D}_1(z,\Delta,t)\,d\Delta, \tag{4.7}$$

where the subscript one is indicative of the time region. These equations will be referred to as the *ground state Maxwell-Bloch equations*.

Equation 4.6 is a simply first order linear equation with the following solution,

$$\hat{D}_1(z,t,\Delta) = i\int_{-\infty}^{\infty}\hat{a}_1(z,t')\,u(t-t')\,e^{i\Delta(t-t')}\,dt' + e^{i\Delta t}\hat{D}_1(z,t_0,\Delta)\,, \tag{4.8}$$

where $\hat{D}_1(z, t_0, \Delta)$ describes the state of the atoms at $t = t_0$ and $u(t)$ is the unit step function. The Fourier transform of Equation 4.8 is taken, then this result is substituted into the Fourier transform of Equation 4.7, this is seen below:

$$\begin{aligned}\frac{\partial}{\partial z}\hat{a}_1(z,\omega) &= \frac{-\alpha}{2\pi}\int_{-\infty}^{\infty} d\Delta\; g(\Delta)\;\hat{a}_1(z,\omega)\left[\frac{1}{i(\omega-\Delta)} + \pi\delta(\omega-\Delta)\right] \\ &\quad + i\alpha\int_{-\infty}^{\infty} d\Delta\; g(\Delta)\;\delta(\omega-\Delta)\hat{D}_1(z,t_0,\Delta)\;, \\ &= \frac{-\alpha}{2}\hat{a}_1(z,\omega) + i\alpha\;\hat{D}_1(z,t_0,\omega). \end{aligned} \tag{4.9}$$

Solving this equation and then Fourier transforming back to the time domain, one arrives at the ground state optical solution

$$\hat{a}_1(z,t) = \hat{a}_1(0,t)e^{-\alpha z/2} + i\alpha\int_0^z dz'\; e^{\alpha(z'-z)/2}\;\hat{\mathcal{D}}_1(z',t)\;, \tag{4.10}$$

where $\hat{a}_1(0,t)$ denotes the input photonic field at $z = 0$ and $\hat{\mathcal{D}}_1(z,t)$ is given by

$$\hat{\mathcal{D}}_1(z,t) = \int_{-\infty}^{\infty}\;\hat{\mathcal{D}}_1(z,t=0,\omega)\;e^{i\omega t}\;d\omega \tag{4.11}$$

Equations 4.8 and 4.10 form the ground state solutions for all input times.

The solutions obtained for region 1 can be interpreted graphically in Figure 4.2. The optical boundary condition, which is a function of time t, is propagated along the z direction, whereas the atomic boundary condition, which is a function of position z, is propagated forward in time. This region is analogous to a beamsplitter. The input fields are the boundary optical and atomic states. There is coherent mixing of the two fields resulting in the output states as linear combinations of atoms and light. It can be immediately seen that the output optical state requires the additional atomic degrees of freedom, as the commutation relations would be unphysical for the case of very large optical depths.

It is interesting to consider the classical case when the atomic boundary condition vanishes. Equation 4.10 reduces to the simple case of absorption of the input field, where the degree of energy absorption is dependent on the optical depth and is given by $1 - e^{-\alpha z}$. This factor can be referred to as the *write efficiency* η_w, that is, the efficiency of writing an optical input to the memory medium.

After the π pulse the atoms, using an identical argument to region 1, are all very close to the excited state ($\sigma_z \approx +1$) in which case we can approximate σ_+

by a harmonic oscillator field D_2. This then gives the *excited state Maxwell-Bloch equations*

$$\frac{\partial}{\partial t}\hat{D}_2^\dagger(z,\Delta,t) = i\Delta\,\hat{D}_2^\dagger(z,\Delta,t) - i\,\hat{a}_2(z,t) \tag{4.12}$$

$$\frac{\partial}{\partial z}\hat{a}_2(z,t) = \frac{i\alpha}{2\pi}\int_{-\infty}^{\infty}\hat{D}_2^\dagger(z,\Delta,t)\,d\Delta, \tag{4.13}$$

where the subscript 2 indicates the region. It is noted that the atomic field $\hat{D}_2$ need not be a creation operator but has been labelled as one here to indicate that this is the excited state atomic field.

The π pulse is treated as being being a perfect π pulse leading to the instantaneous transformation $\hat{D}_2 \leftarrow \hat{D}_1$. The treatment of the π pulse will be discussed later in Section 4.5. Bringing Equations 4.12 and 4.13 through the same mathematical process as Equations 4.6 and 4.7, we arrive at the excited state solutions:

$$\hat{D}_2^\dagger(z,t,\Delta) = -i\int_{-\infty}^{t} dt'\;\hat{a}_2(z,t')e^{i\Delta(t-t')} + e^{i\Delta(t-t_2)}\hat{D}_2^\dagger(z,t_2,\Delta)\;, \tag{4.14}$$

$$\hat{a}_2(z,t) = \hat{a}_2(0,t)e^{\alpha z/2} + i\alpha\int_0^z dz'\;e^{\alpha(z-z')/2}\;\hat{\mathcal{D}}_2^\dagger(z',t)\;, \tag{4.15}$$

where $\hat{a}_2(0,t)$ and $\hat{\mathcal{D}}_2^\dagger(z,t)$ are initial conditions for the photonic and atomic excited fields respectively.

Again the solutions can be interpreted graphically via Figure 4.2. The input fields are the boundary conditions on region 2 resulting in the mixing of atoms and light for the region 2 optical output. The optical boundary condition for region 2 is simply the unavoidable optical vacuum state, denoted $\hat{a}_2(0,t)$. The atomic boundary condition can be obtained by first evaluating the atomic field solution for region 1 at the time of the π pulse, and then taking the hermitian conjugate due to the π pulse inversion. Mathematically, this is

$$\hat{D}_2^\dagger(z,t=t_1,\Delta) = \left[\hat{D}_1(z,t_1,\Delta)\right]^\dagger. \tag{4.16}$$

The second term in the optical solution for region 2 (Equation 4.15) then has $\hat{\mathcal{D}}_2^\dagger(z',t) \equiv \mathcal{F}^{-1}\left[\hat{D}_1^\dagger(z,t_1,\omega)e^{-i\omega t_1}\right]$.

The final optical field solution for region 2 can be obtained by using the above boundary conditions, and is given as

$$\hat{a}_2(z,t) = \hat{a}_2(0,t)e^{\alpha z/2} + 2\sinh\left(\frac{\alpha z}{2}\right)\hat{a}_1^\dagger(0,2t_1-t)$$
$$+ i\alpha e^{\alpha z/2}\int_0^z dz'\left[e^{-\alpha z'/2}\mathcal{D}_1^\dagger(z',t-2t_1) + \left(1-e^{-\alpha z}\right)e^{\alpha z'/2}\mathcal{D}_1^\dagger(z',2t_1-t)\right]. \quad (4.17)$$

There are three terms here. The first term is the unavoidable vacuum input on region 2 which receives an amplitude gain of $e^{\alpha z/2}$. The second term is the echo, which contains the input state $\hat{a}_1(0,t)$. It is noted that the echo is a time reversed copy of the input state and appears at a time symmetrical about the π pulse. The third term contains the atomic degrees of freedom which again keeps the commutation relations of the optical output physical for any optical depth.

In the classical regime where the vacuum operators are replaced with zero, the solution is simply the second term only. The energy efficiency of the two pulse photon echo $\eta_{2\mathrm{PE}}$ is then $4\sinh^2\left(\frac{\alpha z}{2}\right)$. As stated earlier, it is easy to obtain efficiencies exceeding 100% by having optical depths larger than ~ 1. A physical explanation as to why this is the case follows. In the small input pulse regime, after absorption the atomic state of the ensemble is mainly in the ground state. The application of a π pulse results in the inversion of the ensemble. The echo then forms in the inverted medium and is thus subject to amplification due to stimulated emission into the echo mode. The degree of energy amplification is determined by the optical depth and is given by $e^{\alpha z}$. The *read efficiency* η_r is then given as $e^{\alpha z}-1$. It is noted that the total efficiency can be obtained from the write and read efficiencies,

$$\eta_{2\mathrm{PE}} = \eta_w\eta_r = \left(1-e^{-\alpha z}\right)\left(e^{\alpha z}-1\right) = 4\sinh^2\left(\frac{\alpha z}{2}\right). \quad (4.18)$$

4.3 Amplified Spontaneous Emission

The previous section gave the solutions to the quantum Maxwell-Bloch equations for the two pulse photon echo. It is interesting to consider the case of a vacuum input in region 1. This allows a measure of the noise on the output state. If the optical boundary condition is a vacuum, then the boundary condition for region two is simply the inverted atomic vacuum state, and the output solution takes the form of Equation 4.15. The output state for this case is simply the input vacuum state $\hat{a}_2(0,t)$ amplified by an energy gain factor of $e^{\alpha z}$ (first term of Equation 4.15) plus atomic degrees of freedom. This amplification of the vacuum noise will from now on

be termed *amplified spontaneous emission*. Amplified spontaneous emission (ASE) is the *collective* emission of photons into the output mode due to gain created by the π pulse along the direction of propagation. This collective emission phenomena is the downfall of the two pulse photon echo as a quantum memory for light. The output state of the quantum memory has with it additional noise, reducing the fidelity of the memory and ultimately rendering the two pulse photon echo as an unsuitable candidate as a quantum memory for light.

Quantitatively, it is interesting to consider the average number of photons per mode $\langle a^\dagger(t)a(t')\rangle$ in the output region (Appendix D shows why this is the average photon number per mode). Equation 4.10 has two terms, a term consisting of annihilation operators ($\hat{a}$) and a term consisting of creation operators ($\hat{D}^\dagger$). For simplicity let us define

$$\hat{a}(z,t) = A + B^\dagger.$$

Now it is easy to form the mean photon number per mode for a vacuum input,

$$\begin{aligned}\langle a^\dagger(t)a(t')\rangle &= \langle \left(A + B^\dagger\right)^\dagger \left(A + B^\dagger\right)\rangle \\ &= \langle A^\dagger A + A^\dagger B^\dagger + BA + BB^\dagger\rangle \\ &= \langle BB^\dagger\rangle \\ &= \langle [B, B^\dagger]\rangle \ \left(\text{since } \langle B^\dagger B\rangle = 0\right). \end{aligned} \tag{4.19}$$

Appendix C shows that $[B, B^\dagger] = \delta(t-t')(\exp(\alpha z)-1)$, where the bra and ket have been omitted since the commutator has no operators. Hence, in the case of no input pulse, we get an incoherent output field with $\langle a^\dagger(t)a(t')\rangle = \delta(t-t')(\exp(\alpha z)-1)$. That is, for an input with an average of zero photons per mode, the memory output is a state with $[\exp(\alpha z)-1]$ photons per mode. The number of photons per mode grows exponentially with optical depth and hence the larger the optical depth, the more additional noise is on the output of the memory. This then makes the quantum two pulse photon echo an unsuitable candidate for a quantum memory for light, as stated earlier. Especially since this type of memory would want to have a large optical depth in order to absorb as much of the input pulse as possible.

It is interesting to consider the source of this noise. In this model we do not couple to a thermal bath of states and we have no dissipation. The total system evolves through pure states.

The solution for the ground state (Equation 4.8) is analogous to the output of a

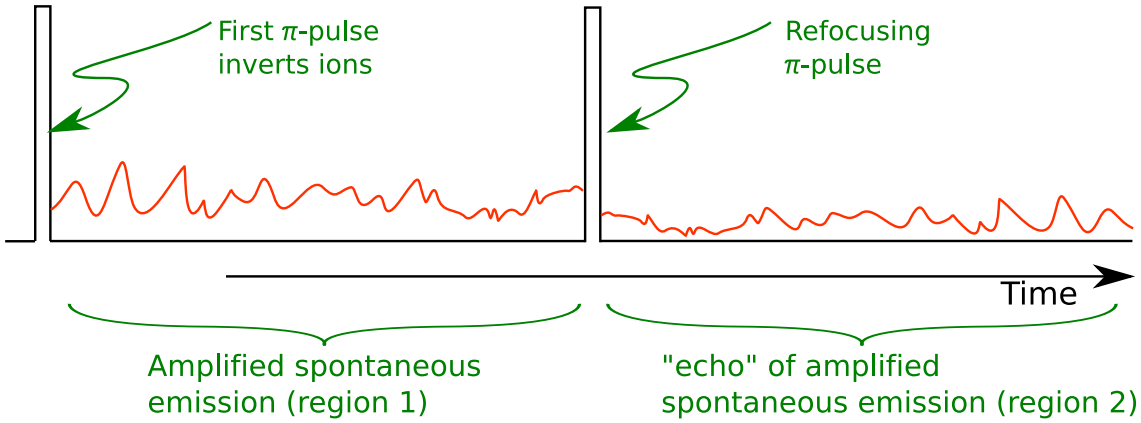

Figure 4.3: Two π pulse photon echo sequence proposed for generating rephased amplified spontaneous emission (RASE).

50-50 beam splitter. The input fields being light and atoms, with the output fields consisting of combinations of photonic and atomic excitations. One can see that the addition of atomic excitations in the solution 4.10 is necessary for the conservation of the commutation relations since the input photonic field contribution decays to zero in the limit of large optical depth. The excited state solution is analogous to a non-degenerate parametric amplifier [47], here the input field is amplified, and the commutation relations are preserved by the addition of atomic creation operators. If the system is looked at as a whole, the output optical state is entangled with the atomic degrees of freedom of the sample.

4.4 Rephased Amplified Spontaneous Emission

The previous section explained the phenomena of amplified spontaneous emission caused by an inverting π pulse on a two level inhomogeneously broadened system. The π pulse promotes all atoms into the excited state, and they are then subject to spontaneous emission. It was seen that the output photonic field is entangled with the atomic degrees of freedom; an emission event creates coherence on the two level system. The application of another 'inverting' π pulse applied to the system will bring excited state atoms down to the ground state (with the energy going back into the driving field) and the atoms that fell to the ground state due to ASE are promoted back to the excited state. Then, the atoms in the excited state can spontaneously emit a photon once again, in fact the photon will be emitted at a time symmetrical about the π pulse. This 'refocusing' π pulse allows the atomic degrees of freedom to be read out into photonic modes, rephasing the coherence left by the

emission events. This is the *rephased amplified spontaneous emission* (RASE) field. Remembering that the ASE field was entangled with atomic degrees of freedom, the ASE field is thus entangled with the RASE field.

This protocol is analogous to the two pulse photon echo. The ASE field can be thought of as the input state, and the RASE field can be thought of as the output of the memory. Since this is like a 2PE, it is readily seen that this protocol is broadband, the bandwidth is given by the Fourier width of the inverting pulse which can be made broad for large laser powers. Also, like the 2PE, this protocol is necessarily temporally multimode. The multimode capacity is given by the optical depth and the coherence time, both of which can be large in rare earth ion doped systems (see Chapter 2).

We now quantitatively show the equations that describe RASE. We consider the two π pulse sequence shown in Figure 4.3. The input fields for each region are illustrated in Figure 4.4, where it is noted that region 1 is now the excited state and region 2 is now the ground state (contrary to Figure 4.2). For region 1 the atoms will be inverted due to the first π pulse and hence Equations (4.12, 4.13) will apply. For region 2 the atoms will be near the ground state due to the refocusing π pulse, hence Equations (4.6, 4.7) describe the dynamics. We take the second π pulse to occur at $t = 0$.

The photonic solution in region 1 is given by Equations 4.14 and 4.15 and the solution in region 2 is given by Equations 4.8 and 4.10. For clarity we will now denote photonic and atomic fields with the subscript 1 when referring to the ASE fields (region 1) and subscript 2 when referring to the RASE fields (region 2). For boundary conditions we take the incident field, $\hat{a}_1(0,t)$, to be in it's vacuum state as we do for the initial condition $D_1^\dagger(z,t_i,\Delta)$. The initial condition for region 2 is obtained from the atomic solution from region 1 evaluated at $t = 0$, and the Hermitian conjugate is taken:

$$\begin{aligned}\hat{D}_2(z,t_0,\Delta) = ie^{\alpha z/2}\int_{-\infty}^{0} dt'\ \hat{a}_1^\dagger(0,t')\,e^{i\Delta t'} \\ + \alpha\int_{-\infty}^{0} dt'\ e^{i\Delta t'}\int_0^z dz'\ e^{\alpha(z-z')/2}\,\hat{\mathcal{D}}_1(z',t') \\ + \hat{D}_1(z,\Delta)\ . \end{aligned} \tag{4.20}$$

To make the analytics simpler, the initial phase of the atomic field is chosen to be zero.

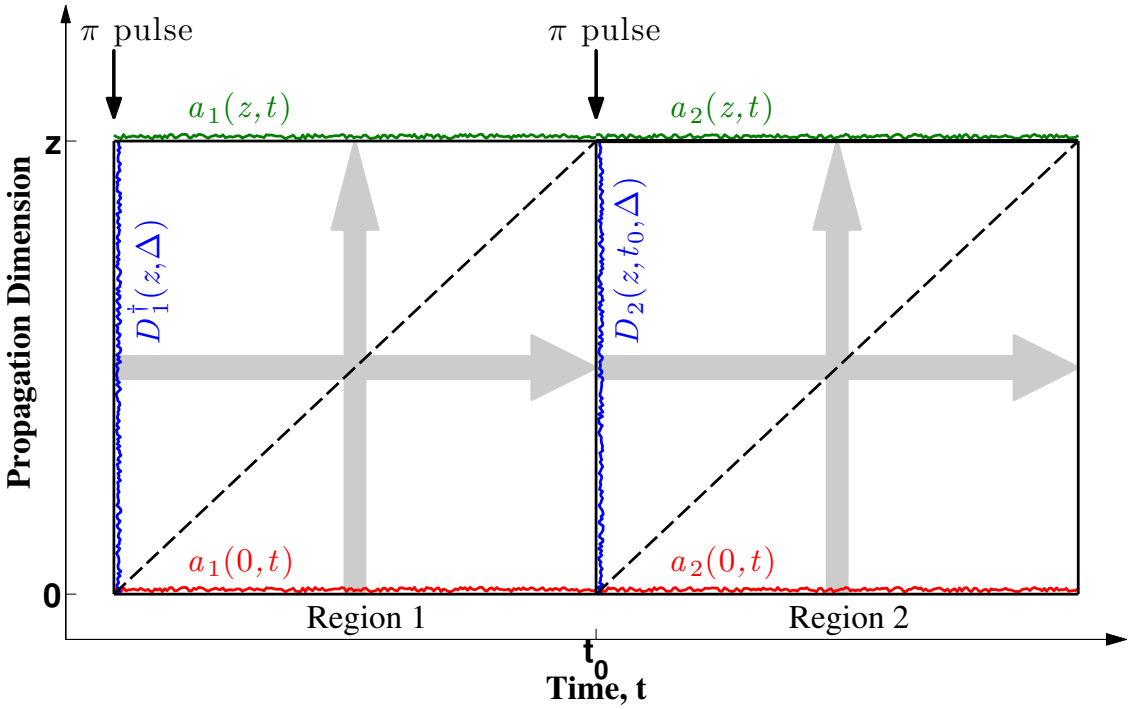

Figure 4.4: The time regions for the RASE protocol. It is noted that now region 1 is in the excited state, and region 2 is the ground state. A π pulse is applied at a time t_i, the beginning of region 1, causing amplified spontaneous emission. A second π pulse is applied at t_0 resulting in rephased amplified spontaneous emission in region 2. t_0 is set to zero to simplify the analytics.

The ground state optical solution (4.10) describes the RASE field, with the above as the initial condition. Now we may substitute in this boundary condition and solve to find the analytic form of the RASE field. Note that we substitute into the frequency domain version of Equation 4.10 and that in the substitution $\omega \rightarrow \Delta$, such that $\hat{D}_2(z', t_0, \Delta) \rightarrow \hat{D}_2(z', t_0, \omega)$.

$$\begin{aligned}\hat{a}_2(z,\omega) &= \hat{a}_2(0,\omega)e^{-\alpha z/2} + i\alpha \int_0^z dz'\, e^{\alpha(z'-z)/2}\hat{D}_2(z', t_0, \omega) \\ &= \hat{a}_2(0,\omega)e^{-\alpha z/2} + i\alpha \int_0^z dz'\, e^{\alpha(z'-z)/2} \Bigg[ie^{\alpha z'/2} \int_{-\infty}^{\infty} dt'\, \hat{a}_1^\dagger(0,t')\, e^{i\omega t'} \\ &+ \alpha \int_0^z dz''\, e^{\alpha(z'-z'')/2} \int_{-\infty}^{\infty} dt'\, e^{i\omega t'}\, \hat{\mathcal{D}}_1(z'', t') \\ &+ \hat{D}_1(z', \omega) \Bigg] . \end{aligned} \tag{4.21}$$

Now Fourier transforming and evaluating the integrals to get

$$\begin{aligned}\hat{a}_2(z,t) = \hat{a}_2(0,t)e^{-\alpha z/2} \\ - \alpha \int_0^z dz'\ e^{\alpha(2z'-z)/2}\ \hat{a}_1^\dagger(0,-t) \\ + i\alpha^2 \int_0^z dz' \int_0^{z'} dz'' e^{\alpha(2z'-z''-z)/2}\ \hat{\mathcal{D}}_1(z'',-t) \\ + i\alpha \int_0^z dz'\ e^{\alpha(z'-z)/2}\ \hat{\mathcal{D}}_1(z',t)\ . \end{aligned} \tag{4.22}$$

We now have the photonic solutions for region 1's ASE field (Equation 4.15) and region 2's RASE field (Eq. 4.22).

It is interesting to look at the mean number of photons per mode for the RASE fields, $\langle \hat{a}_2^\dagger(t)\hat{a}_2(t')\rangle$. As was done to the ASE field, we can split Equation 4.22 into annihilation and creation operator terms, and with the same analysis as was shown in Equation 4.19, we get that the mean photon per mode is $\langle \hat{a}_2^\dagger(t)\hat{a}_2(t')\rangle = 4\delta(t-t')\sinh^2\left(\frac{\alpha z}{2}\right)$. See Appendix C for more detail. It is seen that the mean number of photons per mode is identical to the two pulse photon echo efficiency. The mean photon per mode for the ASE and RASE fields is plotted in Figure 4.5.

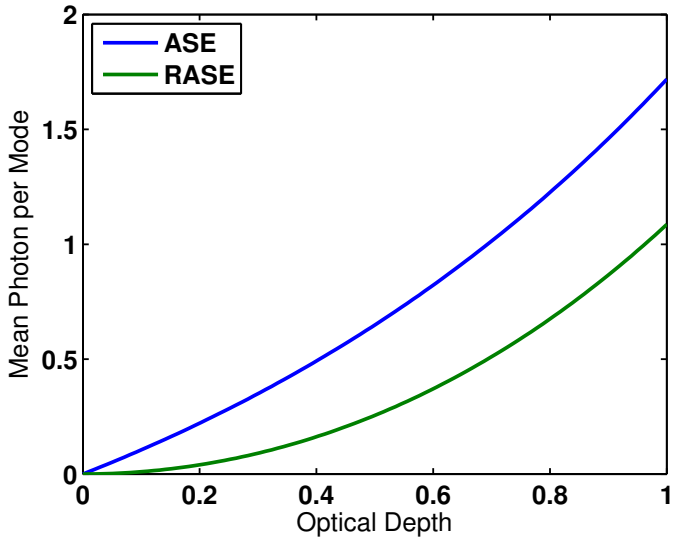

Figure 4.5: Mean photon per mode for the ASE and RASE fields. The ASE curve is $e^{\alpha z} - 1$, the RASE curve $4\sinh^2\left(\frac{\alpha z}{2}\right)$.

Violation of the Cauchy-Schwarz inequality

To determine whether the ASE and RASE fields show non-classicality, we consider the Cauchy-Schwarz inequality. Physically, this inequality is simply a ratio of the probability of having two photons at different times (t_1 and t_2) to the probability of having two photons at the same time. The Cauchy-Schwarz inequality is given by,

$$R \equiv \frac{p(t_1,t_2)^2}{p(t_1,t_1)\,p(t_2,t_2)}, \tag{4.23}$$

where $p(t_i,t_j) = \langle\, \hat{a}^\dagger(l,t_i)\,\hat{a}(l,t_i)\,\hat{a}^\dagger(l,t_j)\,\hat{a}(l,t_j)\,\rangle$ and $p(t_i,t_i) = \langle\, (\,\hat{a}^\dagger(l,t_i)\,\hat{a}(l,t_i)\,)^2\,\rangle$. For classical fields the Cauchy-Schwartz inequality states that $R \leq 1$ (see page 78 of [47]). Considering times equally separated about the second π pulse, from the expression for the output fields derived above we get

$$R(\alpha l) = \left[\frac{1}{2} + \frac{1}{2}\left(1 - e^{-\alpha l}\right)^{-2} - \frac{1}{8}\mathrm{csch}^2\left(\frac{\alpha l}{2}\right)\right]^2. \tag{4.24}$$

A more detailed derivation of this equation can be found in Appendix C.

It is easy to see from this equation that in the limit of large optical depth the inequality goes to one, and in the limit of small optical depth the inequality tends to infinity. The inequality is undefined when the optical depth is zero since the denominator of Equation 4.23 is zero in this case.

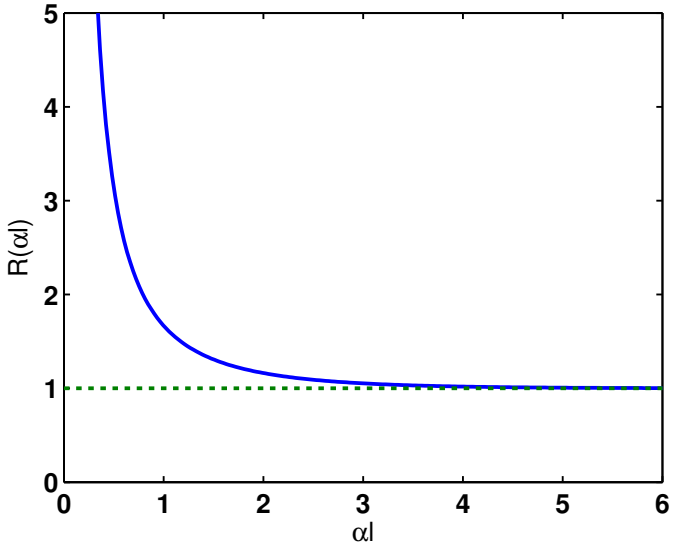

Figure 4.6: Plot of $R(\alpha l)$, showing the violations of the Cauchy-Schwartz inequality for small optical depths.

Figure 4.6 shows that for optical depths less than 1, the output at times equally

separated from the refocusing π pulse show nonclassical correlations. For the optically thin case $\alpha l << 1$, the non-classicality is high.

It should be noted that this is not perfect entanglement. The entanglement between the optical (ASE) and atomic modes is perfect but mapping the atomic modes back to optical modes (RASE) is not perfect. This is because the read efficiency is low for low optical depths. Before we saw that the echo efficiency is $\eta = 4\sinh^2\left(\frac{\alpha l}{2}\right)$, so for low optical depths the efficiency is less than 100%.

Variance and Inseparability

Another way to determine the nonclassical nature of the ASE and RASE fields is to invoke the inseparability criterion created by Duan et al. [118]. This criterion is for continuous variable systems. This is in contrast with the Cauchy-Schwarz inequality introduced above, which is best used for discrete photons.

Using this criterion involves making a measurement of the two quadrature amplitudes of the quantum state of light. In our case, the two quadrature amplitudes of the ASE(RASE) field are given by the quantum mechanical operators $\hat{x}_{1(2)}$ and $\hat{p}_{1(2)}$. One can express a maximally entangled state as a co-eigenstate of a pair of EPR type operators [10] such as,

$$\begin{aligned} \hat{u} &= \sqrt{b}\,\hat{x}_1 + \sqrt{1-b}\,\hat{x}_2 \\ \hat{v} &= \sqrt{b}\,\hat{p}_1 - \sqrt{1-b}\,\hat{p}_2, \end{aligned} \tag{4.25}$$

where b is an arbitrary real number. The criterion then states that for any separable quantum state ρ, the total variance of a pair of EPR-like operators given by the above equations satisfies

$$\langle(\Delta\hat{u})^2\rangle_\rho + \langle(\Delta\hat{v})^2\rangle_\rho \geq 2. \tag{4.26}$$

For inseparable states, the total variance of the $\hat{u}$ and $\hat{v}$ operators is bound from below by zero.

We now form the operators $\hat{u}$ and $\hat{v}$. Forming these operators involves obtaining the variance in each quadrature in each region ($\langle\hat{x}_1^2\rangle$) and the covariance between the same quadrature in different regions ($\langle\hat{x}_1\hat{x}_2\rangle$), with the assumption that the mean quadrature value is zero. As stated earlier, we can simplify the ASE and RASE fields as the following, $\hat{a}_1 = A + B^\dagger$ and $\hat{a}_2 = C + D^\dagger$. The functional form of the

quadrature operators is the following,

$$\hat{x}_i = \hat{a}_i + \hat{a}_i^\dagger \qquad \hat{p}_i = -i\left(\hat{a}_i - \hat{a}_i^\dagger\right) \tag{4.27}$$

where $i = \{1, 2\}$. Substituting in the simplified versions of the ASE and RASE fields, it is easy to get the following for the $\hat{x}$ quadrature,

$$\langle \hat{x}_1^2 \rangle = [A, A^\dagger] + [B, B^\dagger],\ \langle \hat{x}_2^2 \rangle = [C, C^\dagger] + [D, D^\dagger],\ \langle \hat{x}_1 \hat{x}_2 \rangle = [A, D^\dagger] + [B, C^\dagger]. \tag{4.28}$$

It is easy to see from Equation 4.27 that,

$$\langle \hat{x}_i^2 \rangle = \langle \hat{p}_i^2 \rangle \text{ and } \langle \hat{x}_i \hat{x}_j \rangle = -\langle \hat{p}_i \hat{p}_j \rangle, \tag{4.29}$$

where $i, j = \{1, 2\}$ and $i \neq j$.

The terms in Equations 4.28 are derived in the Appendix C, and we get the following,

$$\begin{aligned} \langle \hat{x}_1^2 \rangle &= 2\mathrm{e}^{\alpha z} - 1 \\ \langle \hat{x}_2^2 \rangle &= 1 + 8\sinh^2\left(\frac{\alpha z}{2}\right) \\ \langle \hat{x}_1 \hat{x}_2 \rangle &= 2\left(1 - \mathrm{e}^{\alpha z}\right). \end{aligned} \tag{4.30}$$

We see that the covariance term is negative, and increase in magnitude with increasing optical depth. When the optical depth is zero, we retain the expected vacuum variance of 1 and a covariance of zero. Figure 4.7 plots the equations.

We can now form the inseparability criterion by taking the variance of Equations 4.25 and substituting in Equations 4.30. This is demonstrated below, where the mean fields are set to zero,

$$\begin{aligned} \langle \hat{u}^2 \rangle + \langle \hat{v}^2 \rangle &= b\,\langle \hat{x}_1^2 \rangle + (1-b)\,\langle \hat{x}_2^2 \rangle + \sqrt{b\,(b-1)}\,\langle \hat{x}_1 \hat{x}_2 \rangle \\ &\quad + b\,\langle \hat{p}_1^2 \rangle + (1-b)\,\langle \hat{p}_2^2 \rangle - \sqrt{b\,(b-1)}\,\langle -\hat{p}_1 \hat{p}_2 \rangle \\ &= 2b\,(2\mathrm{e}^{\alpha z} - 1) + 2(1-b)\left(1 + 8\sinh^2\left(\frac{\alpha z}{2}\right)\right) + 4\sqrt{b(1-b)}\,\left(1 - \mathrm{e}^{\alpha z}\right). \end{aligned} \tag{4.31}$$

The inseparability criterion (Equation 4.31) is plotted for αz from 0 to 10 and for

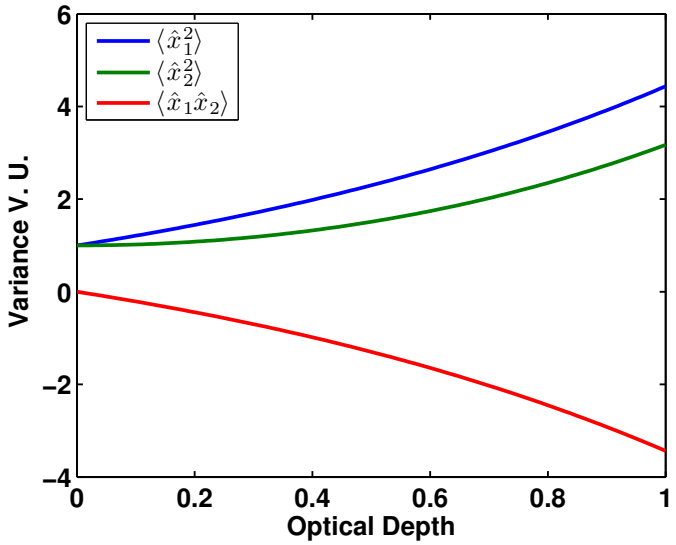

Figure 4.7: Plot of Equations 4.30 vs optical depth. The y-axis is the variance in terms of the variance of the vacuum.

b from 0 to 1 in Figure 4.8(a). The curve in Figure 4.8(b) represents the minimum inseparability value for a given optical depth. This curve is found by taking the minimum value for each optical depth value using Matlab. As can be seen, the minimum criterion decays as a function of optical depth indicating that the criterion is violated.

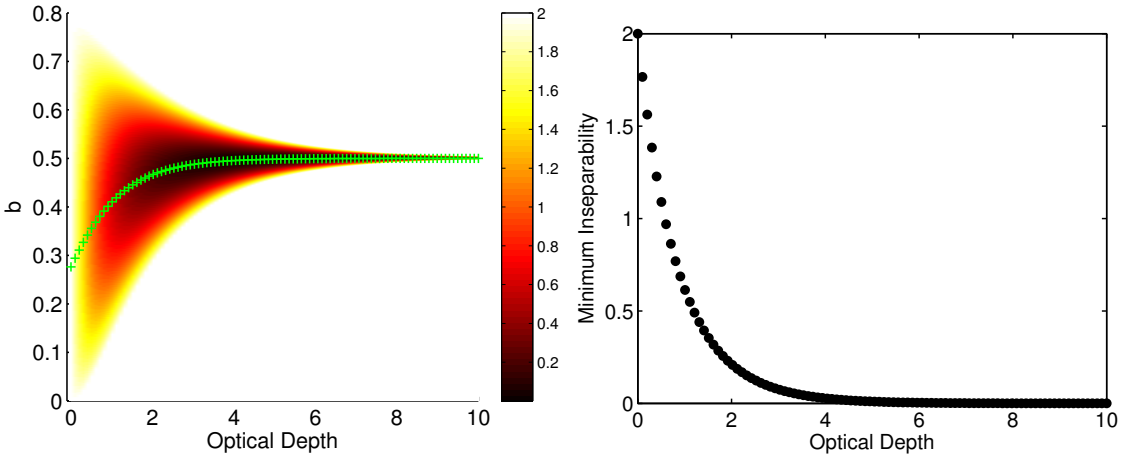

(a) (b)

Figure 4.8: (a) Inseparability criterion image for varying optical depth. White space indicates when the criterion exceeds 2. Green plus symbols indicate the value of b that minimizes the criterion for a given optical depth. (b) Minimum of inseparability criterion as a function of optical depth.

4.5 Implementation of RASE

In this section we discuss the experimental implementation of the RASE protocol.

System

One advantage of RASE is that this protocol can be implemented in a large range of atomic systems. RASE, in the simplest case, is implemented on the inhomogeneous line of a two level atomic ensemble. This is in contrast with the implementation of other quantum memory based technology. Protocols such as AFC and CRIB require long lived spectral features burnt into the inhomogeneous line. Rare earth ion systems such as europium and praseodymium are the ideal systems for long lived spectral features, but have inconvenient operational wavelengths ($\approx$ 580 nm and $\approx$ 606 nm). AFC and CRIB have been implemented in other rare earth systems such as thulium and erbium. These systems are more suitable to cheap diode laser systems and optical fiber networks ($\approx$ 790 nm and $\approx$ 1550 nm). However, these systems have poor optical pumping making high efficiency operation difficult to achieve.

Imperfect π pulses

The model described in the previous sections relies on the inverting π pulses to be ideal. The ideal π pulse inverts perfectly over the bandwidth of the pulse. Experimental implementation of such ideal π pulses can be challenging, so one must consider the effect of non-ideal π pulses. One can model a non-ideal pulse as an ideal pulse plus some coherence on the two level ensemble. This coherence will be temporally brief and if the inhomogeneous broadening is truly flat, will dephase quickly resulting in no net polarization after the ideal π pulse. The only way to have effects of the non-ideal π pulse interact with the optical field of interest is to rephase it with yet another π pulse, which is not the case here. The ability to prepare an ideal inverted medium for classical information processing has been investigated experimentally [119, 120].

Imperfect π pulses can result in random FID phenomena due to structure in the inhomogenous line, as mentioned in Section 2.4. These FIDs are difficult to avoid,

in particular with materials that have long lived spectral holes (e.g. Pr^{3+}:Y_2SiO_5). To avoid FIDs in these experiments, the poor holeburning material Tm^{3+}:YAG is used. Other methods to avoid this are the use of a four level echo scheme [3] or phase mismatching [121].

Phase Matching

The effect of phase matching is considered by extending to a 3D treatment in the paraxial approximation. Note, the above treatment is a 1D treatment. In the 3D case $a(z,t) \rightarrow a(z,\mathbf{k}_t,t)$ and $\sigma_-(z,\Delta,t) \rightarrow \sigma_-(z,\rho,\Delta,t)$ where $\mathbf{k}_t = (k_x,k_y)$ is the transverse wavevector and $\rho = (x,y)$ is the transverse position. This then results in the following equations of motion for the ground state

$$\frac{\partial}{\partial t}\hat{D}_g(z,\rho,\Delta,t) = i\Delta\,\hat{D}_g(z,\rho,\Delta,t) + i\int d^2\mathbf{k_t}\,\hat{a}(z,\mathbf{k}_t,t)e^{i\mathbf{k}_t.\rho} \tag{4.32}$$

$$\frac{\partial}{\partial z}\hat{a}(z,\mathbf{k}_t,t) = \frac{i\alpha}{2\pi}\int d^2\rho\int_{-\infty}^{\infty} d\Delta\,\hat{D}_g(z,\rho,\Delta,t)e^{-i\mathbf{k}_t.\rho}. \tag{4.33}$$

Fourier transforming the atomic operators along the transverse dimensions by defining

$$\hat{D}_g(z,\mathbf{k}_t,\Delta,t) = \int d^2\rho\,\hat{D}_g(z,\rho,\Delta,t)\exp(-i\mathbf{k}_t.\rho) \tag{4.34}$$

leads to Maxwell Bloch equations which are diagonal in the transverse wave vector

$$\frac{\partial}{\partial t}\hat{D}_g(z,\mathbf{k}_t,\Delta,t) = i\Delta\,\hat{D}_g(z,\mathbf{k}_t,\Delta,t) + i\hat{a}(z,\mathbf{k}_t,t) \tag{4.35}$$

$$\frac{\partial}{\partial z}\hat{a}(z,\mathbf{k}_t,t) = \frac{i\alpha}{2\pi}\int_{-\infty}^{\infty} d\Delta\,\hat{D}_g(z,\mathbf{k}_t\Delta,t). \tag{4.36}$$

For the excited state Maxwell Bloch, the same procedure gives

$$\frac{\partial}{\partial t}\hat{D}_e^{\dagger}(z,\mathbf{k}_t,\Delta,t) = i\Delta\,\hat{D}_e^{\dagger}(z,\mathbf{k}_t,\Delta,t) - i\,\hat{a}(z,-\mathbf{k}_t,t) \tag{4.37}$$

$$\frac{\partial}{\partial z}\hat{a}(z,\mathbf{k}_t,t) = \frac{i\alpha}{2\pi}\int_{-\infty}^{\infty}\hat{D}_e^{\dagger}(z,-\mathbf{k}_t,\Delta,t)\,d\Delta. \tag{4.38}$$

In the situation where the π pulse is applied off axis the phase of the π pulse

depends on the transverse position leading to the transformation

$$\hat{D}_e(z,\rho,\Delta,t) \leftarrow \hat{D}_g(z,\rho,\Delta,t)\exp(2i\mathbf{k}_\pi.\rho), \tag{4.39}$$

or after Fourier transforming

$$\hat{D}_e(z,\mathbf{k}_t,\Delta,t) \leftarrow \hat{D}_g(z,\mathbf{k}_t-2\mathbf{k}_\pi,\Delta,t). \tag{4.40}$$

For the RASE sequence, the phase of the first π pulse is irrelevant to the sequence. Regardless of the phase of this π pulse, the atoms will be inverted into the excited state. An imperfect π pulse will result in some small coherent excitation, but this can be ignored as it will dephase quickly (on the order of the π pulse duration) and any echo formed from this excitation will occur outside the time window of interest. The ASE caused by the inversion due to this π pulse is spatially multimode, with the amount of ASE in a particular mode determined by the gain experienced traversing the sample.

The first π pulse produces ASE with wavevector $\mathbf{k}_{\mathrm{ASE}}$, from Equations 4.37 and 4.38. The light with this wavevector is entangled with the atomic excitation with mode $-\mathbf{k}_{\mathrm{ASE}}$. The second π pulse transfers this to the wavevector $-\mathbf{k}_{\mathrm{ASE}}+2\mathbf{k}_\pi$ according to Equation 4.40. Equations 4.35 and 4.36 connect atomic and optical modes with the same wavevector so the wavevector for the RASE is $\mathbf{k}_{\mathrm{RASE}}=-\mathbf{k}_{\mathrm{ASE}}+2\mathbf{k}_\pi$ or

$$\mathbf{k}_{\mathrm{ASE}}+\mathbf{k}_{\mathrm{RASE}}=2\mathbf{k}_\pi. \tag{4.41}$$

This is the same phase matching condition as a two pulse photon echo, $\mathbf{k}_{\mathrm{input}}+\mathbf{k}_{\mathrm{echo}}=2\mathbf{k}_\pi$. The RASE protocol is thus identical to the two pulse photon echo with the input pulse as ASE and the output as RASE. While this phase matching condition is valid outside the paraxial regime, the only way to achieve phase matching is with the beams collinear or close to collinear, because the ASE, RASE and π pulse must all be at the same frequency.

4.6 Application to the DLCZ Protocol

It is interesting to consider the relationship of the current scheme with the DLCZ protocol [105]. The DLCZ protocol involves the creation of entanglement between distant ensembles. The relevant energy level diagrams are shown in Figure 4.9a. Once the level $|3\rangle$ has been adiabatically eliminated the write process is formally

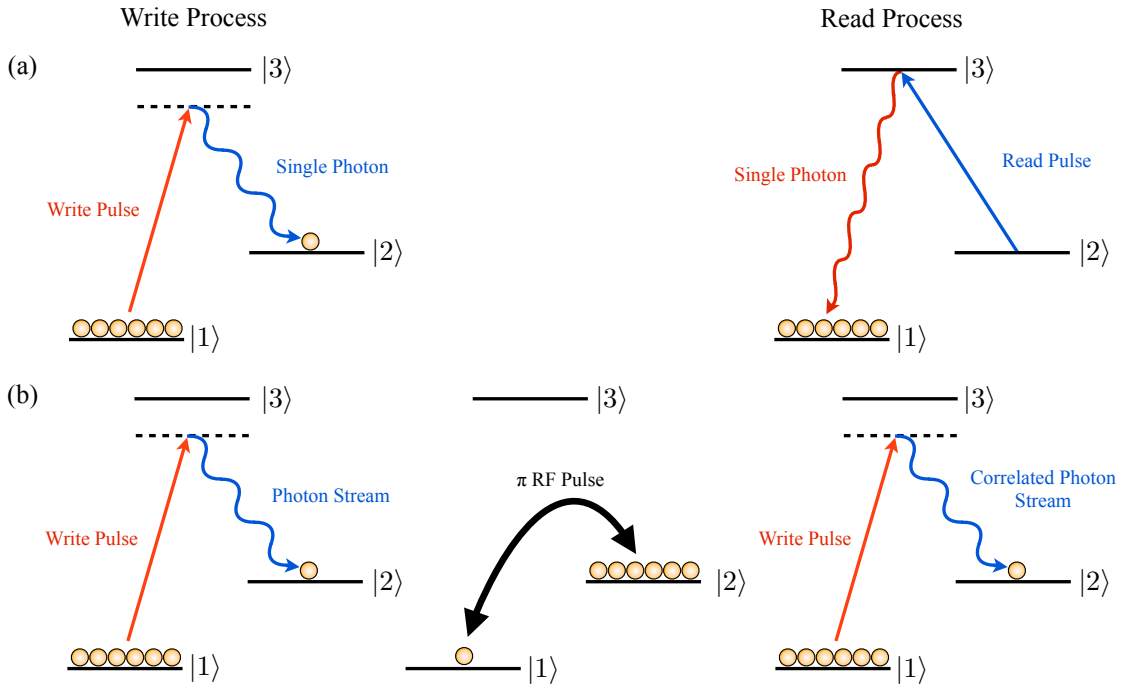

Figure 4.9: (a) DLCZ protocol showing write and read process. (b) Modified protocol. The inhomogeneous broadening of the $|1\rangle$-$|2\rangle$ transition now leads to an increase in bandwidth.

equivalent to a set of excited state atoms ($|1\rangle$) spontaneously emitting into the level $|2\rangle$. The emitted optical field is then steered elsewhere for entanglement generation with another ensemble of atoms [105]. Once entanglement is generated between two ensembles, one wishes to read out one ensemble's atomic field to a photonic field in order to implement entanglement swapping [105]. For the read process, state $|2\rangle$ becomes the excited state and state $|1\rangle$ the ground state.

One problem with this is the inhomogeneous broadening of the $|1\rangle$-$|2\rangle$ transition causes dephasing limiting the time separation between the writing and reading process. A modified DLCZ protocol, in close analogy with RASE, would overcome this problem. A rephasing pulse on the $|1\rangle$-$|2\rangle$ transition utilizes the inhomogeneous broadening, now increasing the bandwidth of the process rather than reducing the time separations. The sequence of events for this modified DLCZ protocol are shown in Figure 4.9b. It is worth noting that the modified DLCZ protocol does not have the same issue with echo efficiency as the two level scheme because the classical coupling field can be altered meaning that the ensemble can be optically thin for the writing process and thicker for the reading process.

The phase matching conditions for the modified DLCZ protocol will be the same

as given in Equation 4.41 for RASE. However with a Raman transition it is the wavevector difference for the two optical fields that is important. This means that one has a lot more freedom in the implementation because one is not restricted by the requirement that $\omega = ck$, as one is in the two level case.

4.7 Hybrid Photon Echo Rephasing

The previous sections described the RASE protocol. This protocol takes advantage of the seemingly undesirable additional noise on the output of the 2PE, by rephasing it at a later time and creating time separated entangled photon streams. In this section we return to the question of whether a quantum memory protocol can be implemented using strong optical rephasing pulses. Obviously, using only optical rephasing pulses, this can not be done. In this section we propose the idea of hybrid photon echo rephasing. This protocol uses a combination of strong optical pulses and external static electric fields. The pulse sequence is identical to the RASE protocol, with the exception of some input pulse to be stored. The optical pulses have the familiar role of rephasing the coherence due to the absorption of the input pulse. The electric fields have the role of Stark shifting the atoms, a property that is desirable, particularly with the CRIB protocol for quantum memory. Having the ability to Stark shift atoms allows for the elimination of the irritating gain feature created by a strong optical π pulse. This then allows spontaneous emission events to not be amplified and hence additional noise will not be seen on the output memory state.

Figure 4.10 shows the pulse sequence for the hybrid photon echo rephasing. This pulse sequence can be viewed as three time regions. The first region ($0 < t < t_1$) an input pulse is applied centered at $t = 0$, then followed by a strong Stark shifting pulse and rephasing π pulse at $t = t_1$. The π pulse creates the gain feature in which a 2PE echo and spontaneous emission events would propagate through and undergo amplification. To eliminate this effect, a temporally long position dependent Stark shifting field is applied over the duration of the second time region ($t_1 < t < t_2$). This broadens out the gain feature which eliminates the noise and also the formation of the two pulse photon echo since an additional position dependent phase shift has been added to the atoms. The effect of preventing the 2PE formation and broadening the gain feature effectively decouples the optical fields with the atomic fields . While the dephasing caused by the applied broadening stops the two pulse echo forming, so long as the broadening applied after the first π pulse exactly balances the additional

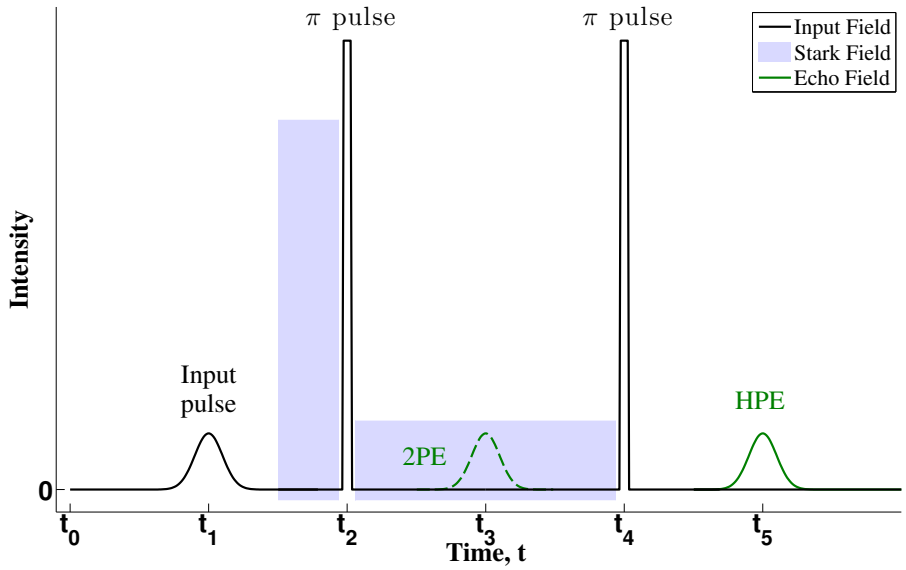

Figure 4.10: HYPER pulse sequence. The black solid line shows the applied fields where the green lines are the echo fields. Stark shifting electric fields are shown by the blue shaded areas. The green dashed line illustrates where the 2PE would form in the case of no electric fields.

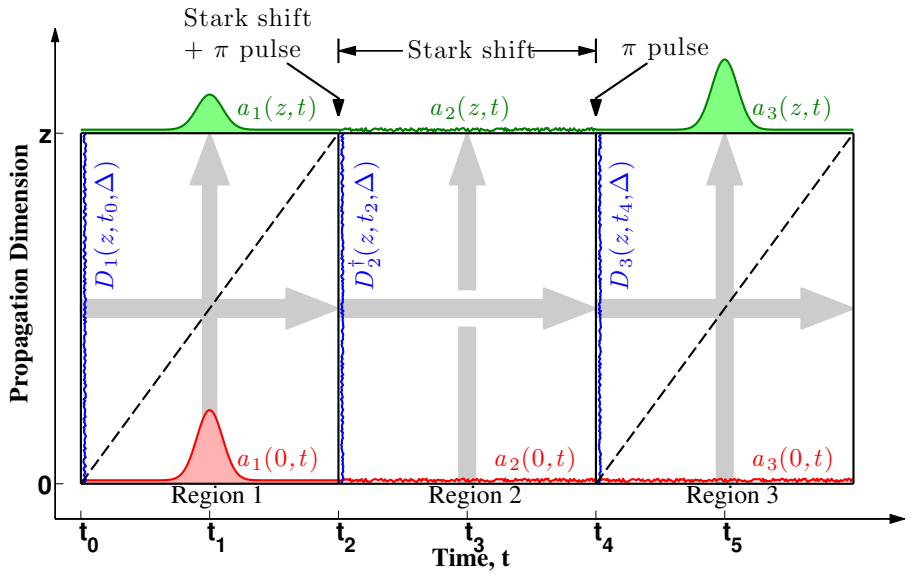

Figure 4.11: The 3 time regions for the HYPER sequence. For simplicity in the analytics, t_0 is set to zero. The input pulse is absorbed in region 1 ($t_0 < t < t_2$). It is assumed that the Stark and π pulse occur instantaneously at time $t = t_2$. A Stark pulse is then applied over region 2 ($t_2 < t < t_4$) followed by a π pulse at $t = t_4$. The output region is region 3 ($t_4 < t$). Red curves indicate optical inputs, green curves indicate optical outputs and blue curves are the atomic boundaries. The application of the Stark field over region 2 has the effect of decoupling the light from the atoms in that region.

phase shift acquired before the first π pulse, the echo of the echo will form after a second π pulse at $t = 2t_2 - 2t_1$. This is the output from the memory, the hybrid photon echo.

Analytical Theory

We now present some analytics. A full derivation of obtaining the solutions is presented in Appendix B. It is assumed, as before, that the input quantum state of light to be stored is of weak intensity. Thus, we can apply the quantum Maxwell-Bloch equations that were developed at the start of this chapter. As can be seen from the pulse sequence, regions 1 and 3 have the atoms near the ground state, and region 2 the atoms are near the excited state. We can use Equations (4.6, 4.7) for regions 1 and 3, and Equations (4.12, 4.13) for region 2. Of course, these equations and boundary conditions will need to be modified appropriately to take into account the effect of the Stark shift.

For region 1 before the Stark pulse is applied the equations of motion are exactly Equations 4.6 and 4.7 which have the solutions given by Equations 4.8 and 4.10.

Now the Stark shifting field is taken into account. It is assumed that this field is placed just before the first π pulse and is strong and temporally short, allowing the dynamics of the optical field to be ignored at the boundary. The Stark shifting field shifts an atom's detuning dependent on its position by ηz such that $\Delta \rightarrow \Delta + \eta z$ and the π pulse inverts an atoms detuning such that $\hat{D} \rightarrow \hat{D}^\dagger$. The Stark shift and π pulse results in the following transformation on the atomic field at the region 2 ($t = t_2$) boundary,

$$\hat{D}_2^\dagger(z, t = t_2, \Delta) = \left[\hat{D}_1(z, t_2, \Delta)\mathrm{e}^{i\eta_1 z}\right]^\dagger \tag{4.42}$$

where $\hat{D}_1$ is given by Equation 4.6 and $\eta_1 = \eta(t_f - t_i)$. Here, η is the size of the Stark shifting field and $t_f - t_i$ is the duration of that field.

Region 2 has a Stark shift applied over the duration of the region. The equations of motion that describe the dynamics are Equations 4.12 and 4.13 with the addition of the Stark shift

$$\frac{\partial}{\partial t}\hat{D}_2^\dagger(z, t, \Delta) = i(\Delta + \eta' z)\hat{D}_2^\dagger \; - \; i\hat{a}_2 \tag{4.43a}$$

$$\frac{\partial}{\partial z}\hat{a}_2(z, t) = \frac{i\alpha}{2\pi}\int_{-\infty}^{\infty} d\Delta \; \hat{D}_2^\dagger \, , \tag{4.43b}$$

The atomic field solution for region 2 is given by

$$\hat{D}_2^\dagger(z,t,\Delta) = -i\int_{-\infty}^{t} \hat{a}_2(z,t')e^{i(\Delta+\eta' z)(t-t')} + \hat{D}_2^\dagger(z,t_2,\Delta)e^{i(\Delta+\eta' z)(t-t_2)}. \tag{4.44}$$

The optical field solution is obtained using similar mathematical techniques seen at the start of this chapter, given below as

$$\hat{a}_2(z,t) = \hat{b}_2(0,t)e^{\alpha z/2} + \hat{b}_1^\dagger(0,2t_2-t)e^{\alpha z/2}\frac{\alpha\left[1-e^{-(\alpha+i(\eta_1-\eta'(t-t_2)))z}\right]}{\alpha+i(\eta_1-\eta'(t-t_2))} \tag{4.45}$$

where we have defined the following operators

$$\hat{b}_2(0,t) = \hat{a}_2(0,t) + i\alpha\int_0^z dz' e^{-(\alpha/2+i(\eta_1-\eta'(t+t_2)))z'}\hat{D}_1^\dagger(z',t-2t_2)$$
$$\hat{b}_1(0,t) = \hat{a}_1(0,t) + i\alpha\int_0^z dz' e^{\alpha z'/2}\hat{D}_1(z',t).$$

It is noted that when the Stark fields are set to zero, the two pulse photon echo solutions are retained with efficiency $\eta_{2\mathrm{PE}} = 4\sinh^2(\frac{\alpha z}{2})$.

We can now form the region 3 boundary condition, in a similar fashion as the region 2 boundary condition was formed, namely $\hat{D}_3(z,t=t_4,\Delta) = \left[\hat{D}_2^\dagger(z,t_4,\Delta)\right]^\dagger$.

The equations of motion that describe the dynamics of region 3 are exactly those stated for region 1, Equations 4.6 and 4.7. Hence the optical solution for region 3 is identical in form to Equation 4.10, with subscript $1 \rightarrow 3$ and $\hat{D}_3(z,t) \equiv \mathcal{F}^{-1}\left[\hat{D}_3(z,t_4,\omega)e^{-i\omega t_4}\right]$. For balanced Stark fields, the output optical solution in region 3 is,

$$\hat{a}_3(z,t) = \hat{b}_3(0,t)e^{-\alpha z/2} - \hat{b}_2^\dagger(0,2t_4-t)\,\frac{\alpha\left[e^{(\alpha-i\eta'(t-t_4))z}-1\right]}{\alpha-i\eta'(t-t_4)}\,e^{-\alpha z/2}$$
$$-\hat{b}_1(0,t-2t_4+2t_2)\left[\alpha z+\alpha^2\left(\frac{\left[e^{(\alpha-i\eta'(t-t_4))z}-1\right]}{(\alpha-i\eta'(t-t_4))^2} - \frac{z}{\alpha-i\eta'(t-t_4)}\right)\right]e^{-\alpha z/2}. \tag{4.46}$$

where we have defined the operator

$$\hat{b}_3(0,t) = \hat{a}_3(0,t) + i\alpha\int_0^z dz' e^{\alpha z'/2}\hat{D}_1(z',t-2t_4+2t_2).$$

In the limit as the Stark shift over region 2 tends toward infinite intensity, Equa-

tion 4.46 becomes

$$\hat{a}_3(z,t) = \hat{a}_3(0,t)e^{-\alpha z/2} \; - \; \hat{a}_1(0,t-2t_4+2t_2)\alpha z e^{-\alpha z/2} \\ + i\left[\alpha(1-\alpha z)e^{-\alpha z/2}\int_0^z dz' e^{\alpha z'/2}\hat{D}_1(z',t-2t_4+2t_2)\right]. \tag{4.47}$$

The solution has three terms. The first term is the inevitable optical vacuum input at the region 3 time boundary which decays as a function of the optical depth. The second term is the HYPER echo which forms at a time $t_5 = t_1 - 2t_4 + 2t_2$ for an input at $t_1$and has efficiency of $\eta_{\mathrm{HPE}} = (\alpha z)^2 \mathrm{e}^{-\alpha z}$. This echo has a maximum efficiency of 54% at $\alpha l = 2$. The third term contains the atomic degrees of freedom.

It can be seen that the Stark shifting field over region 2 eliminates contributions from region 2 on the region 3 output. Taking the limit of infinite Stark shift is physically equivalent to decoupling the optical and atomic fields in the equations of motion in region 2, thus 'switching off' the collective atom-light interaction in this region and reducing the noise on the output field. In the decoupled regime, the atomic boundary condition at region 3 ($t = t_4$) is found by propagating the region 2 boundary condition ($t = t_2$) forward in time by $t_4 - t_2$. The result obtained for the output field in region 3 is then identical to Equation 4.47.

The HYPER echo efficiency of 54% in the forward direction is reminiscent of the efficiency of the CRIB protocol in the forward direction (Chapter 3). To determine the efficiency in the backward retrieval regime, a semi-classical analysis is considered. The crystal exists from $0 < z < L$ and fields propagating in the forward direction are described by Equations 4.6 and 4.7, where for clarity the subscript is now f. In the backward direction, the equation of motion for the optical field a_b is similar to Equation 4.7 except with a minus sign on the left-hand side since the propagation is in the opposite direction.

Consider an input optical field at the front of the crystal $a_f(z = 0, t) = a_{in}(t)$ which is non-zero for times $t < 0$ and the atomic fields are in the ground state. The solutions are the semi-classical equivalent of Equations 4.8 and 4.10, stated below as

$$a_f(z,t) = a_f(0,t)e^{-\alpha z/2} \\ D_f(z,t,\Delta) = i\int_{-\infty}^{\infty} a_f(z,t')\, e^{i\Delta(t-t')}\, dt'. \tag{4.48}$$

The integral for the atomic solution has an upper limit of infinity as the optical field

is zero for $t > 0$. At time $t = 0$, the integral becomes

$$D_f(z, t = 0, \Delta) = i \int_{-\infty}^{\infty} a_f(z, t')\, e^{-i\Delta t'}\, dt' = i\, e^{-\alpha z/2}\, a_{in}(\omega = \Delta). \tag{4.49}$$

The dynamics of the two Stark shifts and the two π pulses are reduced to an instantaneous operation at $t = 0$. For the case of counter-propagating π pulses, the operation has the effect

$$D_b(z, t = 0, \Delta) \leftarrow D_f(z, t = 0, \Delta) e^{-i\Delta t_d}, \tag{4.50}$$

where t_d is the the time difference between the atoms being in the excited and ground state during the rephasing period. The solution for the optical field is in the form of 4.10

$$a_b(z, \omega) = a_b(L, \omega) e^{-\alpha(L-z)/2} + i\alpha \int_L^z dz'\, e^{-\alpha(z'-z)/2}\, D_b(z', 0, \omega)\ . \tag{4.51}$$

This equation has two terms. The first term is zero in the semi-classical regime as the backward field at $z = L$ is zero. The second term is an integral that is easily evaluated. At the front of the crystal ($z = 0$) the output field $a_{out}(\omega) = a_b(o, \omega)$ is given by

$$a_{out}(\omega) = a_{in}(\omega)(1 - e^{-\alpha L}) e^{-i\omega t_d} \tag{4.52}$$

which in the time domain is

$$a_{out}(t) = a_{in}(t - t_d)(1 - e^{-\alpha L}). \tag{4.53}$$

The efficiency in the backward direction is therefore $(1-e^{-\alpha L})^2$ which is identical in form to the CRIB efficiency in the backward direction (Equation 3.1). In the limit of large optical depth, the efficiency tends to 100%.

Experimental implementation of retrieval in the backward direction can be achieved by using counter-propagating rephasing π pulses. For example, if the input pulse co-propagates with one of the π pulses then, due to phase matching conditions, the recalled light co-propagates with the other π pulse and hence is retrieved in the backward direction.

Figure 4.12 shows the experimental implementation of hybrid photon echo rephasing technique [7].

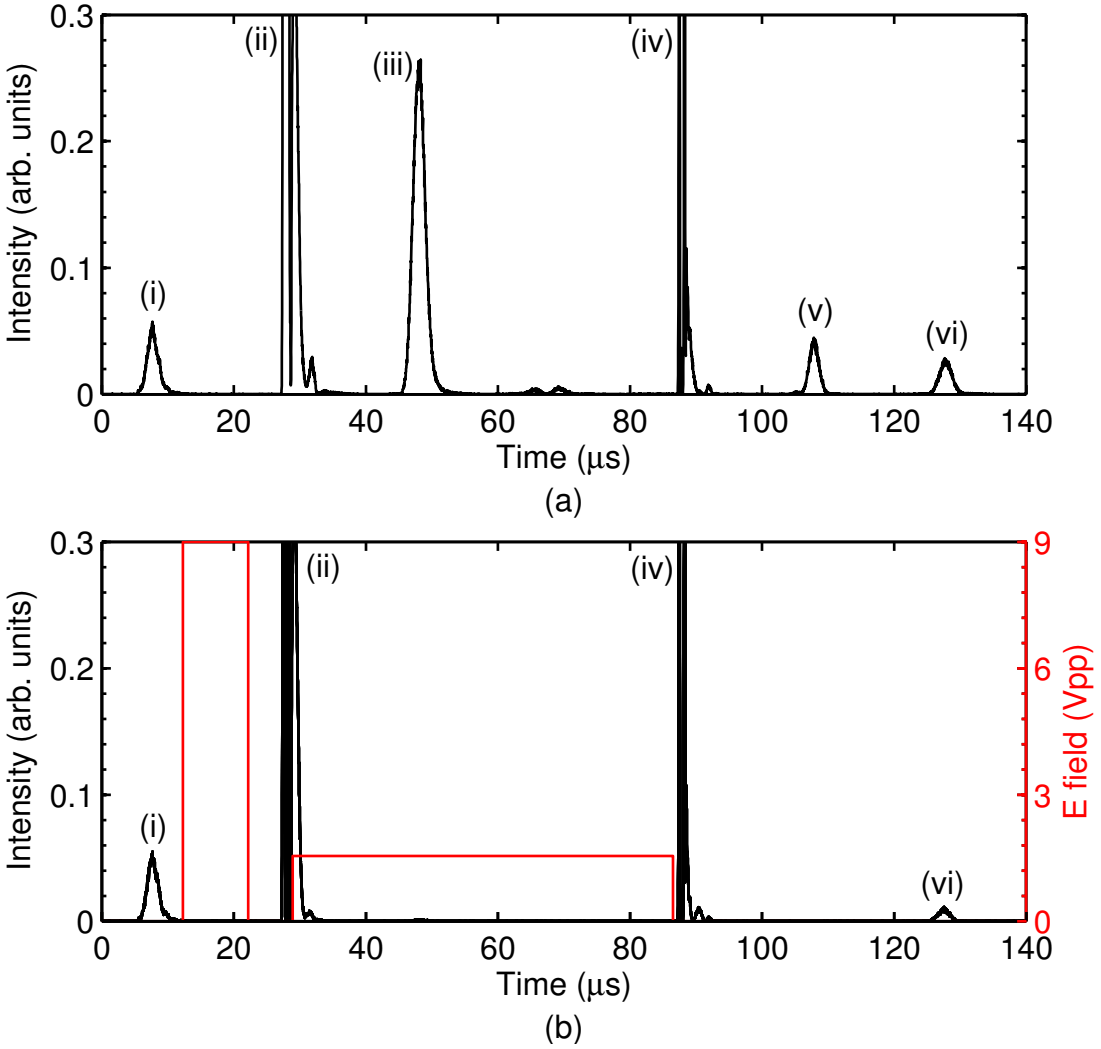

Figure 4.12: Experimental implementation of the hybrid photon echo rephasing technique from D. L. McAuslan [4, 7]. (a) shows the case when the external fields are off, (b) the case when they are on. The black line is the detector output showing the applied optical fields, the red lines are the applied external field. Pulse (i) is the input pulse. This is then followed by pulse (ii) the rephasing π pulse which results in the creation of the photon echo (iii) at a time symmetric about the π pulse. A second π pulse is applied (iv) which creates a three pulse photon echo (v) and then the echo of (iii) i.e (vi). When the external fields are applied, we see that the two and three pulse photon echos are eliminated, but the echo of the two pulse photon echo remains.

Chapter 5

Experimental Description

In this chapter we present the details of the experimental set-up used to obtain the results of this thesis. The chapter is in two parts. In the first part of this chapter the laser set-up and locking is described. The laser used in this experiment was also used for other experiments conducted by Jian Wei Tay [2], Warrick G. Farr and Dmitry Korystov [5]. The external cavity diode laser system was built by JWT. The servo used for locking was designed by JWT. My role in the locking was the tweaking of gain and bandwidth of the laser servo. JWT and I jointly worked on the optical feedback of the locking, producing the measurement of the noise on the error signal, Figure 5.6(a). WGF and DK provided the beat measurement of the two identical laser systems, Figure 5.7, and the Allen variance plot, Figure 5.8. A paper has been prepared on the frequency stabilizing of this laser [5].

In the second part of this chapter, the heterodyne detection system used to measure the ASE and RASE fields is described and characterized.

5.1 Laser

The experimental results presented in this thesis are obtained using a thulium yttrium aluminum garnet crystal. The transition of interest has the wavelength 793.156nm in air. The laser used is a laser diode supplied by Eagleyard model number EYP-RWE-0840-06010-1500-SOT02-0000. The centre wavelength of this diode is 810nm, and the manufacturer claims a tuning range of 35nm either side of 815nm, dependent on the external cavity used. Our set up involves an external cavity in the Littrow configuration [122], shown in Figure 5.1. The grating used in the cavity has 1800 lines/mm. The diode laser output is steered onto the diffraction grating, and

the first order diffraction beam is steered back toward the diode laser facet. This allows for wavelength selectively by adjusting the angle of the grating with respect to the beam output direction of the bare diode. This is the case because the wavelength of the diffracted beam is related to the angle of incidence. Of course, this particular configuration has the disadvantage of the beam spatially moving when scanning the grating angle, but the advantage of more optical power compared to the Littman-Metcalf scheme [123]. The Littman-Metcalf scheme has the added advantage of a narrower linewidth than the Littrow configuration.

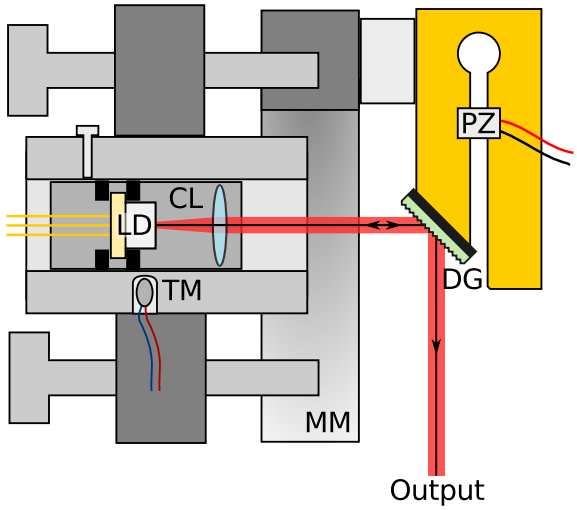

Figure 5.1: ECDL set-up (figure courtesy of Tay [6]). Refer to the text for description of set-up. Elements include: LD = Laser Diode, CL = Collimating Lens, TM = Thermistor, MM = Mirror Mount, DG = Diffraction Grating, PZ = Piezo Electric Transducer.

Figure 5.1 illustrates the laser diode mounting. The diode is mounted in a casing which is then attached to a modified mirror mount, which allows for angle adjustment between the bare diode and the grating. The grating is mounted to a peg shaped piece of metal with a piezo stack placed between the two prongs, allowing the grating angle to be adjusted independently. This combined diode laser mirror mount and grating mount is then mounted to a piece of metal which is in thermal contact with a thermistor. The thermistor allows for frequency scanning of the laser frequency by scanning the temperature. A lens is placed after the laser diode to collimate the output beam.

The current driver used is a home-built version of Libbrecht and Halls current supply [124]. The current can also be used to scan the frequency. This is because the current can change the temperature of the diode cavity and hence the cavity length. The optical length of the diode can also change due to a refractive index

change of the diode junction. The maximum current that this particular diode can take is 200 mA. Typical operational current is 180 mA. At this current, the output power is 42 mW.

The major advantage diode lasers have over other laser systems at these wavelengths is that they are cost effective. The laser diodes used here were purchased for around 500 euros and cheaper alternatives exist. Other systems such as Ti:Sapphire systems require expensive components and a powerful green pumping laser, also expensive. Compared to this diode lasers seem to be the better option. The disadvantage of laser diodes is the large amounts of broadband (MHz) phase noise they have. To take full advantage of the narrow homogenous linewidths that rare earth ions boast, a laser of comparable linewidth must be used. Thus, bare diode lasers have limited use in continuous variable quantum optics applications. This phase noise is associated with the broad Schawlow-Townes linewidths of bare diode lasers, due to their short length and the low Q-factor of their resonators. The stability of the output frequency is limited by the current supply used as diodes are sensitive to current fluctuations.

5.2 Locking

For continuous variable experiments in rare earth ion doped crystals, frequency stabilization to the order of the homogenous linewidth of rare earths is required. In this section we detail the method of Pound-Drever-Hall locking [125].

Pound Drever Hall

The locking technique employed here is the well known technique of Pound Drever Hall (PDH) locking [125]. This technique involves locking to a narrow frequency reference, for example, a high finesse cavity. The laser phase is dithered using an electro-optic modulator (EOM) creating frequency sidebands. The light is then steered toward a cavity, and the transmitted, but more importantly, reflected and leakage fields are detected. The reflected field can tell you which side of the resonance the laser is at, perfect for a feedback signal. The reflected and leakage fields can then be mixed with an RF local oscillator of identical frequency to the dithering RF field on the EOM. This is effectively taking the derivative of the transmitted signal. The result is the locking error signal. The sign of the error signal is different on either side of resonance, and is zero on resonance. The error signal is fed through

some amplification and then into the laser current driver, which will compensate for frequency fluctuations dependent on the characteristics of the servo amplifier.

The electric field of a laser beam is given by $E_0 e^{i\omega t}$ where ω is the frequency of the laser. Dithering the phase using an EOM has the following effect on the electric field,

$$\begin{aligned} E_i =& E_0 e^{i(\omega t + \beta \sin(\Omega t)} = E_0 \sum_{-\infty}^{\infty} J_n(\beta) e^{i(\omega + n\Omega)t} \approx E_0 \sum_{-1}^{1} J_n(\beta) e^{i(\omega+n\Omega)t} \\ =& E_0 \left[J_0(\beta) e^{i\omega t} + J_1(\beta) e^{i(\omega+\Omega)t} - J_1(\beta) e^{i(\omega-\Omega)t} \right], \end{aligned} \tag{5.1}$$

where higher order terms have been omitted under the assumption of small β. Here, ω is the carrier frequency and the sideband frequencies are $\omega \pm \Omega$. Ω is the modulation frequency and β is the modulation depth, a measure of how much power is put into the sidebands. J_n are the nth order Bessel functions. If P_0 is the total power in the beam, then the power in the carrier (P_c) is $J_0^2(\beta) P_0$ and the power in each sideband (P_s) is $J_1^2(\beta) P_0$. For small modulation depths, $P_0 \approx P_c + 2P_s$.

Steering the above beam into a Fabry-Perot cavity results in some of the beam being reflected, and some being transmitted. The reflected beam is given by $E_r = F E_i$, where F is the coefficient of reflection. For a symmetric lossless cavity the reflection coefficient is

$$F = \frac{r(e^{i\phi} - 1)}{1 - r^2 e^{i\phi}}. \tag{5.2}$$

Here, r is the amplitude reflection coefficient of the mirrors in the cavity and $\phi = \omega \frac{2L}{c}$ is the phase shift from one round trip of the cavity length L. The reflected beam then becomes,

$$E_r = E_0 \left[F(\omega)\ J_0(\beta) e^{i\omega t} + F(\omega + \Omega)\ J_1(\beta) e^{i(\omega+\Omega)t} - F(\omega - \Omega)\ J_1(\beta) e^{i(\omega-\Omega)t} \right]. \tag{5.3}$$

The reflected beam is measured on a detector, so the power in the reflected beam is $P_r = |E_r|^2$,

$$\begin{aligned} P_r =& P_c |F(\omega)|^2 + P_s \left[|F(\omega+\Omega)|^2 + |F(\omega-\Omega)|^2 \right] \\ &+ 2\sqrt{P_c P_s} \left[\mathrm{Re}\left[F(\omega) F^*(\omega+\Omega) - F^*(\omega) F(\omega-\Omega) \right] \cos(\Omega t) \right] \\ &+ 2\sqrt{P_c P_s} \left[\mathrm{Im}\left[F(\omega) F^*(\omega+\Omega) - F^*(\omega) F(\omega-\Omega) \right] \sin(\Omega t) \right] \\ &+ \mathcal{O}(2\Omega), \end{aligned} \tag{5.4}$$

where $\mathcal{O}(2\Omega)$ contains the terms as a function of 2Ω.

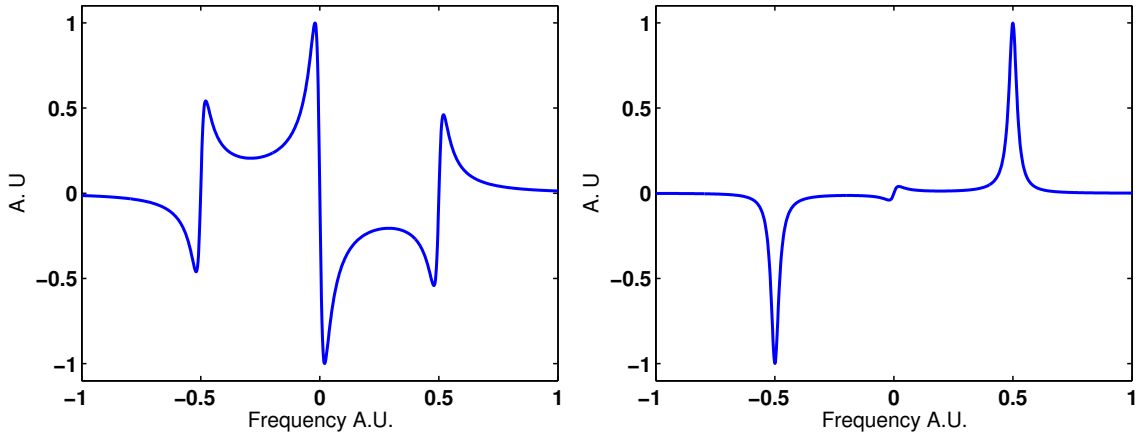

(a) Error Signal (b) Quadrature Error Signal

Figure 5.2: Example of in phase and in quadrature error signals produced with a lossless cavity. The modulation frequency is 5% of the free spectral range of the cavity. The cavity has a finesse of about 3100.

We can now mix this signal with a local oscillator of $\sin(\Omega t)$ to get the error signal, or with $\cos(\Omega t)$ to get the quadrature error signal. Figure 5.2 shows both cases. It is noted for the error signal that it is zero when the carrier or sidebands resonate in the cavity. However, the slope of the error signal is opposite for the carrier and sidebands.

The signal of most use is the error signal. However, the quadrature error signal is useful if you want to know which side of the resonance you are on, as it is always positive on one side and always negative on the other.

The Pound-Drever-Hall technique requires the laser beam to be well mode-matched to a high finesse cavity at the right wavelength. Such cavities are time consuming to construct. Temperature stability is required for a fixed cavity length and the cavity needs to be isolated from sources of vibration. A technique that does not rely on being well mode-matched or require a high finesse cavity is to lock using persistent spectral hole burning [126–129]. In this technique, the frequency reference is a spectral hole burnt into the inhomogeneously broadened optical transition of a rare earth ion doped crystal. In particular, a thulium yttrium aluminum garnet crystal. In this case, no mode-matching is required, one only requires the laser beam to be steered through the crystal. In contrast with the traditional PDH locking, here we can only detect the transmitted field. One can still obtain the error signal using the transmitted signal.

Locking using spectral hole burning

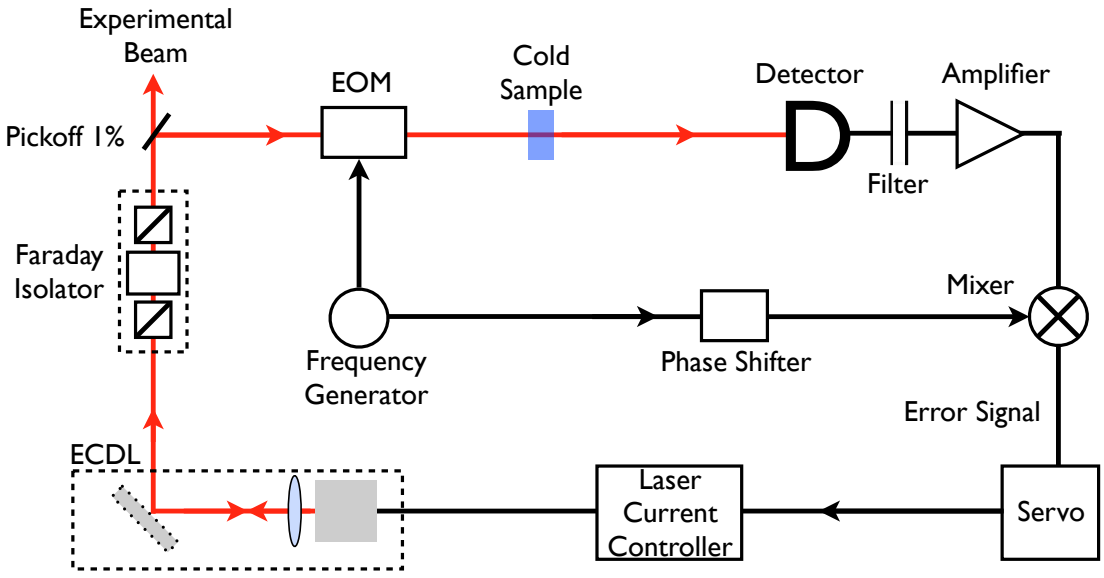

Figure 5.3: Electronic locking set-up.

Figure 5.3 shows a schematic of the electronic locking set-up. To generate the error signal, the beam is directed through an electro-optic phase modulator (EOM) to generate the frequency modulated sidebands at 30 MHz. The dithered beam is then directed through a Tm^{3+}:YAG 0.1% sample cryogenically cooled to 2.7 K. The sample used has dimensions 8×4×4 mm, with light propagating 4 mm along the $[1\,\bar{1}\,0]$ direction. The incident beam on the sample had a power of 150 μW and a diameter of 4 mm. The laser frequency is then kept at the center of the hole by using a servo loop on the laser current. Details of the servo loop can be found in Tay's thesis [6]. As the holes are transient, the error signal frequency response drops off at a low frequency given by the hole lifetime. Also, the response of the error signal will drop off at a high frequency given by the hole width. Due to this, the servo gain is rolled off at both low and high frequencies. This ensured that the servo would not be driven to its rails by integrator-like transfer functions acting on small offsets.

An example of the measured error signal is given in Figure 5.4. With this locking, the laser linewidth achieved was able to produce a 100 kHz wide holeburnt feature in cryogenically cooled Tm^{3+}:YAG.

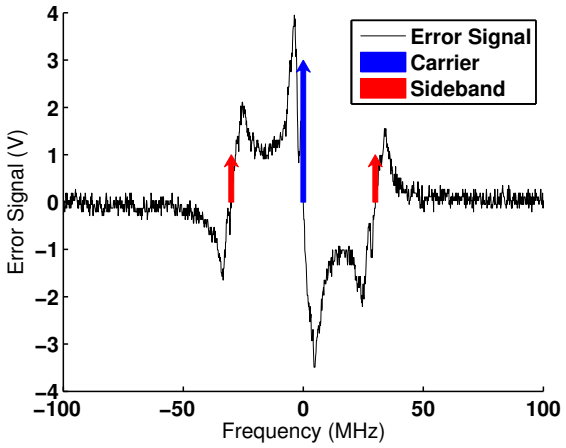

Figure 5.4: Measured error signal for our locking system. Arrows have been placed at the carrier and sideband frequencies for the benefit of the reader. The modulation frequency is 30 MHz. The figure is obtained by sweeping the laser frequency, achieved by sweeping the current input to the controller.

5.3 Hybrid Laser Locking

Electronic locking is less effective at high frequencies as propagation delays and causality limit the servo bandwidth. A method of locking that is not limited like this is optical feedback to the laser. In this section we describe the hybrid laser locking technique [5].

This technique involves two forms of feedback. As well as using PDH locking to lock the laser to a spectral hole we feed some of the light transmitted through the hole back into the laser diode. An analysis of the case in which the output of a laser is put through an optical network and then fed back into the laser is given by Agrawal [130]. The main result there is that the laser linewidth becomes narrower when the round trip time τ of the larger cavity is increased. Also, the laser frequency becomes less sensitive to the current noise fluctuations.

We now present a theoretical treatment similar to Agrawal [130] taking into account that we have a spectral hole in the larger cavity. As stated in [130], the equation of motion for the case where output light from a laser is steered through a cavity and then injected back into the laser cavity is

$$\dot{E}(t) = -i\delta E(t) + \frac{1}{2}(G-\gamma)(1-i\eta)E(t) + H(t) * E(t), \tag{5.5}$$

where $\delta = \omega - \omega_0$ is the relative frequency of the laser ω to the center of the spectral hole ω_0, G is the total rate of gain of the cavity, γ is the cavity decay rate and η is the

linewidth enhancement factor which is proportional to the carrier induced refractive index change. The last term in this equation describes the optical feedback, where $H(t)$ is the impulse response of the external optical network. The impulse response is convolved with the electric field in the last term of Equation 5.5.

In our system we have two contributions to the external optical network, the propagation delay of the large cavity and the spectral hole inside the large cavity. The impulse response of the cavity propagation is

$$h(\omega)_{\mathrm{c}} = \kappa \exp\left(i\left[-\omega\tau + \phi_0\right]\right) \tag{5.6}$$

where κ is the feedback coupling rate, $\phi_0 = \omega_0\tau + \phi_m$ and ϕ_m is the phase shift due to mirrors. For the spectral hole, the impulse response is described by the following [127]

$$h(\omega)_{\mathrm{h}} = \exp\left(-\frac{\alpha L}{2}\left[1 - \frac{\Gamma}{\Gamma + i\delta}\right]\right), \tag{5.7}$$

where αL is the optical depth of the sample and $\frac{\Gamma}{2\pi}$ is the width of the spectral hole. The total impulse response $h(\omega)$ is the multiplication of the two responses, giving

$$H(t) = \mathscr{F}^{-1}\left[h(\omega)\right] = \mathscr{F}^{-1}\left[h(\omega)_{\mathrm{c}} h(\omega)_{\mathrm{h}}\right]. \tag{5.8}$$

We can now easily form $h(\omega)$,

$$\begin{aligned} h(\omega) &= \kappa \exp\left(-\frac{\alpha L}{2}\left[1 - \frac{\Gamma}{\Gamma + i\delta}\right] + i\left[-\omega\tau + \omega_0\tau + \phi_m\right]\right) \\ &= \kappa \exp\left(-\frac{\alpha L}{2\Gamma}\left[\frac{\Gamma}{1 + (\frac{\Gamma}{\delta})^2} + \frac{i\delta}{1 + (\frac{\delta}{\Gamma})^2}\right] + i\left[-\delta\tau + \phi_m\right]\right) \\ &= \kappa \exp\left(-\frac{\alpha L}{2}\left[\frac{1}{1 + (\frac{\Gamma}{\delta})^2}\right]\right) \exp\left(-\frac{\alpha L}{2\Gamma}\left[\frac{i\delta}{1 + (\frac{\delta}{\Gamma})^2}\right] + i\left[-\delta\tau + \phi_m\right]\right). \end{aligned} \tag{5.9}$$

For the case when the laser is tightly locked to the hole ($\omega \approx \omega_0$), we can approximate the above expression as

$$\begin{aligned} h(\omega) &\approx \kappa_{\mathrm{eff}} \exp\left(-i\frac{\alpha L}{2\Gamma}\delta\right) \exp\left(i\left[-\delta\tau + \phi_m\right]\right), \text{ where } \kappa_{\mathrm{eff}} = \kappa\ \mathrm{Re}[h(\omega \approx \omega_0)] \\ &= \kappa_{\mathrm{eff}} \exp\left(-i\left[\tau\delta - \phi_m + \frac{\alpha L}{2\Gamma}\delta\right]\right) \end{aligned}$$

$$= \kappa_{\text{eff}} \exp\left(-i\left[\tau_{\text{eff}}\delta - \phi_m\right]\right), \text{ where } \tau_{\text{eff}} = \tau + \frac{\alpha L}{2\Gamma}$$
$$h(\omega) \approx \kappa_{\text{eff}} \exp\left(i\phi_{0\text{eff}}\right) \exp\left(-i\omega\tau_{\text{eff}}\right), \text{ where } \phi_{0\text{eff}} = \omega_0\tau_{\text{eff}} + \phi_m. \tag{5.10}$$

It is now easy to form the last term of Equation 5.5,

$$H(t) * E(t) = \mathscr{F}^{-1}\left[h(\omega)E(\omega)\right] \approx \mathscr{F}^{-1}\left[\kappa_{\text{eff}} \exp\left(i\phi_{0\text{eff}}\right) \exp\left(-i\omega\tau_{\text{eff}}\right) E(\omega)\right]$$
$$= \kappa_{\text{eff}} \exp\left(i\phi_{0\text{eff}}\right) E(t - \tau_{\text{eff}}). \tag{5.11}$$

The above equation is identical in form to a propagation delay only. The effect of having a spectral hole is to simply introduce an additional delay ($\alpha L/2\Gamma$) to the propagation delay (τ). We can estimate values for the effective time delay for our experiment to be $\Gamma = 50$ kHz and $\alpha L = 0.5$. Hence we get a large effective time delay $\tau_{\text{eff}} = 5$ μs due to dispersion of the hole. This large effective time delay is equivalent to an external cavity that is 1.5 km long.

The phase of the laser light will vary with each introduction of a photon in the laser mode. Feeding back these photons into the laser diode will cause the phase of the laser to vary less resulting in a reduced linewidth. The effect that this feedback has on the laser linewidth can be shown in the following expression [130],

$$\Delta f = \Delta f_0 \frac{1}{\left[1 + X\cos(\phi_{0\text{eff}} + \phi_R)\right]^2}, \tag{5.12}$$

where $X = \kappa_{\text{eff}}\tau_{\text{eff}}\sqrt{1+\eta^2}$, $\phi_R = \tan^{-1}\eta$, Δf_0 is the linewidth of the bare diode and Δf is the linewidth of the laser with optical feedback. It can be seen qualitatively that for a large dispersion, $\tau_{\text{eff}} \gg 1$, and the appropriate feedback phase, $\phi_{0\text{eff}} + \phi_R \approx 2\pi m$, we can obtain a large reduction in laser linewidth.

As well as reducing the fundamental linewidth, the optical feedback also greatly reduces the sensitivity of the laser to current noise. This sensitivity is characterized by $\partial\omega/\partial\nu$, the change in laser frequency with the change in the resonant frequency of the diode ν. Optical feedback reduces this from one to [131]

$$\frac{\partial\omega}{\partial\nu} = \frac{1}{1 + X\cos(\phi_{0\text{eff}} + \phi_R)}. \tag{5.13}$$

We can make an estimate of the laser linewidth reduction by estimating κ_{eff}. Assuming perfect mode matching we estimate $\kappa_{\text{eff}} = 7 \times 10^8 \text{s}^{-1}$. Having τ_{eff} as 5 μs and assuming that $\phi_{0\text{eff}} + \phi_R = 2\pi\text{m}$, a theoretical linewidth reduction of 12×10^6

is estimated. This method hence suggests a large reduction in the Littrow ECDL linewidth. This value of κ_{eff} is overestimated as it is difficult to independently measure the coupling rate.

Experimental Results

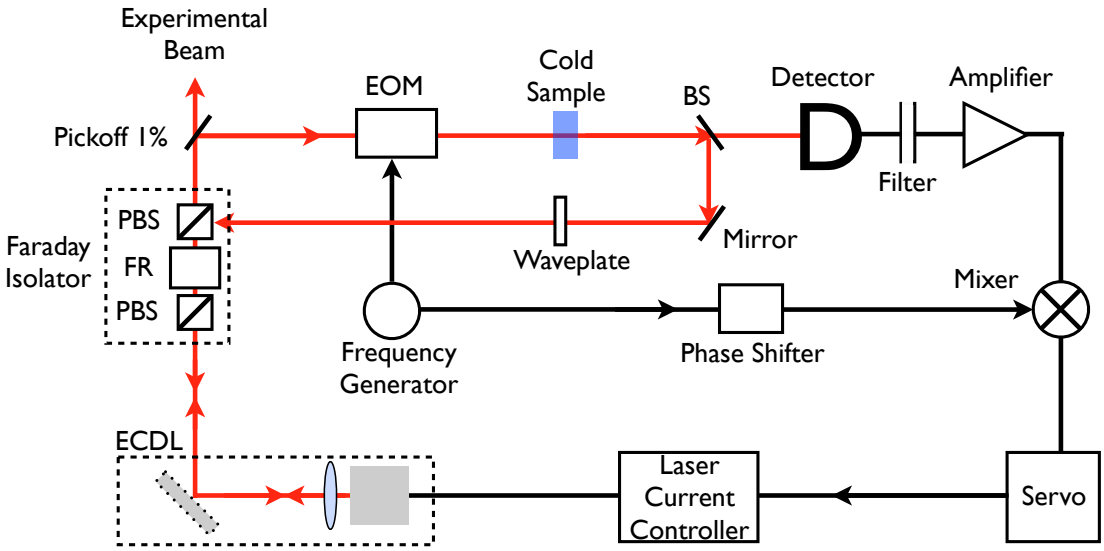

Figure 5.5: Laser locking set-up. The light is steered through the cryogenic sample, the transmitted light is detected for PDH locking (previous section) and the remaining light is re-injected into the diode. Optical components include: PBS, Polarizing Beam Splitter; FR, Faraday Rotator; EOM, Electro-Optic Modulator and BS, Beam Splitter. The External Cavity Diode Laser (ECDL) set-up is detailed in a previous section.

We now present some experimental results of the locking system. Figure 5.5 is a schematic of the experimental set-up. This figure shows the electronic locking with the addition of the optical locking. A beam splitter is placed after the cold sample and before the PDH detector. The resulting additional beam is then steered into the free port of the polarizing beam splitter associated with the Faraday isolator. A waveplate is used on this beam to ensure all of the light couples to the Faraday rotator.

Another way to couple the transmitted beam to the ECDL is to add a beam splitter between the isolator and the ECDL. The disadvantage this has is that one loses power in the experimental beam. It is noted that the initial noise measurements were obtained by locking the laser using this method.

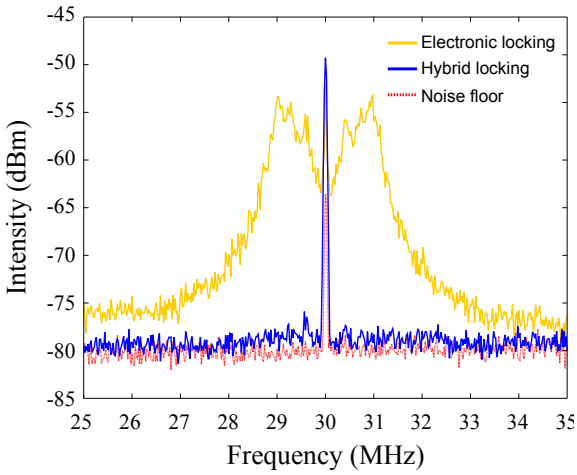

(a) Spectrum of the signal on the locking detector.

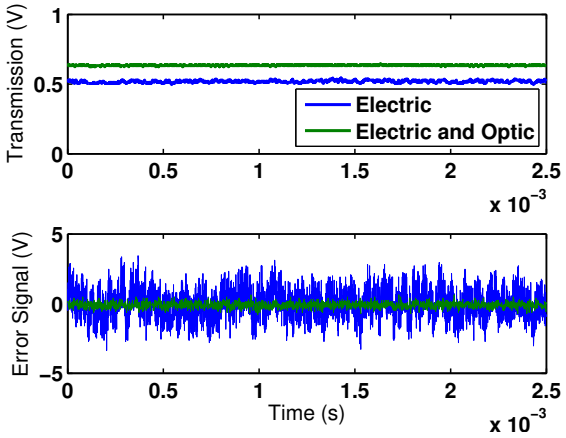

(b) Transmission and Error Signals vs time for two different locking techniques.

Figure 5.6: Error signal analysis for electronic locking only and hybrid locking techniques.

An indication of how well the locking system works is seen in the error signal. The error signal is a measure of the laser phase noise. Figure 5.6(a) shows the spectrum of the signal on the electronic locking detector. This signal is mixed down 30 MHz to create the error signal. For the case of electronic locking only, we see that the servo corrects for noise at very low frequencies (with respect to the dithering frequency of 30 MHz). We see that there are noisy peaks at 1 MHz. These noisy peaks correspond to the rolling off of the servo gain. When the optical locking is introduced, a large reduction is seen in the spectrum of the transmitted signal, indicating that indeed this technique removes phase noise at large frequencies. The

noise spectrum is close to being limited by the electronic noise of the detector.

A further indication of the effectiveness of the hybrid locking can be seen in Figure 5.6(b). Here we plot the two cases of electronic and hybrid locking, and the effect this has on the transmitted signal and the error signal as a function of time. For the hybrid case, the transmission is maximized meaning that the laser frequency is tightly locked to the centre of the hole. The error signal has lots of high frequency noise when the locking is electronic only. This noise is eliminated when the hybrid locking is activated. Figure 5.6(b) also gives an indication of the time scale at which locking is achievable.

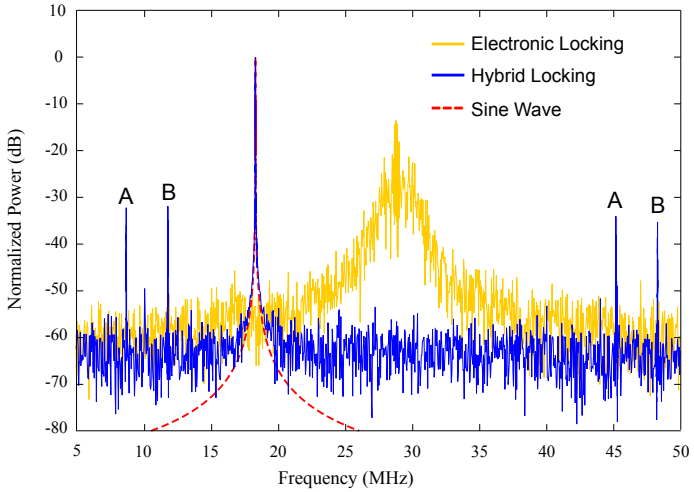

Figure 5.7: The power spectrum for beating two lasers, both with electronic feedback only (yellow) or with electronic and optical feedback applied (blue). The red dashed line is the result of applying the same windowing and FFT procedure used for the data to a sine wave. The two lasers are independent in that the locking frequency dither was 27 MHz for the second laser, and the second laser used a different spot on the same crystal to lock to. We see that the linewidth of the beat from electronic locking is largely reduced when the hybrid locking is activated. The spectrum of the beat signal for the optically locked lasers was either limited by the finite sampling time (100 μs) or the noise floor of -111 dBc/Hz. The peaks around 45 and 48 MHz are 27 and 30 MHz from the beat frequency respectively. These are due to the fact that a portion of the PDH locking sidebands is injected into the diode. The two other peaks are aliases of the other sidebands.

A beat measurement experiment is conducted between two independent lasers locked using the hybrid technique. Figure 5.7 shows the beat spectra for the cases where the lasers are locked using only electronic feedback and where the lasers are locked using the hybrid technique. The main feature of the spectra is that the hybrid case shows a narrower beat note indicating that the linewidth of the laser locked

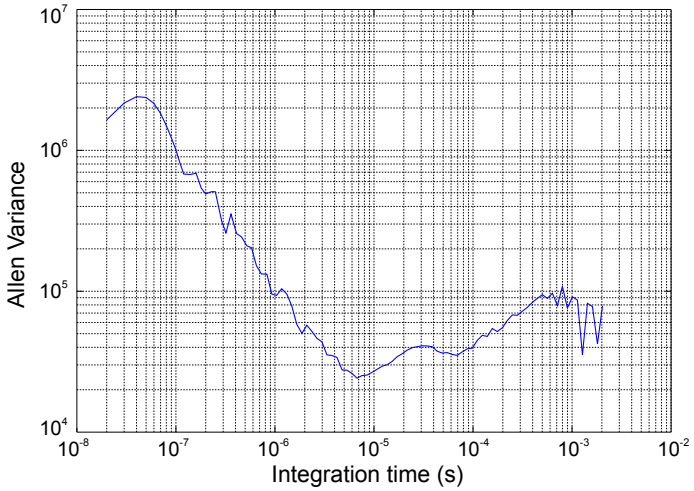

Figure 5.8: Allen Variance of the beat measurements.

using hybrid techniques is narrower.

The Allen variance of the beat signal is shown in Figure 5.8. There is a minimum frequency deviation of 23 kHz at an integration time of 7 μs. For a timescale of 100 μs which is the order required in the experiments conducted in Chapters 7 and 8, the frequency deviation is 40 kHz. The deviation increases at shorter integration times because of the noise in the beat measurements, and for longer times due to frequency drifting. The long term drifts were around 100kHz per second.

Locking the diode laser using this technique was convenient in terms of resources needed. No additional resources, such as a high finesse cavity, were required. Implementation of this locking was straight forward and allowed for quantum optics type experiments to be conducted. The laser locking did however suffer from mode hops of the external cavity of the laser which would cause frequency jumps of a few MHz.

Comment on Cryogenic Set-up

The cryogenic system used was purchased from Oxford cryogenic systems, with a Cryomech compressor unit. This style of cryogenic system was closed cycle, helium is compressed and de-compressed allowing cooling of a cold finger. The process of compression and de-compression causes vibrational and acoustic noise. The laser locking system suffers as there is no isolation between the cryostat and the frequency stabilization. Better stability is achieved when the compressor is turned off. Of course, the deactivation of the compressor results in the immediate warming of the

sample which degrades the coherence properties of the rare earth ions. Provided the sample temperature is not too high, frequency stability is retained. Timescales of 2-3 minutes were acceptable timescales for the compressor to remain off whilst retaining laser stability and photon echo efficiency reduction of less than a factor of 2.

5.4 Detection of ASE and RASE

In this section we describe the experimental set-up regarding the detection system used to make measurements of the ASE and RASE fields described in the Chapter 4.

Homodyne Detection

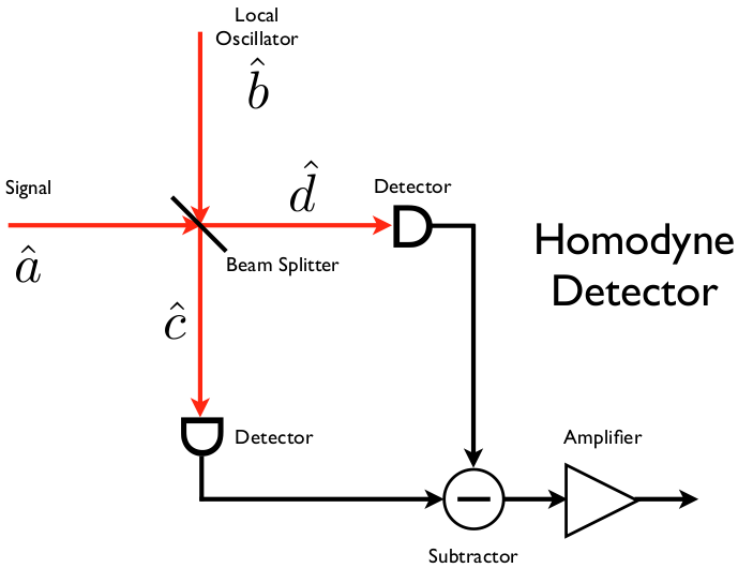

Figure 5.9: Homodyne set-up schematic. Mode $\hat{a}$ is the signal to be measured and mode $\hat{b}$ is the local oscillator.

In conducting continuous variable quantum optics experiments, balanced homodyne and heterodyne detection are ways of making measurements of the amplitude and phase quadratures of the quantum state of light [47, 49, 117, 132, 133]. We define the amplitude and phase quadratures as,

$$\hat{x} = \hat{a} + \hat{a}^\dagger \quad \text{and} \quad \hat{p} = -i(\hat{a} - \hat{a}^\dagger), \tag{5.14}$$

where $\hat{a}(\hat{a}^\dagger)$ is the annihilation (creation) operator for the quantized electromagnetic field.

Figure 5.9 shows a schematic for homodyne detection. The signal to be measured $\hat{a}$ interferes with an optically strong local oscillator $\hat{b}$ at a balanced 50:50 beam splitter. The local oscillator provides the phase reference for the quadrature measurement. We will assume that the local oscillator is strong enough to be treated classically, i.e. neglecting the quantum fluctuations of the local oscillator. Each port of the beam splitter is directed onto a photodiode detector. The photocurrents I_c and I_d are measured, subtracted and amplified. The quantity of interest is the current difference $I_{cd} = I_c - I_d$, as it contains the information about the measured signal. For simplicity we assume that the photocurrents I_c and I_d are proportional to the photon numbers $\hat{n}_c$ and $\hat{n}_d$ hitting each detector. They are given by

$$\hat{n}_c = \hat{c}^\dagger \hat{c} \;\text{ and }\; \hat{n}_d = \hat{d}^\dagger \hat{d}, \tag{5.15}$$

where the mode operators $\hat{c}$ and $\hat{d}$ are the fields emerging from the beam splitter and are given by,

$$\hat{c} = \frac{1}{\sqrt{2}}(\hat{a} + \hat{b}) \;\text{ and }\; \hat{d} = \frac{1}{\sqrt{2}}(\hat{a} - \hat{b}). \tag{5.16}$$

Here, $\hat{a}$ denotes the annihilation operator of the signal mode and b is the annihilation operator of the local oscillator. Assuming the quantum efficiency of the photodetectors is unity, the difference current I_{cd} is proportional to the difference of the photon number $\hat{n}_{cd}$,

$$\begin{aligned}
\hat{n}_{cd} &= \hat{n}_c - \hat{n}_d \\
&= \frac{1}{2}(\hat{a}^\dagger\hat{a} + \hat{b}^\dagger\hat{b} + \hat{b}\hat{a}^\dagger + \hat{b}^\dagger\hat{a}) - \frac{1}{2}(\hat{a}^\dagger\hat{a} + \hat{b}^\dagger\hat{b} - \hat{b}\hat{a}^\dagger - \hat{b}^\dagger\hat{a}) \\
&= \hat{a}^\dagger\hat{b} + \hat{b}^\dagger\hat{a}.
\end{aligned} \tag{5.17}$$

The local oscillator is an intense coherent state and can be treated classically. The annihilation operator $\hat{b}$ can then be replaced by the complex amplitude b in Equation 5.17 such that $b = |b|e^{i\theta}$, where θ is the local oscillator phase. It is easy to see that the difference photocurrent is indeed proportional to the quadrature component because,

$$\hat{n}_{cd} = |b|(\hat{a}^\dagger e^{i\theta} + \hat{a}e^{-i\theta}) = |b|\hat{x}_\theta. \tag{5.18}$$

We can see that one only needs to adjust the phase of the local oscillator to make a measurement of either quadrature. To measure the $\hat{x}$ quadrature, choose a phase

of $\theta = 0$ and for the $\hat{p}$ quadrature, choose a phase of $\theta = \frac{\pi}{2}$.

The homodyne detector is like an "amplifier" of the signal mode, evident in Equation 5.18. The local oscillator is a strong field, and so the amplified signal can be well above the electronic noise floor of the photodiodes. This greatly increases the sensitivity allowing even photodiodes without internal amplification to detect quantum signals. Also, one can take advantage of the high quantum efficiency that photodiodes offer.

Another characteristic of homodyne detection is that the local oscillator chooses the signal mode of detection. That is, the local oscillator selects only the spatial and frequency mode of the signal quantum field that matches exactly the local oscillator field. This allows for supreme filtering of the quantum signal that one wishes to detect.

Heterodyne Detection

In homodyne detection, the frequency of the signal mode and the local oscillator mode are the same, resulting in a 'perfect' measurement of a quadrature component. Another method of quantum light measurement is heterodyne detection. Here, the frequency of the signal mode differs from that of the local oscillator, producing a beat at a frequency ω_0. The effect this has on the detection system is that a measurement of both the $\hat{x}$ and $\hat{p}$ quadrature is being made simultaneously.

To understand this, consider the case of splitting the signal beam into two beams and performing a homodyne measurement of $\hat{x}$ on one beam and $\hat{p}$ on the other beam. The uncertainty principle is not violated here. The unused port of the beamsplitter that splits the signal beam allows vacuum noise to couple into the system. Thus, heterodyne detection allows a 'noisy' simultaneous measurement of both field quadratures.

Another way to understand this is that a heterodyne detector simultaneously measures a linear combination of $\hat{x}$ and $\hat{p}$ of the signal mode at ω_0 and $\hat{x}$ and $\hat{p}$ of the vacuum mode at $-\omega_0$. One could avoid this vacuum mode by somehow having the signal mode at both ω_0 and $-\omega_0$. This is easiest done at $\omega_0 = 0$, that is, homodyne detection.

It is noted that heterodyne detection has the same detection properties as homodyne detection regarding "amplification" of the signal and mode selection using the local oscillator.

ASE and RASE Detection

For the ASE and RASE experiment we use heterodyne detection. Using heterodyne detection may seem to be a poor choice when wanting to measure the quantum state of light, since we are making a 'noisy' measure of the field quadratures. The advantage heterodyne has experimentally is twofold. Firstly, the $\hat{x}$ and $\hat{p}$ quadratures are measured simultaneously, meaning that one only requires to take half as many measurements compared to homodyne detection. Secondly, the experimentalist has the freedom to choose the beat frequency at which the detectors recover best at. Particularly in these experiments, strong temporally short pulses will be fed into the detection system, making the recovery time of the detectors crucial to detecting the signal mode you want, which is immediately after the strong pulse. Designing detectors to recover fast ($\sim \mu$s) at DC is challenging, a feat easily achievable for a signal frequency of, for example, 10 MHz.

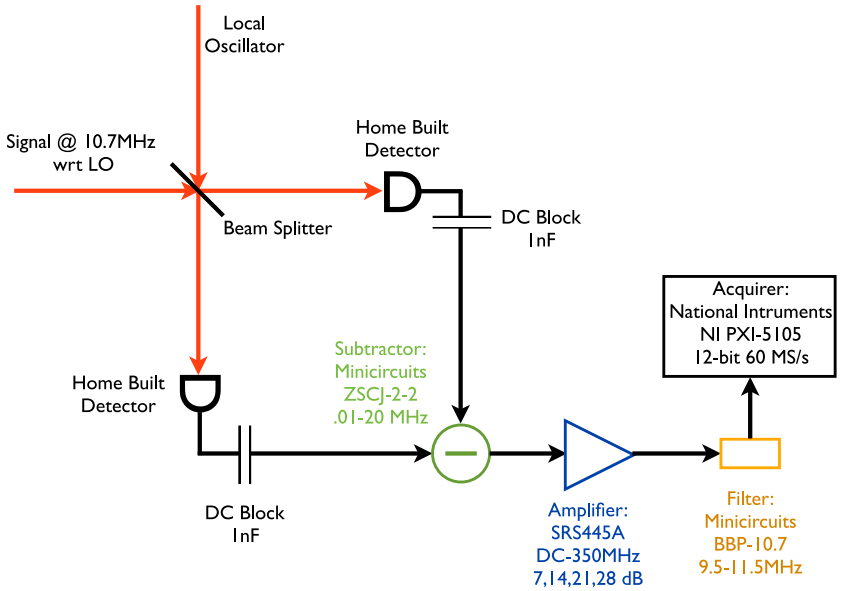

Figure 5.10: Experimental set-up of ASE and RASE detector.

Figure 5.10 shows a schematic of the ASE and RASE detector. The wavelength of light as indicated in a previous section of this chapter is 793nm. The signal field is at 10.7 MHz with respect to the local oscillator. The polarization of the beams are adjusted prior to hitting the beamsplitter, allowing the beam splitter to be 50:50. Two identical as possible home built detectors are used to detect each port of the beam splitter. The detectors are based on the low noise DC coupled general purpose detector presented in [134]. Appendix A has more details. To filter out

the DC component from the signal in order to prevent saturating the downstream electronic components, the signal from each detector is passed through a DC block, a 1 nF capacitor. The two signals are then subtracted on a Minicircuits subtractor, with a bandwidth of 0.1 MHz up to 20 MHz. The signal is then amplified by a Stanford Research Systems DC-350 MHz amplifier which has 4 channels, each providing about 7 dB of amplification. This signal is then band pass filtered about 10.7 MHz with a bandwidth of 2 MHz. Finally, the signal is acquired using a 12-bit 60 MS/s digitizer from National Instruments.

To characterize the detection system, a measure of the electronic dark noise of the detector compared to the shot noise of the local oscillator incident on the detector is implemented. The variance of the signal should have a linear relationship with the power in the local oscillator (Equation 5.18). Figure 5.11 shows the variance response to the local oscillator power. The variance is calculated by acquiring for 3 ms at 60 MS/s. As can be seen, the response is linear for powers not exceeding 5 mW. Powers exceeding this show a plateauing of the variance, meaning that for these powers the detection is not as sensitive as it should be. For a power of 4 mW, the shot noise is 8 dB above the dark noise.

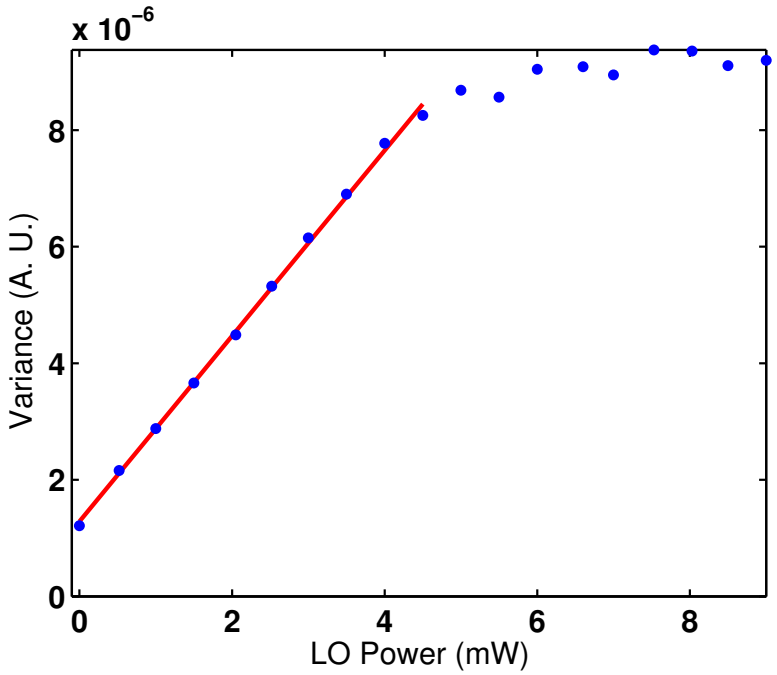

Figure 5.11: Variance response to local oscillator power. A fit is present for the first 10 measures to guide the eye.

It is also useful to know the maximum subtraction the subtractor is providing.

Comparing the noise measured by blocking one detector to the case of both detectors unblocked gives a difference of 5 dB. To probe the maximum subtraction we inject some large classical signal at 10.7 MHz into the local oscillator port of the beam splitter. It was measured that the subtracter provides 30 dB of subtraction on a large 10.7 MHz signal at a power of 4 mW. It is seen that this detection system is limited by the shot noise on the local oscillator.

Chapter 6

Experimental Techniques

The phenomena that this thesis is interested in is the noise caused from amplified spontaneous emission on a inhomogeneously broadened two level ensemble of rare earth ions and the rephasing of this noise. To better characterize these phenomena and to 'know if the experiment is functioning correctly', a few key experimental techniques are implemented. These techniques include the two pulse photon echo and optical nutation.

For the two pulse photon echo, the technique to implement is measuring the amplitude and phase of the echo relative to the input pulse as a function of delay time of the memory. This measurement allows knowledge of the laser frequency stability as a function of time, the echo efficiency and the echo (coherence) lifetime. A benchmark value can be assigned to each of these properties. One can tell if the experiment as a whole is not functioning correctly by making regular measurements of these properties and comparing with the benchmark value. Of the most importance is the phase stability and often the constraints on the efficiency and echo lifetime are relaxed provided the phase stability of the echo is acceptable.

The optical nutation technique allows the Rabi frequency to be measured, as well as the optical depth. The Rabi frequency is the rate of inversion of a two level system requiring the Rabi frequency to be faster than the memory bandwidth. It is important to have a 'unique' Rabi frequency, it is possible to adjust the polarization of the laser to interact with different orientated dipoles equally [46]. Monitoring the Rabi frequency is done by making regular optical nutation measurements. It is easily seen if the experiment is not functioning correctly by simply noting the Rabi frequency and optical depth.

To further characterize the ASE and RASE phenomena, the detection mode of

the local oscillator is measured. There is freedom to change the mode of the local oscillator to optimize the photon echo efficiency or to detect only the centre of the rephasing beam.

In this chapter, we first detail the experimental set up. Then, we discuss the local oscillator mode and present the measurements of the mode. Finally, the 'benchmark' results of implementing the experimental techniques of the two pulse photon echo and optical nutation experiments are presented.

6.1 Experimental Set-up

Figure 6.1 shows a schematic of the set up. A Mach-Zehnder interferometer is used to make phase sensitive shot noise limited measurements of the quantum state of light, namely the $\hat{x}$ and $\hat{p}$ quadratures. A polarizing beamsplitter separates a single beam into a probe and local oscillator beam. A half wave plate placed prior to the entry of the interferometer allows freedom to adjust the power distribution between the two beams.

The probe beam is then allowed to pass through two Intra-Action acousto-optic modulators (AOM), whose modulation frequency is centered on 80MHz with approximately a 20MHz bandwidth. The first AOM is driven at 80MHz and the first order beam on the negative side is then steered into the second AOM, which is driven at 90.7MHz, and the first order on the positive side is used for the experiment. The beam used thus has a frequency difference of 10.7MHz with respect to the local oscillator.

The RF used to drive the AOMs is provided by a Pulseblaster (PulseBlaster DDS-II-300 USB). This particular model has two high RF outputs with programmable frequency, amplitude and phase. The outputs of the Pulseblaster are subject to filtering, switching, attenuation and amplification as outlined in Figure 6.2 before driving the AOM.

The beam is then passed through a polarization rotator such that the optical nutation signal reads with a unique Rabi frequency [46]. The beam is then focused onto a Tm^{3+}:YAG sample. Typical power in the focused beam is 10mW. The sample is clamped down on a steel plate which is bolted to the cold finger of the cryogenic cooler. To ensure sufficient thermal contact 'Apiezon N' vacuum grease is applied between the sample and the steel plate, the steel plate and the cold finger. Typical temperature readings are 2.7K and are measured from the top of the cold finger. However, there is the possibility of a temperature increase from the top of the cold

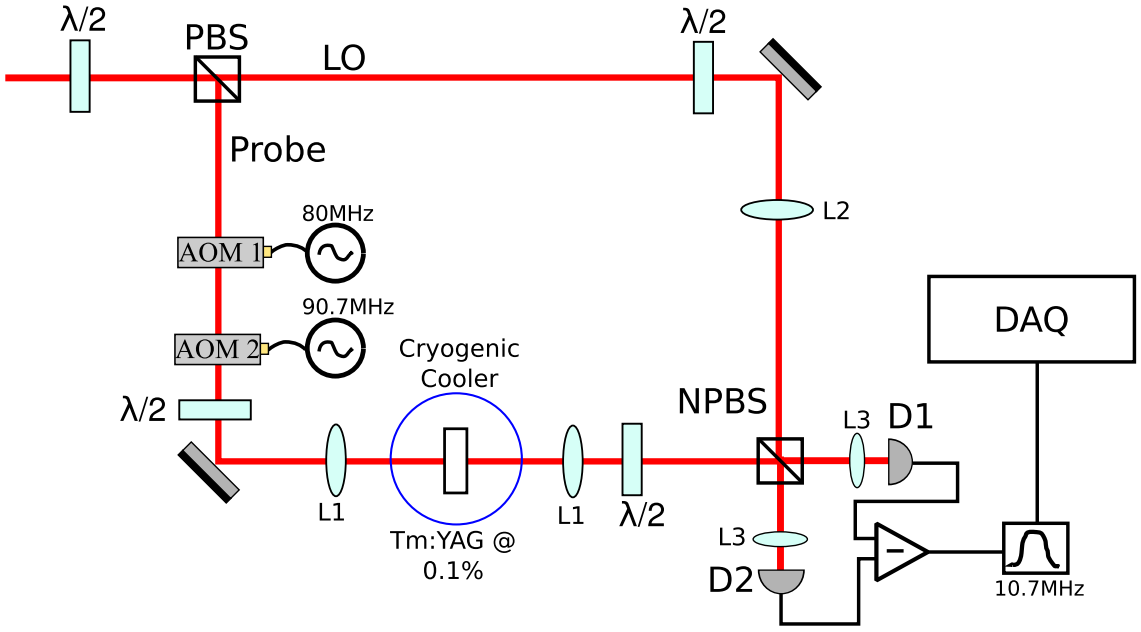

Figure 6.1: Interferometric setup. Laser beam passes through a polarizing beamsplitter (PBS). The probe arm is steered through two Acousto-Optic Modulators (AOM) for pulse generation, then steered toward the cryogenic Tm^{3+}:YAG. The signal is then combined with the local oscillator (LO) on a non-polarizing beamsplitter (NPBS) and sent to a balanced heterodyne detection system. Various half waveplates ($\lambda/2$) are used for polarization control. $L_1 = 100$mm, $L_2 = 500$mm, $L_3 = 50$mm. There are differing modes used for the LO as outlined later in this chapter. Shown here is the focusing LO where the L_2 lens is placed 285mm from the NPBS.

finger to the bottom where the crystal is mounted.

The sample dimensions vary dependent on the experiment. There are three different sample sizes used. For optically thick experiments ($\alpha l \approx 3$) the crystal is 20mm along the direction of propagation direction, 4mm in height and 5mm wide. For optical depths near $\alpha l \approx 0.5$, a 4mm thick crystal is used. The width of this crystal is 8mm with a height of 4mm. For optical depths near $\alpha l \approx 0.05$, a 0.5mm thick crystal is used with a height of 4mm and a 5mm width. It is noted that all crystals are cut such that light propagates along the $[1\bar{1}0]$ axis. It is also noted that the laser is locked to the 8mm wide crystal (Chapter 5) at one point and noise experiments are conducted at a spatially different point of the crystal.

For all experiments conducted, the waist at the sample is measured to be $53.3\mu m$ giving a Rayleigh range of 11.3mm. It is noted that this Rayleigh range is comparable to the 20mm long crystal.

After light has passed through the sample, it is then mode matched with an identical lens placed at an equal distance from the sample. Then the beam is combined

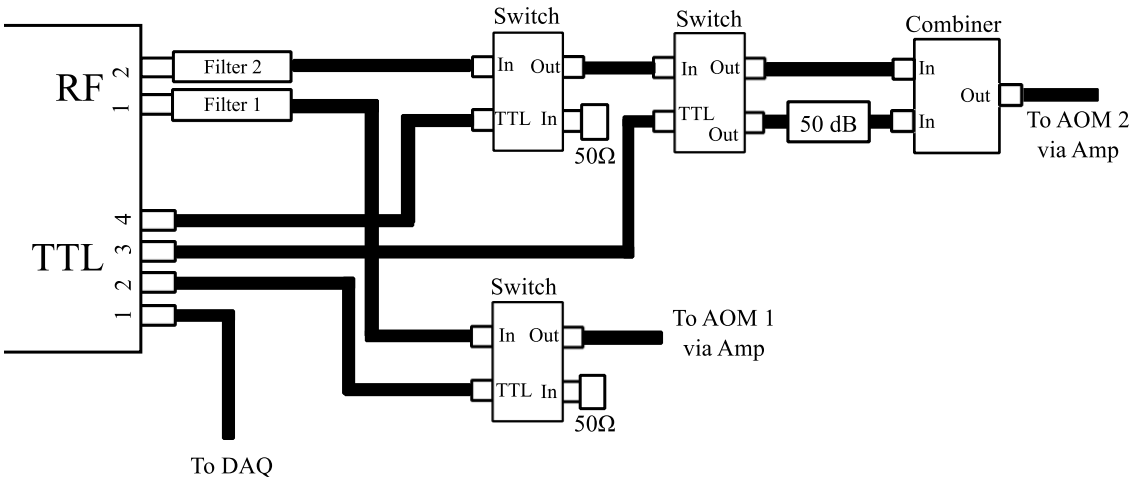

Figure 6.2: RF production. The Pulseblaster has two RF outputs that are filtered using Minicircuits low pass filters (Filter 1 = BLP-90 Low Pass, DC-81MHz. Filter 2 = BLP-150 Low Pass, DC-140MHz). RF 1 is set to 80MHz and RF 2 is set to 90.7MHz. After going through the filter, each RF signal is sent through a switch. Each switch (Minicircuits ZASWA-2-50DR+) takes two RF inputs, one of which is terminated with a 50Ω resistor, and also a TTL that switches between the two inputs. The switch allows for pulsed RF. After the switch, RF 1 is sent to AOM 1 whereas RF 2 is sent through another switch. This signal is then switched between a 0 dB attenuation path and a 50 dB attenuation path. The 0 dB path is used for strong pulses and the 50 dB path is used for small pulses. RF 2 is then sent to AOM 2. Both RF signals are amplified (Minicircuits ZHL-1-2W, 29 dB gain) before being sent to the AOM.

with the local oscillator using a non-polarizing beam splitter. A half wave plate is used before the beam splitter for both the probe and the local oscillator to balance the power into each output port of the non-polarizing beamsplitter.

Both exit ports of the interferometer are focused using 50mm lenses onto two homemade detectors (see Appendix A). The response of the detectors is made as similar as possible at 10.7MHz. The signals from each detector are subtracted with a Minicircuits mixer that provides 30 dB of subtraction at 10.7MHz. The RF signal is amplified by 21 dB (Stanford SR445A), then bandpass filtered (Minicircuits) at a centre frequency of 10.7MHz and bandwidth of about 2MHz. The resulting filtered RF signal is acquired at 60MS/s with a National instruments card (NI-PXI). Details of the response of the detection system as a function of power are provided in Chapter 5.

6.2 The Local Oscillator Mode

A degree of freedom that interferometry has is the freedom to choose the local oscillator mode and hence detection mode. In these experiments we use three differing spatial modes for the local oscillator, all of which will be described in this section.

A figure of merit that characterizes the alignment of an interferometer is the *visibility* or *contrast*. If there is a frequency difference between the two arms of an interferometer, when combined on a beam splitter a *beat* can be measured with a photodetector whose bandwidth includes the beat frequency. If the two arms of the interferometer are equal in spatial mode shape and power, the measured signal will beat down to zero. In this case, the visibility is said to be 100%. The introduction of mode changing elements in one or unequal power between the beams results in a reduction of this visibility. Traditionally, an interferometer wants to be constructed with 100% visibility in order to obtain maximum information about the probe.

In these experiments, visibilities exceeding 95% were achieved. The main source of visibility reduction can be found in the probe beam where the AOMs have some mode shaping associated with them.

To motivate why one would deviate from the 100% visibility, consider the following. For optical rephasing experiments a common issue is the fact that there is spatial inhomogeneity of the laser beam used to drive the atomic system, namely a Gaussian profile. The 'perfect' π pulse is one with a top-hat spatial profile, such that the spatial set of ions being inverted see an identical intensity and are perfectly inverted to the excited state, emptying the ground state. Ions located within half a standard deviation either side of the mean of a Gaussian (illustrated in Figure 6.3) see a near top-hat beam. The rest of the Gaussian beam (the wings) create some population difference in the ground and excited states resulting in free induction decay phenomenon. The ions spatially located at the wings of the Gaussian beam will not be rephased resulting in a reduction in efficiency if detecting in the 100% mode-matched regime.

One way to avoid efficiency reduction is to place a pinhole between the sample and the detector. Note that this technique is used without a local oscillator. Here, the pinhole acts as a spatial mode selector, allowing only the center of the beam to be detected, resulting in greater echo efficiency.

The interferometer version of the pinhole technique is achieved with a focusing local oscillator. First, the local oscillator was blocked and a pinhole was placed at an arbitrary distance between the detector and the sample. An increase in photon echo

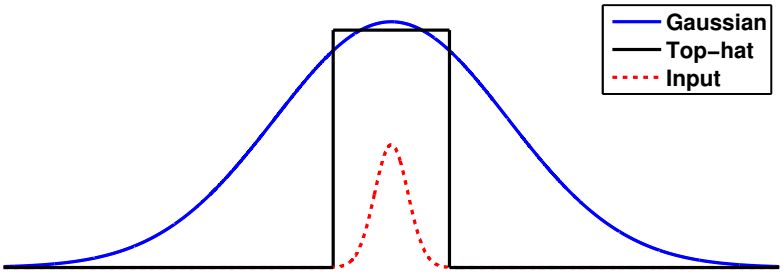

Figure 6.3: A top-hat (black) approximation to the Gaussian profile (blue) of a laser beam. The top-hat sides are at half the standard deviation either side of the mean, with the height given by the mean intensity over this spatial location. The dotted red line represents a better spatial size for the input pulse.

efficiency was noticed, and the position of the pinhole was adjusted to maximize the efficiency. Then, a 500mm focal point lens was placed in the local oscillator arm at a position such that the beam focused at the position of where the pinhole was placed. The pinhole was then removed and the photon echo efficiency was measured. The results of these echo measurements are presented in the next section.

Figure 6.4 shows the beam width measurements of the probe beam and focusing local oscillator. The beam width measurements were obtained with a beam profiler, shown in the top row of plots in Figure 6.4. Knowing the local oscillator mode then allows for the detection mode to be visualized. The procedure is to propagate back the local oscillator mode from the pinhole to the crystal, shown in the bottom row of figures in Figure 6.4.

At the front of the crystal, only ions at the spatial centre of the probe are being detected. However at the back of the crystal, ions that are driven by the entire probe beam are detected as well as ions that do not interact with any light. It is noted that for this physically thicker crystal, the focus of the probe is 2mm from the back of the crystal. When the physically thicker crystal is swapped out for the physically thinner crystal, the focus is still 2mm from the back of the crystal, in which case the focus is located at the centre of the crystal.

Another way to avoid echo efficiency reduction is to use spatially different pulses for input pulse and the π pulse. Figure 6.3 illustrates an ideal input pulse size matched to the centre of the rephasing pulse. In this case all of the initial coherence created by the input would be rephased resulting in a greater photon echo efficiency. The disadvantage that this technique has is that increasing the beam size without increasing the intensity will result in a reduction of the Rabi frequency. This technique was used in [72] where the beam used to create the AFC was twice the width

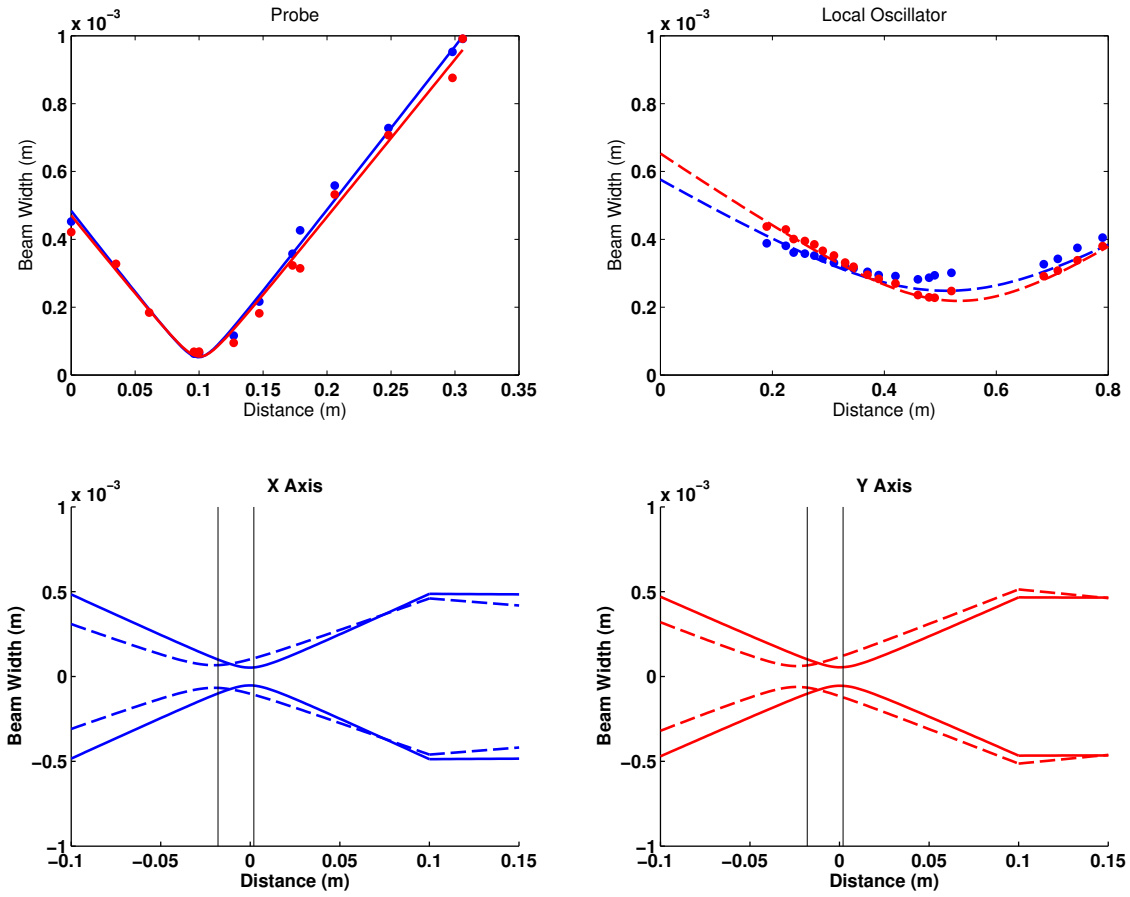

Figure 6.4: Probe and local oscillator characterization. The top left plot is beam width measurements of the probe, where the zero is the location of the 100mm lens that focuses on the sample. The top right is the local oscillator beam measurements, where the zero is the location of the 500mm lens in Figure 6.1. Blue (red) data points and lines are for the x (y) axis. The bottom plots show which mode is being detected (dashed line) and the probe beam (solid line). Black vertical lines represent the crystal.

of the signal beam.

Rather than shaping the rephasing beam, the local oscillator can be used to select only the ions who experienced a π pulse. Here, the local oscillator needs to have a collimated width that is *larger* than the probe. Propagating a larger width beam back to the sample via the imaging lens will result in the detection of a tighter spot on the crystal compared to the probe spot, thus only detecting the ions that see a π pulse. This can be seen directly from the relation between the waist size before and after a thin lens: $w_2 = \frac{f\lambda}{\pi w_1}$, where w_1 is the waist on the sample, w_2 is the waist after the lens, f is the focal length of the lens and λ is the wavelength of light. Of course, the divergence of the beam is increased so this method is only

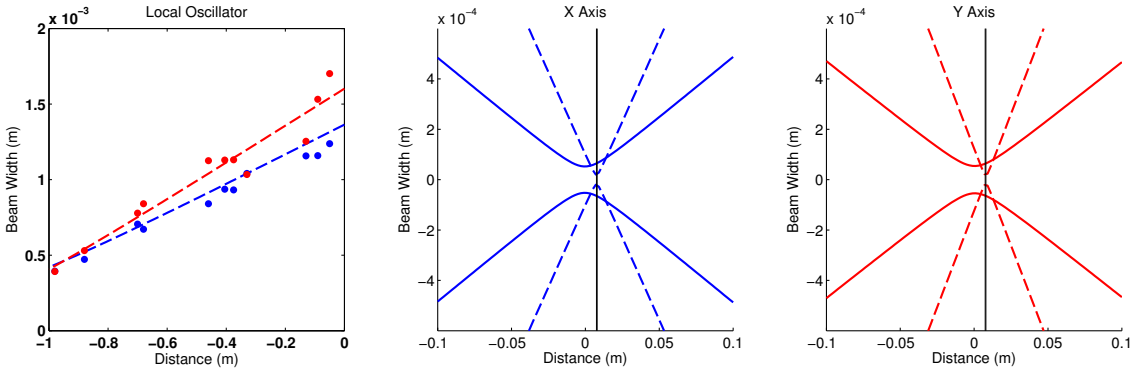

Figure 6.5: Probe and local oscillator characterization. The left panel shows the beam width measurements for the local oscillator where the distance axis is measured from the non-polarizing beamsplitter. The centre and right panels are the x and y axis beam profiles on the sample. The detection mode is the dashed line whereas the probing mode is the solid line. The 0.5mm sample is placed at the focus of the detection mode. Propagating the wide local oscillator beam back to the crystal results in a tighter focus than the probing mode. It is noted that this method is only valid for physically thin samples since the divergence has increased.

suitable for physically thin samples compared to the Rayleigh length.

To generate a local oscillator that is wider than the probe, two 100mm focal length lenses are placed a distance of 145mm and 325mm from the polarizing beam splitter in the local oscillator path (refer to Figure 6.1). This gives a local oscillator that is expanding, shown in the left plot in Figure 6.5. The data is fitted using a least squares curve fitting function. Propagating the local oscillator back from the non-polarizing beam splitter to the sample gives the centre and right plots in Figure 6.5. The crystal used for this configuration is now 0.5mm thick and is placed at the focus of the detection mode. As can be seen, the detection mode detects only the ions near the centre of the driving mode.

6.3 Two Pulse Photon Echoes

Having outlined the local oscillator modes that will be used, we now present photon echo measurements using the different local oscillator modes. Figure 6.6(a) shows a typical photon echo pulse sequence and Figure 6.6(b) shows a typical measurement. The input pulse is chosen to be temporally longer than the π pulse. This is to ensure that the input pulse bandwidth is smaller than the π pulse bandwidth, allowing for maximum efficiency for all frequency components of the input.

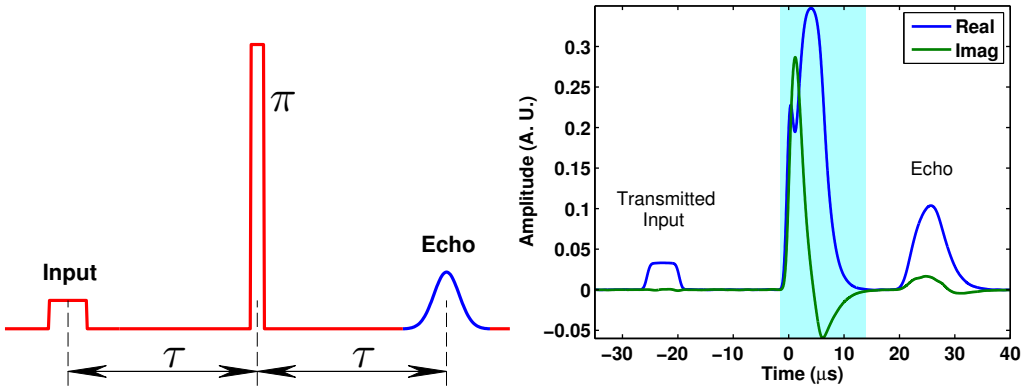

(a) 2PE Sequence (b) Measurement

Figure 6.6: (a) Two pulse photon echo sequence. The red line is the applied laser field, the blue curve is the detected echo. The labelled input pulse has a small area compared to the π pulse. (b) An example of a measured photon echo sequence. The in phase (blue) and in quadrature (green) signals are shown. The shaded area is when the π pulse is applied, in which the detection system takes some μs to recover.

Efficiency and Lifetime

We first present the echo efficiency measurements using the physically and optically *thick* Tm^{3+}:YAG crystal. As mentioned earlier, the crystal length is 20mm along the direction of propagation. Figure 6.7 shows efficiency measurements on this thick crystal for the mode matched local oscillator (left) and the focused local oscillator (right). The optical depth was measured to be $\alpha l = 3.1$ for the mode matched case and also for the focused case. The input pulse is 6 μs while the π pulse length was 2.2 μs for the mode matched case and 1.6 μs for the focused case. The delay between the input and the π pulse is varied. The input pulses are of small area compared to the π pulse, i.e. input area $\ll \pi$.

To calculate the efficiency, the optical depth is measured before the echo sequence is implemented. Measuring the transmitted part of the input and knowing the optical depth allows the inferred intensity of the input pulse to be calculated and hence the efficiency.

The first feature to note of these decaying efficiencies is that the decay is non-exponential (see Section 7.1.3.2 of [16]) and the behavior can be fit by $e^{-(4\tau/T_M)^x}$. Here T_M is the memory rephasing time and x is an exponent dependent on the details of the nuclear spin dynamics. Following work done by Sun [16], we take $x = 2$ and fit a curve to the measurements to give a zero-delay efficiency. For the mode-matched case, the zero delay efficiency was measured to be 69%. Converting

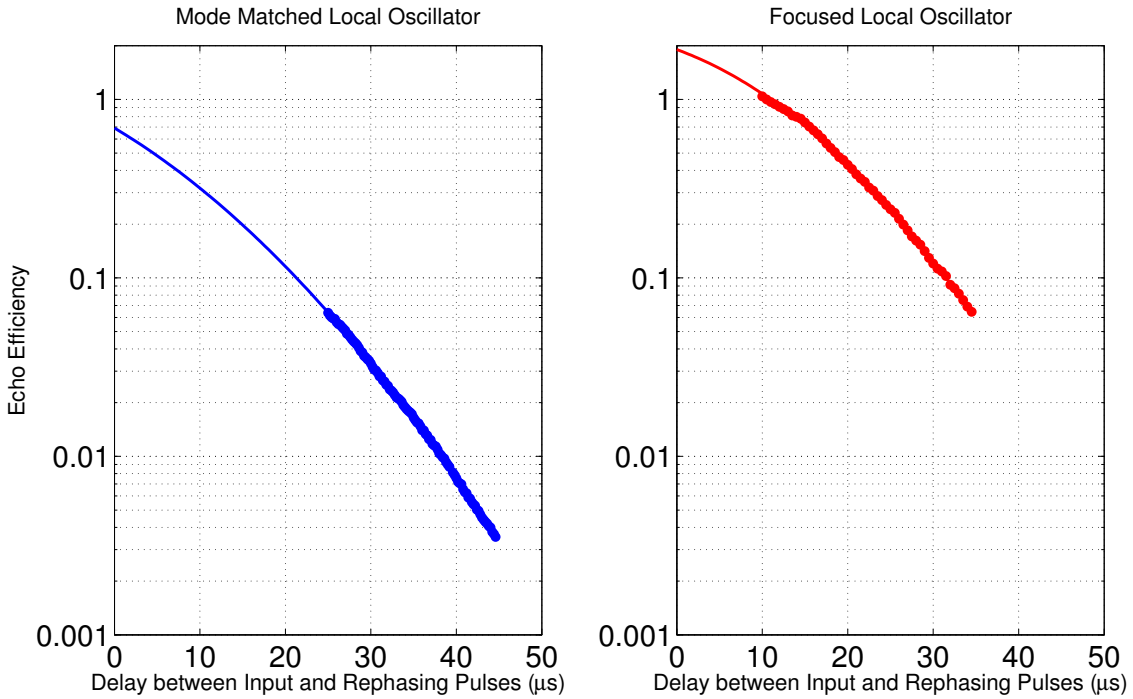

Figure 6.7: Comparison of echo efficiency for differing mode detection options. The left panel is detection in the near 100% mode matched case. The right panel is for a focused local oscillator detection mode. The dots are the measured data points and the solid line is a theoretical fit given by [16].

the local oscillator to the focusing case gave a measured efficiency of 190%, which is in close agreement with the work of Carrie Cornish done on the same system [55]. These efficiencies measured for the thick crystal can be considered the benchmark efficiencies.

It is clear that the focusing local oscillator gives a greater photon echo efficiency. This increase in efficiency was consistent with the increase witnessed when using a pinhole in front of the detector and blocking the local oscillator. Indeed the set-up has been optimized for greater photon echo efficiency.

We now focus our attention to the optimized efficiency case and extract a coherence time measurement from the data. It is noted that the measurements presented previously were taken with the cryogenic cooler off for greater laser frequency stability. Here we present measurements for both the cooler off and on.

Figure 6.8 shows the echo efficiency as a function of delay for both the cooler off (top) and on (bottom). The experiment is run 8 times for the cooler off case and 4 times for the cooler on case and the maximum echo at each time point is taken. Fitting a straight line to this log plot of the efficiencies at short delay times (10 μs

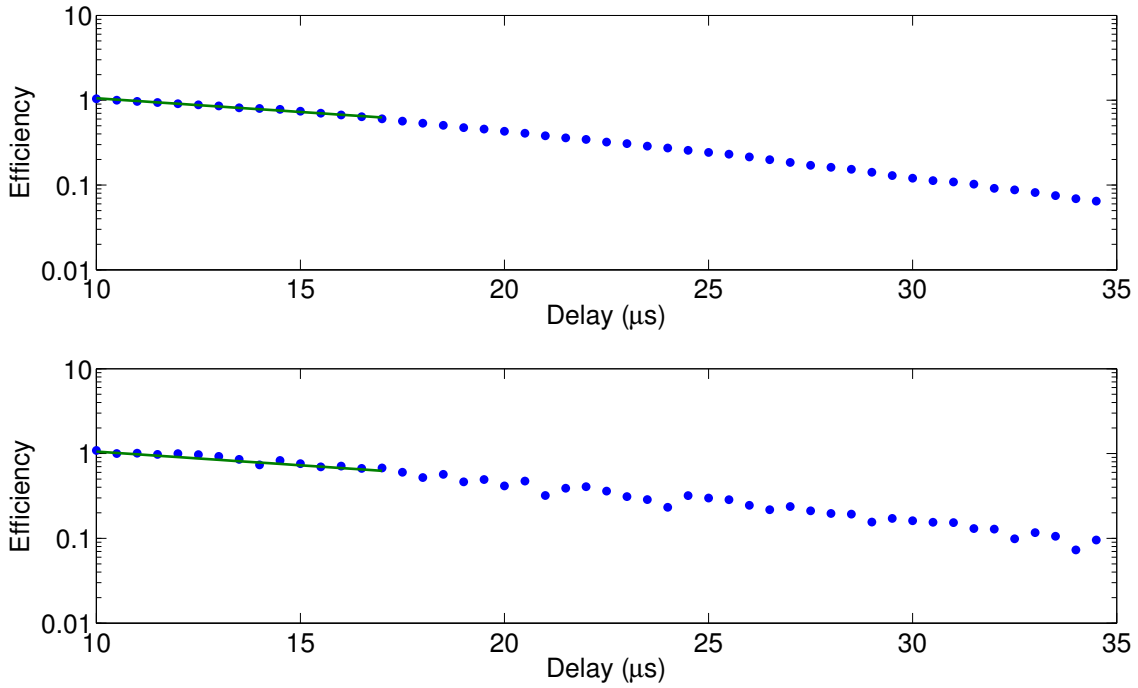

Figure 6.8: Coherence time. The upper plot is the efficiency for the case of the cooler off, the lower plot being the case for the cooler on.

to 17 μs) gives a measure of the coherence time. For both cases here, the coherence time is $T_2 = 13.4$ μs. This measurement is a typical coherence lifetime time scale and is considered the benchmark.

We now look at the photon echo efficiency for the physically and optically *thin* crystals of thickness 4mm and 0.5mm. Figure 6.9 shows the efficiency as a function of delay for an optical depth of $\alpha l = 0.24$. The experiment was carried out on the 4mm thick crystal placed at the focus of the probe in Figure 6.4. The zero delay efficiency is calculated as 1.69%, whereas the coherence time is measured as $T_2 = 23.15$ μs. The expected zero delay efficiency is 5.93%, a factor of 3.5 greater than the measured efficiency. This discrepancy is due to the detection mode including ions who do not see a π pulse.

Figure 6.10 shows the same experiment as Figure 6.9, but for an optical depth of $\alpha l = 0.046$ using the 0.5mm thick crystal and a local oscillator mode as described by Figure 6.5. Here, the zero delay efficiency is 0.142% with an expected efficiency of 0.215%. It is seen that the discrepancy between the measured and expected efficiencies is reduced, due to the change in local oscillator mode. The coherence time is 10.60 μs.

It is noted the coherence time is measured to be different for different crystal

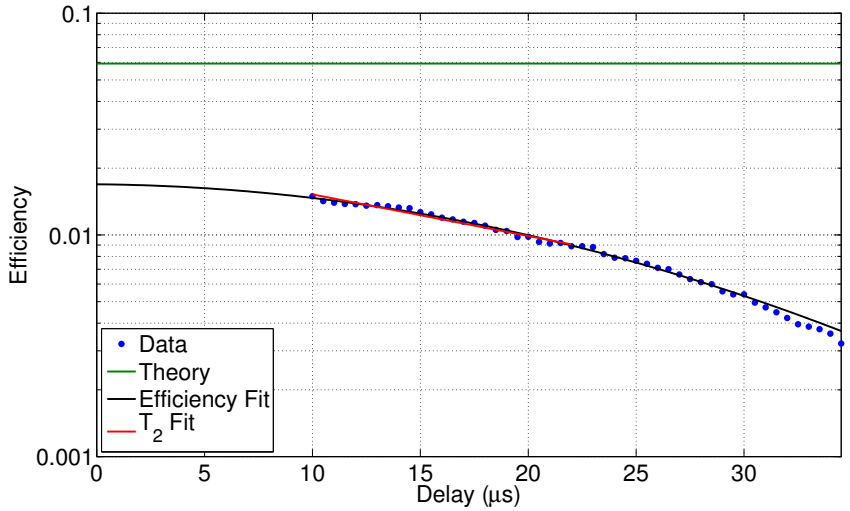

Figure 6.9: Echo efficiency as a function of delay for $\alpha l = 0.24$. The blue dots are the measured echo efficiencies, the black curve is the non-exponential fit to the data to give the zero-delay efficiency. The red curve is an exponential fit to short delay times to give the coherence time. The green curve is the expected efficiency for this optical depth.

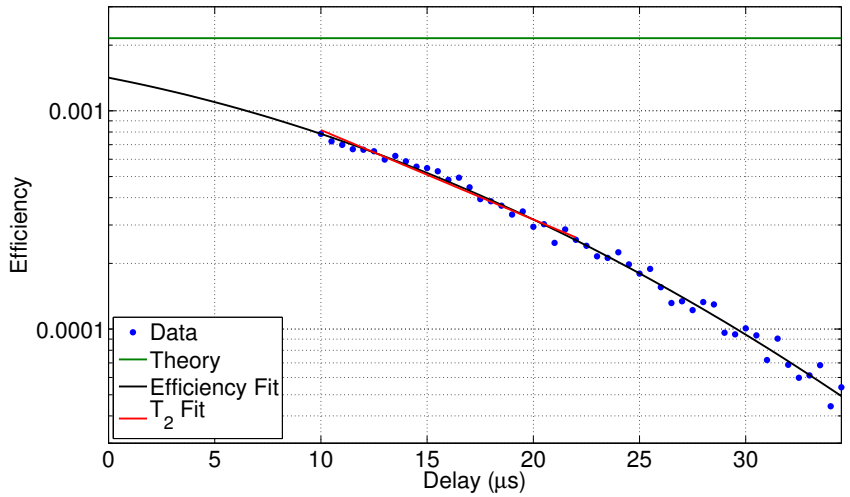

Figure 6.10: Echo efficiency as a function of delay for $\alpha l = 0.046$. The colour scheme is identical to Figure 6.9.

lengths. Since the doping concentration is the same for all crystals, it is expected that the coherence time should be the same. The difference between the experiments is most likely the crystal temperature. The crystal temperature was not able to be measured, the temperature sensor in the cryostat is located at the top of the cold finger, whereas the crystals are mounted to the bottom.

Due to space limitations, the 20mm crystal is placed closer to the cryostat win-

dow than the 4mm crystal, thus receiving additional heat load from the window. Moreover, the 4mm crystal had a base of 8mm by 4mm making it easy to mount to the cryostat with good thermal contact. The 0.5mm crystal was inherently difficult to mount such that there was good thermal contact between the it and the cold finger of the cryostat. The issues with the 20mm and 0.5mm crystals are reflected in the measured coherence times, being a factor of 2 less than that of the 4mm crystal.

Phase Stability

The phase stability of a photon echo sequence is best characterized by comparing the phase of the echo with the phase of the input pulse as the delay is increased. The experiments conducted in the previous section were done so with phase information known. Here we present the phase information for the optically thick photon echoes for both the cryostat on and off cases. For the cryostat off, the echo phase as a function of delay time is executed 8 times and the result is shown in Figure 6.11(a). The phase of the echo follows closely that of the input. The error bar represents a standard deviation either side of the mean phase. The mean phase of the echo for all delay times is 0.1135 $\pm$0.033.

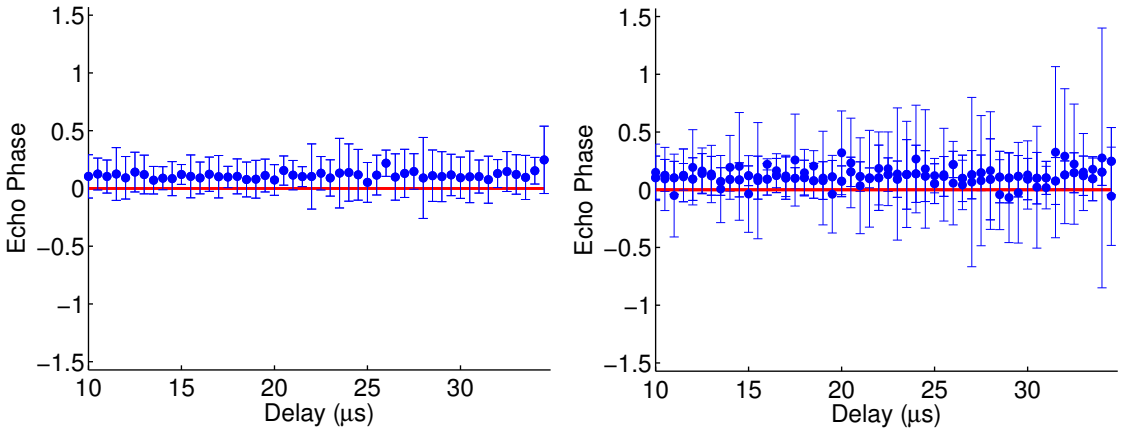

(a) Cryostat off

(b) Cryostat on

Figure 6.11: Phase of the echo compared to the phase of the input as a function of delay. Two cases are presented: (a) cryostat off and (b) cryostat on. For (a) the sequence is run 8 times, and each blue dot represents the mean phase measured at that time and the error bar is the standard deviation either side of that mean. For (b) the experiment is run 4 times.

For the case where the cryostat is left on (Figure 6.11(b)) the echo phase still

follows the input, but there is a noticeable increase in phase noise. In this case the experiment was run 4 times and the error bars naturally are larger. The mean phase of the echo for all delay times is 0.1252 ± 0.1017. The phase of the echo is good to 0.1 radians, the benchmark of phase stability. It is noted that for the optically thinner cases, the echo phase for all delay times had errors within this benchmark.

6.4 Optical Nutation

An optical nutation signal allows the Rabi frequency and the optical depth to be measured [46]. A two-level system driven resonantly with an electric field oscillates between the two levels at the Rabi frequency $\Omega = \mathbf{d}.\mathbf{E}/\hbar$, where $\mathbf{d}$ is the transition dipole moment and $\mathbf{E}$ is the electric field. This oscillation of the atomic population emits radiation and modulates the driving field at the Rabi frequency. Thus, by detecting the transmitted electric field the Rabi frequency can be measured.

To observe the nutation a strong pulse of temporal length much larger than a π pulse is applied to the cryogenic sample and the output is detected without mixing with a local oscillator. Figure 6.12 shows an example of a nutation signal.

There are 6 sites and orientations of the thulium ion electric dipoles when doped in YAG (see Figure 2.5). The Rabi frequency is proportional to the dot product of the electric dipole vector and electric field vector. For particular electric field polarizations, there is a unique Rabi frequency. The polarization of the probe beam is controlled with a polarization rotator placed before the sample.

The Rabi frequency measured in Figure 6.12 is 0.382MHz for a pulse intensity of 10mW. The value is obtained by fitting a curve to the signal as done in [46]. This order of magnitude is considered the benchmark Rabi frequency. The optical depth is found from the ratio of the signal at the point where the nutation starts and at $t = +\infty$, where the a steady state is reached. The point at which the nutation starts is the maximum absorption of the signal, whereas the point at $+\infty$ is maximum transmission. In this case, the optical depth is 0.22.

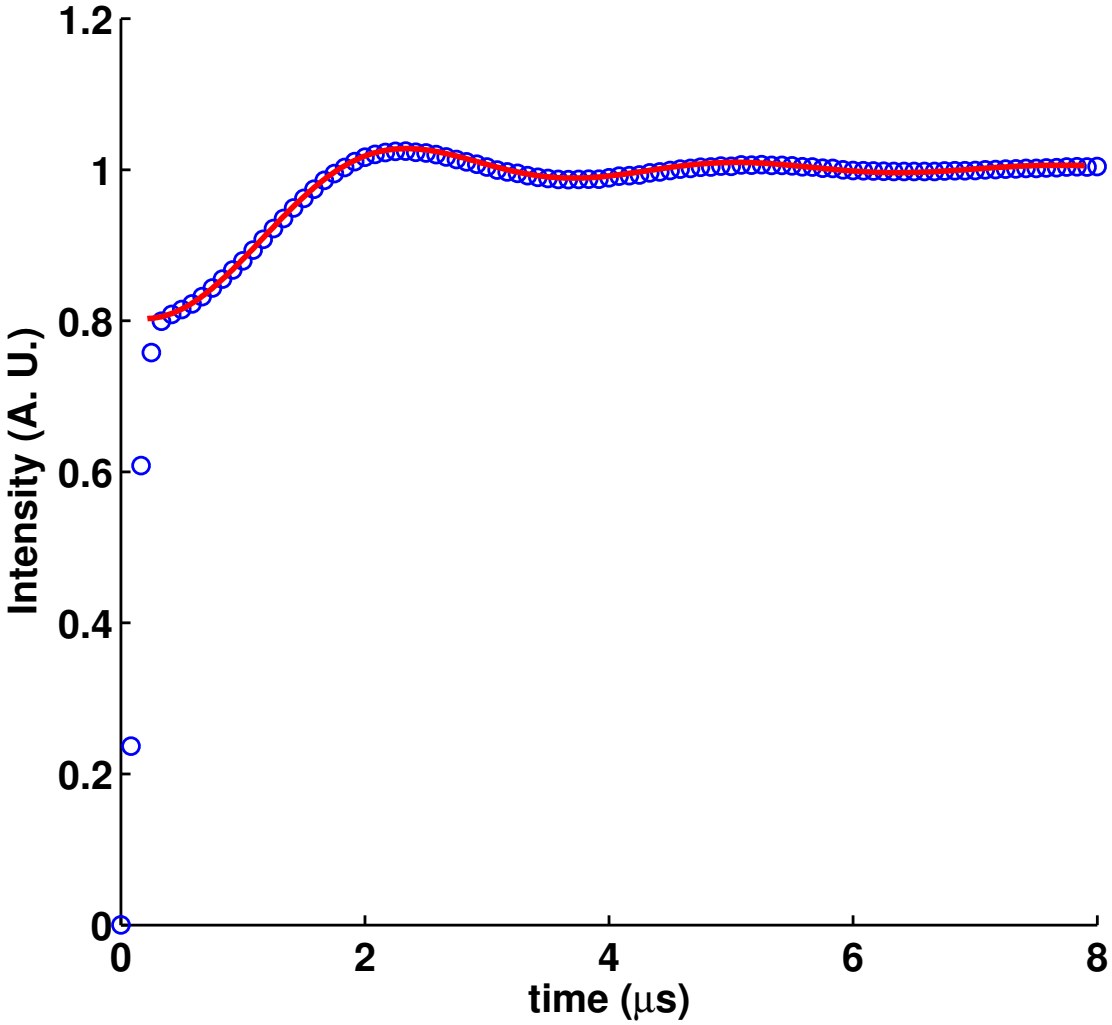

Figure 6.12: Measured nutation signal (open circles) for a strong pulse applied at $t = 0$. The solid line shows a theoretical fit [46] with a Rabi frequency of 0.382MHz

Chapter 7

Amplified Spontaneous Emission: Experiment

This chapter describes the experimental measurements of amplified spontaneous emission. The theoretical framework for these experiments have been discussed in Chapter 4 and the experimental set-up, techniques and benchmarks has been discussed in Chapter 6.

To characterize the amplified spontaneous emission, an exciting π pulse is applied to the Tm^{3+}:YAG sample. To detect the atoms that see a similar Rabi frequency the focusing local oscillator (FLO) is used as outlined in Chapter 6. The noise is measured in the variance of the $\hat{x}$ and $\hat{p}$ quadratures. The results presented are from 2 differing experimental settings and are presented in 2 sections. Firstly, the optically and physically thick crystal (20mm) is used with the FLO detection system. Then, the thick sample is swapped out with the 4mm crystal.

The final section will compare the measured ASE fields to the expected fields given by the theory.

7.1 Experiment with 20mm Crystal

For this Tm^{3+}:YAG sample, the optical depth was measured to be $\alpha l = 3.1$ using a nutation signal (Chapter 6). The optically thick sample was chosen as it should be easy to see the increase of noise in the $\hat{x}$ and $\hat{p}$ quadratures, since the amount of ASE is proportional to the number of atoms excited. For the following results, the cryogenic cooler was left on such that more data can be acquired as the experiment is not limited by the warming of the crystal when the cooler is turned off. The laser

stability was of a sufficient level to conduct the experiment with the cryostat on.

Figure 7.1a shows the laser field that is applied to the cryogenic Tm^{3+}:YAG. The sequence consists of a rephasing pulse and a phase pulse. The π pulse length is $t_\pi = 1.6$ μs and the phase pulse is 6 μs. The phase pulse intensity is low such that the detection system is not saturated. Four different rephasing pulse areas are used; $\frac{\pi}{2}$, π, $\frac{3\pi}{2}$ and 2π. The intensity of the pulses were kept the same, hence the duration is adjusted. We make a measurement of the variance of the $\hat{x}$ and $\hat{p}$ quadratures simultaneously using heterodyne detection. To measure this variance the pulse sequence is applied 2500 times at a repetition rate of 10Hz. This repetition rate ensures that all population has decayed to the ground state between pulses.

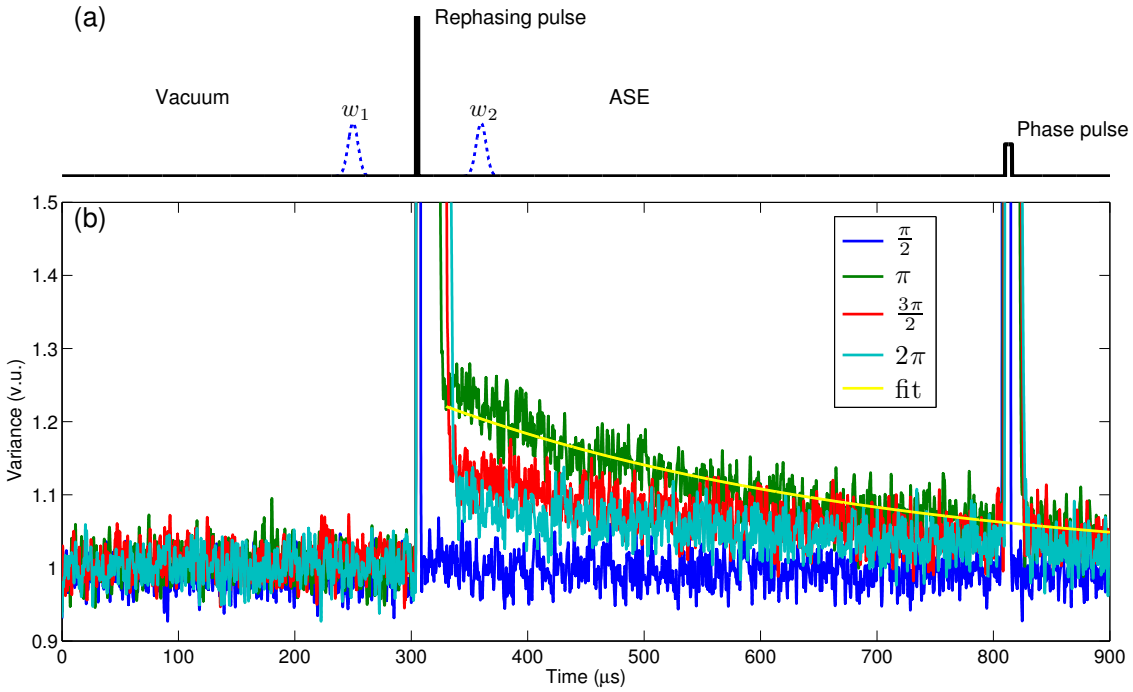

Figure 7.1: (a) The solid black line shows the applied laser field, consisting of a strong rephasing pulse which creates the amplified spontaneous emission, and a phase pulse which allows for the knowledge of the phase of the laser field. The blue dotted curves (w_1, w_2) are the Gaussian temporal mode functions used to investigate the spectrum and the statistics of the vacuum and ASE regions and are placed 50 μs either side of the rephasing pulse. The Gaussian windows have FWHM = 10 μs. (b) The measured amplified spontaneous emission for 4 differing rephasing pulse areas. An exponential curve is fitted to the π pulse case, with a decay constant of 378 μs.

Results

Figure 7.1b plots the total variance in both quadratures as a function of time for the 4 different rephasing pulse areas. The signal has been digitally filtered with a 1 MHz wide Gaussian filter and has been normalized to the vacuum variance.

For the case of a $\pi/2$ pulse, there is no additional noise after the application of it. The case of the π pulse sees the most additional noise after its application. The noise decays away at a decay rate of 378 μs. For the case of $3\pi/2$ and 2π, the additional noise is less than that of the π pulse case. Another feature seen in Figure 7.1b is that the length of the π pulse has increased from 1.6 μs to $\sim$ 30 μs.

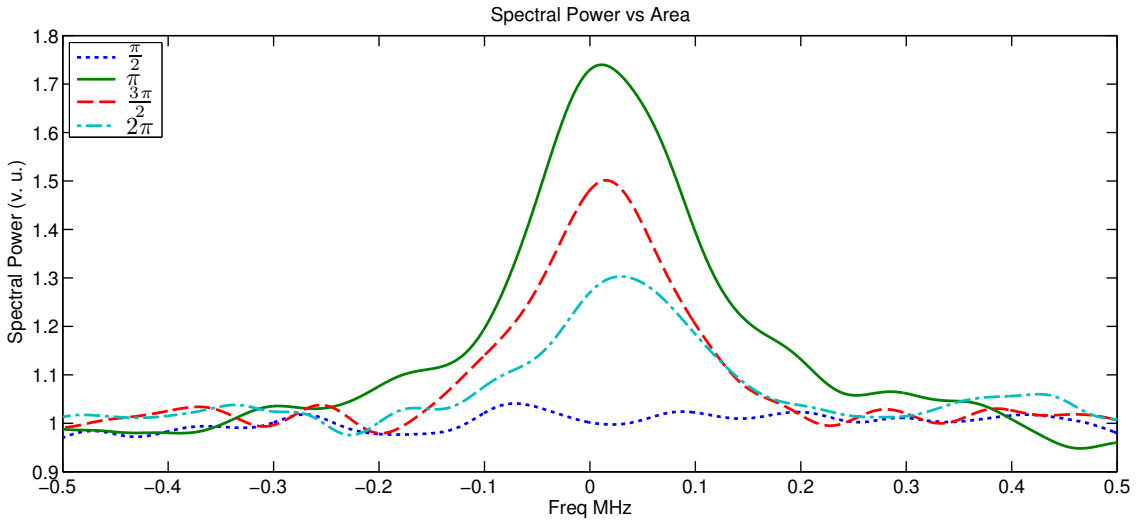

Figure 7.2: Spectral power of the ASE.

The mean spectral power in a 10 μs Gaussian window 50 μs either side of the rephasing pulse (w_1 and w_2 in Figure 7.1) is measured. Each shot has the Gaussian window applied to it, the spectral power is calculated and the mean of the 2500 shots is taken. The result is illustrated in Figure 7.2. The curves are normalized to the vacuum spectral power. As seen before, the $\pi/2$ case sees no additional noise, whereas additional noise is seen for the $\pi, 3\pi/2$ and 2π cases. The π pulse gives the most increase in noise. Fitting a Lorentzian curve to the π pulse noise peak gives a bandwidth of 170 kHz.

We now wish to investigate further the statistics in the vacuum and ASE regions. Multiplying each shot with the temporal mode functions w_1 and w_2 (Figure 7.1) and then integrating, results in 2500 quadrature measures of the vacuum and the ASE, from which statistics can be taken. Figure 7.3 shows the mean quadrature amplitude, vacuum variance and the ASE variance. The mean quadrature amplitude (top row

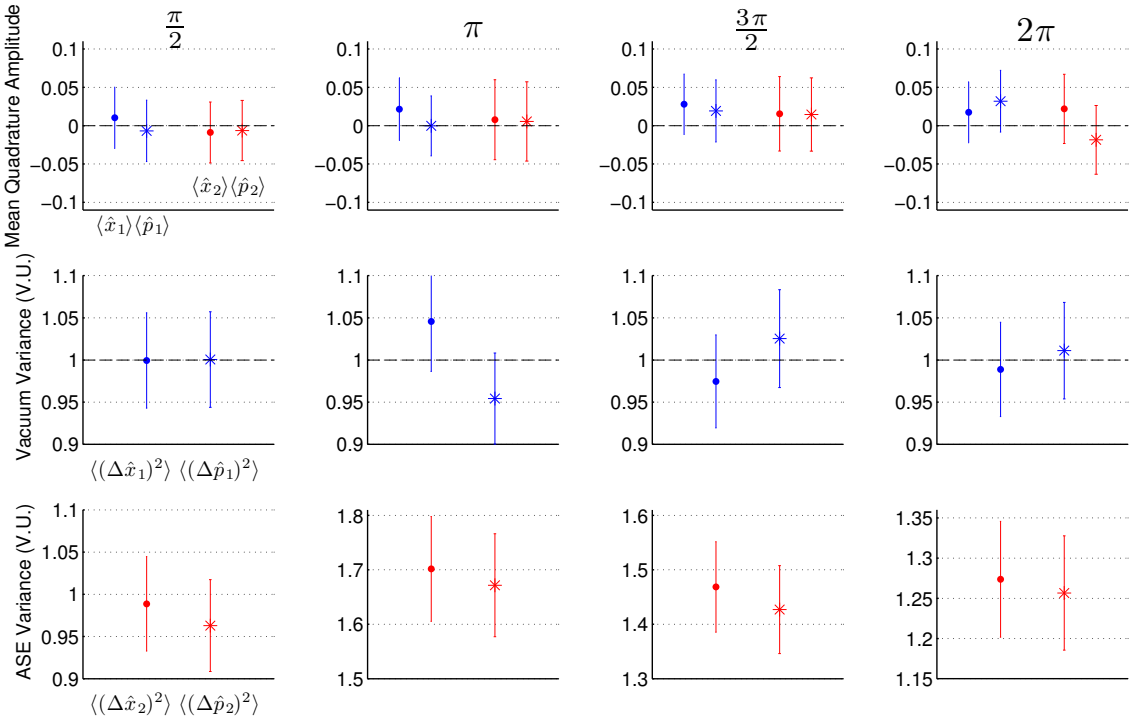

Figure 7.3: Statistics for the four different pulse areas ($\frac{\pi}{2}, \pi, \frac{3\pi}{2}, 2\pi$). The top row shows the mean quadrature amplitude ($\langle\hat{x}\rangle, \langle\hat{p}\rangle$). The marker $\bullet(*)$ labels the $\hat{x}(\hat{p})$ quadrature and the subscript 1(2) labels the vacuum(ASE) region. The error bars are 2σ. The middle row shows the variance measured in the vacuum region, the bottom row showing the variance measured in the ASE region. The error bars are calculated as in [135], with confidence interval of 95%.

Figure 7.3) is always zero within the error bars. The vacuum variance (middle row Figure 7.3) is normalized to the mean variance over the two quadratures, and is seen to have a variance of 1 within the error bar for each case. The ASE variance is seen in the bottom row of figures in Figure 7.3.

For the $\pi/2$ case, there is no addition noise in the ASE region. The π case sees a variance 1.6863 ± 0.0367 times greater than the variance measured in the vacuum region over the two quadratures. The $3\pi/2$ and 2π cases see a variance of 1.4474 ± 0.0340 and 1.2653 ± 0.0318 respectively over the two quadratures.

The gain of the sample is measured using the pulse sequence shown in Figure 7.4(a). Two small inputs are used, one placed before the rephasing pulse, and one placed after. The input pulse before the inversion propagates through the ground state and is absorbed according to the optical depth. Hence, one can infer the true input intensity by measuring the transferred intensity and the optical depth. The input pulse after inversion propagates through an excited medium (at least for the π

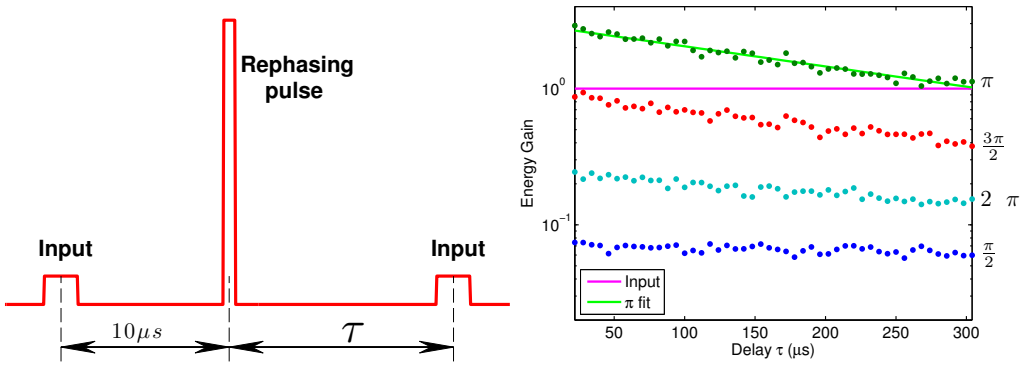

(a) Pulse Sequence (b) Energy Gain

Figure 7.4: (a) Pulse sequence used to measure gain. A small input pulse ($<< \pi$) is placed 10 μs before the rephasing pulse. Another small input pulse is placed after the exciting pulse at a variable time τ. (b) Gain of small input pulses for 4 different inversion pulse areas. The gain is calculated by knowing the optical depth and inferring the input size from the transmitted size of the input pulse before the π pulse. The inverting pulse size is labelled to the right of each data set. The solid line indicates the input area.

pulse case) and hence is amplified. The level of amplification is given by comparing the amplified input pulse energy to the true input energy. Figure 7.4(b) log plots the pulse energy gain. A straight line fit is given for the gain giving a decay time of 293 μs and an energy gain of 2.42 at 50 μs delay.

7.2 Experiment with 4mm Crystal

For this case the 20mm crystal is replaced with the 4mm crystal resulting in a factor of 5 reduction in the optical depth. Here the measurement of ASE is performed at 3 different optical depths: $\alpha l = \{0.78, 0.47, 0.25\}$, measured using a nutation signal. To change the optical depth, the laser frequency is scanned to a different part of the line. This of course changes the position of the line in which the laser is locked to resulting in minor adjustment of the electronic and optical feedback.

The pulse sequence used is similar to that in Figure 7.1a. The π pulse length is 1.6 μs. A phase pulse is applied 100 μs prior to the π pulse. The echo of this phase pulse will be very small as the T_2 is near 20 μs. Also, this echo appears outside the time window of interest.

The noise that will be detected here is smaller in intensity due to the reduction in optical depth. For the three optical depths the pulse sequences are applied

$\{18500, 14500, 20000\}$ times at a repetition rate of 10Hz. The laser stability was not as good as the previous experiment so these experiments were conducted with the cryogenic cooler off for better laser frequency stability. Since the sample undergoes heating almost immediately after deactivating the cooler, the experiment is limited to groups of 500 shots at a time. Before each set of 500 shots, the optical depth and Rabi frequency are measured, while the photon echo efficiency and coherence time are measured a few times over the course of the entire experiment.

Results

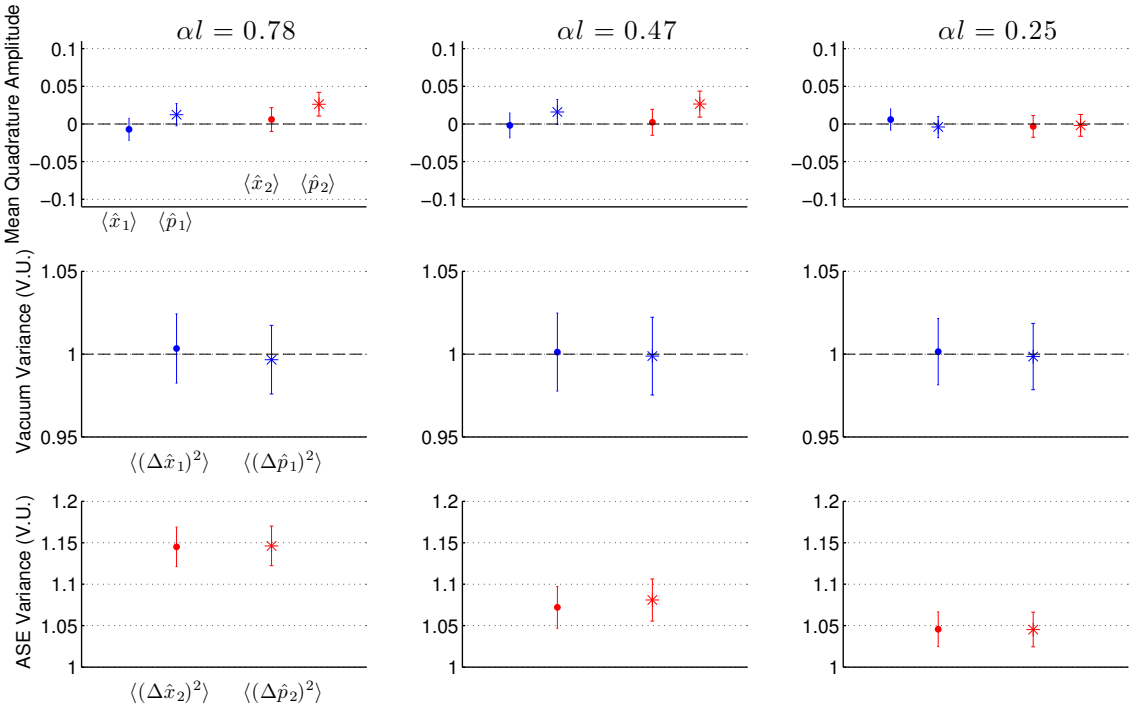

Figure 7.5: Mean quadrature amplitude and variances for the vacuum region (subscript 1) and ASE region (subscript 2). Each column of plots contains the data for the optical depth specified at the top. The symbol and colour scheme is identical to Figure 7.3.

To process statistics of the ASE field, a 10 μs square window is applied to each shot centered 45 μs after the π pulse. An identically sized window is applied in the vacuum region centered at an arbitrary time. Figure 7.5 shows the mean quadrature amplitude, the vacuum variance and the ASE variance using these windows. In this case, the mean quadrature amplitude is almost always zero within the error bar. The variances in each quadrature for each region is normalized to the total vacuum

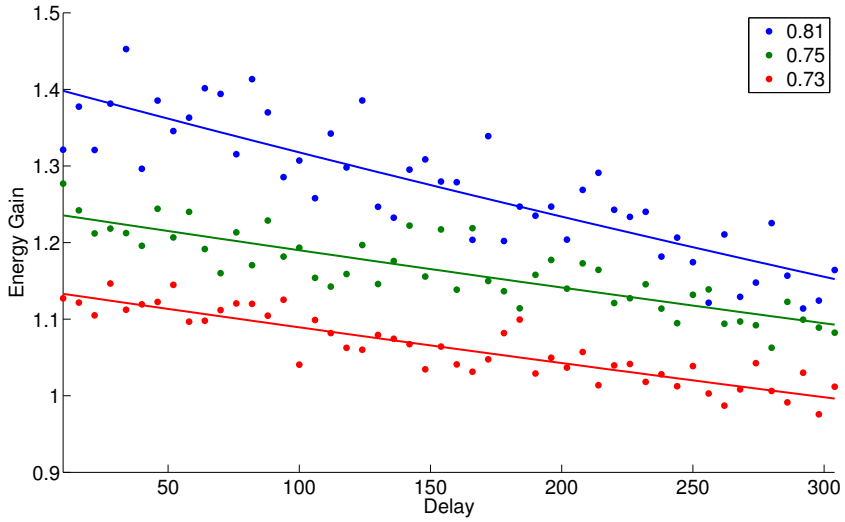

Figure 7.6: Energy gain for different optical depths.

variance for both quadratures. The ASE variance for $\alpha l = 0.78$ is 1.1457 ± 0.0168, for $\alpha l = 0.47$ is 1.0766 ± 0.0179, and for $\alpha l = 0.25$ is 1.0455 ± 0.0148.

The gain is measured in an identical manner as Figure 7.4(b). Figure 7.6 shows the gain a small input pulse receives as it propagates through an excited medium for various optical depths. The delay between the inverting pulse and small input is increased and exponential fits are shown. The ASE calculated in Figure 7.5 has a 10 μs window centered 45 μs from the inverting pulse. For an optical depth of 0.78, the gain at 45 μs can be estimated to be 1.3.

7.3 Discussion

In the optically thick medium, the case of the π pulse results in the most amplified spontaneous emission. For the variance trace in Figure 7.1b, it was seen that the length of the π pulse increased from 1.6 μs to around 30 μs. This can be explained using the area theorem [48], which states that a π pulse will remain a π pulse as it propagates through the medium. Since the medium is optically thick, the length of the π pulse necessarily needs to increase since the intensity is being reduced by the absorbers [120].

For the case of a $\pi/2$ pulse, there is no additional noise after the application of it. The $\pi/2$ pulse propagates through the sample losing area as it is absorbed in the optically thick medium. The excited state effects are negated by the optical thickness and variance at the shot noise level is measured after the pulse.

For the case of $3\pi/2$ and 2π, the additional noise is less than that of the π pulse case. In the optically thin case, the effect of a $3\pi/2$ pulse should be the same as a $\pi/2$ pulse and the effect of a 2π pulse should be the same as no pulse at all. The optically thick case will see propagation effects of these pulses. The pulse enters the thick medium and loses area until it becomes a π pulse in which case it will then propagate whilst remaining a π pulse.

It was seen that the noise resulting from the π pulse decayed with a timescale of 378 μs. This noise should decay away as the excited state lifetime, which is given as 800 μs in [16]. There is a discrepancy here of a factor of 2. This reduction in the excited state lifetime could be due to non-radiative decay, where the excited state population depletes via phonons. As mentioned before, the coherence time varied dependent on the crystal mounting and location in the cryostat and so a high crystal temperature will see an increase in non-radiative decay. It is noted that the noise here is not the result of free induction decay from structure on the line or atomic shot noise. These phenomena would result in noise decay at a time scale of the coherence lifetime (T_2 = 13.4 μs from Chapter 6). The noise here has a time constant an order of magnitude larger than the coherence lifetime.

The bandwidth of the noise is 170 kHz which is a lower bandwidth than expected from the Fourier width of the π pulse used (1.6 μs). The reduction in bandwidth is due to the temporal increase of the π pulse as it propagates in the medium.

For all optical depths it is seen that the same amount of noise is added to each of the two quadratures, to within the error bar. This is an indication that the ASE is independent of phase.

For the ideal amplifier, the gain measured should correspond to the minimum noise measured. For an optical depth of 3.1, the π pulse gave a measured variance of 1.69 times greater than the variance in the vacuum region and a gain of 2.42 at 50 μs after the π pulse. The expected gain from the optical depth is $e^{3.1} = 22.2$. For an optical depth of 0.78, the π pulse gave a measured variance of 1.15 times greater than the variance measured in the vacuum state and a gain of 1.3. The expected gain from this optical depth is $e^{0.78} = 2.18$. We see that the measured values for the gain and ASE are less than that expected from the optical depth. The measured ASE is less than that expected from the measured gain. This suggests that we have the unphysical noiseless amplifier. We carefully checked the clearance above the dark noise and the behaviour of the detectors because of this, but the results remained unchanged.

One reason as to why the gain is larger than the noise is argument of 'lensing'.

Since the probing beam is spatially inhomogeneous, when the ensemble is inverted there is a spatially varying excitation profile. This can result in a varying refractive index over the sample. This becomes an issue since no such phenomena exists for the ground state. It is conceivable that a 'lensing' effect is occurring such that more light is coupling into the mode of the pulse propagating through the excited state. This would result in an over-estimate of the gain. No such effect happens for the vacuum and will not be seen in the measurement of the noise.

It is evident that we do not have anywhere near the right amount of ASE we would expect from this optical depth. Recall the predicted amount of variance in the ASE field as a function of optical depth is given by Equation 4.30, $\langle \hat{x}_1^2 \rangle = 2\mathrm{e}^{\alpha l} - 1$. This expression corresponds to the variance measured using a homodyne detector. For a heterodyne detector we are coupling the vacuum into our simultaneous measurement of the $\hat{x}$ and $\hat{p}$ quadratures. The coupling is 50:50 and so for the ASE field,

$$\langle \hat{x}_1^2 \rangle = \frac{(2\mathrm{e}^{\alpha l} - 1) + 1}{2} = \mathrm{e}^{\alpha l}. \tag{7.1}$$

For an optical depth of 3.1 the expected ASE field variance at 50 μs is about 20, an order of magnitude larger than the measured value of 1.69. Of course, the theory relies on an ideal π pulse, which in the case of the optically and physically thick crystal is difficult to achieve. Propagation effects of the π pulse are important in this case. The beam is being focused so there is a changing Rabi frequency over the length of the crystal. Also, the wavefronts are curved for a focusing Gaussian beam which results in phase shifts over the beam spot.

These measurements were obtained using the FLO detection system which optimized the photon echo efficiency in the optically thick sample. The photon echo efficiency is important for reading out the RASE field. However, the detection mode for noise is not ideal over the length of the sample. This is the case since the beam is focused tightly resulting in a short Rayleigh range compared to the physical length of the crystal. Referring to Figure 6.4, the detection mode is ideal at the front of the sample where only the centre of the probe is being detected. The detection mode at the centre of the sample is about the same size as the probe, so in this case we detect the unwanted 'wings' of the Gaussian mode shape resulting in a reduction in the ASE field. Perhaps the worse feature of this detection is that the mode at the back of the sample is almost twice the size of the driving field, hence additional vacuum noise is being detected from the atoms which do not see any driving field. For the optically thin case, the detection mode is twice the size of the driving mode

and again additional vacuum noise is being detected.

Summary of ASE

The first section presented the result of amplified spontaneous emission for an optical depth of 3.1 and the second section presented results for optical depths 0.78, 0.47 and 0.25. Both situations used the focusing local oscillator detection mode. Figure 7.7 shows the total variance measured for both light quadratures as a function of optical depth. Included in this figure is the case for a warm crystal where the coherence times are shorter than any relevant time scale for the cold case. The theoretical expression for the variance for a given optical depth using heterodyne detection is given by Equation 7.1 and is $e^{\alpha l}$. As already noted, the variance of the ASE field measured is significantly less than expected from the optical depth and this is illustrated explicitly in Figure 7.7. The ASE field is also less than is expected from the gain measured.

The measured variance for the ASE field does scale exponentially with 0.173 times the optical depth. The blue dotted line in Figure 7.7 is this fit. This could indicate that the measurement of the optical depth is grossly overestimated. However, measuring the optical depth by burning a hole and sweeping across it in frequency gives an answer in agreement with the optical nutation method. It is more likely that the π pulse is to blame here. The π pulse is simply not inverting the atomic ensemble correctly resulting in noise less than expected from the optical depth.

To improve the measurement of the gain such that the lensing effect of the probe mode is avoided, a spatially larger π pulse compared to the probe pulse can be used. In this case the probe beam will see a more spatially homogeneous excitation preventing the effect of lensing. This technique will require more laser power for the Rabi frequency of the driving field to be the same.

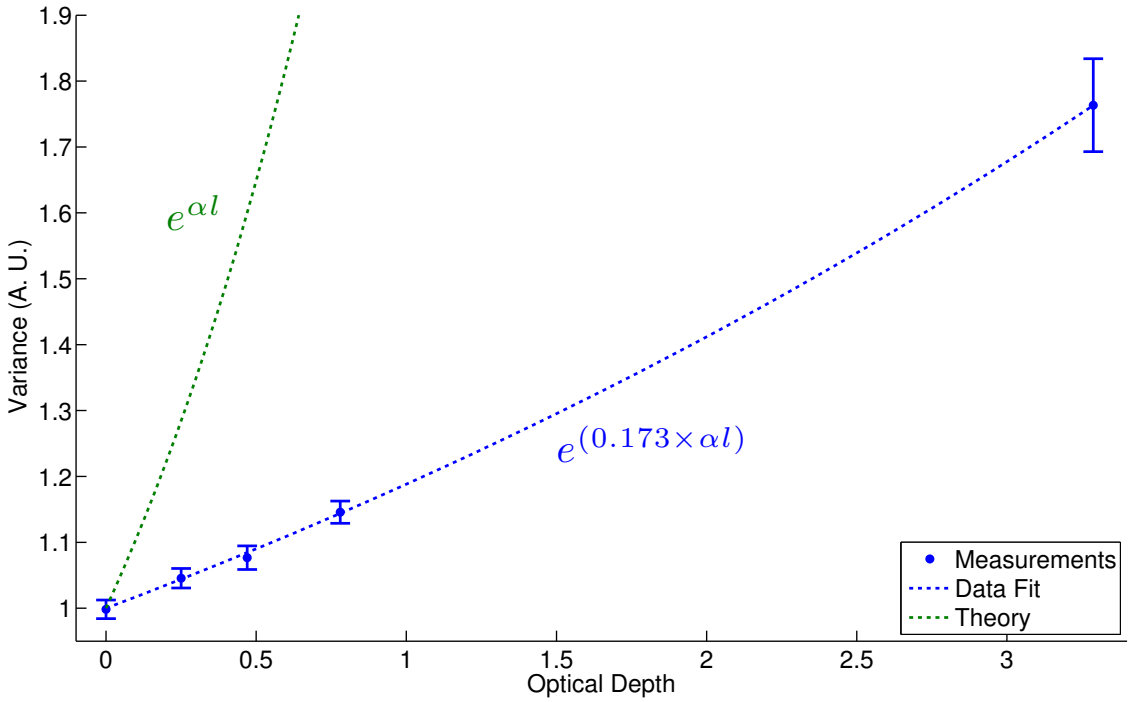

Figure 7.7: Measured variances vs optical depth using the focused local oscillator detection mode. The variance is for both quadratures and the error bar is a 95% confidence interval. The green dotted line is the variance expected from the optical depth, the mathematical expression indicated in green text. The blue dotted line is an exponential fit to the data. As indicated by the blue text, the data fits well to $e^{(0.173\times\alpha l)}$.

Chapter 8

Rephased Amplified Spontaneous Emission: Experiment

This chapter presents the experimental progress toward rephased amplified spontaneous emission. The theoretical framework for these experiments has been discussed in Chapter 4. The experiment involves the rephasing of the amplified spontaneous emission that was experimentally investigated in Chapter 7.

This chapter is in 4 parts. First, the pulse sequence used to generate ASE and RASE fields is presented. In convention with the chapter on amplified spontaneous emission, this chapter presents 3 differing experimental settings. Firstly, RASE is investigated in the optically thick, 20mm long crystal with the focusing local oscillator. Then, the crystal is swapped out for the 4mm long crystal while the detection mode is kept the same. Finally, the 0.5mm thin sample is used with a local oscillator spatially larger than the probe such that when it is traced back to the sample, it detects only the centre of the exciting field. The detection modes are described in detail in Chapter 6.

8.1 Pulse Sequence

The pulse sequence that is used is illustrated in Figure 8.1. The solid red line is the applied laser field, with the blue dotted line being an artist's rendition of the ASE and RASE fields. There are three timescales to note here, labelled T, a and b.

The temporal separation between the π pulses is labelled T. There is a definite lower bound on this timescale as the detection system takes around 10 μs to recover from a strong intensity pulse. For these experiments the choice of T is short com-

pared to the excited state lifetime. In this regime it is expected that the population is mainly in the excited state when the second π pulse is applied resulting in the noise measured in the ASE region to be greater than the RASE region.

The timescale a is the delay between the second rephasing pulse and the end(start) of the ASE(RASE) window. As the coherence times are around 10 to 20 μs, this timescale ideally should be as close to zero as possible. There is a technical limitation on this value in that the detection system, as stated before, takes around 10 μs to recover from a strong pulse.

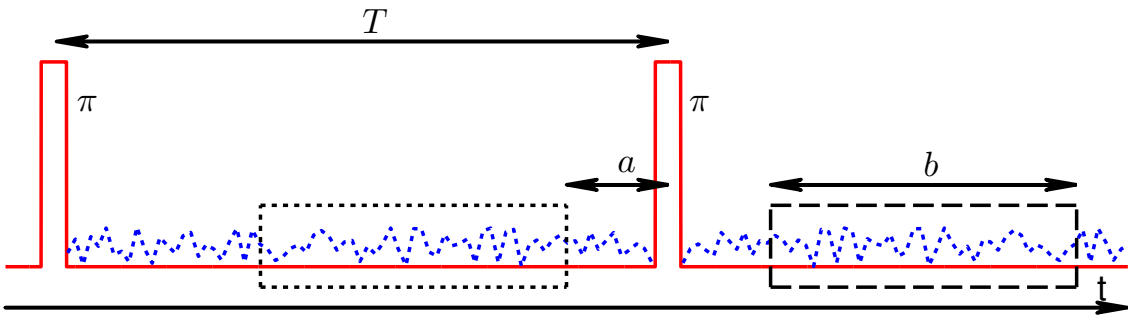

Figure 8.1: RASE pulse sequence. The solid red line is the applied laser light field, the dotted blue line is the detected signal. The black dotted(dashed) box is the ASE(RASE) region which is processed for correlations. T is the time between rephasing pulses, a is the time delay between the end(start) of the ASE(RASE) window and the second rephasing pulse and b is the time window for the ASE and RASE time regions. Ideally, $a = 0$, but additional noise appears after the rephasing pulse in the form of FIDs and detection recovery time.

Finally, the timescale b defines the temporal mode function which when integrated over gives the quadrature values for the ASE and RASE regions. There are two things to consider when choosing the length of this window. The ASE and RASE fields are decaying fields dependent on the excited and coherence times respectively, so the width of the integration window needs to be short compared to these lifetimes. Also to consider is the spectral width of the window. The spectral width of the window should closely match the bandwidth of the ASE noise, so as not to lose this signal to the white noise.

8.2 Experiment with 20mm Crystal

For this experiment, the cryogenic cooler is left on. The phase stability in the photon echos is good to 0.1 radians, which was good enough for ASE and RASE signals to

be detected. The optical depth is measured to be $\alpha l = 3.2$. Referring to Figure 8.1, $T = 100$ μs, $a = 20$ μs and $b = 55$ μs. The π pulse length is found to be $t_\pi = 1.6$ μs.

Results

Figure 8.2 shows the variance measured for the RASE sequence. The variance here is normalized to the variance in the vacuum region (shaded blue). Each shot is digitally filtered with a 1 MHz Gaussian filter before the variance is calculated. To obtain the phase of the laser, a phase pulse is placed 100 μs before the first π pulse. This phase pulse is very weak such that the detection system is not saturated, and the delay between the phase pulse and the π pulse exceeds the coherence time by a factor of 4, so an echo of this pulse will be extremely weak at best. This echo would appear when the second π pulse is applied, and would have little effect on the RASE field. Also, an echo of the first π pulse is seen after the RASE region.

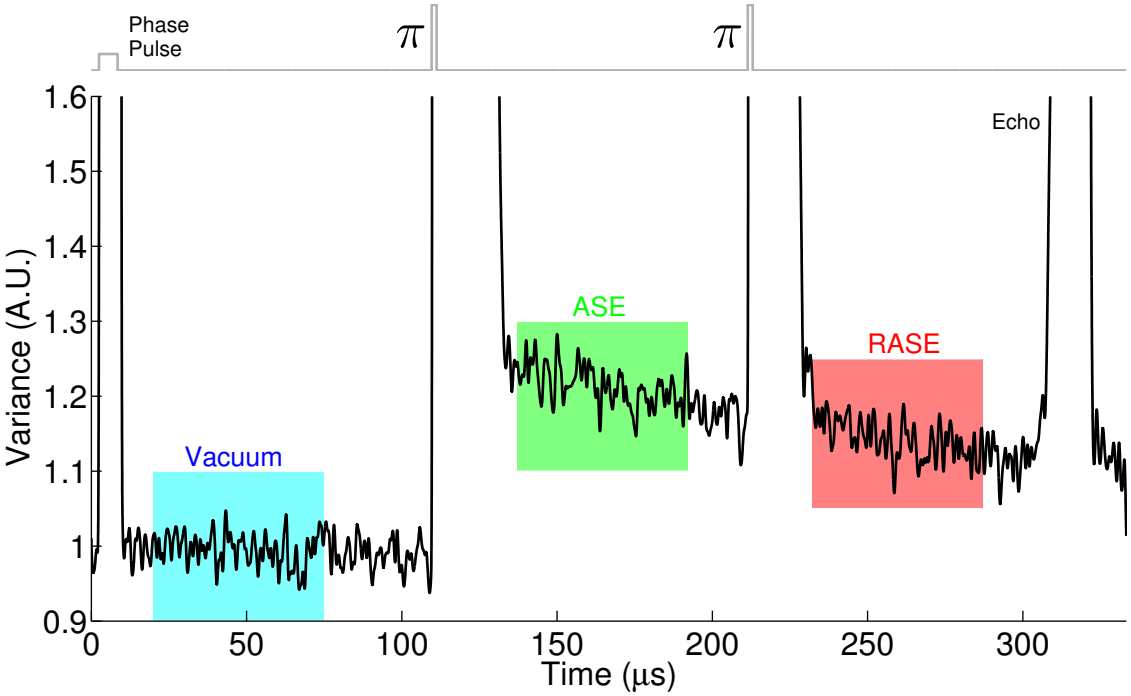

Figure 8.2: Variance measured for the RASE pulse sequence. The applied laser field is shown in the above plot in gray. The three shaded regions are vacuum (blue), ASE (green) and RASE (red) fields. The pulse at $t = 0$ is a phase pulse and after the RASE region an echo of the fist π pulse is present.

It is evident from Figure 8.2 that the RASE region has less noise than the ASE region. However, one can come to the same conclusion if the second π pulse is omitted, since the magnitude of the ASE field naturally decays. A better measure

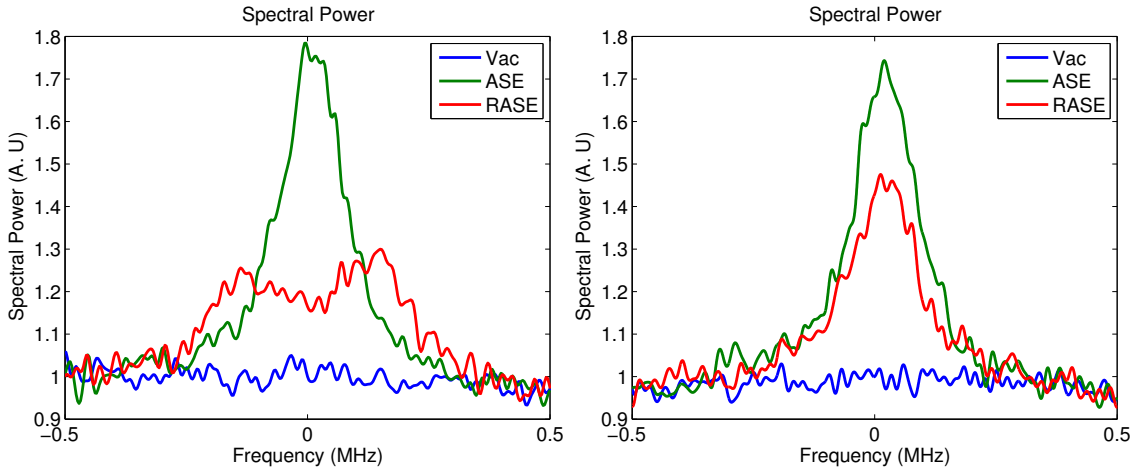

(a) (b)

Figure 8.3: (a) Spectral power of the vacuum, ASE and RASE time regions. (b) Spectral power of the vacuum, ASE and 'would be' RASE time regions when the second π pulse is omitted.

of the noise in each of the time regions is given in Figure 8.3(a). Here, the mean spectral power for the vacuum, ASE and RASE time regions are shown. The spectral power of each region is taken for each shot ($|V_i(f)|^2$) and the mean spectral power is calculated $\sum_i |V_i(f)|^2/N$ and normalized to the vacuum region. The familiar noise spectrum of the ASE region is seen. The RASE region sees a decreased spectral power on resonance with the driving laser, suggesting a decrease in noise in the RASE region compared to the ASE region. As a comparison, Figure 8.3(b) shows the spectral power for the case when the second π pulse is omitted. It can be seen that the RASE region in this case does have a decreased spectral power at DC. This effect is purely due to the fact that the ASE decays over time. It is noted that the spectral power at DC for the RASE region in Figure 8.3(a) is less than the RASE region in Figure 8.3(b), suggesting that the second π pulse indeed does have the expected effect of returning the excited state ions close to the ground state.

We now analyse the statistics of each region. Integrating over the square time regions for each shot results in 2500 quadrature values, of which statistics can be done. Figure 8.4 shows the quadrature measures in phase space and Figure 8.5 shows the mean quadrature amplitude and variance in each quadrature for each time region. It can be seen that in this case, the mean quadrature amplitude is zero for the vacuum and RASE regions, but not for the $\hat{x}$ quadrature in the ASE region. The total variance over the two quadratures in the ASE region is 1.7634 ± 0.0376

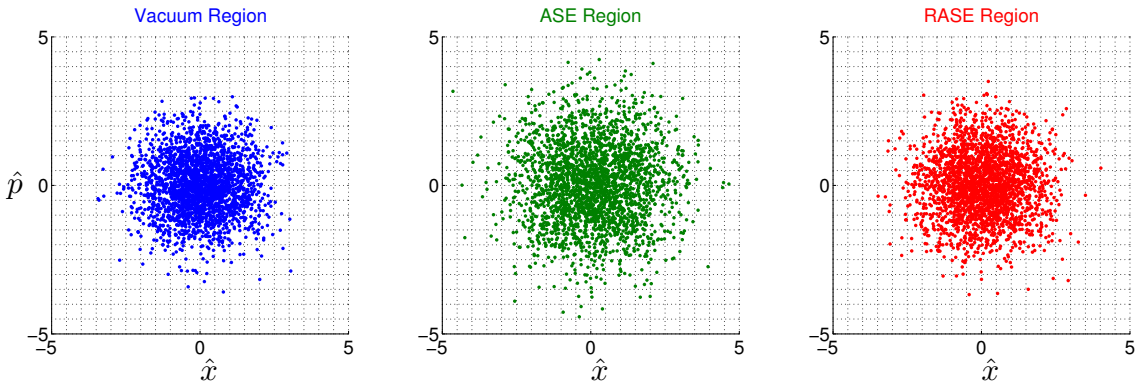

Figure 8.4: Heterodyne measurements for each shot and for each time region. Each point is obtained by integrating over the temporal regions illustrated in Figure 8.2 for each of the 2500 shots. The points are normalized such that the vacuum variance is 1.

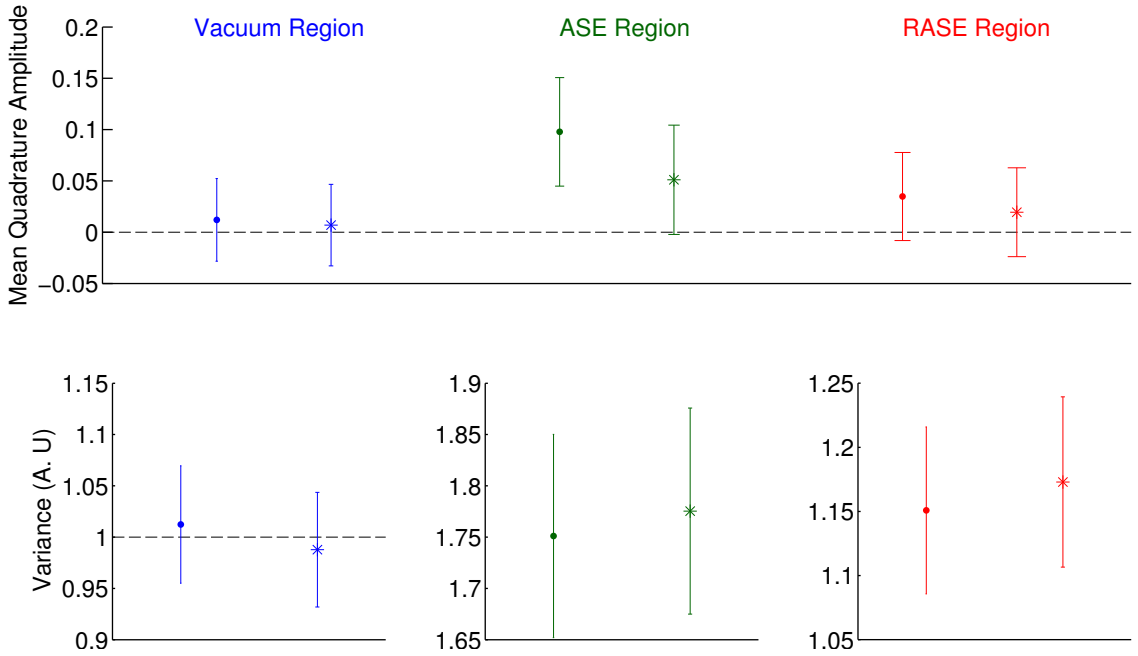

Figure 8.5: Statistics for the 3 time regions. The symbol $\bullet(*)$ represents a measurement in the $\hat{x}(\hat{p})$ quadrature. The error bars are 2σ.

greater than the variance measured in the vacuum, and the total variance over the two quadratures in the RASE region is 1.1617 ± 0.0305.

Cross-Correlation

To determine whether or not a time separated correlation exists, we investigate the cross-correlation between the ASE and RASE field. The cross-correlation is a

measure of how similar two time separated fields are and is formed by shifting one field along the time axis and integrating the product of the two fields at each time point. If the two fields in question are f and g, the cross-correlation is defined as

$$(f \star g)(t) = \int_{-\infty}^{\infty} f^*(\tau) g(t+\tau) d\tau, \tag{8.1}$$

where the f field is complex conjugated in the integral. When calculating the cross-correlation between the ASE and RASE fields we note that the RASE field is an echo of the ASE field and thus a time reversed version of the ASE field. Also, the ASE field is complex conjugated with respect to the RASE field. Labeling the ASE field as $A(t)$ and the RASE field as $R(t)$ and noting that for Equation 8.1 $f \rightarrow A(t)^*$ and $g \rightarrow R(-t)$, the cross-correlation is given by

$$A(t)^* \star R(-t) \equiv \int_{-\infty}^{\infty} A(\tau) R(t-\tau) d\tau \equiv (A * R)(t), \tag{8.2}$$

where $*$ denotes a convolution. Hence to obtain the cross-correlation one takes the convolution of $A(t)$ and $R(t)$.

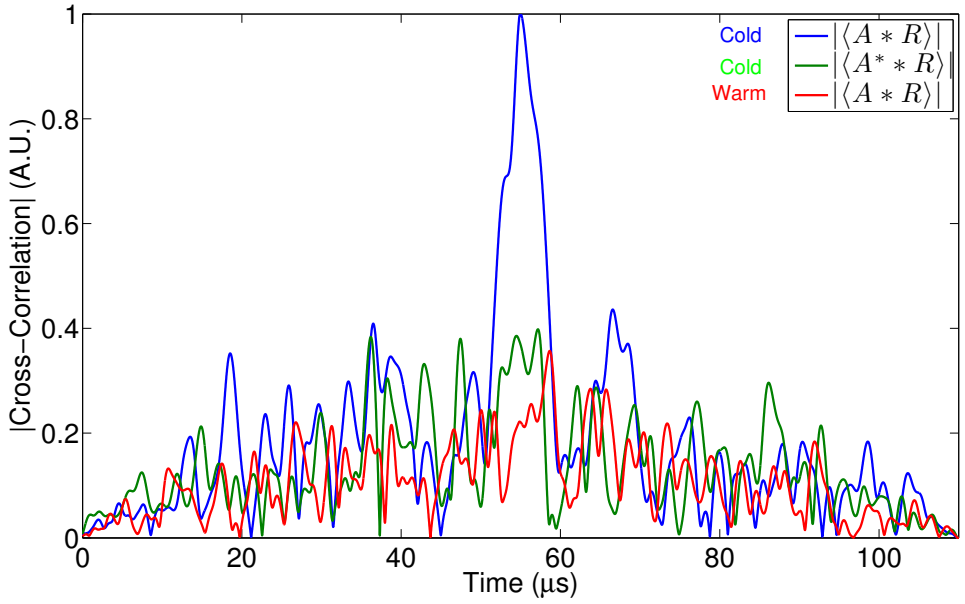

Figure 8.6: The cross correlation between ASE and RASE regions. The convolution is taken for each shot and the magnitude of the mean is plotted. Details of the curve can be found in the text.

Figure 8.6 shows the magnitude of the mean cross-correlation, where the mean is obtained from taking the convolution of the time regions for each shot. The

blue curve is the case when the crystal is cold and the convolution of the ASE and RASE fields are taken. The green curve is the same data set, where the incorrect convolution is taken between the complex conjugated version of the ASE field and the RASE field. The red curve is the case of when the crystal is warmed to ~ 40K and hence the coherence times are far shorter than any other relevant timescales. The same processing was done to this data set that was done to produce the blue curve.

The correlation peak has a full width at half max of 6.44 μs. This peak is also 2.5 times greater than the noise in the warm case.

Inseparability

To investigate the nonclassicality of the correlation, we look at the inseparability criterion outlined in Chapter 4. It is noted that since the detection system used is for continuous variables, only the inseparability criterion is used to test the nonclassicality of the correlation. The criterion is

$$\langle(\Delta\hat{u})^2\rangle_\rho + \langle(\Delta\hat{v})^2\rangle_\rho \geq 2, \tag{8.3}$$

where $\hat{u} = \sqrt{b}\,\hat{x}_1 + \sqrt{1-b}\,\hat{x}_2$ and $\hat{v} = \sqrt{b}\,\hat{p}_1 - \sqrt{1-b}\,\hat{p}_2$. That is, the variance of $\hat{u}$ and $\hat{v}$ is bound from below by 2 for separable states. The variance of $\hat{u}$ and $\hat{v}$ is given by

$$\begin{aligned}\langle\hat{u}^2\rangle &= b\langle\hat{x}_1^2\rangle + (1-b)\langle\hat{x}_2^2\rangle + 2\sqrt{b(1-b)}\langle\hat{x}_1\hat{x}_2\rangle,\\ \langle\hat{v}^2\rangle &= b\langle\hat{p}_1^2\rangle + (1-b)\langle\hat{p}_2^2\rangle + 2\sqrt{b(1-b)}\langle-\hat{p}_1\hat{p}_2\rangle.\end{aligned} \tag{8.4}$$

The heterodyne detector measures $\hat{x}_1$, $\hat{x}_2$, $\hat{p}_1$ and $\hat{p}_2$ a total of N times, producing an N length vector of measurements for each region. A 4×4 covariance matrix can be formed with these vectors,

$$\begin{pmatrix}\hat{x}_1\\ \hat{x}_2\\ \hat{p}_1\\ -\hat{p}_2\end{pmatrix}\begin{pmatrix}\hat{x}_1 & \hat{x}_2 & \hat{p}_1 & -\hat{p}_2\end{pmatrix}/N = \begin{pmatrix}\langle\hat{x}_1\hat{x}_1\rangle & \langle\hat{x}_2\hat{x}_1\rangle & \langle\hat{p}_1\hat{x}_1\rangle & \langle-\hat{p}_2\hat{x}_1\rangle\\ \langle\hat{x}_1\hat{x}_2\rangle & \langle\hat{x}_2\hat{x}_2\rangle & \langle\hat{p}_1\hat{x}_2\rangle & \langle-\hat{p}_2\hat{x}_2\rangle\\ \langle\hat{x}_1\hat{p}_1\rangle & \langle\hat{x}_2\hat{p}_1\rangle & \langle\hat{p}_1\hat{p}_1\rangle & \langle-\hat{p}_2\hat{p}_1\rangle\\ \langle-\hat{x}_1\hat{p}_2\rangle & -\langle-\hat{x}_2\hat{p}_2\rangle & \langle-\hat{p}_1\hat{p}_2\rangle & \langle\hat{p}_2\hat{p}_2\rangle\end{pmatrix}.$$

Taking into account the mean of each quadrature, it is then easy to form the variance of $\hat{u}$ and $\hat{v}$.

The variances used for the inseparability criterion in Equation 8.3 are those measured with a homodyne detector. Even though heterodyne detection is a 'noisy'

measurement of variance, the criterion is still valid with the same classical bound. However, the noisy measurement of the covariance term will weaken the correlation between the ASE and RASE fields (see Appendix E for more details).

Figure 8.7 shows the measured sum of the variances of $\hat{u}$ and $\hat{v}$. It is clear that when $b = 1(0)$, the variance is completely that of the ASE(RASE) region. The important number here is the covariance between the two regions ($\langle \hat{x}_1 \hat{x}_2 \rangle$ and $\langle -\hat{p}_1 \hat{p}_2 \rangle$). The case of no correlation between the two regions results in a very low covariance, hence the inseparability line is straight. The fact that the line in Figure 8.7 is near straight, suggests that there is very little correlation between the two regions. A comparison to the theory in Chapter 4 suggests that in the optically thick case the inseparability criterion should be well violated.

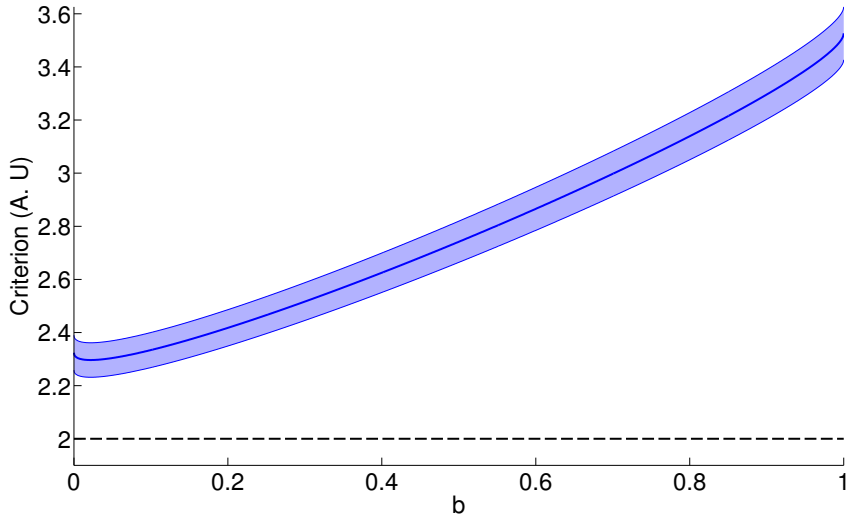

Figure 8.7: Inseparability criterion for optically thick Tm^{3+}:YAG. The blue line is the measured criterion with the shaded area representing a 66% confidence interval. The black dotted line is the lower bound on separability.

Discussion

It was seen in Chapter 7 that for the ASE region, the measured variance and the theoretically predicted variance had a large discrepancy. It is therefore expected that the variance in the RASE region to be less than is expected from the measured optical depth. For heterodyne detection, the quadrature variance in the RASE region using 1D theory and perfect π pulses (Chapter 4) is

$$\langle \hat{x}^2 \rangle = 1 + 4 \sinh^2 \left(\frac{\alpha l}{2} \right). \tag{8.5}$$

For an optical depth of 3.2, the expected variance for the ASE region is 24.53 and the RASE region is 23.57. The measured value for the ASE region was 1.76 and for the RASE region, 1.16. It was seen from Chapter 7 that the ASE was exponential with an effective optical depth of $0.173 \times \alpha l$. Using this effective optical depth in Equation 8.5 gives a value of 1.31. The measured value of RASE is still less than what is expected from the measured ASE field. This would suggest that the π pulse does not read out the RASE efficiently.

From Figure 8.6, it is evident from the clear peak in the cross-correlation appearing above the noise, that the ASE and RASE fields are indeed correlated. This peak is 2.5 times greater than the noise. One can be confident that this is indeed the correct signal and not a detection artifact by considering the following two cases. For the case of complex conjugating the ASE field the correlation peak disappears. For this case the convolved fields are out of phase, which hence causes the integral of the product to disappear. For the case of a warm crystal the correlation peak also disappears. This is expected as the coherence times decrease rapidly with increasing crystal temperature, resulting in a reduction of ASE and the RASE field not being rephased at all.

This correlation peak has a full width at half max of 6.44 μs which is temporally broader compared to the π pulse time $t_\pi = 1.6$ μs. This is acceptable in the sense that the bandwidth of the correlation does not exceed the bandwidth of the ASE. Of course, the contrasting case is unphysical. The π pulse undergoes temporal stretching due to absorption, as was seen in the previous chapter. The same effect is seen here as the correlation width is larger than expected.

Although a distinctive peak can be seen when the cross-correlation between the ASE and RASE regions is taken, a very small covariance is measured between the two regions, resulting in a classical correlation seen in Figure 8.7. The RASE field is expected to have decayed as the coherence time for this experiment is 13.4 μs and the RASE integration window starts 20 μs after the π pulse, resulting in a small covariance. Another contribution to the reduced covariance is other photons appearing in the RASE time region. These other photons are ASE, the second π pulse does not read out the RASE correctly. Another source of these photons is found by considering that atoms in the excited state can fall to the ground state via a metastable state. The photons resulting from that process are not detected as they are at a different frequency to the local oscillator. Hence, there will be photons rephased and detected in the RASE region whose corresponding ASE photon was at a different frequency.

8.3 Experiment with 4mm Crystal

Now we look at RASE using the 4mm crystal. The RASE generated here is the rephasing of the ASE presented in Chapter 7, where the optical depths investigated were $\alpha l = \{0.78, 0.47, 0.25\}$. The pulse sequence is similar to before. Referring to Figure 8.1, the time scales used were $T = 60$ μs, $a = 10$ μs and $b = 20$ μs. This sequence is applied $\{18500, 14500, 20000\}$ times for statistics to be calculated. Like for the ASE measurement, the cryostat is deactivated and groups of 500 shots are collected at a time. The Rabi frequency and optical depth are monitored per group of 500 shots.

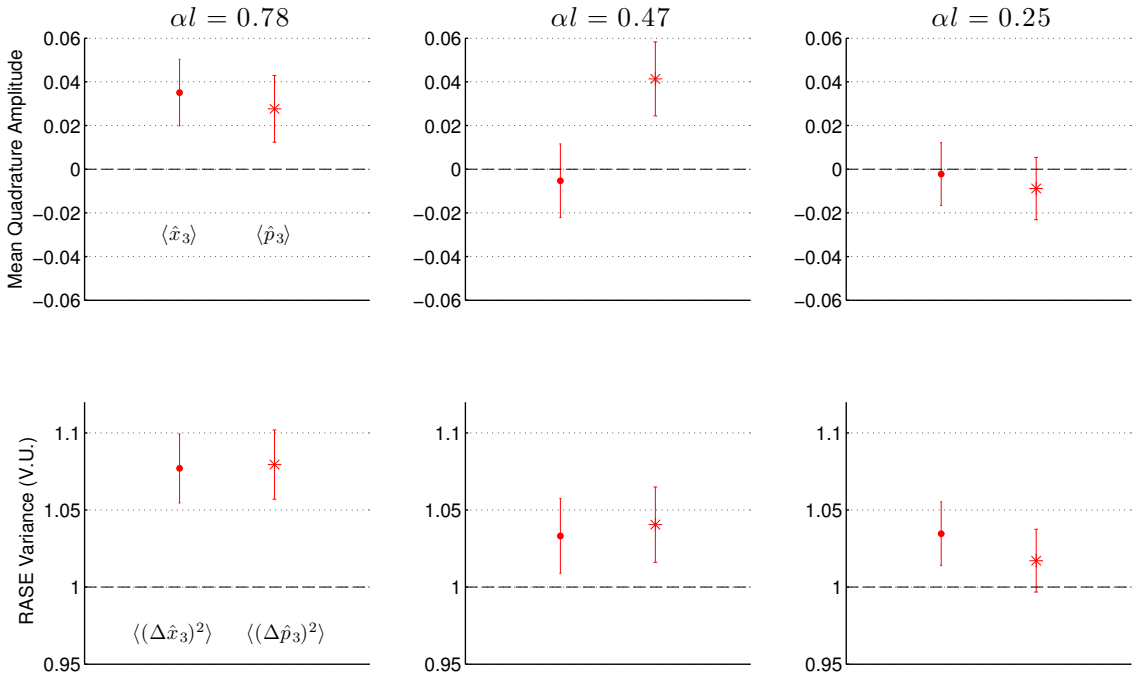

Figure 8.8: Mean quadrature amplitude and variance measured for the RASE time region for three different optical depths. The subscript 3 labels the RASE region as time region 3. The symbol $\bullet(*)$ is the measurement for the $\hat{x}(\hat{p})$ quadrature. The variance values are normalized to the vacuum variance presented in Figure 7.5. The error bar is a 95% confidence interval.

Results

Figure 8.8 shows the mean quadrature amplitude and the variance in each quadrature for the three different optical depths investigated. For the $\alpha l = 0.78$ experiment the mean quadrature amplitude is unexpectedly non-zero. The variance in each quadrature for each optical depth is the same to within the error bar meaning

the RASE is phase independent. As the optical depth decreases, the RASE variance measured decreases as expected. The error bars do overlap for different optical depths suggesting that more shots need to be taken. A summary of the measured RASE variances will be given at the end of the chapter.

Cross-Correlation

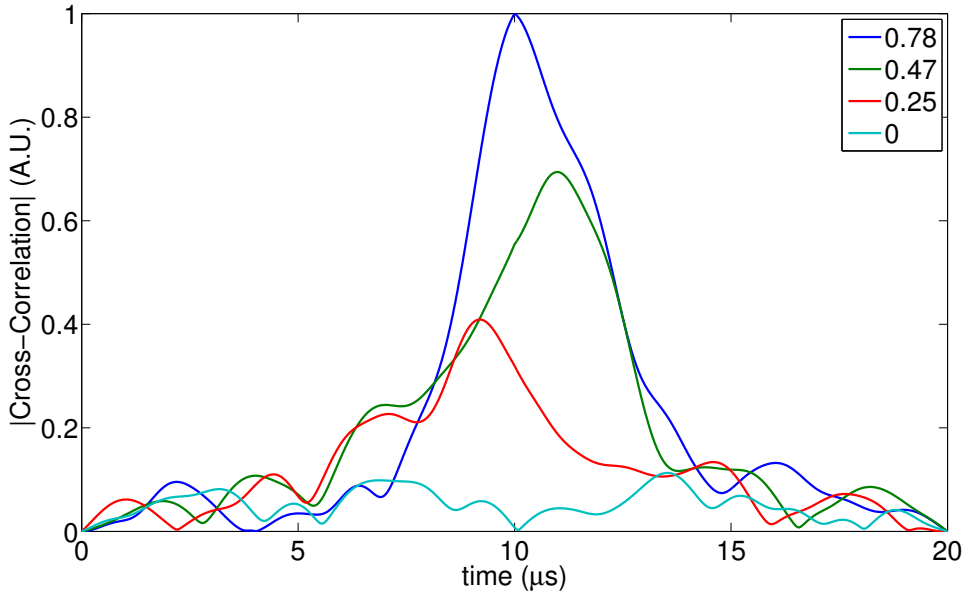

Figure 8.9: The magnitude of the cross correlation measured between the ASE and RASE time regions.

Figure 8.9 shows the magnitude of the cross correlation for each of the optical depths. The cross-correlation is calculated for each shot and the mean is taken and the magnitude is plotted. As was seen for the optically thick case, there is a clear correlation peak above the background noise for all three cases. The case for where the crystal is warmed such that the coherence times are short compared to any relevant timescale in the cold case is also plotted as a comparison. The data has been normalized to the highest peak, and it can be seen that as the optical depth is decreased the size of the peak also decreases. This is the expected case as the covariance is decreased as the optical depth decreases as seen in Equation 4.30. Considering that the photon echo efficiency decreases as the optical depth is decreased and also that less atoms means less photons, it makes sense that the correlation between the two regions gets weaker.

For the case of $\alpha l = \{0.78, 0.47, 0.25\}$, the full width at half max is $\{3.5, 3.9, 4.4\}$ μs. The timescale increases since the peak becomes more comparable to the background

noise. Each time scale is temporally longer than the π pulse used to rephase the ASE which is physical. The correlation widths are decreased compared to the optically thick case (6.44 μs). This can be explained by noting that propagation effects are reduced for reduced optical and physical interaction thickness of the sample.

Inseparability Criterion

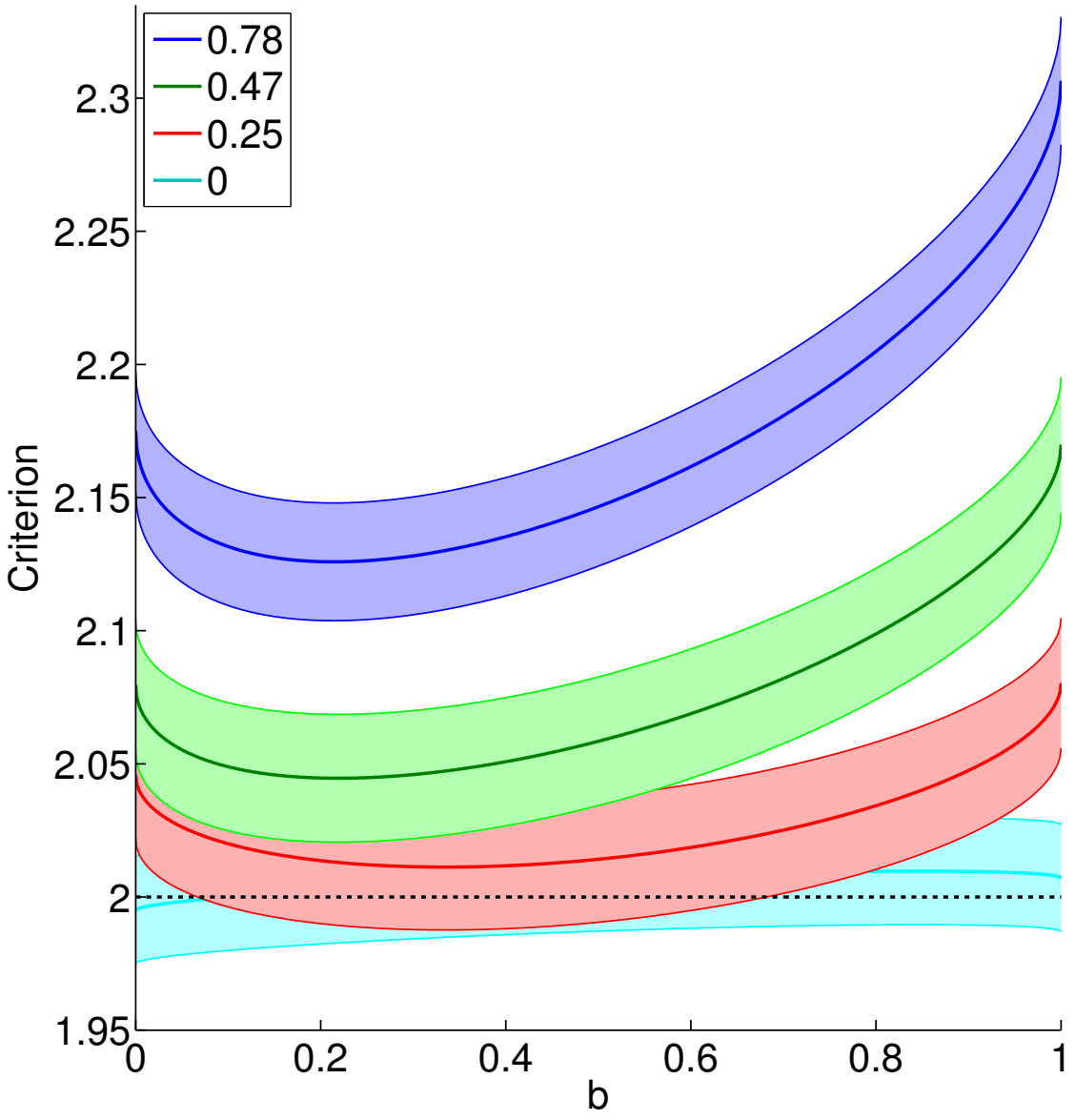

Figure 8.10: Inseparability criterion measured for the ASE and RASE regions. The shaded area represents a 95% confidence interval.

We now present the inseparability criterion for the three different optical depths.

Figure 8.10 shows the criterion. It is noted that an arbitrary phase shift is applied to all RASE quadrature values in order to maximize the correlation between the ASE and RASE fields. The fact that this has to be done suggests the phase stability of the photon echo procedure that creates the RASE field is of an insufficient level. Recall that the important number is the covariance between the same quadrature in two different time regions. The higher the covariance, the more quadratic the curve becomes. It can be seen that the optically thickest case ($\alpha l = 0.78$) has the most quadratic curve compared to all thinner cases. Again, this is expected due to the physical nature of the correlation for varying optical depth. The error bar is a 95% confidence interval and it is evident that more shots are required in order to reduce this error.

The first curve that was obtained was for the $\alpha l = 0.78$. This curve was promising as the correlation between the two fields was significant resulting in a large dip below the uncorrelated case (straight line from ASE to RASE). It was hoped that as the optical depth was reduced, the ASE and RASE levels would reduce getting closer to the classical bound allowing the criterion to be violated. Of course, as the optical depth is reduced, the correlation between the ASE and RASE fields is reduced and the result is that the criterion is respected. It is concluded that these are *classical* time separated correlations.

Discussion

The measured variances over both quadratures for the 4mm crystal are plotted versus optical depth in Figure 8.11. The expected RASE curve is also plotted (green dotted line). It is evident that the RASE measured is lower than the analytic expression. This is somewhat expected from the fact that the amount of ASE measured was lower than theoretically predicted and it was seen that for optical depths of 0.173 times the actual measured optical depth fitted the data well.

As a comparison, the variance expected from the level of ASE measured is included in Figure 8.11 (red dotted line). The result is that the measured variance in the RASE region exceeds the expected variance from the ASE measured. This is evidence that the rephasing π pulse is not perfect, there is an extra source of noise giving more noise in the RASE time region than is expected. This extra noise source is simply ASE, there are excited state atoms giving photons in the RASE region who do not correspond to a photon in the ASE region. This effect would result from an imperfect π pulse.

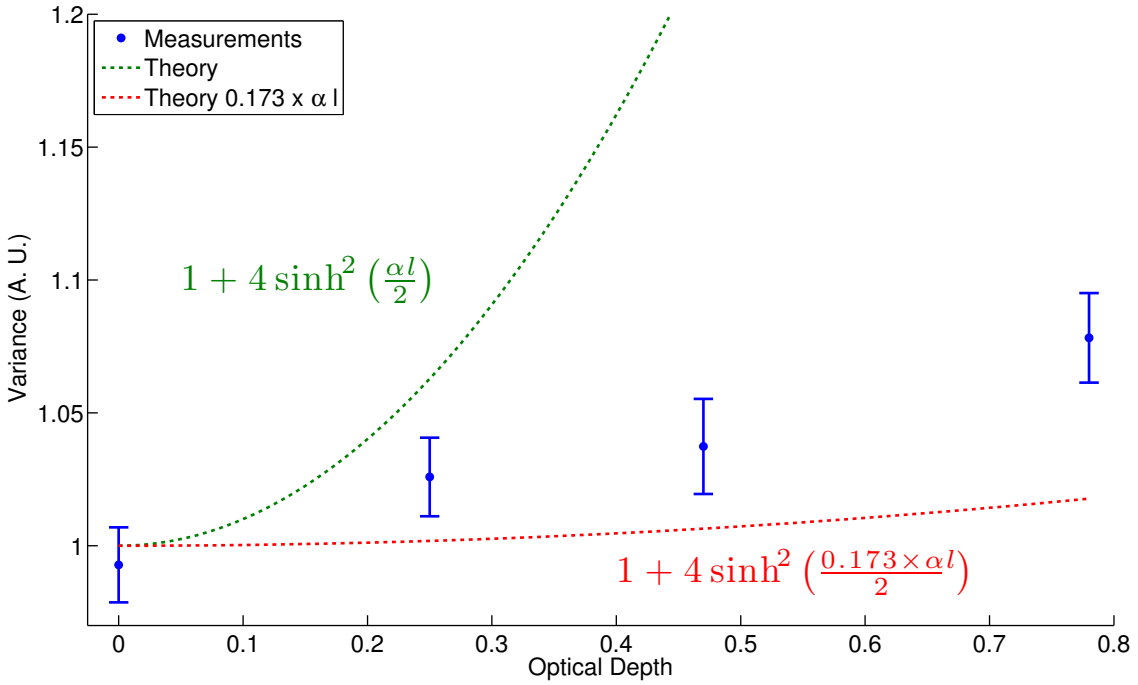

Figure 8.11: Measured RASE variances versus optical depth. The variance is over both $\hat{x}$ and $\hat{p}$ quadratures, the error bar is a 95% confidence interval. The blue points represent the measured variances. The green dotted line is the expected variance to measure using a heterodyne detector, the mathematical expression given by the green text. The measured ASE was fitted with an effective optical depth of $0.173\alpha l$ (Figure 7.7). The red curve is the RASE one would expect from the ASE measured.

The spectrum of the RASE field from Figure 8.3(a) show that the noise at DC is reduced but there are peaks around 200 kHz. This is another indication that the π is imperfect.

Since the π pulse is imperfect, the cross correlation between the ASE and RASE regions will suffer. This in combination with low echo efficiency and short lived coherence lifetimes cause the correlation between the ASE and RASE fields to be classical.

The mean quadrature value was not zero for cases of $\alpha l = 0.78$ and 0.47, suggesting that the ASE is displaced from the centre by a small amount compared to the vacuum state. This effect could be due to an FID appearing in the temporal window of interest. This is supported by the fact that the displacement of the ASE is reduced as the optical depth is decreased.

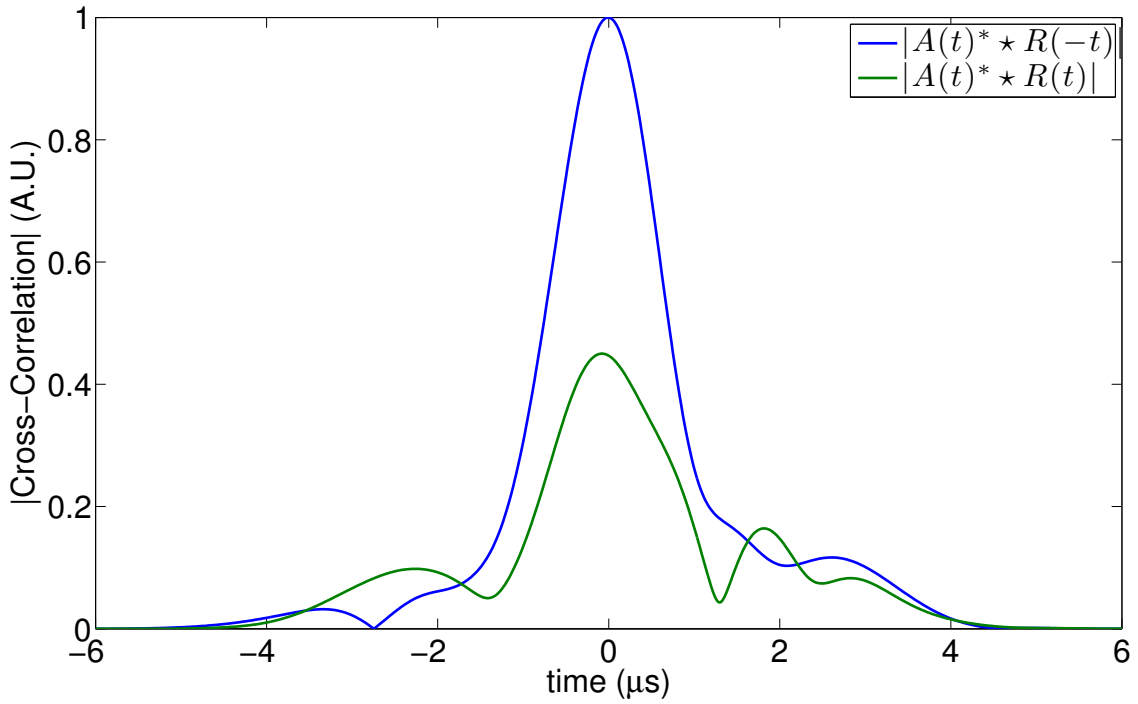

Figure 8.12: Magnitude of the cross correlation between the ASE and the RASE fields. The blue curve shows the correct case of time reversing the RASE field with respect to the ASE field. The green curve shows the uncorrelated case and can be considered the noise in the correlation measurement. The blue curve sees a clear peak above this noise with a width given by the π pulse.

8.4 Experiment with 0.5mm Crystal

The inseparability criterion was close to being violated in the 4mm sample with the criterion getting closer to being violated as the optical depth is decreased. This then motivated the final experiment: looking at RASE in a 0.5mm crystal. Presented here is the case for an optical depth of 0.046 $\pm$0.004. The local oscillator is adjusted to detect the ions that see a similar Rabi frequency, as discussed in Chapter 6. For this experiment, the π pulse time was 1.52 μs. Rather than square time windows, the windows used are Gaussian with full-width half max of 2.5 μs placed 10.5 μs either side of the second π pulse. There is a time distance of 40 μs between the two π pulses. The sequence is applied 22000 times at rep rate of 10Hz. The experiment is performed in groups of 500 shots as the cryostat is deactivated during acquisition.

The cross correlation is shown in Figure 8.12. Two cases are presented here. The blue curve is the cross correlation between the ASE and RASE fields and the green curve is the uncorrelated case. The uncorrelated case is obtained by not time reversing the RASE field when calculating the cross correlation (Equation 8.2). This

uncorrelated case represents the noise for the correlated case. The blue curve shows a distinct peak above the noise. This shows that there is a clear time separated correlation. The full-width half max of the peak is 1.5 μs which is in good agreement with the π pulse width of 1.52 μs.

Figure 8.13 shows the gain a small pulse receives propagating through the inverted medium. The gain measurement, identical to Figure 7.4(a), is conducted 5 times on the crystal. The optical depth is measured to be 0.045 ± 0.004 for the 5 runs. The figure shows the energy gain for times up to 40 μs. As can be seen, the energy gain is 1 within the error bar suggesting that there is no gain for this optically very thin case.

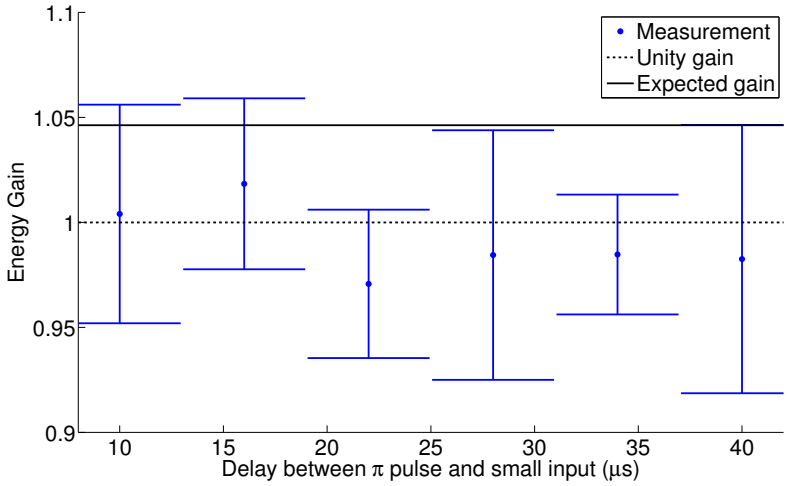

Figure 8.13: Energy gain for a small pulse propagating through the inverted medium. The gain measurement (see Figure 7.4(a)) is run 5 times. The data points are the mean gain for that delay time and the error bar is 2σ. The dotted line is the unity gain level and the solid line is the expected gain from the optical depth.

Figure 8.14 is the inseparability criterion. It is seen that the ASE and RASE levels are the vacuum level within the error bar. There is again a discrepancy between the expected (1.0475) and measured values of ASE suggesting that still the creation of the ASE is non-optimal. The measured ASE field is in agreement with the measured gain from Figure 8.13. There is good agreement between the expected (1.0005) and measured RASE field which is expected since for an optical depth this low, the RASE field is very close to the vacuum.

For the inseparability criterion in Figure 8.14, no arbitrary phase shift is applied to the RASE field with respect to the ASE field, as was done for the previous examples. Shown in the figure is the 1σ and 1.66σ uncertainty levels. It is noted that the uncertainty of the vacuum noise is improved compared to earlier results as

10 independent measures of the vacuum are made for each shot. It is clear that for values of b around 0.5, the criterion is *violated*. Figure 8.15 shows the probability distribution for $b = 0.5015$, the minimum of the inseparability curve in Figure 8.14. The percentage of the curve that is greater than 2 is 4.85%. There is a confidence interval of 95.15% that the criterion is less than 2. Hence, for one temporal mode, the ASE and RASE fields can not be represented as a separable state. We have successfully shown nonclassical correlations between time separated ASE and RASE fields.

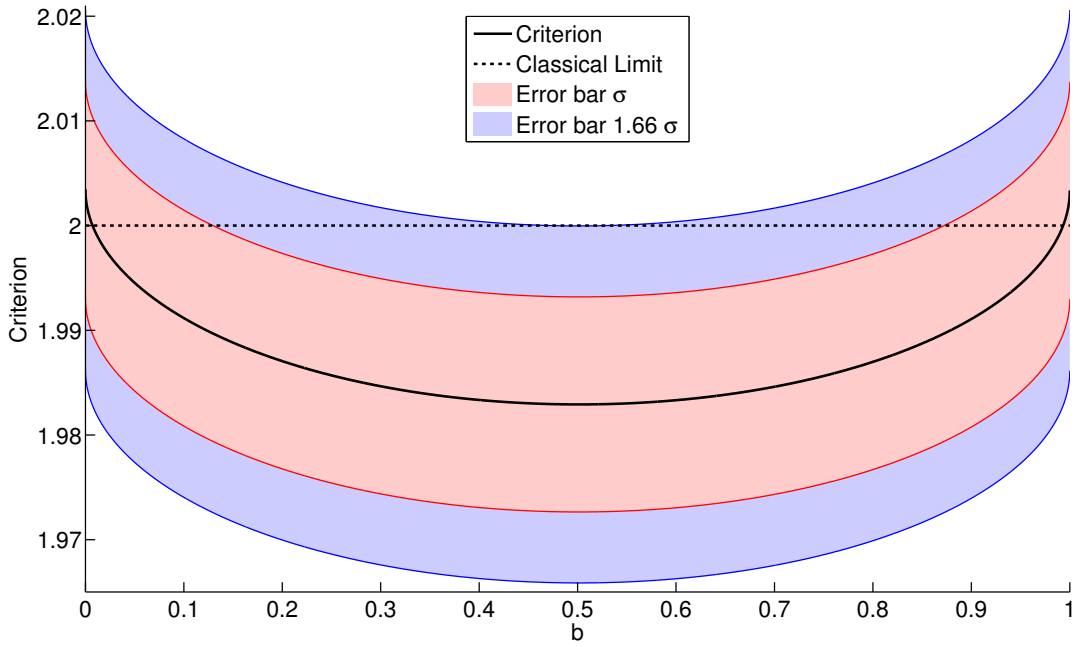

Figure 8.14: The inseparability criterion. The solid black curve is var($\hat{u}$) + var($\hat{v}$). The boundary of red shaded area is one σ of uncertainty and the boundary of the blue shaded area is 1.66 σ of uncertainty, where the uncertainty is calculated as in [135]. The black dotted line is the classical limit.

Figure 8.16 shows a comparison between the theoretical and experimentally measured inseparability curve. The theoretical curve is calculated using an optical depth of 0.046 and using a heterodyne detector. The theoretical curve highlights the fact that the ASE field measured is significantly lower than expected. The measured curve does not dip below the classical bound as much as the theoretical curve does. This is due to the short coherence time of 10.60μs. The time windows used for processing were centered 10μs either side of the second π pulse, a time comparable to the coherence time. One can say that, at the 95% confidence level, experiment and theory both show a violation of the criterion.

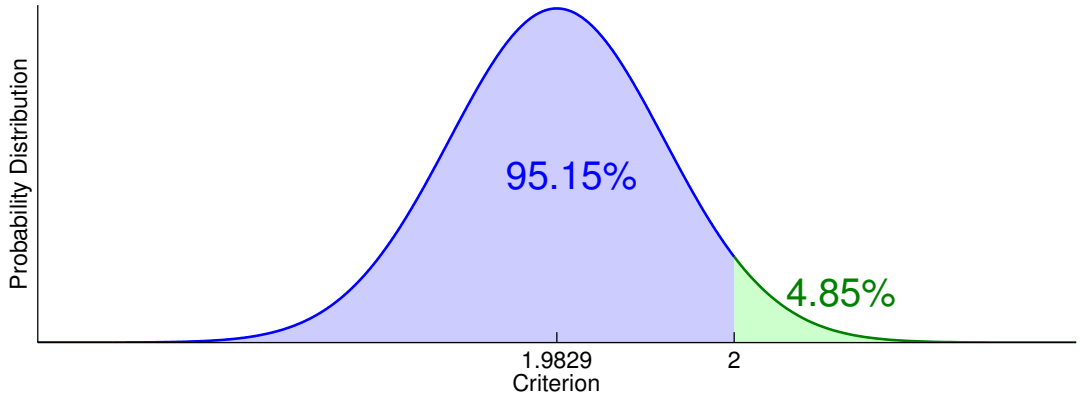

Figure 8.15: The probability distribution for the lowest point (b = 0.5015) on the inseparability curve in Figure 8.14. The curve indicates that a confidence interval of 95.15% for the value being less than 2.

The experiment in its current form was unable to demonstrate the multimode ability of this entanglement protocol. There were three experimental constraints on the timescales and bandwidth of operation. These were the coherence lifetime T_2, the detection recovery time and the available laser power (and therefore the bandwidth of the π pulses). These constraints opened a large enough time window to demonstrate entanglement with one temporal mode.

The inseparability was measured for a temporal mode orthogonal to the mode used to produce the inseparable state. The result was that the inseparability criterion was not violated. For a temporal mode that is shifted such that the overlap is zero gives little correlation as the RASE field has decayed. For an orthogonal temporal mode shape, such as the first derivative of a Gaussian, the correlation is weakened by the increase in bandwidth that this temporal mode has. Also, the frequency component at DC is zero so the correlation becomes weaker.

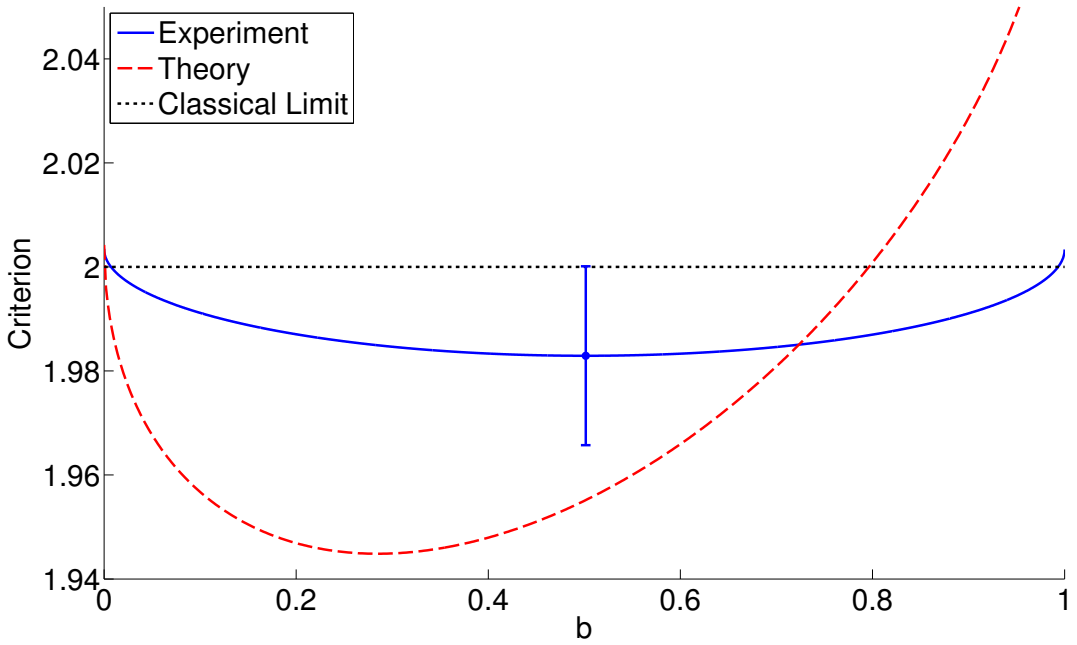

Figure 8.16: Comparison of the measured inseparability curve to the theoretical curve. The theoretical curve is calculated for an optical depth of 0.046 and using heterodyne detection. The solid blue line is the measured curve, the dashed red line is the theoretical curve and the dotted line is the classical bound. The error bar at the location of maximum violation is 1.66σ with a confidence level of 95.15% of being below the classical bound.

Chapter 9

Conclusion

This thesis explores the use of cryogenic rare earth ion doped solids for applications in quantum information science. A theoretical analysis of optical rephased memory protocols is presented and three experiments were performed. Before these experiments were conducted, the locking of the laser frequency of a laser diode to a spectral hole in cryogenic Tm^{3+}:YAG was implemented. The method used is referred to as the 'hybrid lock' as the lock uses a combination of electronic and optical feedback. The aim was to lock the laser with stability suitable for conducting phase stable photon echo experiments and to use existing resources rather than some custom-built cavity. This aim was achieved and this method of locking was the first realization of a hybrid locking scheme for diode lasers.

The first experiment was the characterization of benchmarks for a photon echo experiment and the local oscillator detection mode. The aim was to easily determine the state of the experimental apparatus by measuring the photon echo efficiency, lifetime and phase stability.

The second experiment was the measurement of amplified spontaneous emission from inverting a two level ensemble of rare earth ions. These experiments were conducted on different optical depths on the inhomogeneous line of Tm^{3+}:YAG. The aim was to characterize this noise using different rephasing pulse areas and different optical depths. Although the effects of the π pulse used in the two pulse photon echo are well known, a noise characterization such as presented in this thesis has not been done. It was shown that the amount of noise on the two pulse photon echo increased exponentially with optical depth, as expected from the theoretical analysis.

The third experiment was the measurement of rephased amplified spontaneous

emission and the time separated correlation between the noise and rephased noise. These experiments were conducted with the aim of showing that the amplified spontaneous emission can be rephased to create two time regions of photon streams that share non-classical correlations. The experiment successfully demonstrated that time separated correlations between the ASE and the RASE fields are measurable. For optical depths of 0.25 and greater, it was seen that the correlations were classical. For an optical depth of 0.046, the correlation was seen to violate the inseparability criterion. This violation of the criterion means that the ASE and RASE fields can not be described as a separable state. This experiment successfully demonstrated at a 95.15% confidence interval time separated nonclassical correlations between ASE and RASE fields.

The outlook of rephased spontaneous emission as a broadband entangler of photons is promising. Nonclassical correlations were demonstrated in this work but variations of this experiment can be implemented. Changing to a material with a greater coherence time is a possibility. Tm^{3+}:YAG was chosen for its ineffective holeburning feature so as to avoid FID phenomena resulting from holeburnt features. Changing to a material such as Pr:YSO will see an increase in coherence time and FID phenomena can be avoided by implementing a four level echo scheme [3] or phase mismatching [121].

The most promising approach in my opinion is to use a rare earth ion doped whispering gallery mode resonator [136]. Here, the optical depth can be effectively tuned by tuning the coupling to the resonator. The advantage is that the optical depth of the rephasing can be increased so as to increase the photon echo efficiency while the optical depth of the creation of the ASE can be kept low so as to still violate the Cauchy-Schwarz inequality.

This thesis paves the way for a broadband DLCZ protocol using rare earth ion doped media.

Appendix A

General Purpose Detector

In this appendix chapter the general purpose detector is presented. Figure A.1 shows the electronic schematic and is based on the low noise general purpose detector in [134].

The design has two stages. The first stage is an operational amplifier [137] (op-amp) stage using a AD829 op-amp. This op-amp provides the virtual earth to sink the photocurrent from the photodiode. The input impedance on the inverting input is large such that all photocurrent passes through resistor R_2 (see Figure A.1). The voltage drop across this resistor is the output voltage of the first stage. The second stage consists of two voltage following AD829 op-amps. These provide two buffered outputs capable of driving 50 Ω loads.

The resistance value of 1.6kΩ for the feedback resistor in the first stage is chosen such that the clearance above the dark noise is maximized. The bandwidth of detection is determined by the characteristic frequency of the feedback resistance of the first stage (R_2) and the intrinsic capacitance of the photodiode (C_t). A spike in the transfer function occurs at this characteristic frequency and an additional capacitor is placed in parallel with R_2 in order to smooth the transfer function of the circuit.

The circuit is designed such that two different photodiodes can be used. Only one diode is present when operational, that photodiode being the Hamamatsu S5971. This photodiode has a sensitivity of 0.55 Amps/Watt at 780nm giving a quantum efficiency of 88%. In the circuit, the photodiode is reversed biased with 15V in order to reduce the intrinsic capacitance below 3pF and hence increase the bandwidth beyond 33MHz.

A technical feature to consider is that the maximum power rating for the photo-

diode is 50mW with an effective active area of 1.1mm^2. To ensure that the detectors are not saturated, the size of the beam is adjusted to the size of the maximum effective area.

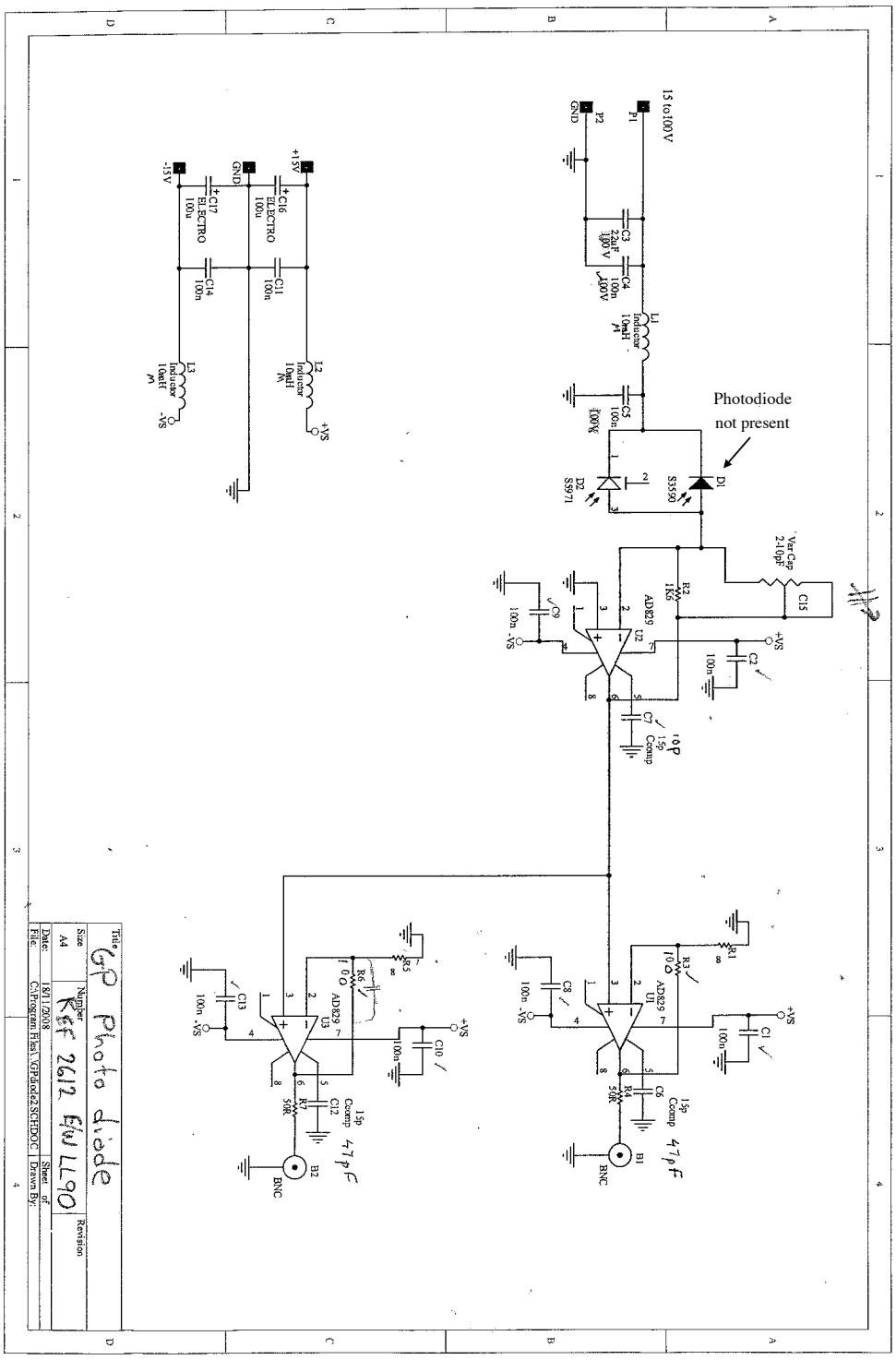

Figure A.1: Electronic schematic of the detectors used in the ASE/RASE experiments. The S3590 photodiode is not present, the S5971 photodiode is used.

Appendix B

Hybrid Photon Echo Rephasing - Workings

In this appendix chapter the analytic solutions for the hybrid photon echo rephasing (HYPER) technique are derived. The time regions are those indicated in Figure 4.11 in Chapter 4. It is noted that the procedure to obtain the solutions for the RASE protocol is similar to the derivation that follows setting the Stark shifts to zero and adjusting the boundary conditions.

B.1 Region 1 - before Stark shift

The equations of motion for time region 1 before Stark shifting is applied are given by

$$\frac{\partial}{\partial t}\hat{D}_1(z,t,\Delta) = i\Delta\hat{D}_1 + i\hat{a}_1 \tag{B.1a}$$

$$\frac{\partial}{\partial z}\hat{a}_1(z,t) = \frac{i\alpha}{2\pi}\int_{-\infty}^{\infty} d\Delta\ \hat{D}_1\ , \tag{B.1b}$$

where explanation of the symbols can be found in Chapter 4. Equation B.1a is a first order linear differential equation which can be solved using integration factor methods. The solution to Equation B.1a is

$$\begin{aligned}\hat{D}_1(z,t,\Delta) &= i\int_{-\infty}^{t} \hat{a}_1(z,t')\, e^{i\Delta(t-t')}\, dt' + \hat{D}_1(z,t_0,\Delta)e^{i\Delta t} \\ &= i\int_{-\infty}^{\infty} \hat{a}_1(z,t')\, u(t-t')\, e^{i\Delta(t-t')}\, dt' + \hat{D}_1(z,t_0,\Delta)e^{i\Delta t}\ ,\end{aligned} \tag{B.2}$$

where $u(t)$ is the unit step function. The above equation is then Fourier transformed to the frequency domain, shown below

$$\hat{D}_1(z,\omega,\Delta) = i\hat{a}_1(z,\omega)\left[\frac{1}{i(\omega-\Delta)} + \pi\delta(\omega-\Delta)\right] + 2\pi\delta(\omega-\Delta)\hat{D}_1(z,t_0,\Delta)\ . \quad \text{(B.3)}$$

This equation is then substituted into the Fourier transformed version of Equation B.1b, given below as

$$\begin{aligned}\frac{\partial}{\partial z}\hat{a}_1(z,\omega) = -\frac{\alpha}{2}\hat{a}_1(z,\omega)\int_{-\infty}^{\infty}\frac{d\Delta}{i\pi(\omega-\Delta)} - \frac{\alpha}{2}\hat{a}_1(z,\omega)\int_{-\infty}^{\infty}d\Delta\ \delta(\omega-\Delta) \\ + i\alpha\int_{-\infty}^{\infty}d\Delta\ \left[\delta(\omega-\Delta)\hat{D}_1(z,t_0,\Delta)\right]. \quad \text{(B.4)}\end{aligned}$$

The first term in this equation vanishes as an odd function in Δ integrated over all Δ is zero. This then reduces to the following differential equation

$$\frac{\partial}{\partial z}\hat{a}_1(z,\omega) + \frac{\alpha}{2}\hat{a}_1(z,\omega) = i\alpha\ \hat{D}_1(z,t_0,\omega), \quad \text{(B.5)}$$

with solution

$$\hat{a}_1(z,t) = \hat{a}_1(0,t)e^{-\alpha z/2} + i\alpha\int_0^z dz' e^{\alpha(z'-z)/2}\hat{\mathcal{D}}_1(z',t), \quad \text{(B.6)}$$

where the inverse Fourier transform has been taken and we have defined $\hat{\mathcal{D}}_1(z',t) = \mathcal{F}^{-1}\{\hat{D}_1(z,t_0,\omega)\}$.

Equations B.2 and B.6 are the solutions for region 1 for when the Stark shift is zero.

B.2 Boundary 1 - Region 1 and 2

The Stark shift and π pulse are applied. The Stark shift is applied before the π pulse and both fields are assumed to be temporally short and of a large size. With these assumptions, the dynamics of the optical field can be ignored at the boundary. The Stark shifting field alters an atoms detuning dependent on its position, given by ηz, such that $\Delta \to \Delta + \eta z$. The application of a π inverts the atomic field, $\hat{D} \to \hat{D}^\dagger$. The boundary condition at time $t = t_2$ is

$$\hat{D}_2^\dagger(z, t = t_2, \Delta) = \left[\hat{D}_1(z,t_2,\Delta)e^{i\eta_1 z}\right]^\dagger, \quad \text{(B.7)}$$

where $\eta_1 = \eta(t_f - t_i)$, η is the size of the Stark shifting interaction, $t_f - t_i$ is the duration of that field and $\hat{D}_1$ is given by Equation B.2.

B.3 Region 2

In this region a Stark shifting field is applied over the entire time region. The equations of motion are

$$\frac{\partial}{\partial t}\hat{D}_2^\dagger(z,t,\Delta) = i(\Delta + \eta' z)\hat{D}_2^\dagger - i\hat{a}_2 \tag{B.8a}$$

$$\frac{\partial}{\partial z}\hat{a}_2(z,t) = \frac{i\alpha}{2\pi}\int_{-\infty}^{\infty} d\Delta\ \hat{D}_2^\dagger\ . \tag{B.8b}$$

A similar procedure done to obtain the solutions for region 1 can be applied here. The solution to Equation B.8a is

$$\begin{aligned}\hat{D}_2^\dagger(z,t,\Delta) &= -i\int_{-\infty}^{\infty} \hat{a}_2(z,t')\,u(t-t')\,e^{i(\Delta+\eta' z)(t-t')}\ dt' + \hat{D}_2^\dagger(z,t_2,\Delta)e^{i(\Delta+\eta' z)(t-t_2)} \\ &= -i\int_{-\infty}^{\infty} \hat{a}_2(z,t')\,u(t-t')\,e^{i(\Delta+\eta' z)(t-t')}\ dt' + \hat{D}_1^\dagger(z,t_2,\Delta)e^{-i\eta_1 z}e^{i(\Delta+\eta' z)(t-t_2)}\ ,\end{aligned} \tag{B.9}$$

where the last line has had the boundary condition substituted in. This equation is then Fourier transformed and substituted into the Fourier transformed version of Equation B.8b . The solution obtained when this is done is the following,

$$\hat{a}_2(z,\omega) = \hat{a}_2(0,\omega)e^{\alpha z/2} + i\alpha e^{-i\omega t_2}\int_0^z dz' e^{\alpha(z-z')/2}\hat{D}_1^\dagger(z',t_2,\omega-\eta' z')e^{-i\eta_1 z'}. \tag{B.10}$$

We now directly substitute in for $\hat{D}_1^\dagger(z',t_2,\omega-\eta' z')$ and group the ω terms

$$\begin{aligned}\hat{a}_2(z,\omega) &= \hat{a}_2(0,\omega)e^{\alpha z/2} \\ &\quad + i\alpha\int_0^z dz' e^{\alpha(z-z')/2}\Bigg[-i\int_{-\infty}^{\infty}\hat{a}_1^\dagger(z',t')\,u(t_2-t')\,e^{i\eta'(t_2-t')z'}\ e^{-i\omega(2t_2-t')}dt' \\ &\quad + \hat{D}_1^\dagger(z',t_0,\omega-\eta' z')e^{i\eta' t_2 z'}e^{-i\omega(2t_2)}\Bigg]e^{-i\eta_1 z'}.\end{aligned} \tag{B.11}$$

The above equation is inverse Fourier transformed to the time domain, the result

shown below,

$$\hat{a}_2(z,t) = \hat{a}_2(0,t)e^{\alpha z/2} + i\alpha \int_0^z dz' e^{\alpha(z-z')/2} \Bigg[-i \int_{-\infty}^{\infty} \hat{a}_1^\dagger(z',t')\, u(t_2-t')\, e^{i\eta'(t_2-t')z'}\, \delta(t'-(2t_2-t))dt' + \hat{\mathcal{D}}_1^\dagger(z', t-2t_2)e^{i\eta' z' t} e^{i\eta' t_2 z'} \Bigg] e^{-i\eta_1 z'}. \tag{B.12}$$

Evaluating the time integral and rearranging the terms gives,

$$\hat{a}_2(z,t) = \hat{a}_2(0,t)e^{\alpha z/2} + i\alpha e^{\alpha z/2} \int_0^z dz'\, e^{-(\alpha z/2 - i\eta'(t+t_2)+i\eta_1)z'} \hat{\mathcal{D}}_1^\dagger(z', t-2t_2) + \alpha e^{\alpha z/2} u(t-t_2) \int_0^z dz'\, e^{-(\alpha/2 - i\eta'(t-t_2)+i\eta_1)z'} \hat{a}_1^\dagger(z', 2t_2-t). \tag{B.13}$$

The following definitions are made to simplify the above expression

$$\hat{b}_1(0,t) \equiv \hat{a}_1(0,t) + i\alpha \int_0^z dz' e^{\alpha z'/2} \mathcal{D}_1(z',t)$$
$$\hat{b}_2(0,t) \equiv \hat{a}_2(0,t) + i\alpha \int_0^z dz' e^{-(\alpha/2 - i\eta'(t+t_2)+i\eta_1)z'} \mathcal{D}_1(z', t-2t_2), \tag{B.14}$$

resulting in the reduced form of Equation B.13,

$$\hat{a}_2(z,t) = \hat{b}_2(0,t)e^{\alpha z/2} + \alpha\, \hat{b}_1^\dagger(0, 2t_2-t)e^{\alpha z/2}\, u(t-t_2) \int_0^z dz'\, e^{-(\alpha - i\eta'(t-t_2)+i\eta_1)z'}. \tag{B.15}$$

The integral over z' can be done to give the optical solution for region 2

$$\hat{a}_2(z,t) = \hat{b}_2(0,t)e^{\alpha z/2} + \hat{b}_1^\dagger(0, 2t_2-t)e^{\alpha z/2}\, u(t-t_2)\, \frac{\alpha\left[1 - e^{-(\alpha - i\eta'(t-t_2)+i\eta_1)z}\right]}{\alpha - i\eta'(t-t_2) + i\eta_1}. \tag{B.16}$$

Equations B.9 and B.16 are the solutions for region 2.

B.4 Boundary 2 - Region 2 and 3

A π pulse is applied at time $t = t_4$ and has the effect of $\hat{D}^\dagger \rightarrow \hat{D}$, that is, transferring the excited state population back to the ground state. The boundary condition at

time $t = t_4$ is

$$\hat{D}_3(z, t = t_4, \Delta) = \left[\hat{D}_2^{\dagger}(z, t_4, \Delta)\right]^{\dagger}, \tag{B.17}$$

where $\hat{D}_2^{\dagger}(z, t_4, \Delta)$ is given by Equation B.9.

B.5 Region 3

The equations of motion for region 3 are similar in form to the equations of motion in region 1 as both regions are ground state regions. We first state the optical solution in the frequency domain (similar to Equation B.6),

$$\hat{a}_3(z, \omega) = \hat{a}_3(0, \omega)e^{-\alpha z/2} + i\alpha e^{-i\omega t_4} \int_0^z dz' e^{\alpha(z'-z)/2} \hat{D}_3(z', t_4, \omega). \tag{B.18}$$

We now substitute in for the boundary condition

$$\hat{a}_3(z, \omega) = \hat{a}_3(0, \omega)e^{-\alpha z/2} + i\alpha e^{-i\omega t_4} \int_0^z dz' e^{\alpha(z'-z)/2} \Bigg[i \int_{-\infty}^{\infty} \hat{a}_2^{\dagger}(z', t')\, u(t_4 - t') \times e^{-i(\omega + \eta' z')(t_4 - t')}\, dt' + \hat{D}_1(z', t_2, \omega) e^{i\eta_1 z'} e^{-i(\omega + \eta' z')(t_4 - t_2)} \Bigg]. \tag{B.19}$$

The next step is to substitute in for $\hat{D}_1(z', t_2, \omega)$ (Equation B.2) as this term has ω dependance. Then, the equation is rearranged into a tidier form, resulting in the following,

$$\begin{aligned} \hat{a}_3(z, \omega) = \hat{a}_3(0, \omega)e^{-\alpha z/2} &- \alpha \int_0^z dz' e^{\alpha(z'-z)/2} \\ &\times \int_{-\infty}^{\infty} \hat{a}_2^{\dagger}(z', t')\, u(t_4 - t')\, e^{-i\eta'(t_4 - t')z'}\ e^{-i\omega(2t_4 - t')} dt' \\ &- \alpha \int_0^z dz' e^{\alpha(z'-z)/2} \int_{-\infty}^{\infty} \hat{b}_1(0, t') e^{-\alpha z'/2}\, u(t_2 - t')\, e^{-i\eta'(t_4 - t_2)z'} e^{i\eta_1 z'} e^{-i\omega(2t_4 - 2t_2 + t')}\, dt' \\ &+ i\alpha \int_0^z dz' e^{\alpha(z'-z)/2} \hat{D}_1(z', t_0, \omega) e^{-i\omega(2t_4 - 2t_2)} e^{i\eta_1 z'} e^{-i\eta'(t_4 - t_2)z'}. \end{aligned} \tag{B.20}$$

We now inverse Fourier transform the above to the time domain, the result is shown below,

$$\hat{a}_3(z,t) = \hat{a}_3(0,t)e^{-\alpha z/2} - \alpha \int_0^z dz' e^{\alpha(z'-z)/2} \times \int_{-\infty}^{\infty} \hat{a}_2^\dagger(z',t')\, u(t_4-t')\, e^{-i\eta'(t_4-t')z'}\, \delta(t-(2t_4-t'))dt' - \alpha \int_0^z dz' e^{\alpha(z'-z)/2} \int_{-\infty}^{\infty} \hat{b}_1(0,t') e^{-\alpha z'/2}\, u(t_2-t')\, e^{-i(\eta'(t_4-t_2)-\eta_1)z'} \delta(t-(2t_4-2t_2+t'))\, dt' + i\alpha \int_0^z dz' e^{\alpha(z'-z)/2} \hat{\mathcal{D}}_1(z', t-(2t_4-2t_2))\, e^{-i(\eta'(t_4-t_2)z'-\eta_1)}. \quad \text{(B.21)}$$

The time integrals can now be evaluated,

$$\begin{aligned}\hat{a}_3(z,t) = \hat{a}_3(0,t)e^{-\alpha z/2} &- \alpha e^{-\alpha z/2} \int_0^z dz' e^{\alpha z'/2} \hat{a}_2^\dagger(z', 2t_4-t)\, u(t-t_4)\, e^{-i\eta'(t-t_4)z'} \\ &- \alpha e^{-\alpha z/2} \int_0^z dz' e^{\alpha z'/2} \hat{b}_1(0, t-2t_4+2t_2) e^{-\alpha z'/2}\, u(2t_4-t_2-t)\, e^{-i(\eta'(t_4-t_2)-\eta_1)z'} \\ &+ i\alpha e^{-\alpha z/2} \int_0^z dz' e^{\alpha z'/2} \hat{\mathcal{D}}_1(z', t-(2t_4-2t_2))\, e^{-i(\eta'(t_4-t_2)-\eta_1)z'}. \end{aligned} \quad \text{(B.22)}$$

The Stark shifting fields are balanced such that $\eta'(t_4-t_2) = \eta_1$ resulting in,

$$\begin{aligned}\hat{a}_3(z,t) = \hat{b}_3(0,t)e^{-\alpha z/2} &- \alpha e^{-\alpha z/2} \int_0^z dz' \hat{a}_2^\dagger(z', 2t_4-t)\, u(t-t_4)\, e^{(\alpha/2-i\eta'(t-t_4))z'} \\ &- \alpha e^{-\alpha z/2} \hat{b}_1(0, t-2t_4+2t_2)\, u(2t_4-t_2-t) \int_0^z dz' \end{aligned} \quad \text{(B.23)}$$

where we have made the following definition

$$\hat{b}_3(0,t) \equiv \hat{a}_3(0,t) + i\alpha \int_0^z dz' e^{\alpha z'/2} \hat{\mathcal{D}}_1(z', t-2t_4+2t_2). \quad \text{(B.24)}$$

We now substitute $\hat{a}_2^\dagger(z', 2t_4-t)$ into Equation B.25 noting the balanced Stark fields,

$$\begin{aligned}\hat{a}_3(z,t) = \hat{b}_3(0,t)e^{-\alpha z/2} &- \alpha e^{-\alpha z/2} \int_0^z dz' \Bigg[\hat{b}_2^\dagger(0, 2t_4-t) \\ &+ \hat{b}_1(0, t-2t_4+2t_2)\, \frac{\alpha\left[1-e^{-(\alpha-i\eta'(t-t_4))z'}\right]}{\alpha - i\eta'(t-t_4)} \Bigg] e^{(\alpha-i\eta'(t-t_4))z'} \\ &- \alpha e^{-\alpha z/2} \hat{b}_1(0, t-2t_4+2t_2) \int_0^z dz', \end{aligned} \quad \text{(B.25)}$$

where the unit step functions have been ignored as they equate to unity in the time window of interest.

Finally, the integrals over z' are evaluated to give the final answer

$$\hat{a}_3(z,t) = \hat{b}_3(0,t)e^{-\alpha z/2} - \hat{b}_2^{\dagger}(0,2t_4-t)\,\frac{\alpha\left[e^{(\alpha-i\eta'(t-t_4))z}-1\right]}{\alpha-i\eta'(t-t_4)}\,e^{-\alpha z/2}$$
$$-\hat{b}_1(0,t-2t_4+2t_2)\left[\alpha z+\alpha^2\left(\frac{\left[e^{(\alpha-i\eta'(t-t_4))z}-1\right]}{(\alpha-i\eta'(t-t_4))^2}-\frac{z}{\alpha-i\eta'(t-t_4)}\right)\right]e^{-\alpha z/2}. \tag{B.26}$$

In the limit of infinite Stark shift, Equation B.26 reduces to the following form

$$\hat{a}_3(z,t) = \hat{b}_3(0,t)e^{-\alpha z/2} - \hat{b}_1(0,t-2t_4+2t_2)\alpha z\,e^{-\alpha z/2}. \tag{B.27}$$

Appendix C

Rephased Amplified Spontaneous Emission - Workings

This appendix chapter shows explicitly the analytics for calculating the Cauchy-Schwarz inequality and also the variance of the quadrature fields for the ASE and RASE time regions detailed in Chapter 4. The author would like to acknowledge T. Chanelière for the reviewing of the workings in this appendix.

We start by restating the quantum optical solutions for time regions 1 (ASE) and 2 (RASE):

$$\hat{a}_1(z,t) = \hat{a}_1(0,t)e^{\alpha z/2} + i\alpha \int_0^z dz'\, e^{\alpha(z-z')/2}\, \hat{\mathcal{D}}_1^\dagger(z',t), \tag{C.1}$$

$$\begin{aligned}\hat{a}_2(z,t) = \hat{a}_2(0,t)e^{-\alpha z/2} &\\ - \alpha \int_0^z dz'\, e^{\alpha(2z'-z)/2}\, \hat{a}_1^\dagger(0,-t) &\\ + i\alpha^2 \int_0^z dz' \int_0^{z'} dz'' e^{\alpha(2z'-z''-z)/2}\, \hat{\mathcal{D}}_1(z'',-t) &\\ + i\alpha \int_0^z dz'\, e^{\alpha(z'-z)/2}\, \hat{\mathcal{D}}_1(z',t)\ . &\end{aligned} \tag{C.2}$$

It is convenient to group the creation and annihilation operators to make the following definitions:

$$\hat{a}_1(z,t) \equiv A + B^\dagger \quad \text{and} \quad \hat{a}_2(z,t) \equiv C + D^\dagger\ , \tag{C.3}$$

where,

$$A \equiv \hat{a}_1(0,t)e^{\alpha z/2} \tag{C.4a}$$

$$B^\dagger \equiv i\alpha \int_0^z dz'\; e^{\alpha(z-z')/2}\; \hat{\mathcal{D}}_1^\dagger(z',t) \tag{C.4b}$$

$$\begin{aligned} C \equiv\; & \hat{a}_2(0,t)e^{-\alpha z/2} \\ & + i\alpha^2 \int_0^z dz' \int_0^{z'} dz'' e^{\alpha(2z'-z''-z)/2}\; \hat{\mathcal{D}}_1(z'',-t) \\ & + i\alpha \int_0^z dz'\; e^{\alpha(z'-z)/2}\; \hat{\mathcal{D}}_1(z,t) \end{aligned} \tag{C.4c}$$

$$D^\dagger \equiv -\alpha \int_0^z dz'\; e^{\alpha(2z'-z)/2}\; \hat{a}_1^\dagger(0,-t)\;. \tag{C.4d}$$

We can now state the Cauchy-Schwarz inequality and variance in terms of these newly defined operators. It is noted that the commutation relations for the quantum optical boundary and quantum atomic boundary fields are

$$\begin{aligned} [\hat{a}_1(0,t), \hat{a}_1^\dagger(0,t')] &\equiv \delta(t-t') \\ [\hat{\mathcal{D}}_1(z,\Delta), \hat{\mathcal{D}}_1^\dagger(z',\Delta')] &\equiv \frac{1}{\alpha}\delta(z-z')\delta(\Delta-\Delta'). \end{aligned} \tag{C.5}$$

C.1 Cauchy-Schwarz Inequality

The inequality is defined as

$$R(z) \equiv \frac{p(t_1,t_2)^2}{p(t_1,t_1)\,p(t_2,t_2)} \tag{C.6}$$

where $p(t_i,t_j) = \langle\, \hat{a}^\dagger(l,t_i)\,\hat{a}(l,t_i)\,\hat{a}^\dagger(l,t_j)\,\hat{a}(l,t_j)\,\rangle$ is the probability of having a photon each at times t_i and t_j and $p(t_i,t_i) = \langle\, (\hat{a}^\dagger(l,t_i)\;\hat{a}(l,t_i))^2\,\rangle$ is the probability of have two photons at time t_i. The inequality then becomes

$$R(z) = \frac{\langle\, \hat{a}_1^\dagger(z,t)\,\hat{a}_1(z,t)\,\hat{a}_2^\dagger(z,t')\,\hat{a}_2(z,t')\,\rangle^2}{\langle\, \hat{a}_1^\dagger(z,t)\,\hat{a}_1^\dagger(z,t)\,\hat{a}_1(z,t)\,\hat{a}_1(z,t)\,\rangle\,\langle\, \hat{a}_2^\dagger(z,t')\,\hat{a}_2^\dagger(z,t')\,\hat{a}_2(z,t')\,\hat{a}_2(z,t')\,\rangle}. \tag{C.7}$$

Let us now consider the case of $p(t_1,t_2) = \langle\, \hat{a}_1^\dagger(z,t)\,\hat{a}_1(z,t)\,\hat{a}_2^\dagger(z,t')\,\hat{a}_2(z,t')\,\rangle$. Substituting in Equations C.3,

$$\begin{aligned} p(t_1,t_2) &= \langle\, \hat{a}_1^\dagger(z,t)\, \hat{a}_1(z,t)\, \hat{a}_2^\dagger(z,t')\, \hat{a}_2(z,t')\,\rangle \\ &= \langle (A+B^\dagger)^\dagger (A+B^\dagger)(C+D^\dagger)^\dagger (C+D^\dagger)\rangle \\ &= \langle B(A+B^\dagger)(C^\dagger+D)D^\dagger\rangle \end{aligned} \tag{C.8}$$

where it is noted that $\langle 0|A^\dagger = C|0\rangle = 0$ is used to obtain the last line. Expanding this out and noting that the expectation value of an odd number of creation or annihilation operators equals zero in this case gives the following

$$p(t_1,t_2) = \langle BAC^\dagger D^\dagger\rangle + \langle BB^\dagger DD^\dagger\rangle. \tag{C.9}$$

To simplify this further, we can use the commutation relations between neighbouring operators in the above equation. For example, $BB^\dagger$ can be replaced by $[B,B^\dagger] + B^\dagger B$. Then, the $B^\dagger B$ term can be eliminated since this is inside the expectation value braces and equals zero as $B|0\rangle = \langle 0|B^\dagger = 0$. Using this we get the following

$$\begin{aligned} p(t_1,t_2) &= \langle BAC^\dagger D^\dagger\rangle + \langle BB^\dagger DD^\dagger\rangle. \\ &= \langle B([A,C^\dagger] + C^\dagger A)D^\dagger\rangle + \langle ([B,B^\dagger] + B^\dagger B)([D,D^\dagger] + D^\dagger D)\rangle. \\ &= \langle BD^\dagger[A,C^\dagger]\rangle + \langle BC^\dagger AD^\dagger\rangle + \langle [B,B^\dagger][D,D^\dagger]\rangle. \\ &= \langle [B,C^\dagger][A,D^\dagger]\rangle + \langle [B,B^\dagger][D,D^\dagger]\rangle. \end{aligned} \tag{C.10}$$

where in the third line the term containing $[A,C^\dagger]$ is eliminated as the functional form of operators A and C give a commutation relation of zero.

A similar procedure can be done for $p(t_1,t_1)$ and $p(t_2,t_2)$, and the Cauchy-Schwarz inequality is then

$$R(z) = \frac{\left([B,B^\dagger]\,[D,D^\dagger] + [B,C^\dagger]\,[A,D^\dagger]\right)^2}{4[B,B^\dagger]^2\,[D,D^\dagger]^2} = \left[\frac{1}{2} + \frac{[B,C^\dagger]\,[A,D^\dagger]}{2[B,B^\dagger][D,D^\dagger]}\right]^2. \tag{C.11}$$

C.2 ASE and RASE Variance

We now obtain analytic expressions for the variance of the quadratures of light, $\hat{x}$ and $\hat{p}$, for time regions 1 and 2 in terms of the operators A, B, C and D. The quadratures can be expressed as quantum optical field operators:

$$\hat{x}_i = \hat{a}_i + \hat{a}_i^\dagger \qquad \hat{p}_i = -i(\hat{a}_i - \hat{a}_i^\dagger), \tag{C.12}$$

where $i = \{1, 2\}$ referring to the ASE and RASE regions respectively.

Let us now look at the $\hat{x}$ quadrature. Assuming the mean is zero, the variance in the ASE region is $\langle \hat{x}_1^2 \rangle$, the variance in the RASE region is $\langle \hat{x}_2^2 \rangle$ and the covariance is $\langle \hat{x}_1 \hat{x}_2 \rangle$. For the ASE variance

$$\begin{aligned} \langle \hat{x}_1^2 \rangle &= \langle (\hat{a}_1 + \hat{a}_1^\dagger)^2 \rangle = \langle (A + B^\dagger + A^\dagger + B)^2 \rangle \\ &= \langle\ A^2 + A^{\dagger 2} + AA^\dagger + A^\dagger A + B^2 + B^{\dagger 2} \\ &\qquad + BB^\dagger + B^\dagger B + AB + AB^\dagger + A^\dagger B + A^\dagger B^\dagger\ \rangle. \end{aligned} \tag{C.13}$$

Again, terms like $A|0\rangle$ and $\langle 0|A^2|0\rangle$ are equal to zero, so the above equation reduces to

$$\langle \hat{x}_1^2 \rangle = \langle\ AA^\dagger + BB^\dagger + AB^\dagger\ \rangle. \tag{C.14}$$

We can use the commutation relations to get the final form below,

$$\langle \hat{x}_1^2 \rangle = [A, A^\dagger] + [B, B^\dagger]. \tag{C.15}$$

It is noted that the commutation relation between A and $B^\dagger$ is zero. Similar steps can be taken to obtain the variance for the RASE region and the covariance, stated below as

$$\langle \hat{x}_2^2 \rangle = [C, C^\dagger] + [D, D^\dagger] \ \text{ and } \ \langle \hat{x}_1 \hat{x}_2 \rangle = [A, D^\dagger] + [B, C^\dagger]. \tag{C.16}$$

C.3 Commutation Relations

From the above sections the required commutation relations are: $[A, A^\dagger]$, $[B, B^\dagger]$, $[C, C^\dagger]$, $[D, D^\dagger]$, $[A, D^\dagger]$ and $[B, C^\dagger]$. In this section we form these commutation relations.

It is useful to form the commutation relation of the quantum optical fields $\hat{a}_i$ and $\hat{a}_i^\dagger$. The optical field satisfies the common boson commutation relations [47, 117]

$$[\hat{a}_i, \hat{a}_j] = [\hat{a}_i^\dagger, \hat{a}_j^\dagger] = 0, \qquad [\hat{a}_i, \hat{a}_j^\dagger] = \delta_{ij}. \tag{C.17}$$

For $[\hat{a}_i, \hat{a}_j^\dagger]$ and $i = j = 1$ and using the definitions C.3, the following results

$$\begin{aligned}[\hat{a}_1, \hat{a}_1^\dagger] &= [A + B^\dagger, A^\dagger + B] = [A, A^\dagger] + [A, B] + [B^\dagger, A^\dagger] + [B^\dagger, B] \\ &= [A, A^\dagger] + [B^\dagger, B] = 1 \\ &\Rightarrow [A, A^\dagger] - [B, B^\dagger] = 1.\end{aligned} \tag{C.18}$$

Using this relation allows for a explicit calculation to be avoided. For example, one could calculate $[A, A^\dagger]$ and hence $[B, B^\dagger]$ is given from the relation. A similar procedure can be done for the case $[\hat{a}_i, \hat{a}_j^\dagger]$ and $i = j = 2$ giving the relation

$$[C, C^\dagger] - [D, D^\dagger] = 1. \tag{C.19}$$

Also, for $[\hat{a}_i, \hat{a}_j]$, $i = 1$ and $j = 2$, the following relation is obtained

$$[A, D^\dagger] = [B, C^\dagger]. \tag{C.20}$$

We now form the needed commutation relations for the Cauchy-Schwarz inequality and variance:

$[\boldsymbol{B}, \boldsymbol{B}^\dagger]$:

$$\begin{aligned}B &= -i\alpha \int_0^z dz' \mathrm{e}^{\alpha(z-z')/2} \hat{\mathcal{D}}_1(z', t) \\ B^\dagger &= i\alpha \int_0^z dz'' \mathrm{e}^{\alpha(z-z'')/2} \hat{\mathcal{D}}^\dagger{}_1(z'', t')\end{aligned}$$

$$\begin{aligned}[B, B^\dagger] &= -i\alpha \; i\alpha \int_0^z dz' \mathrm{e}^{\alpha(z-z')/2} \int_0^z dz'' \mathrm{e}^{\alpha(z-z'')/2} [\hat{\mathcal{D}}_1(z', t), \hat{\mathcal{D}}^\dagger{}_1(z'', t')] \\ &\quad \text{realize } [\hat{\mathcal{D}}_{10}(z', t), \hat{\mathcal{D}}^\dagger{}_{10}(z'', t')] = \frac{1}{\alpha}\delta(z' - z'')\delta(t - t') \\ &= -i^2\alpha^2 \frac{1}{\alpha} \int_0^z dz' \mathrm{e}^{\alpha(z-z')/2} \int_0^z dz'' \mathrm{e}^{\alpha(z-z'')/2} \delta(z' - z'')\delta(t - t') \\ &= \alpha\delta(t - t') \int_0^z dz' \mathrm{e}^{\alpha(z-z')/2} \mathrm{e}^{\alpha(z-z')/2}\end{aligned}$$

$$= \alpha\delta(t-t')\int_0^z dz' \mathrm{e}^{\alpha(z-z')} = \alpha\delta(t-t')\left[\frac{-1}{\alpha}\left(\mathrm{e}^{\alpha(z-z)} - \mathrm{e}^{\alpha(z-0)}\right)\right]$$

$$[B, B^\dagger] = \delta(t-t')\left[\mathrm{e}^{\alpha z} - 1\right].$$

$[\boldsymbol{A}, \boldsymbol{A}^\dagger]$:

$$A = \hat{a}_1(0,t)e^{\alpha z/2}$$
$$A^\dagger = \hat{a}_1^\dagger(0,t')e^{\alpha z/2}$$

$$[A, A^\dagger] = [\hat{a}_1(0,t), \hat{a}_1^\dagger(0,t')]e^{\alpha z} \qquad \text{(C.21)}$$
$$= \delta(t-t')e^{\alpha z}$$

Using the relation in Equation C.18, the same result can be achieved.

$[\boldsymbol{D}, \boldsymbol{D}^\dagger]$:

$$D = -\alpha\int_0^z dz' \mathrm{e}^{\alpha(2z'-z)/2}\hat{a_1}(0,-t)$$
$$D^\dagger = -\alpha\int_0^z dz'' \mathrm{e}^{\alpha(2z''-z)/2}\hat{a}_1^\dagger(0,-t')$$

$$[D, D^\dagger] = (-\alpha)(-\alpha)\int_0^z dz' \mathrm{e}^{\alpha(2z'-z)/2}\int_0^z dz'' \mathrm{e}^{\alpha(2z''-z)/2}[\hat{a_1}(0,-t), \hat{a}_1^\dagger(0,-t')]$$

realize $[\hat{a_1}(0,-t), \hat{a}_1^\dagger(0,-t')] = \delta(t-t')$

$$= \alpha^2\delta(t-t')\int_0^z dz' \int_0^z dz'' \mathrm{e}^{\alpha(2z'+2z''-z-z)/2} = \alpha^2\delta(t-t')\mathrm{e}^{-\alpha z}\int_0^z dz' \mathrm{e}^{\alpha z'}\int_0^z dz'' \mathrm{e}^{\alpha z''}$$

$$= \alpha^2\delta(t-t')\left(\mathrm{e}^{-\alpha z/2}\right)^2\left[\frac{1}{\alpha}\left(\mathrm{e}^{\alpha z} - \mathrm{e}^{\alpha(0)}\right)\right]^2$$

$$= \delta(t-t')\left[\mathrm{e}^{\alpha z/2} - \mathrm{e}^{-\alpha z/2}\right]^2, \quad \left[\sinh(x) = \frac{1}{2}\left[\mathrm{e}^x - \mathrm{e}^{-x}\right]\right],$$

$$[D, D^\dagger] = 4\delta(t-t')\sinh^2\left(\frac{\alpha z}{2}\right).$$

$[\boldsymbol{C}, \boldsymbol{C}^\dagger]$:

For $[C, C^\dagger]$, the relation from Equation C.19 is used to give

$$[C, C^\dagger] = 1 + 4\delta(t - t') \sinh^2\left(\frac{\alpha z}{2}\right). \tag{C.22}$$

$[\boldsymbol{A}, \boldsymbol{D}^\dagger]$:

$$\begin{aligned} A &= \hat{a_1}(0,t)\mathrm{e}^{\alpha z/2} \\ D^\dagger &= -\alpha \int_0^z dz'\ e^{\alpha(2z'-z)/2}\ \hat{a}_1^\dagger(0,-t') \end{aligned}$$

$$\begin{aligned} [A, D^\dagger] &= -\alpha\ \mathrm{e}^{\alpha z/2}\ \mathrm{e}^{-\alpha z/2} \int_0^z dz'\ e^{\alpha z'}\ [\hat{a_1}(0,t), \hat{a}_1^\dagger(0,-t')] \\ &= -\alpha\delta(t+t') \left[\frac{1}{\alpha}\left(\mathrm{e}^{\alpha z} - \mathrm{e}^{\alpha(0)}\right)\right] \\ &= -\delta(t+t')\left[\mathrm{e}^{\alpha z} - 1\right] \\ [A, D^\dagger] &= \delta(t+t')\left[1 - \mathrm{e}^{\alpha z}\right]. \end{aligned} \tag{C.23}$$

$[\boldsymbol{B}, \boldsymbol{C}^\dagger]$:

$$\begin{aligned} B &= -i\alpha \int_0^z dz' \mathrm{e}^{\alpha(z-z')/2} \hat{\mathcal{D}}_1(z',t) \\ C^\dagger &= \hat{a}_2^\dagger(0,t')\mathrm{e}^{-\alpha z/2} - i\alpha^2 \int_0^z dz'' \int_0^{z''} dz''' \mathrm{e}^{\alpha(2z''-z'''-z)/2} \hat{\mathcal{D}^\dagger}_1(z''', -t') \\ &\quad - i\alpha \int_0^z dz'' \mathrm{e}^{\alpha(z''-z)/2} \hat{\mathcal{D}^\dagger}_1(z'', t') \end{aligned}$$

$$\begin{aligned} [B, C^\dagger] &= -i\alpha \int_0^z dz' \mathrm{e}^{\alpha(z-z')/2} [\hat{\mathcal{D}}_1(z',t), \hat{a}_2^\dagger(0,t')] \\ &\quad + (-i\alpha)\left(-i\alpha^2\right) \int_0^z dz' \mathrm{e}^{\alpha(z-z')/2} \int_0^z dz'' \int_0^{z''} dz''' \mathrm{e}^{\alpha(2z''-z'''-z)/2} [\hat{\mathcal{D}}_1(z',t), \hat{\mathcal{D}^\dagger}_1(z''', -t')] \\ &\quad + (-i\alpha)\,(-i\alpha) \int_0^z dz' \mathrm{e}^{\alpha(z-z')/2} \int_0^z dz'' \mathrm{e}^{\alpha(z''-z)/2} [\hat{\mathcal{D}}_1(z',t), \hat{\mathcal{D}^\dagger}_1(z'', t')] \\ &\quad \text{Commutation relations as before and } [\hat{\mathcal{D}}_1(z',t), \hat{a}_2^\dagger(0,t')] = 0 \end{aligned}$$

$$
\begin{aligned}
&= \frac{1}{\alpha} i^2 \alpha^3 \delta(t+t') \, \mathrm{e}^{\alpha z/2} \, \mathrm{e}^{-\alpha z/2} \int_0^z dz' \mathrm{e}^{-\alpha z'/2} \int_0^z dz'' \mathrm{e}^{\alpha z''} \int_0^{z''} dz''' \mathrm{e}^{-\alpha z'''/2} \, \delta(z'-z''') \\
&\quad + \frac{1}{\alpha} i^2 \alpha^2 \delta(t-t') \, \mathrm{e}^{\alpha z/2} \, \mathrm{e}^{-\alpha z/2} \int_0^z dz' \mathrm{e}^{-\alpha z'/2} \int_0^z dz'' \mathrm{e}^{-\alpha z''/2} \delta(z'-z'') \\
&= i^2 \alpha^2 \delta(t+t') \int_0^z dz' \mathrm{e}^{-\alpha z'/2} \int_0^z dz'' \mathrm{e}^{\alpha z''} \mathrm{e}^{-\alpha z'/2} u(z''-z') \\
&\quad + i^2 \alpha \delta(t-t') \int_0^z dz' \mathrm{e}^{-\alpha z'/2} \mathrm{e}^{\alpha z'/2} \\
&= -\alpha^2 \delta(t+t') \int_0^z dz' \mathrm{e}^{-\alpha z'} \int_0^z dz'' \mathrm{e}^{\alpha z''} u(z''-z') - \alpha \delta(t-t') \int_0^z dz' \\
&= -\alpha^2 \delta(t+t') \int_0^z dz' \mathrm{e}^{-\alpha z'} \int_{z'}^z dz'' \mathrm{e}^{\alpha z''} - \alpha z \delta(t-t') \\
&= -\alpha^2 \delta(t+t') \int_0^z dz' \mathrm{e}^{-\alpha z'} \frac{1}{\alpha} \left[e^{\alpha z} - e^{\alpha z'} \right] - \alpha z \delta(t-t') \\
&= -\alpha \delta(t+t') \int_0^z dz' \mathrm{e}^{-\alpha z'} \left[e^{\alpha z} - e^{\alpha z'} \right] - \alpha z \delta(t-t') \\
&= -\alpha \delta(t+t') \left[e^{\alpha z} \frac{-1}{\alpha} \left[e^{-\alpha z} - 1 \right] - z \right] - \alpha z \delta(t-t') \\
&= \delta(t+t') \left[[1 - e^{\alpha z}] + \alpha z \right] - \alpha z \delta(t-t') \\
[B, C^\dagger] &= \delta(t+t') \left[1 - e^{\alpha z} \right] . \qquad \text{(C.24)}
\end{aligned}
$$

It is noted that the same answer can be obtained using the relation C.20.

C.4 Cauchy-Schwarz Inequality and Variance - Final Form

For the case of $t = t' = 0$, the final form of the Cauchy-Schwarz inequality is the following

$$
\begin{aligned}
R(\alpha z) &= \left[\frac{1}{2} + \frac{[B, C^\dagger] \, [A, D^\dagger]}{2[B, B^\dagger][D, D^\dagger]} \right]^2 \\
&= \left[\frac{1}{2} + \frac{[1 - e^{\alpha z}] \, [1 - \mathrm{e}^{\alpha z}]}{8 \, [\mathrm{e}^{\alpha z} - 1] \sinh^2 \left(\frac{\alpha z}{2} \right)} \right]^2 \\
&= \left[\frac{1}{2} + \frac{[e^{\alpha z} - 1]}{8 \sinh^2 \left(\frac{\alpha z}{2} \right)} \right]^2
\end{aligned}
$$

$$= \left[\frac{1}{2} + \frac{1}{2}\left(1 - e^{-\alpha z}\right)^{-2} - \frac{1}{8}\mathrm{csch}^2\left(\frac{\alpha z}{2}\right)\right]^2 \tag{C.25}$$

For the the ASE variance, RASE variance and covariance, the final form is given as

$$\begin{aligned} \langle \hat{x}_1^2 \rangle &= [A, A^\dagger] + [B, B^\dagger] = 2e^{\alpha z} - 1 \\ \langle \hat{x}_2^2 \rangle &= [C, C^\dagger] + [D, D^\dagger] = 1 + 8\sinh^2\left(\frac{\alpha z}{2}\right) \\ \langle \hat{x}_1 \hat{x}_2 \rangle &= [A, D^\dagger] + [B, C^\dagger] = 2(1 - e^{\alpha z}). \end{aligned} \tag{C.26}$$

Appendix D

Average Photon Number per Mode

This appendix chapter clarifies the use of the units 'average photon number per mode' used in Chapter 4 when referring to the quantity $\langle \hat{a}_i^\dagger(t')\hat{a}_i(t)\rangle$ for $i = 1, 2$.

Consider the number of photons in a gaussian temporal mode $k(t)$ in the ASE field $\hat{a}_1(t)$. We can form the following

$$\langle K^\dagger(t')K(t)\rangle,$$

where $K(t)$ describes the overlap of the temporal mode $k(t)$ with the ASE operator $\hat{a}_1(t)$,

$$K(t) = \int_{-\infty}^{\infty} dt\ k(t)\ \hat{a}_1(t).$$

Hence

$$\begin{aligned}
\langle K^\dagger(t')K(t)\rangle &= \left\langle \int dt'\ k^*(t')\ \hat{a}_1^\dagger(t')\ \int dt\ k(t)\ \hat{a}_1(t) \right\rangle \\
&= \left\langle \int\int dt'dt\ k^*(t')k(t)\ \hat{a}_1^\dagger(t')\hat{a}_1(t) \right\rangle \\
&= \int\int dt'dt\ |k^*(t')k(t)\ \langle \hat{a}_1^\dagger(t')\hat{a}_1(t)\rangle, \qquad \text{(D.1)}
\end{aligned}$$

where the integral is over all time and in the last line the expectation only acts on the operators.

The expectation of $\hat{a}_1^\dagger(t')\hat{a}_1(t)$ is given in Chapter 4 and Appendix C as

$$\langle \hat{a}_1^\dagger(t')\hat{a}_1(t)\rangle = \delta(t-t')\ [\mathrm{e}^{\alpha z}-1].$$

Substituting this into Equation D.1

$$\begin{aligned}\langle K^\dagger(t')K(t)\rangle &= \int\int dt'dt\ k^*(t')k(t)\ \langle \hat{a}_1^\dagger(t')\hat{a}_1(t)\rangle \\ &= [\mathrm{e}^{\alpha z}-1]\ \int\int dt'dt\ k^*(t')k(t)\ \delta(t-t') \\ &= [\mathrm{e}^{\alpha z}-1]\ \int dt\ |k(t)|^2 = 1. \end{aligned} \tag{D.2}$$

The normalization of $k(t)$ can be chosen such that the integral in Equation D.2 evaluates to 1. So, the average photon number for a gaussian temporal mode function in the ASE field is $\langle K^\dagger(t')K(t)\rangle = \exp(\alpha z) - 1$. More generally, one can say that the average photon number *per mode* in the ASE field is $\langle \hat{a}_i^\dagger(t')\hat{a}_i(t)\rangle = \exp(\alpha z) - 1$.

Appendix E

Inseparability Criterion with a Heterodyne Detector

This appendix chapter shows that the inseparability criterion of Duan et. al. [118] has the same bound for heterodyne detection as for homodyne detection.

As mentioned in Chapter 5, heterodyne detection can be described as 'noisy' homodyne detection. When measuring the quadrature $\hat{x}_i$ with a heterodyne detector, one measures

$$\hat{x}_i \rightarrow \frac{\hat{x}_i + \widehat{\text{vac}}_i}{\sqrt{2}}, \tag{E.1}$$

where $i = 1$ or 2 and $\widehat{vac}_i$ is the vacuum that enters the unused port of the 50:50 beamsplitter or equivalently the vacuum noise at $-\omega$. For the inseparability criterion given by Equations 8.4, the variance of the operator $\hat{u}$ becomes,

$$\begin{aligned}
\text{var}(u) \rightarrow\ & b\left\langle\left(\frac{\hat{x}_1 + \widehat{\text{vac}}_1}{\sqrt{2}}\right)^2\right\rangle + (1-b)\left\langle\left(\frac{\hat{x}_2 + \widehat{\text{vac}}_2}{\sqrt{2}}\right)^2\right\rangle \\
& + 2\sqrt{b(1-b)}\left\langle\left(\frac{\hat{x}_1 + \widehat{\text{vac}}_1}{\sqrt{2}}\right)\left(\frac{\hat{x}_2 + \widehat{\text{vac}}_2}{\sqrt{2}}\right)\right\rangle \\
=\ & \frac{b}{2}\left(\langle\hat{x}_1^2\rangle + \langle\widehat{\text{vac}}_1^2\rangle + \langle\hat{x}_1\widehat{\text{vac}}_1\rangle + \langle\widehat{\text{vac}}_1\hat{x}_1\rangle\right) \\
& + \frac{1-b}{2}\left(\langle\hat{x}_2^2\rangle + \langle\widehat{\text{vac}}_2^2\rangle + \langle\hat{x}_2\widehat{\text{vac}}_2\rangle + \langle\widehat{\text{vac}}_2\hat{x}_2\rangle\right) \\
& + \sqrt{b(1-b)}\left(\langle\hat{x}_1\hat{x}_2\rangle + \langle\widehat{\text{vac}}_1\widehat{\text{vac}}_2\rangle + \langle\hat{x}_1\widehat{\text{vac}}_2\rangle + \langle\widehat{\text{vac}}_1\hat{x}_2\rangle\right).
\end{aligned} \tag{E.2}$$

Since the variance of the vacuum is 1 and that the covariance terms between $\hat{x}$ and

the vacuum equate to zero then,

$$\mathrm{var}(u) = \frac{b}{2}\left(\langle \hat{x}_1^2 \rangle + 1\right) + \frac{1-b}{2}\left(\langle \hat{x}_2^2 \rangle + 1\right) + \sqrt{b(1-b)}\left(\langle \hat{x}_1 \hat{x}_2 \rangle\right) \tag{E.3}$$

For the case where the ASE and RASE fields ($\hat{x}_1$ and $\hat{x}_2$) are the vacuum, then the variance measured for the operator $\hat{u}$ is 1. A similar treatment to above can be done to the $\hat{p}$ quadrature resulting in the variance of the $\hat{v}$ operator to be 1 for the case of vacuum ASE and RASE fields. The result is that the classical bound for violating the inseparability criterion using a heterodyne detector is $\mathrm{var}(\hat{u}) + \mathrm{var}(\hat{v}) = 2$.

When comparing the above equation to the homodyne case, a factor of 2 is lost in front of the covariance term $\langle \hat{x}_1 \hat{x}_2 \rangle$. Hence, the correlation between the ASE and RASE fields (or equivalently, the 'dip' below the classical bound) is reduced by a factor of 2 when using a heterodyne detector. Figure E.1 show the theoretical inseparability curves for homodyne and heterodyne detection for the experimentally relevant case of $\alpha l = 0.046$.

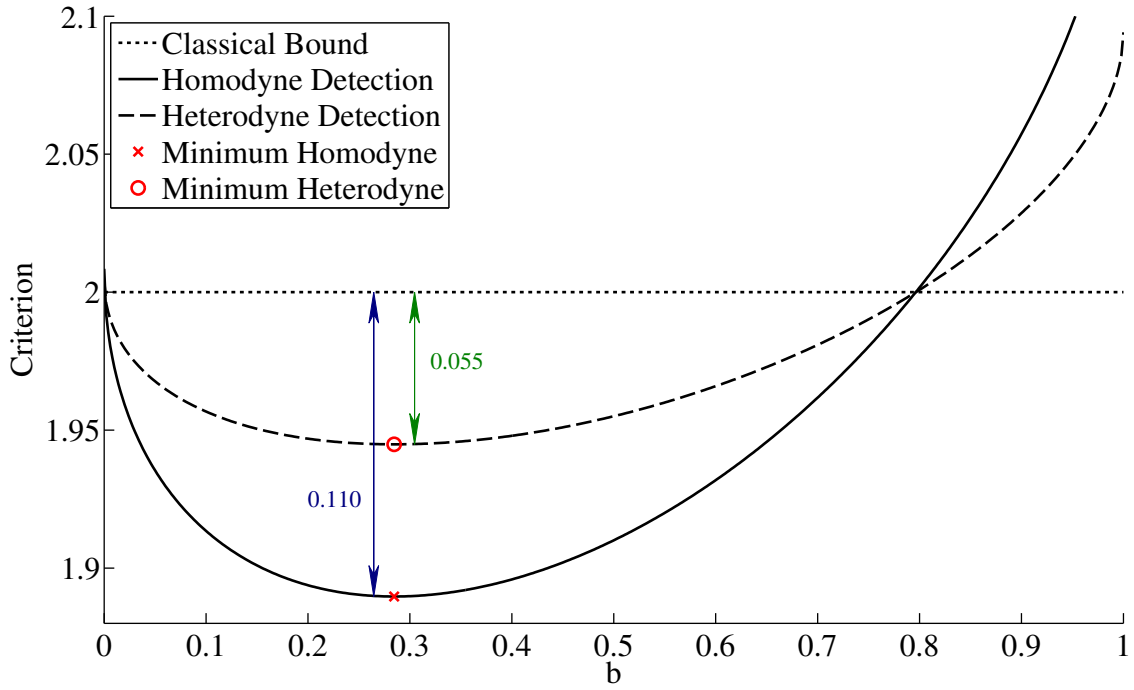

Figure E.1: Inseparability criterion for homodyne (solid line) and heterodyne (dashed line) detection. The classical bound (dotted line) is the same for both cases (see text). The curves are plotted for the experimentally relevant case of $\alpha l = 0.046$. The cross and circle indicate the minimum of the curve for homodyne and heterodyne detection respectively. Arrows indicate the 'dip' below the classical bound for the minima. Heterodyne detection results in a factor of 2 less 'dip' compared to homodyne detection. This factor of 2 is the case for any point on the curve dipping below the classical bound.

References

[1] P. M. Ledingham, W. R. Naylor, J. J. Longdell, S. E. Beavan, and M. J. Sellars, "Nonclassical photon streams using rephased amplified spontaneous emission," *Phys. Rev. A*, vol. 81, p. 012301, Jan 2010.

[2] J. W. Tay, P. M. Ledingham, and J. J. Longdell, "Coherent optical ultrasound detection with rare-earth ion dopants," *Appl. Opt.*, vol. 49, pp. 4331–4334, Aug 2010.

[3] S. E. Beavan, P. M. Ledingham, J. J. Longdell, and M. J. Sellars, "Photon echo without a free induction decay in a double-Λ system," *Opt. Lett.*, vol. 36, pp. 1272–1274, Apr 2011.

[4] D. L. McAuslan, P. M. Ledingham, W. R. Naylor, S. E. Beavan, M. P. Hedges, M. J. Sellars, and J. J. Longdell, "Photon echo quantum memories in inhomogeneously broadened two level atoms," *ArXiv e-prints*, 2011.

[5] W. G. Farr, J. W. Tay, P. M. Ledingham, D. Korystov, and J. J. Longdell, "Hybrid optical and electronic laser locking using spectral hole burning," *ArXiv e-prints*, Aug. 2010.

[6] J. W. Tay, *Optical Motion Detection*. PhD thesis, The University of Otago, 2011.

[7] D. L. McAuslan, *Quantum Computing Hardware Based on Rare-Earth-Ion Doped Whispering-Gallery Mode Resonators*. PhD thesis, The University of Otago, 2011.

[8] S. E. Beavan. PhD thesis, Australian National University.

[9] H. J. Kimble, "The quantum internet," *Nature*, vol. 453, pp. 1023–1030, 06 2008.

[10] A. Einstein, B. Podolsky, and N. Rosen, "Can Quantum-Mechanical Description of Physical Reality Be Considered Complete?," *Phys. Rev.*, vol. 47, pp. 777–780, May 1935.

[11] H.-J. Briegel, W. Dür, J. I. Cirac, and P. Zoller, "Quantum Repeaters: The Role of Imperfect Local Operations in Quantum Communication," *Phys. Rev. Lett.*, vol. 81, pp. 5932–5935, Dec 1998.

[12] C. H. Bennett, G. Brassard, C. Crépeau, R. Jozsa, A. Peres, and W. K. Wootters, "Teleporting an unknown quantum state via dual classical and Einstein-Podolsky-Rosen channels," *Phys. Rev. Lett.*, vol. 70, pp. 1895–1899, Mar 1993.

[13] D. Bouwmeester, J.-W. Pan, K. Mattle, M. Eibl, H. Weinfurter, and A. Zeilinger, "Experimental quantum teleportation," *Nature*, vol. 390, pp. 575–579, 12 1997.

[14] E. L. Hahn, "Spin Echoes," *Phys. Rev.*, vol. 80, pp. 580–594, Nov 1950.

[15] T. W. Mossberg, "Time-domain frequency-selective optical data storage," *Opt. Lett.*, vol. 7, pp. 77–79, Feb 1982.

[16] G. Liu and B. Jacquie, *Spectroscopic Properties of Rare Earths in Optical Materials*. Springer, 2005.

[17] S. Poole, D. Payne, and M. Fermann, "Fabrication of low-loss optical fibres containing rare-earth ions," *Electronics Letters*, vol. 21, no. 17, pp. 737–738, 1985.

[18] L. H. Slooff, A. van Blaaderen, A. Polman, G. A. Hebbink, S. I. Klink, F. C. J. M. Van Veggel, D. N. Reinhoudt, and J. W. Hofstraat, "Rare-earth doped polymers for planar optical amplifiers," *Journal of Applied Physics*, vol. 91, pp. 3955 –3980, apr 2002.

[19] A. J. Freeman and R. E. Watson, "Theoretical Investigation of Some Magnetic and Spectroscopic Properties of Rare-Earth Ions," *Phys. Rev.*, vol. 127, pp. 2058–2075, Sep 1962.

[20] A. A. Kaplyanskii and R. M. Macfarlane, eds., *Spectroscopy of Solids Containing Rare Earth Ions*. North-Holland Physics Publishing, Amsterdam, 1987.

[21] R. M. Macfarlane, "Inhomogeneous broadening of spectral lines in doped insulators," *Journal of Luminescence*, vol. 45, no. 1-6, pp. 1 – 5, 1990.

[22] G. H. Dieke and H. M. Crosswhite, "The Spectra of the Doubly and Triply Ionized Rare Earths," *Appl. Opt.*, vol. 2, pp. 675–686, Jul 1963.

[23] H. A. Kramers *A. Proc. Amsterdam Acad*, vol. 33, p. 959, 1930.

[24] R. W. Equall, Y. Sun, R. L. Cone, and R. M. Macfarlane, "Ultraslow optical dephasing in $Eu^{3+}Y_2SiO_5$," *Phys. Rev. Lett.*, vol. 72, pp. 2179–2182, Apr 1994.

[25] Y. Sun, C. W. Thiel, R. L. Cone, R. W. Equall, and R. L. Hutcheson, "Recent progress in developing new rare earth materials for hole burning and coherent transient applications," *Journal of Luminescence*, vol. 98, no. 1-4, pp. 281 – 287, 2002.

[26] R. Macfarlane and R. Shelby, "Magnetic field dependent optical dephasing in LaF^3:Er^{3+}," *Optics Communications*, vol. 42, no. 5, pp. 346 – 350, 1982.

[27] R. M. Macfarlane, "Photon-echo measurements on the trivalent thulium ion," *Opt. Lett.*, vol. 18, pp. 1958–1960, Nov 1993.

[28] J. Ganem, Y. P. Wang, D. Boye, R. S. Meltzer, W. M. Yen, and R. M. Macfarlane, "Nonexponential photon-echo decays of paramagnetic ions in the superhyperfine limit," *Phys. Rev. Lett.*, vol. 66, pp. 695–698, Feb 1991.

[29] R. M. Macfarlane, T. L. Harris, Y. Sun, R. L. Cone, and R. W. Equall, "Measurement of photon echoes in ErY^2SiO_5 at 1.5μm with a diode laser and an amplifier," *Opt. Lett.*, vol. 22, pp. 871–873, Jun 1997.

[30] D. R. Taylor and J. P. Hessler, "Photon echo decay in ruby: Electric dipole interactions and instantaneous diffusion," *Physics Letters A*, vol. 50, no. 3, pp. 205 – 207, 1974.

[31] J. Huang, J. M. Zhang, A. Lezama, and T. W. Mossberg, "Excess dephasing in photon-echo experiments arising from excitation-induced electronic level shifts," *Phys. Rev. Lett.*, vol. 63, pp. 78–81, Jul 1989.

[32] G. K. Liu and R. L. Cone, "Laser-induced instantaneous spectral diffusion in Tb^{3+} compounds as observed in photon-echo experiments," *Phys. Rev. B*, vol. 41, pp. 6193–6200, Apr 1990.

[33] A. M. Stoneham, "Shapes of Inhomogeneously Broadened Resonance Lines in Solids," *Rev. Mod. Phys.*, vol. 41, p. 82, Jan 1969.

[34] M. Yamaguchi, K. Koyama, T. Suemoto, and M. Mitsunaga, "Perturbed ion sites in $Eu3+:YAlO3$ studied by optical-rf double-resonance spectroscopy," *Phys. Rev. B*, vol. 59, pp. 9126–9131, Apr 1999.

[35] F. Könz, Y. Sun, C. W. Thiel, R. L. Cone, R. W. Equall, R. L. Hutcheson, and R. M. Macfarlane, "Temperature and Concentration Dependence of Optical Dephasing, Spectral-Hole Lifetime, and Anisotropic Absorption in Eu^{3+}:Y_2SiO_5," *Physical Review B*, vol. 68, Aug. 2003.

[36] R. M. Macfarlane, A. Cassanho, and R. S. Meltzer, "Inhomogeneous broadening by nuclear spin fields: A new limit for optical transitions in solids," *Phys. Rev. Lett.*, vol. 69, pp. 542–545, Jul 1992.

[37] R. M. Macfarlane, "High-resolution laser spectroscopy of rare-earth doped insulators: a personal perspective," *Journal of Luminescence*, vol. 100, no. 1-4, pp. 1 – 20, 2002.

[38] B. S. Ham, M. S. Shahriar, M. K. Kim, and P. R. Hemmer, "Spin coherence excitation and rephasing with optically shelved atoms," *Phys. Rev. B*, vol. 58, pp. R11825–R11828, Nov 1998.

[39] E. Fraval, M. J. Sellars, and J. J. Longdell, "Method of Extending Hyperfine Coherence Times in Pr^{3+}:Y_2SiO_5," *Phys. Rev. Lett.*, vol. 92, p. 077601, Feb 2004.

[40] E. Fraval, M. J. Sellars, and J. J. Longdell, "Dynamic Decoherence Control of a Solid-State Nuclear-Quadrupole Qubit," *Phys. Rev. Lett.*, vol. 95, p. 030506, Jul 2005.

[41] K. Holliday, M. Croci, E. Vauthey, and U. P. Wild, "Spectral hole burning and holography in an Y_2SiO_5:Pr^{3+} crystal," *Phys. Rev. B*, vol. 47, pp. 14741–14752, Jun 1993.

[42] L. E. Erickson and K. K. Sharma, "Nuclear quadrupole resonance measurement of the anisotropic magnetic shielding and quadrupole coupling constants of $^{151}Eu^{3+}$ and $^{153}Eu^{3+}$ dilute in $YAlO_3$ single crystal," *Phys. Rev. B*, vol. 24, pp. 3697–3700, Oct 1981.

[43] A. J. Meixner, C. M. Jefferson, and R. M. Macfarlane, "Measurement of the Stark effect with subhomogeneous linewidth resolution in Eu^{3+}:$YAlO_3$3 with the use of photon-echo modulation," *Phys. Rev. B*, vol. 46, pp. 5912–5916, Sep 1992.

[44] M Nilsson and L Rippe and N Ohlsson and T Christiansson and S Kröll, "Initial Experiments Concerning Quantum Information Processing in Rare-Earth-Ion Doped Crystals," *Physica Scripta*, vol. 2002, no. T102, p. 178, 2002.

[45] G. Gorju, A. Louchet, D. Paboeuf, F. Bretenaker, F. Goldfarb, T. Chanelière, I. Lorgeré, J.-L. L. Gouët, O. Guillot-Noël, and P. Goldner, "Stimulated optical pumping in a Tm^{3+} :YAG crystal," *Journal of Physics: Condensed Matter*, vol. 19, no. 38, p. 386226, 2007.

[46] Y. Sun, G. M. Wang, R. L. Cone, R. W. Equall, and M. J. M. Leask, "Symmetry considerations regarding light propagation and light polarization for coherent interactions with ions in crystals," *Phys. Rev. B*, vol. 62, pp. 15443–15451, Dec 2000. Copyright (2000) by the American Physical Society.

[47] D. F. Walls and G. J. Milburn, *Quantum Optics*. Springer-Verlag, Berlin Heidelberg, 1994.

[48] L. Allen and J. H. Eberly, *Optical resonance and two-level atoms*. Wiley New York,, 1975.

[49] M. O. Scully and M. S. Zubairy, *Quantum Optics*. Cambridge University Press, 1997.

[50] N. A. Kurnit, I. D. Abella, and S. R. Hartmann, "Observation of a Photon Echo," *Phys. Rev. Lett.*, vol. 13, pp. 567–568, Nov 1964.

[51] I. D. Abella, N. A. Kurnit, and S. R. Hartmann, "Photon Echoes," *Phys. Rev.*, vol. 141, pp. 391–406, Jan 1966.

[52] M. M. T. Loy, "Observation of Population Inversion by Optical Adiabatic Rapid Passage," *Phys. Rev. Lett.*, vol. 32, pp. 814–817, Apr 1974.

[53] R. Lauro, T. Chanelière, and J.-L. Le Gouët, "Adiabatic refocusing of nuclear spins in Tm^{3+}:YAG," *Phys. Rev. B*, vol. 83, p. 035124, Jan 2011.

[54] W. R. Naylor, "Characterisation of a Proposed Optical Quantum Memory," honours thesis, The University of Otago, 2008.

[55] C. S. Cornish, W. R. Babbitt, and L. Tsang, "Demonstration of highly efficient photon echoes," *Opt. Lett.*, vol. 25, pp. 1276–1278, Sep 2000.

[56] H. de Riedmatten, M. Afzelius, M. U. Staudt, C. Simon, and N. Gisin, "A solid-state light-matter interface at the single-photon level," *Nature*, vol. 456, pp. 773–777, 12 2008.

[57] A. I. Lvovsky, B. C. Sanders, and W. Tittel, "Optical quantum memory," *Nat Photon*, vol. 3, pp. 706–714, 12 2009.

[58] K. Hammerer, A. S. Sørensen, and E. S. Polzik, "Quantum interface between light and atomic ensembles," *Rev. Mod. Phys.*, vol. 82, pp. 1041–1093, Apr 2010.

[59] W. Tittel, M. Afzelius, T. Chaneliére, R. Cone, S. Kröll, S. Moiseev, and M. Sellars, "Photon-echo quantum memory in solid state systems," *Laser & Photonics Reviews*, vol. 4, no. 2, pp. 244–267, 2010.

[60] M. D. Lukin, "Trapping and manipulating photon states in atomic ensembles," *Rev. Mod. Phys.*, vol. 75, pp. 457–472, Apr 2003.

[61] C. Simon, M. Afzelius, J. Appel, A. Boyer de la Giroday, S. J. Dewhurst, N. Gisin, C. Y. Hu, F. Jelezko, S. Kröll, J. H. Müller, J. Nunn, E. S. Polzik, J. G. Rarity, H. De Riedmatten, W. Rosenfeld, A. J. Shields, N. Sköld, R. M. Stevenson, R. Thew, I. A. Walmsley, M. C. Weber, H. Weinfurter, J. Wrachtrup, and R. J. Young, "Quantum memories," *The European Physical Journal D - Atomic, Molecular, Optical and Plasma Physics*, vol. 58, pp. 1–22, 2010. 10.1140/epjd/e2010-00103-y.

[62] S. A. Moiseev and S. Kröll, "Complete Reconstruction of the Quantum State of a Single-Photon Wave Packet Absorbed by a Doppler-Broadened Transition," *Phys. Rev. Lett.*, vol. 87, p. 173601, Oct 2001.

[63] Mattias Nilsson and Stefan Kröll, "Solid state quantum memory using complete absorption and re-emission of photons by tailored and externally controlled inhomogeneous absorption profiles," *Optics Communications*, vol. 247, no. 4-6, pp. 393 – 403, 2005.

[64] A. L. Alexander, J. J. Longdell, M. J. Sellars, and N. B. Manson, "Photon Echoes Produced by Switching Electric Fields," *Phys. Rev. Lett.*, vol. 96, p. 043602, Feb 2006.

[65] B. Kraus, W. Tittel, N. Gisin, M. Nilsson, S. Kröll, and J. I. Cirac, "Quantum memory for nonstationary light fields based on controlled reversible inhomogeneous broadening," *Phys. Rev. A*, vol. 73, p. 020302, Feb 2006.

[66] N. Sangouard, C. Simon, M. Afzelius, and N. Gisin, "Analysis of a quantum memory for photons based on controlled reversible inhomogeneous broadening," *Phys. Rev. A*, vol. 75, p. 032327, Mar 2007.

[67] A. Alexander, J. Longdell, M. Sellars, and N. Manson, "Coherent information storage with photon echoes produced by switching electric fields," *Journal of Luminescence*, vol. 127, no. 1, pp. 94 – 97, 2007. Proceedings of the Ninth International Meeting on Hole Burning, Single Molecule, and Related Spectroscopies: Science and Applications, Hole Burning, Single Molecule, and Related Spectroscopies: Science and Applications.

[68] G. Hétet, J. J. Longdell, A. L. Alexander, P. K. Lam, and M. J. Sellars, "Electro-Optic Quantum Memory for Light Using Two-Level Atoms," *Phys. Rev. Lett.*, vol. 100, p. 023601, Jan 2008.

[69] J. J. Longdell, G. Hétet, P. K. Lam, and M. J. Sellars, "Analytic treatment of controlled reversible inhomogeneous broadening quantum memories for light using two-level atoms," *Phys. Rev. A*, vol. 78, p. 032337, Sep 2008.

[70] B. Lauritzen, J. c. v. Minář, H. de Riedmatten, M. Afzelius, N. Sangouard, C. Simon, and N. Gisin, "Telecommunication-Wavelength Solid-State Memory at the Single Photon Level," *Phys. Rev. Lett.*, vol. 104, p. 080502, Feb 2010.

[71] M. Afzelius, C. Simon, H. de Riedmatten, and N. Gisin, "Multimode quantum memory based on atomic frequency combs," *Phys. Rev. A*, vol. 79, p. 052329, May 2009.

[72] T. Chanelière, J. Ruggiero, M. Bonarota, M. Afzelius, and J.-L. L. Gouët, "Efficient light storage in a crystal using an atomic frequency comb," *New Journal of Physics*, vol. 12, no. 2, p. 023025, 2010.

[73] A. Amari and A. Walther and M. Sabooni and M. Huang and S. Kröll and M. Afzelius and I. Usmani and B. Lauritzen and N. Sangouard and H. de Riedmatten and N. Gisin, "Towards an efficient atomic frequency comb quantum memory," *Journal of Luminescence*, vol. 130, no. 9, pp. 1579 – 1585, 2010. Special Issue based on the Proceedings of the Tenth International Meeting on Hole Burning, Single Molecule, and Related Spectroscopies: Science and Applications (HBSM 2009) - Issue dedicated to Ivan Lorgeré and Oliver Guillot-Noël.

[74] Afzelius, Mikael and Usmani, Imam and Amari, Atia and Lauritzen, Björn and Walther, Andreas and Simon, Christoph and Sangouard, Nicolas and Minář, Jiří and de Riedmatten, Hugues and Gisin, Nicolas and Kröll, Stefan , "Demonstration of Atomic Frequency Comb Memory for Light with Spin-Wave Storage," *Phys. Rev. Lett.*, vol. 104, p. 040503, Jan 2010.

[75] M. A. Nielsen and I. L. Chuang, *Quantum Computation and Quantum Information (Cambridge Series on Information and the Natural Sciences)*. Cambridge University Press, 2004.

[76] R. Feynman, "Simulating physics with computers," *International Journal of Theoretical Physics*, vol. 21, pp. 467–488, 1982. 10.1007/BF02650179.

[77] D. Deutsch, "Quantum Theory, the Church-Turing Principle and the Universal Quantum Computer," *Proceedings of the Royal Society of London. A. Mathematical and Physical Sciences*, vol. 400, no. 1818, pp. 97–117, 1985.

[78] R. Feynman, "Quantum mechanical computers," *Foundations of Physics*, vol. 16, pp. 507–531, 1986. 10.1007/BF01886518.

[79] D. Deutsch, "Quantum Computational Networks," *Proceedings of the Royal Society of London. A. Mathematical and Physical Sciences*, vol. 425, no. 1868, pp. 73–90, 1989.

[80] R. P. Feynman and A. Hey, *Feynman Lectures On Computation*. Westview Press, 2000.

[81] C. H. Bennett and G. Brassard. In Proceedings of IEEE International Conference on Computers, Systems, and Signal Processing, Bangalore, India, (IEEE, New York, 1984), p. 175.

[82] A. K. Ekert, "Quantum cryptography based on Bell's theorem," *Phys. Rev. Lett.*, vol. 67, pp. 661–663, Aug 1991.

[83] J. von Neumann, *Mathematische Grundlagen der Quantenmechanik (German Edition)*. Springer, 1995.

[84] W. Heisenberg, "Über den anschaulichen Inhalt der quantentheoretischen Kinematik und Mechanik," *Zeitschrift für Physik A Hadrons and Nuclei*, vol. 43, pp. 172–198, 1927. 10.1007/BF01397280.

[85] W. K. Wootters and W. H. Zurek, "A single quantum cannot be cloned," *Nature*, vol. 299, pp. 802–803, 10 1982.

[86] D. Dieks, "Communication by EPR devices," *Physics Letters A*, vol. 92, no. 6, pp. 271 – 272, 1982.

[87] P. G. Kwiat, K. Mattle, H. Weinfurter, A. Zeilinger, A. V. Sergienko, and Y. Shih, "New High-Intensity Source of Polarization-Entangled Photon Pairs," *Phys. Rev. Lett.*, vol. 75, pp. 4337–4341, Dec 1995.

[88] S. Takeuchi, R. Okamoto, and K. Sasaki, "A single photon source using parametric down conversion," in *Quantum Electronics Conference, 2003. EQEC '03. European*, p. 320, june 2003.

[89] A. Zavatta, S. Viciani, and M. Bellini, "Tomographic reconstruction of the single-photon Fock state by high-frequency homodyne detection," *Phys. Rev. A*, vol. 70, p. 053821, Nov 2004.

[90] C. Simon, H. de Riedmatten, M. Afzelius, N. Sangouard, H. Zbinden, and N. Gisin, "Quantum Repeaters with Photon Pair Sources and Multimode Memories," *Phys. Rev. Lett.*, vol. 98, p. 190503, May 2007.

[91] M. A. Albota and F. C. Wong, "Efficient single-photon counting at 1.55 μm by means of frequency upconversion," *Opt. Lett.*, vol. 29, pp. 1449–1451, Jul 2004.

[92] C. Langrock, E. Diamanti, R. V. Roussev, Y. Yamamoto, M. M. Fejer, and H. Takesue, "Highly efficient single-photon detection at communication wavelengths by use of upconversion in reverse-proton-exchanged periodically poled $LiNbO_3$ waveguides," *Opt. Lett.*, vol. 30, pp. 1725–1727, Jul 2005.

[93] M. T. Rakher, L. Ma, O. Slattery, X. Tang, and K. Srinivasan, "Quantum transduction of telecommunications-band single photons from a quantum dot by frequency upconversion," *Nat Photon*, vol. advance online publication, pp. – , 10 2010.

[94] M. P. Hedges, J. J. Longdell, Y. Li, and M. J. Sellars, "Efficient quantum memory for light," *Nature*, vol. 465, pp. 1052–1056, June 2010.

[95] S. Moiseev and M. Noskov, "The possibilities of the quantum memory realization for short pulses of light in the photon echo technique," *Laser Physics Letters*, vol. 1, no. 6, pp. 303–310, 2004.

[96] S. A. Moiseev and N. M. Arslanov, "Efficiency and fidelity of photon-echo quantum memory in an atomic system with longitudinal inhomogeneous broadening," *Phys. Rev. A*, vol. 78, p. 023803, Aug 2008.

[97] G. Hétet, J. J. Longdell, A. L. Alexander, P. K. Lam, and M. J. Sellars, "Electro-Optic Quantum Memory for Light Using Two-Level Atoms," *Phys. Rev. Lett.*, vol. 100, p. 023601, Jan 2008.

[98] M. Hosseini, B. M. Sparkes, G. Hetet, J. J. Longdell, P. K. Lam, and B. C. Buchler, "Coherent optical pulse sequencer for quantum applications," *Nature*, vol. 461, pp. 241–245, 09 2009.

[99] J. Nunn, K. Reim, K. C. Lee, V. O. Lorenz, B. J. Sussman, I. A. Walmsley, and D. Jaksch, "Multimode Memories in Atomic Ensembles," *Phys. Rev. Lett.*, vol. 101, p. 260502, Dec 2008.

[100] M. Bonarota, J. Ruggiero, J. L. L. Gouët, and T. Chanelière, "Efficiency optimization for atomic frequency comb storage," *Phys. Rev. A*, vol. 81, p. 033803, Mar 2010.

[101] M. Sabooni, F. Beaudoin, A. Walther, N. Lin, A. Amari, M. Huang, and S. Kröll, "Storage and Recall of Weak Coherent Optical Pulses with an Efficiency of 25%," *Phys. Rev. Lett.*, vol. 105, p. 060501, Aug 2010.

[102] I. Usmani, M. Afzelius, H. de Riedmatten, and N. Gisin, "Mapping multiple photonic qubits into and out of one solid-state atomic ensemble," *Nat Commun*, vol. 1, 04 2010.

[103] M. Bonarota, J.-L. L. Gouët, and T. Chanelière, "Highly multimode storage in a crystal," *New Journal of Physics*, vol. 13, no. 1, p. 013013, 2011.

[104] C. Clausen, I. Usmani, F. Bussieres, N. Sangouard, M. Afzelius, H. de Riedmatten, and N. Gisin, "Quantum storage of photonic entanglement in a crystal," *Nature*, vol. 469, pp. 508–511, 01 2011.

[105] L. M. Duan, M. D. Lukin, J. I. Cirac, and P. Zoller, "Long-distance quantum communication with atomic ensembles and linear optics," *Nature*, vol. 414, pp. 413–418, 11 2001.

[106] L. Childress, J. M. Taylor, A. S. Sørensen, and M. D. Lukin, "Fault-Tolerant Quantum Communication Based on Solid-State Photon Emitters," *Phys. Rev. Lett.*, vol. 96, p. 070504, Feb 2006.

[107] L. Jiang, J. M. Taylor, and M. D. Lukin, "Fast and robust approach to long-distance quantum communication with atomic ensembles," *Phys. Rev. A*, vol. 76, p. 012301, Jul 2007.

[108] Z.-B. Chen, B. Zhao, Y.-A. Chen, J. Schmiedmayer, and J.-W. Pan, "Fault-tolerant quantum repeater with atomic ensembles and linear optics," *Phys. Rev. A*, vol. 76, p. 022329, Aug 2007.

[109] N. Sangouard, C. Simon, J. c. v. Minář, H. Zbinden, H. de Riedmatten, and N. Gisin, "Long-distance entanglement distribution with single-photon sources," *Phys. Rev. A*, vol. 76, p. 050301, Nov 2007.

[110] B. Zhao, Z.-B. Chen, Y.-A. Chen, J. Schmiedmayer, and J.-W. Pan, "Robust Creation of Entanglement between Remote Memory Qubits," *Phys. Rev. Lett.*, vol. 98, p. 240502, Jun 2007.

[111] N. Sangouard, C. Simon, B. Zhao, Y.-A. Chen, H. de Riedmatten, J.-W. Pan, and N. Gisin, "Robust and efficient quantum repeaters with atomic ensembles and linear optics," *Phys. Rev. A*, vol. 77, p. 062301, Jun 2008.

[112] K. S. Choi, H. Deng, J. Laurat, and H. J. Kimble, "Mapping photonic entanglement into and out of a quantum memory," *Nature*, vol. 452, pp. 67–71, 03 2008.

[113] M. Żukowski, A. Zeilinger, M. A. Horne, and A. K. Ekert, ""Event-ready-detectors" Bell experiment via entanglement swapping," *Phys. Rev. Lett.*, vol. 71, pp. 4287–4290, Dec 1993.

[114] E. Saglamyurek, N. Sinclair, J. Jin, J. A. Slater, D. Oblak, F. Bussieres, M. George, R. Ricken, W. Sohler, and W. Tittel, "Broadband waveguide quantum memory for entangled photons," *Nature*, vol. 469, pp. 512–515, 01 2011.

[115] J. Ruggiero, J.-L. Le Gouët, C. Simon, and T. Chanelière, "Why the two-pulse photon echo is not a good quantum memory protocol," *Phys. Rev. A*, vol. 79, p. 053851, May 2009.

[116] C. W. Gardiner and M. J. Collett, "Input and output in damped quantum systems: Quantum stochastic differential equations and the master equation," *Phys. Rev. A*, vol. 31, pp. 3761–3774, Jun 1985.

[117] C. W. Gardiner and P. Zoller, *Quantum Noise (2nd Edition)*. Springer-Verlag, Berlin Heidelberg, 2000.

[118] L.-M. Duan, G. Giedke, J. I. Cirac, and P. Zoller, "Inseparability Criterion for Continuous Variable Systems," *Phys. Rev. Lett.*, vol. 84, pp. 2722–2725, Mar 2000.

[119] I. Zafarullah, M. Tian, T. Chang, and W. R. Babbitt, "Preparation of inverted medium and processing in the inverted medium," *Journal of Luminescence*, vol. 127, no. 1, pp. 158 – 163, 2007. Proceedings of the Ninth International Meeting on Hole Burning, Single Molecule, and Related Spectroscopies: Science and Applications, Hole Burning, Single Molecule, and Related Spectroscopies: Science and Applications.

[120] J. Ruggiero, T. Chanelière, and J.-L. L. Gouët, "Coherent response to optical excitation in a strongly absorbing rare-earth ion-doped crystal," *J. Opt. Soc. Am. B*, vol. 27, pp. 32–37, Jan 2010.

[121] V. Damon, M. Bonarota, A. Louchet-Chauvet, T. Chanelière, and J.-L. L. Gouët, "Revival of Silenced Echo and Quantum Memory for Light," 2011.

[122] J. S. W. A. S. Arnold and M. G. Boshier, "A simple extended-cavity diode laser," *Rev. Sci. Instrum.*, vol. 69, pp. 236–1239, 1998.

[123] K. Liu and M. G. Littman, "Novel geometry for single-mode scanning of tunable lasers," *Opt. Lett.*, vol. 6, pp. 117–118, Mar 1981.

[124] K. G. Libbrecht and J. L. Hall, "A Low-Noise High-Speed Diode Laser Current Controller," *Rev. Sci. Instrum.*, vol. 64, p. 2133, 1993.

[125] R. W. P. Drever, J. L. Hall, F. V. Kowalski, J. Hough, G. M. Ford, A. J. Munley, and H. Ward, "Laser phase and frequency stabilization using an optical resonator," *Applied Physics B: Lasers and Optics*, vol. 31, pp. 97–105, 1983. 10.1007/BF00702605.

[126] G.J. Pryde and T. Böttger and R.L. Cone, "Numerical modeling of laser stabilization by regenerative spectral hole burning," *Journal of Luminescence*, vol. 94-95, pp. 587 – 591, 2001. International Conference on Dynamical Processes in Excited States of Solids.

[127] Thomas Böttger and Y. Sun and G.J. Pryde and G. Reinemer and R.L. Cone, "Diode laser frequency stabilization to transient spectral holes and spectral diffusion in Er^{3+}:Y_2SiO_5 at 1536nm," *Journal of Luminescence*, vol. 94-95, pp. 565 – 568, 2001. International Conference on Dynamical Processes in Excited States of Solids.

[128] G. J. Pryde and T. Böttger and R. L. Cone and R. C. C. Ward, "Semiconductor lasers stabilized to spectral holes in rare earth crystals to a part in 1013 and their application to devices and spectroscopy," *Journal of Luminescence*, vol. 98, no. 1-4, pp. 309 – 315, 2002.

[129] B. Julsgaard, A. Walther, S. Kröll, and L. Rippe, "Understanding laser stabilization using spectral hole burning," *Opt. Express*, vol. 15, pp. 11444–11465, Sep 2007.

[130] G. P. Agrawal, "Line Narrowing in a Single-Mode Injection Laser Due to External Optical Feedback," *Quantum Electron*, vol. 20, pp. 468–471, 1984.

[131] J. K. A. Y. . M. Iannelli, Y. Shevy, "Linewidth Reduction and Frequency Stabilization of Semiconductor Lasers Using Dispersive Losses in Atomic Vapor," *Quantum Electron*, vol. 29, pp. 1253–1261, 1993.

[132] H.-A. Bachor and T. C. Ralph, *A Guide to Experiments in Quantum Optics*. Wiley-VCH, 2004.

[133] U. Leonhardt, *Measuring the Quantum State of Light (Cambridge Studies in Modern Optics)*. Cambridge University Press, 1997.

[134] M. B. Gray, D. A. Shaddock, C. C. Harb, and H.-A. Bachor, "Photodetector designs for low-noise, broadband, and high-power applications," *Review of Scientific Instruments*, vol. 69, no. 11, pp. 3755–3762, 1998.

[135] Y. Bar-Shalom, X. R. Li, and T. Kirubarajan, *Estimation with Applications to Tracking and Navigation*. Wiley-Interscience, 2001.

[136] D. L. McAuslan, D. Korystov, and J. J. Longdell, "Coherent spectroscopy of rare-earth-ion doped whispering-gallery mode resonators," *ArXiv e-prints*, 2011.

[137] P. Horowitz and W. Hill, *The Art of Electronics*. Cambridge University Press, 1989.